Fabrication, Surface Engineering, Cellular Uptake and Cytotoxicity of Metallic and Polymeric Nanoparticles

Dissertation presented to the Department of Applied Chemistry

University of the Basque Country (UPV/EHU), San Sebastián

for the degree of International Doctor

in Applied Chemistry and Polymeric Materials

Presented by

Yuan Qiu

Thesis Supervisor: **Dr. Sergio E. Moya**

University Tutor: **Dr. David Mecerreyes**

Donostia-San Sebastián, Spain
2014

This PhD thesis has been performed at:

CIC biomaGUNE

Biosurfaces Unit

Donostia-San Sebastian, Spain

Ernst-Moritz-Arndt-Universität Greifswald

ZIK HIKE (Humorale Immunreaktionen

bei kardiovaskulären Erkrankungen)

Nanostructure Group

Greifswald, Germany

Acknowledgements

In this page I would like to express my sincere gratitude to my supervisor Dr. Sergio E. Moya. Without his kind support for both my scientific work and my life in San Sebastian, I could not have managed to finish my PhD study on time. I have learned from him not only the scientific knowledge but also the way how to doing scientific research. And to Dr. David Mecerreyes (UPV-EHU), he is my tutor at university and gave me very kind supports in various aspects.

My special thanks to Dr. Richard Murray, we have done a lot of work together, and I have learned so much from him, not just knowledge about fluorescence physics, but also many other things. Many thanks to Dr. Gabriela Romero, our former group member; she has helped me a lot with the study of cells and Raman spectroscopy, as well as many aspects of my life. I am grateful to all the group members, Elena Rojas, María Echeverría, Joseba Irigoyen, Eleftheria Diamanti, Dr. Guocheng Wang, Danijela Gregurec, Dr.Nikolaos Politakos and Dr. Marco Marradi, for their help in my scientific work and my life. I would like to show my acknowledgment to Dr. Irantzu Llarena and Marco Moller, our platform managers, for their support of optical spectroscopy and TEM.

Many Thanks to Dr. Mihaela Delcea, Dr. Raghavendra Palankar, Dr. Mykola Medvidov and all other people from ZIK HIKE, for the good experience of collaboration there in Germany. They all helped me in many aspects with my stay in Greifswald.

For the financial support, I would like show my gratitude to China Scholarship Council and European Commission in the framework of FP7 HINAMOX (CP-FP 228825-2).

My most sincere gratitude to all the people in CIC biomaGUNE and San Sebastian that helped me, in one way or another, during these past four years. It is an unforgettable period of time in my life.

Contents

List of Figures

Introduction

Chapter 1 Materials and Methods

Chapter 2 Materials and Methods Surface modification of CeO2 NPs and their uptake, intracellular distribution and cytotoxicity

Chapter 3 Quantitative Study of Intracellular Dynamics of Metallic Nanoparticles via Fluorescence Correlation Spectroscopy

Chapter 4 Monitoring Intracellular Degradation Kinetics of Poly (lactide-co-glycolide) Nanoparticles by means of Flow Cytomery

Chapter 5 Design of Hybrid Multimodal PLGA Polymeric Nanoparticles for Neutrophil Labeling, Imaging and Tracking

Abstract

This PhD dissertation is focused on the fabrication and surface engineering of metallic, metal oxide and polymeric nanoparticles (NPs), and the study of their cytotoxicity, intracellular behavior, trafficking, localization and biological fate *in vitro*.

The role of the surface coating of NPs and its charge to control the interaction with cells was studied with CeO_2 NPs (CNPs) coated with either positively or negatively charged polyelectrolyte brushes via *in situ* Atomic Transfer Radical Polymerization (ATRP). Polymer brush provides higher surface charge density and better colloidal stability in aqueous media to CNPs. CNPs coated with polyelectrolyte brushes were fluorescently labeled. The fluorescent dye was attached directly to the surface of the CNPs remaining inside the polymer shell. In this way the dye will remain entrapped in the brush and will not impact on the surface properties of polymer brush coated CNPs. Polymer brush coated CNPs showed slower cellular uptake than unmodified CNPs and the uptake mechanisms were also altered. Moreover, polymer brush coated CNPs showed higher colocalization with acidic cell compartments in the cell, meaning that these CNPs were mostly internalized through endosomal and lysosomal involved endocytosis. The different surface charge resulted in different levels of cytotoxicity. The effect of surface modified CNPs on the intracellular generation of reactive oxygen species (ROS) was also examined. Cells with internalized polymer brush coated CNPs showed a much lower ROS level than control cells after exposure to ROS inducer. This indicates that the antioxidant properties of the CNPs were also presented in the polymer coated CNPs.

The intracellular dynamics of NPs inside cells was studied by means of Fluorescence Correlation Spectroscopy (FCS). Glucose derivative conjugated gold NPs (Glc-Au NPs) were chosen as model NPs for these studies since they have little non specific interactions with proteins due to the glucose derivative coating, and should therefore display a lesser degree of aggregation. Glc-Au NPs formed aggregates when incubated in DMEM with

10% FBS, as hinted by the change in their FCS correlation value reflecting a change in the relative concentration of single NPs compared to those in distilled water. The diffusion time increased from 113.2 μs in distilled water to 243.3 μs in DMEM with 10% FBS. The corresponding concentration decreased from 77.4 nM to 37.0 nM. The hydrodynamic size increased from 2 nm to 4.4 nm.

Intracellularly, the formation of large aggregates of NPs that behave as an immobilized fraction limits the applicability of FCS. To apply FCS intracellularly to measure NP diffusion, a prebleaching strategy was employed. The prebleaching eliminates the fluorescence of large aggregates and makes it possible to obtain meaningful correlation curves by FCS. Then, intracellular dynamics, concentration, hydrodynamic radius, etc. of Glc-Au-Hi NPs were studied. Measured diffusion times range from 238 μs to 780 μs. The narrow range of diffusion times allowed us to conclude that only single NPs and small aggregates of NPs contribute to the mobile fraction. Approximately 88 % of the aggregates are between 3.5 nm and 7.0 nm. Occasionally aggregates over 780 μs (~12%) can be measured but most of these aggregates can be considered as immobile. In addition, FCS data hinted that NPs are localized in aqueous environments within the cell.

Biodegradable poly (lactide-co-glycolide) (PLGA) NPs with BSA as a stabilizer were fabricated through O/W emulsion method. The NPs were prepared with PLGA polymers with 15 % or 35 % glycolide. The degradation of PLGA NPs has been studied under physiological and intracellular conditions by means of flow cytometry (FACS). In a physiological solution, FACS can trace the variations in the fluorescence of rhodamine B labeled PLGA NPs with 15 % glycolide (PLGA 15) due to the release of labeled polymer as degradation proceeds over 20 days while no change in fluorescence is observed for the PLGA NPs with 35 % (PLGA 35) after 70 days. Degradation was confirmed by Transmission Electron Microscopy, Dynamic Light Scattering and zeta potential measurements. Intracellular degradation of PLGA NPs was followed by FACS measuring the changes in fluorescence intensity per cell over time. Rhodamine B displays a higher quantum yield in a polar environment like that of the cells than in a non-polar media like inside the PLGA NPs. When labeled PLGA molecules are released from the PLGA NPs

into the cell environment, their fluorescence will increase. An increase in fluorescence intensity was observed during the first 24h for cells with PLGA15 NPs while no changes in fluorescence were observed of PLGA35, meaning that PLGA15 degraded during the first 24 hours while PLGA35 did not. Additionally, Confocal Raman Microscopy (CRM) was used to trace degradation intracellularly at single cell level by recording the relative changes of the bands at 1768 cm^{-1} and at 872 cm^{-1}. The band at 1768 cm^{-1} corresponds to C=O vibration of the ester group of PLGA. As degradation takes place, the hydrolysis of the ester should decrease the intensity of the band at 1768 cm-1. The band at 872 cm^{-1} is assigned to the C-COO vibration of lactic acid, which will not be affected by the hydrolysis process during the degradation. Therefore, the change of ratio between the band at 1768cm^{-1} and that of 872 cm^{-1} reveals the change of the amount of ester group during the degradation. The results from CRM showed that intracellular PLGA15 NPs had a decrease in the intensity of the ester group after incubated with cells for 120h.Whereas PLGA35 NPs did not show a significant change after 120h incubation with cells. The decrease intensity of the ester group indicates the break of ester bond and the degradation of NPs. This corroborated the degradation of the PLGA15 and the stability of the PLGA35 NPs intracellularly.

Finally, PLGA NPs incorporating quantum dots (QDs), superparamagnetic iron oxide nanoparticles (SPIONs) and gold NPs (Au NPs) were fabricated via the W/O/W double emulsion method. QDs and SPIONs were entrapped inside PLGA NPs during emulsification while Au NPs were assembled on top of the PLGA NPs via electrostatic interactions. The uptake of the hybrid PLGA NPs by human neutrophils was studied by FACS and Confocal Laser Scanning Microscopy (CLSM). In addition, the induction of reactive oxygen species (ROS) in neutrophils after incubation with the hybrid PLGA NPs was assessed. Magnetophoresis experiments showed that neutrophils with internalized hybrid PLGA NPs can be effectively laterally displaced twoards the magnetic field. Magnetic Resonance Imaging (MRI) of the hybrid PLGA NPs resulted in images with a contrast enhancement linearly dependent on the concentration of the hybrid PLGA NPs. The hybrid NPs have potential for in vivo applications, e.g., tumor visualization and localized photothermal treatment.

Resumen

La nanotecnología es una de las áreas de la ciencia que más rápidamente se ha desarrollado en los últimos años. La producción estimada de nanomateriales (NMs) se incrementará de 2.300 toneladas en 2008 a 58.000 toneladas en 2020. Esta enorme cantidad de materiales puede traer beneficios, pero también conlleva riesgos potenciales para humanos y el medio ambiente. En unos casos, los seres humanos se exponen a los NMs durante la fabricación, la manipulación y el uso de dispositivos o materiales que incluyen nanoestructuras en su formulación. En este tipo de casos se da una exposición no intencional. En el caso de las aplicaciones médicas de los NMs, la exposición es intencional. En ambos casos, el impacto de los NMs en la salud humana todavía no se conoce completamente. Los NMs, dependiendo de la ruta de exposición: tópica, oral, intravenosa (nanomedicina), o por inhalación, pueden circular en el cuerpo y traslocarse entre los diferentes órganos y tejidos. Finalmente llegan al interior de la célula donde pueden interferir con las funciones celulares.

Esta tesis se centrará en la fabricación e ingeniería superficial de NPs , de óxidos metálicos y poliméricas, la combinación de las tres para formar NPs híbridas , el estudio de su citotoxicidad, comportamiento intracelular, cinética, localización y el destino *in vitro*.

El trabajo realizado en esta tesis, está organizado en una introducción y seis capítulos que se resumen a continuación:

En el **Capítulo 1**, se detallan los materiales, métodos y técnicas necesarias para la realización del trabajo experimental presentado en esta tesis.

En el **Capítulo 2**, se presenta la modificación de la superficie de las NPs de óxido de cerio (CNPs) mediante cepillos de polielectrolitos sintetizados a partir de la superficie de las NPs, y los efectos de esta modificación en la asimilación celular, distribución

intracellular y toxicidad de las NPs. Se han empleado dos tipos de cepillos de polielectrolito: poli (3-sulfopropilamino metacrilato) (PSPM) y cloruro de poli [2-(metacriloiloxi) etil trimetilamonio] (PMETAC). El PSPM tiene una carga superficial negativa y el PMETAC positiva. Los cepillos poliméricos mejoran la estabilidad coloidal de las NPs de óxido cerio en medio acuoso. Las CNPs se marcaron con fluoróforos unidos directamente a la superficie de la propia nanoparticula, de la cual posteriormente se sintetizará el cepillo, quedando por tanto el fluoróforo encapsulado dentro del cepillo, no afectando las propiedades superficiales de las NPs recubiertas de cepillo. El marcaje posibilita el uso de técnicas que requieren fluorescencia tales como la citometría de flujo (FACS) y microscopía láser confocal de barrido (CLSM).

Los resultados obtenidos sobre la asimilación celular muestran que las CNPs con cepillos poliméricos tienen una cinética de asimilación más lenta que las CNPs sin modificar. Sin embargo, las CNPs modificadas con PMETAC (CeO_2@PMETAC) tienen una cinética de asimilación continua las primeras 48 horas, mientras la cantidad asimilada de otros tipos de CNPs no aumenta después de las primeras 24h. Además, los resultados de CLSM muestran que las CNPs modificadas presentan una mayor co localización con los orgánulos ácidos que las CNPs sin modificar. Los resultados obtenidos por Microscopia Raman Confocal (CRM) muestran que las CNPs modificadas presentan mayor colocalización con las regiones de cuerpos lipídicos que las CNPs sin modificar. Ambas técnicas demuestran que las CNPs modificadas se internalizan en las células por endocitosis interviniendo endosomas y lisosomas. El mecanismo de asimilación celular también cambia con la modificación de las CNPs. En relación a toxicidad de las CNPs, se observan diferencias según la línea de celular testada. Pero las CNPs modificadas con PSPM (CeO_2@PSPM) resultan más tóxicas que otras. Esto se puede atribuir a su alta carga superficial y los grupos sulfonato del PSPM.

Sabemos que las CNPs normalmente presentan propiedades antioxidantes, para saber si la modificación afecta a estas propiedades antioxidantes se ha estudiado los efectos de las CNPs modificadas respecto a las especies reactivas de oxígeno (ROS) intracelular . Una vez expuestas las células a tert-Butyl hydroperoxide, inductor de ROS, las células con

CNPs modificadas internalizadas muestran un nivel de ROS más bajo que las células control. Esto significa que las CNP tanto modificadas como sin modificar se pueden utilizar como agentes antioxidantes que protegerían las células de la generación de ROS. .

En el **Capítulo 3** se muestra la dinámica intracelular de las NPs dentro las células por medio de la espectroscopía de correlación de fluorescencia (FCS). Se ha elegido como modelo NPs de oro conjugadas con glico conjugados (Glc-Au NPs), ya que estos tienen protegen a las NPs de interacciones no especificas con proteínas.

Se ha estudiado la dinámica de las Glc-Au NPs por medio FCS. Las variaciones en los tiempos de difusión de las Glc-Au NPs en medio celular,DMEM con 10% de FBS, demuestran una agregación moderada conrespecto a las NPs incubadas en agua destilada. El tiempo de difusión de las NPs aumentó de 113,2 μs en agua destilada a 243,3 μs en DMEM con 10% de FBS. La concentración de NPs se redujo desde el 77,4 nM y 37,0 nM, como consecuencia de la agregación. El tamaño aumentó de 2 nm a 4,4 nm .

También se aplicó FCS para el estudio de la dinámica intracelular de Glc-Au NPs. No se pudo aplicar FCS directamente ya que las NPs internalizadas forman grandes agregados que no presentan movimiento, no observándose fluctuaciones de la fluorescencia en volumen focal. Sin embargo, aplicando un pulso intenso de laser durante un segundo se consigue destruir la fluorescencia de los agregados inmóviles (prebleaching). . Al eliminarse la fluorescencia de los agregados y medir FCS se pudieron observar fluctuaciones de la fluorescencia en el volumen confocal donde se aplicó el prebleaching.

Los resultados de FCS después del prebleaching reflejan una población de NPs con concentración y tamaños monodispersos para la fracción intracelular móvil de NPs. Se puede concluir que esta fracción móvil está constituida únicamente por NPs individuales y pequeños agregados ; aproximadamente el 88% de los agregados tienen un tamaño entre 3.5nm y 7.0nm,, con una concentración local dealrededor de 11.8nM.

Este trabajo amplía el campo de aplicación de FCS en el estudio de las dinámicas intracelulares de NPs, en base al uso de prebleaching. FCS puede ser aplicada para

estudiar el grado de agregación de las NPs en el interior de las células y como cambia la agregación con las características superficialesde las NPs. FCS puede ser aplicada a otros tipos de NPs fluorescentes.

En el **Capítulo 4**, se fabricaron NPs biodegradables de poli (láctico-co-glicólico) (PLGA) por el método de emulsión de O/W (aceite-en-agua). La degradación de las NPs de PLGA se estudió en condiciones fisiológicas e intracelulares mediante citometría de flujo (FACS).

Se prepararon dos tipos de NPs de PLGA mediante el método de emulsión de O/W utilizando en la formulación dos proporciones diferentes de la D, L-láctico y glicólico. Mediante FACSse monitorearon las variaciones en la fluorescencia de las NPs de PLGA con 15% de glicólido (PLGA 15) marcado con rodamina B, por la liberación de polímero marcado como producto de degradación en solución fisiológica, después de 20 días. Mientras no se observa ningún cambio de la fluorescencia de las NPs de PLGA con 35% de glicólido (PLGA35) marcado con rodamina B después de 70 días. La degradación fue confirmada por microscopía electrónica de transmisión (TEM), dispersión dinámica de luz (DLS) y medidas de potencial zeta. Los resultados corroboran la degradación de las NPs de PLGA15 y la estabilidad de las NPs de PLGA35 en condiciones fisiológicas.

La degradación intracelular de las NPs de PLGA se estudió mediante FACS, midiendo los cambios en la intensidad de fluorescencia por célula incubadas previamente con NPs de PLGA durante5 días. Para las NPs de PLGA35, no se observó ningún cambio en la distribución de la intensidad de fluorescencia de las células con las NPs de PLGA35 internalizadas después de 5 días. Para las NPs de PLGA15, la intensidad de la fluorescencia de las células con las NPs de PLGA15 internalizadas aumentó de forma continua durante las primeras 24 h para luego mantenerse constante hasta 72 h. Además, se utilizó microscopía raman confocal (CRM) para monitorizar la degradación intracelular a nivel de células individuales mediante el registro de los cambios relativos de las bandas en 1768 cm^{-1} y en 872 cm^{-1} del espectro de PLGA. La banda en 1768 cm^{-1} corresponde a C = O vibración del grupo de éster de PLGA. La hidrólisis del éster durante la degradación del PLGA debe resultar en la reducción de la intensidad de la

banda en 1768 cm^{-1} durante. La banda en 872 cm^{-1} corresponde a la vibración C-COO de ácido láctico, que no se ve afectada por el proceso de hidrólisis durante la degradación. Por lo tanto, el cambio de la relación entre la banda a 1768cm^{-1} y la de 872 cm^{-1} indica el grado de hidrólisis de los grupos éster durante la degradación. Los resultados de CRM muestran que las NPs de PLGA15 dentro de la célula presentan una disminución en la intensidad del grupo de éster después 120h de incubación, mientras que las NPs PLGA35 no muestran ninguno cambio significativo después de la 120h de incubación con las células. Estos resultados corroboran la degradación de las NPs de PLGA15 dentro de la célula y la estabilidad de las NPs de PLGA35 intracelularmente.

En el **Capítulo 5**, se presenta la fabricación de NPs de PLGA que incorporan puntos cuánticos (QDs), nanopartículas de óxido de hierro superparamagnéticas (SPIONs) y las NPs de oro (Au NPs) usando la método de doble emulsión W/O/W (agua en aceite en agua).

Los QDs y los SPIONs se encapsularon dentro las NPs de PLGA durante la emulsión y Au NPs se ensamblaron sobre la superficie de las NPs de PLGA a través de interacciones electrostáticas. La asimilación de las NPs híbridas de PLGA por neutrófilos humanos se estudió mediante FACS y microscopía confocal. Además, se evaluó la inducción de ROS en los neutrófilos después de la incubación con los híbridos NPs de PLGA. Experimentos de Magnetoforesis mostraron que los neutrófilos con internalizados híbridos NPs de PLGA pueden ser efectivamente desplazadas lateralmente a través el campo magnético. Medidas de imágen por Resonancia Magnética (MRI) de los NPs híbridos de PLGA mostraron una mejora del contraste que depende linealmente de la concentración de los NPs híbridos de PLGA. Los NPs híbridos tienen potenciales aplicaciones in vivo, por ejemplo, para la visualización de tumores y el tratamiento fototérmico localizado.

Finalmente, en el **Capítulo 6**, se resumen con detalle las conclusiones obtenidas de los capítulos anteriores.

Introduction

Nanotechnology has been one of the leading and most rapidly developing technologies in recent years. It involves many different fields from science like chemistry, materials science, physics and biology, and spans a wide range of industries, such as food, cosmetics, household, pharmacy and electronics [1]. Typically, nanomaterials are defined as having a size, at least in one dimension, in the nanometer scale. At this scale, quantum mechanical effects and expanded surface area can bring unique physical properties [2]. In the biomedical field, there are four main applications of nanomaterials, namely: drug delivery, contrast imaging, biosensors and tissue engineering. For instance, to give just some examples of a very large list of applications in imaging: iron oxide nanoparticles (NPs) [3–5], gadollium NPs [6–8] can be used as contrast agents for Magnetic Resonance Imaging (MRI); NPs with intrinsic fluorescence such as quantum dots (QDs) are promising nanoscale visualization tools for biomedical applications [9]; Gold NPs with different shapes and sizes have been employed as contrast agents for optical imaging [10], photo-acoustic tomography [11,12], and X-ray imaging [13,14]; and carbon nanotubes [15,16], graphene [17,18], metal oxide NPs (zirconium dioxide [19,20], nickel(I) oxide [21], titanium oxide [22], zinc oxide [23]), metallic NPs (gold [24,25], silver [26], platinum [27], etc.) and semiconductor nanomaterials (cadmium sulphide [28]) are frequently integrated in biosensors due to their desirable electrochemical or photo-luminescent properties. In addition, liposomes [29], polymeric NPs [30], micelles [31], metallic NPs [32], dendrimers [33] with the capability for targeted and controlled release are often used as drug livery vehicles. In tissue engineering, one commonly used strategy is fabricating 3D matrices that resemble extracellular matrices with nanomaterials, e.g. nanofiber composite fabricated via electrospinning by biodegradable polymers [34,35]. Another frequently used method is incorporating nanomaterials, such as hydroyapatite NPs [36,37], carbon nanotubes [38,39], graphene [40] and magnetic NPs[41], into conventional 3D scaffolds as surface coatings which can either improve biocompatibility or optimize mechanical properties [42]. In addition, polymeric NPs, loaded with growth

factors [43,44], DNA [45,46] or siRNA [47,48], are often incorporated into scaffolds to stimulate tissue regeneration through releasing of the cargo.

The estimated production of nanomaterials will increase from 2,300 tons in 2008 to 58,000 tons in 2020 [49]. This huge amount of material may bring benefits as well as potential risks for humans and the environment. It may be indeed the case that humans become exposed to nanomaterials during the fabrication, handling and usage of devices or materials including nanostructures in their formulation. This is the case of an unintentional exposure. While in medical applications of nanomaterials, the exposure is intentional. In both cases the impact of the nanomaterials in human health is not fully understood. Depending on the exposure route (topical, oral, intravenous, or inhalation), nanomaterials may circulate in the body and translocate among the different organs and tissues. Finally they will reach the cell interior where they may interfere with cellular functions.

Therefore, studying the interactions between nanomaterials and cells is fundamental for understanding the health impact of nanomaterials and improving their properties for biomedical applications. This dissertation is focus on the fabrication and surface engineering of metallic NPs and polymeric NPs, their combination in hybrid multifunctional NPs, and the study of their cytotoxicity, intracellular behavior, their trafficking, localization and fate *in vitro*.

1 Cellular uptake and cytotoxicity of NPs

Understanding the interaction between cells and NPs is a key step to better utilize engineered NPs and evaluate their health impact. On one hand, how easily the NPs can be internalized by cells is critical for fulfilling their function as drug carriers, diagnostic agents or image contrast agents. On the other hand, assessment of NP cytotoxicity, studying how NPs influence the metabolism and other biological process of the cells and how they interact with cell organelles after internalization are vital for later *in vivo* assessment of the potential health risk of NPs [1].

Cytotoxicity caused by NPs

Engineered NPs may cause certain levels of cytotoxicity when exposed to cells. Their small size and large surface area to volume ratio can lead to an alteration in the biological activity of cells [50]. For example, when interacting with the cell surface NPs can cause structural reconstruction and phase transition of the cell membrane. After internalization by cells, they can also interact with intracellular biomolecules even nuclear components which will interfere with normal intracellular biochemical processes and cause cell dysfunction and death [51].

Though there are numerous studies focused on cell uptake and cytotoxicity of engineered NPs, a lack of standardization in experimental set up and the variations in NP types make it difficult to draw general conclusions about how NPs cause cytotoxicity. Nonetheless, the generation of reactive oxygen species (ROS) and the internalization of NPs through the plasma membrane are two general mechanisms that cause cell cytotoxcity [49].

Reactive oxygen species (ROS)

Cells can generate ROS through metabolic biochemical reactions, and some intracellular enzymes such as the glutathione peroxidase enzyme family can buffer a certain amount of ROS and protect cells from oxidative damage. However, engineered NPs may induce excess generation of ROS beyond the buffer ability of cells and lead to cytotoxicity.

It has been reported that there are several different mechanisms of ROS generation induced by NPs [52]:

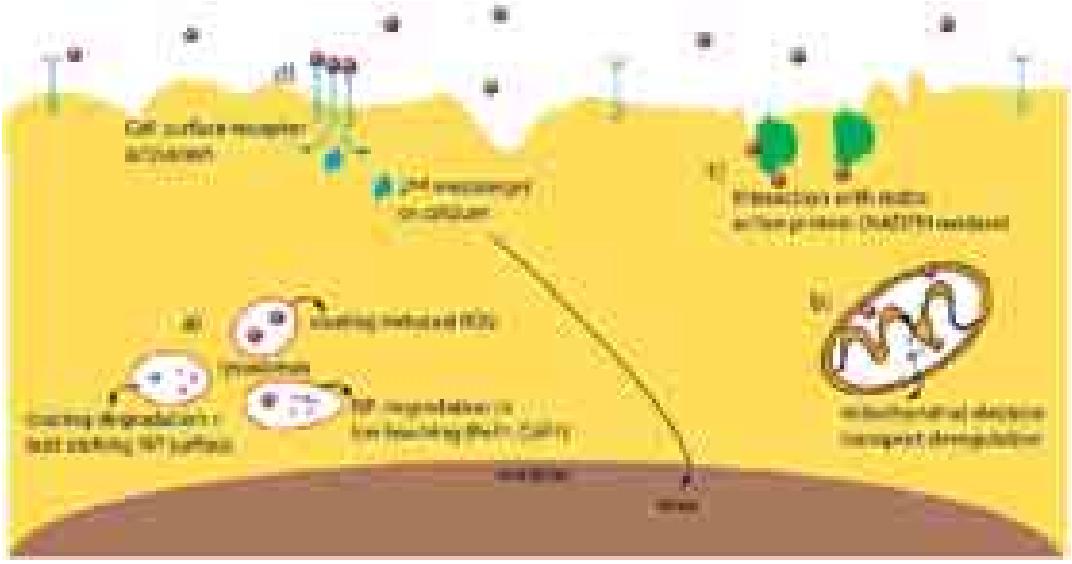

Figure 1 *Schematic overview of the different pathways by which NPs can induce oxidative stress* [52].

(1) Internalized NPs in the acidic cell organelles induce ROS by direct reactivity of their surface coating, degradation of the coating and direct interaction of the acidic media on the metal surface, or the leaching of ions (***Figure 1a***).

(2) Internalized NPs can interact with other cellular organelles, such as mitochondrion, by affecting its metabolic pathway and cause ROS (***Figure 1b***).

(3) NPs may induce ROS by interacting with redox active proteins such as NADPH oxidase (***Figure 1c***).

(4) NPs can also interact with receptors on the cell surface and result in the activation of intracellular signaling pathways that generate ROS (***Figure 1d***).

Cellular uptake of NPs

Engineered NPs can penetrate the cell membrane and be internalized by cells. Cellular uptake is a crucial step for NPs to accomplish their functions such as drug release,

sensing and imaging. However, internalized NPs can affect intracellular biochemical process in different ways and cause cytotoxicity.

Endocytosis pathways

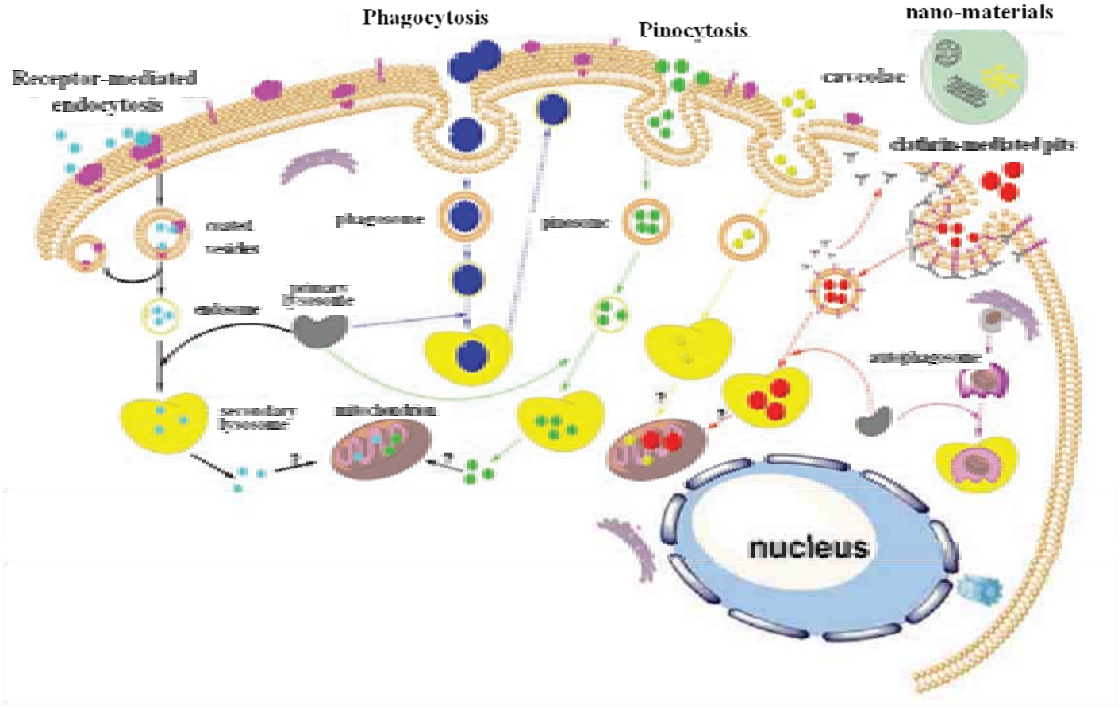

Figure 2 *Schematic of the known endocytosis pathways for intracellular uptake of NPs*[1].

Endocytosis is an energy dependent process in which cells internalize an extracellular substance through the plasma membrane. It is the dominant form of cellular uptake. There four well studied main endocytosis pathways of NPs:

Phagocytosis: Phagocytosis is the endocytosis process primarily conducted by immune cells, including macrophages, monocytes and neutrophils. These cells are able to clear large pathogens such as bacteria and yeast, or large debris like the remnants of dead cells. For example, the antibodies around bacteria can activate receptors on the surface of macrophage which trigger actin reassembly to form cell surface extension that 'zipper up' around the pathogen and engulf it [53]. Many different types of engineered NPs have been reported to be internalized by phagocytic cells via this pathway [54–56].

Macropinocytosis: Macropinocytosis refers to the formation of large, irregular primary endocytic vesicles (macropinosomes) by the closure of lamellipodia generated primarily at ruffling membrane domains. Macropinosomes are dynamic structures, frequently moving inward towards the centre of the cell, and persist for a short time [57].A range of emerging engineered NPs such as calcium phosphate NPs [58] and virus-like particles exploit macropinocytosis for cellular uptake [59,60].

Clathrin mediated endocytosis: Clathrin is the protein playing a major role in the formation of calthrin-coated pit on the cell membrane which can selectively transport cargos through plasma membrane. Clathrin-mediated endocytosis (CME) regulates many cell physiological processes such as the internalization of growth factors and receptors, entry of pathogens, and synaptic transmission [61]. Clathrin mediated endocytosis is also one of the most common pathways for internalization of many NPs which can lead to degradation of NPs in lysosomal compartments and cause cytotocity [62,63].

Caveolae dependent endocytosis: Caveolae are flask-shaped plasma membrane invaginations that are distinct from the clathrin-coated pits. They appear as 'smooth' uncoated pits or vesicles with 50-100 nm size that can be found as singular caveolae or in grapelike clusters (rosette formation) and long tubular structures evolved by the fusion of individual caveolae [64]. NPs for targeted drug delivery are often designed to predominately be internalized via this pathway that can achieve delivery to non-lysosomal compartments [65,66], and help to cross the *in vivo* vascular endothelial barrier[67].

In addition to the four pathways, there are some other clathrin and caveolae independent pathways such as RhoA and ARF6 regulated endocytosis [68]. Moreover, NPs can also be internalized by cells through passive processes such as diffusion [69,70].

Several different physicochemical properties of NPs can affect cellular uptake and cytotoxicity. Besides the effects of the chemical composition, which are similar to those of bulk materials, particle size, shape, surface charge, and agglomeration state play a crucial role on NPs cellular uptake [71].

Effect of size

Particle size is directly associated with surface area to volume ratio of NPs, thus it is an important factor that influences cellular uptake of NPs. Different types of NPs have been considered to have a size-dependent influence on cellular response and [72–75]. In the case of gold NPs, *in vitro* investigation suggests that small NPs with 1 to 2 nm diameter may cause rapid cell death by both necrosis and apoptosis. Studies of TPPMS/TPPTS-modified gold NPs demonstrated that the cytotoxicity they caused depending primarily on their size. NPs of 1–2 nm were highly toxic, 15-nm gold colloids were comparatively nontoxic, irrespective of the cell type tested [76]. In another case, antibody coated gold and silver NPs can regulate the process of membrane receptor internalization. The binding and activation of membrane receptors and subsequent protein expression strongly depend on nanoparticle size. Although NPs within the 2–100 nm size range were found that can alter essential signaling processes for basic cell functions (including cell death), 40 and 50 nm NPs demonstrated the greatest effect [73]. In addition, NPs induced generation of reactive oxygen species (ROS) has also been reported to be affected by size of NPs. Cells exposure to 15 nm silver NPs showed much stronger ROS generation than those exposed to 30 nm and 55 nm silver NPs [77].

Particles of different sizes appear to follow different internalization mechanisms and subsequent intracellular routings. Experiments with polystyrene based latex particles indicated that the endocytosis pathway changed with the increasing size of NPs. The clathrin-mediated pathway of endocytosis shows an upper size limit for internalization of approximately 200 nm, and the internalization of NPs less than 200nm almost exclusively through this pathway rather than via caveolae-mediated pathway. With increasing size, the mechanism shifted to rely more on caveolae-mediated pathway which is the predominant pathway of entry for NPs of 500 nm [78].

Effect of surface charge

Surface charge is another critical factor influencing the cellular uptake of NPs. Many reports have shown that a cationic surface of NPs tends to bind with negative charge

groups on the cell surface and further facilitates in crossing the cell-membrane barrier [1,79–81], which, later leads to effective cell membrane penetration and internalization. For example, the uptake efficiency of mesoporous silica NPs of 3T3-L1 cells was correlated with its positive surface charge [82]. Polymeric NPs with positive surface charge presented a rapid endocytosis by HeLa cells while the negatively charged NPs showed an inferior rate of endocytosis [63]. Based on their high uptake efficiency and electrostatic interaction with the lipid membrane, many positively charged NPs are designed for drug and gene delivery, such as cationic liposomes [83], polycationic peptides [84], cationic polysaccharide complexes [85] and cationic hydrogels [86]. However, several studies suggested that NPs with high surface charge may also contribute to generation of reactive oxygen species (ROS) [87,88].

Regarding the endocytosis mechanism, both positive and negative NPs seem ,mostly, to favor clathrin mediated pathways over other pathways [79,89,90]. It is worth mentioning that when this pathway is blocked, positive NPs may activate a compensatory endocytosis pathway that results in even higher accumulation of NPs [63].

NPs with different surface charge may result in different biodistribution and circulation time as well. Gold NPs with positive charge were found to accumulate more in the kidneys while negative and neutral ones favored to accumulate in liver [91]. And for PEG-oligocholic acid based micelle NPs, liver uptake was very high when NPs are highly positive or negative compared to slightly negatively charged NPs [92]. In addition, neutral NPs and low concentrations of anionic NPs were found to have no effect on blood-brain barrier (BBB) integrity, whereas, high concentrations of anionic NPs and cationic NPs disrupted the BBB. Cationic NPs showed a higher brain uptake rate [93].

Effect of shape

Particle shape plays a role in the interaction of NPs with cells and the biodistribution of NPs [94–96]. Huang *et al* found that different shaped mesoporous silica NPs (MSNs) have different influences on several aspects of cellular function including cell proliferation, apoptosis, cytoskeleton formation, adhesion and migration. Long rod-

shaped MSNs have been found to be more easily taken up via cell endocytosis and to reduce cell viability/apoptosis more dramatically than spherically shaped MSNs [97]. In another case of gold NPs, it also has been found that spherical gold NPs of different sizes are not inherently toxic to human skin cells, but gold nanorods are highly toxic [98].

The physicochemical properties mentioned above normally affect cell uptake of NPs coordinately rather than alone. This means the actual interaction between a certain kind of NP and cell is much more complicated. This needs to be taken into account for the design of engineered NPs. Moreover, the cellular uptake of chemically identical materials can be altered significantly by the manipulation of several physicochemical properties[71].

2 Techniques and methods for studying intracellular behavior of NPs

There are a number of different techniques and methods for studying the interaction between cells and NP. Here we give a general introduction to some of the techniques and methods that have been used in this dissertation. Detailed information of theory and instrumentation of the techniques and methods will be addressed in 'Chapter 1 Materials and Methods'.

Flow cytometry (FACS)

Flow cytometry (Fluorescence Activated Cell Sorting, FACS), is a powerful tool for studying cellular uptake of NPs, which is based upon the light-scattering properties including fluorescence emission of the cells being analyzed. Cells (or particles) in suspension for FACS analysis move in a liquid stream through a laser (or light beam) with the detected signal being passed to a computer for display and analysis [99]. High speed (with thousands of cells can be analyzed in one second) and statistical analysis of particles or cells is the most beneficial aspect of FACS.

It can be used for uptake kinetic and quantitative study of NPs. One common method is based on fluorescently labeled NPs, the amount of internalized NPs can be associated

with the change in fluorescence intensity of cells following uptake compared to control cells [100–102]. Another method is to correlate the change of side scattering intensity to the amount of internalized NPs. The side scattering (SS) intensity gives information about the granular content within a cell and a particle. SS intensity increases according to the amount of NPs taken up by the cells. With proper gating, it can be used for quantitative uptake studies [103–106].

FACS is also frequently used to study cytotoxicity of NPs. For example, it can measure cell apoptosis, oxidative stress and cell cycle. Annexin V/PI assay using FACS is one of the most frequently used assays for cytotoxicity. Annexin V is a protein which has high affinity to bind phospholipids occurring on the plasma membrane only during cell apoptosis. Propidium Iodide (PI) is a membrane impermeable fluorescent molecule and often used to identify dead cells. In a typical Annexin V/PI assay, cells with Annexin V positive and PI negative are undergoing apoptosis; and cells that are positive for both Annexin V and PI can be either in the late stage of apoptosis or already dead [107–109]. Oxidative stress of cells after exposure to NPs can be quantitatively studied by directly measuring reactive oxygen species (ROS) activity within cells or analyzing cellular glutathione (GSH) levels which reveal the level of ROS [110,111]. DNA binding fluorescent molecules such as PI, 4’6’-diamidino-2-phenylindole (DAPI) can used to analyze cell cycles after exposed to NPs. By means of FACS, one can obtain statistical data about which stage of the cell cycle most of the cells are in. This is associated with the influence of NPs on cell growth [112–114].

Transmission electron microscopy (TEM)

Transmission electron microscopy is widely used in cell biology. By heavy metal staining, resin embedment, ultrathin section, intracellular structures can be revealed by TEM as well as internalized NPs and their intracellular location. Metallic NPs usually can be visualized directly by TEM because of their electron dense nature which gives a very dark contrast. However, polymeric NPs are difficult to visualize, usually needed to be pre-treated with certain TEM staining agents [115].

Osmium tetroxide is an electron dense agent which has been used most frequently for post-fixation and staining of cells for TEM. It has high affinity for lipids and has been used for staining lipids in cells and tissue. Therefore, sub-cellular structures like cell vacuoles, mitochondrion and cell nuclei can be visualized by their lipid boundaries and distinguished by their distinct shapes [116]. Moreover, if cells are fixed during the process of endocytosis of NPs, it can sometimes reveal NPs associated with cell compartments involved in the early stages of endocytosis such as macropinosome, clathrin coated pit or caveolae [117].

Nevertheless, the visualization of cell compartments is mostly dependent on the size and shape of the objects. This can sometimes be arbitrary and hence immunostainings are often applied. The main drawback of immuno-EM is that it can be technically challenging, expensive, and require rigorous optimization of tissue fixation and the processing method [118].

Raman spectroscopy

Raman spectroscopy is an emerging noninvasive tool for the *in vitro* study of individual living cells [119]. It is an optical technique based on inelastic scattering of photons by molecular vibrations of biopolymers, which provide a chemical fingerprint of cells or organelles without fixation, lysis or the use of labels and other contrast enhancing chemicals [120].

Raman spectroscopy has been used to study interaction of cells with NPs, e.g. localization and distribution of NPs within single cells, cell viability after exposure to NPs or intracellular degradation of NPs [121,122]. For example, Romero et al. used Raman spectroscopy to study the intracellular distribution and cytotoxicity of PLGA NPs and carbon nanotubes. With the analysis of signals from different cell compartments and NPs, correlation between NPs and specific cell organelles can be calculated to demonstrate the intracellular localization and distribution of NPs inside individual cells [123,124]. Pyrgiotakis et al. studied the interaction of A549 cells with NPs via Raman spectroscopy, investigating the mitochondrial activity of cells after exposure to Jasada

Bhasma NPs [125]. And by investigating the change in chemical composition of degrading particles, van Apeldoorn et al. studied intracellular degradation of PLGA particles within macrophages [126].

In addition, surface-enhanced Raman spectroscopy (SERS) has drawn particular attention because of its strong enhancement of the Raman signal and high sensitivity. Gold and silver NPs with different sizes and shapes have been designed as SERS probes for detecting biomolecules *in vitro* and *in vivo* [127–130].

Fluorescence correlation spectroscopy (FCS)

FCS is a single molecule spectroscopy technique based on recording temporal fluctuations of the fluorescence intensity. It can monitor the motion of fluorescently labeled molecules or NPs within a tiny, optically defined focal volume (typically <1 fL)[131]. Analysis of the recorded data yields information such as translational diffusion coefficients, flow rates, chemical kinetic rate constants, rotational diffusion coefficients, molecular weights, and concentration [132–138]. FCS provides a suitable methodology for measuring mobility, association, and ligand kinetics of biological molecules in the cellular environment [138–140].

The majority of studies related to FCS and NPs have concentrated on the dynamics of NPs or fluorescent proteins in blood serum, human serum and cell culture media [141,142]. However, few attempts have been done to study the dynamics of NPs within cells by means of FCS. A study related to investigating the dynamics of diamond NPs in cells states that diffusion data was rarely found, hinting at the difficulties in obtaining such data [143]. In other studies, primarily by Irudayaraj et al, they have been able to obtain diffusion data, of gold nanostars and gold nanorods inside the cellular environment [144–147].

3 Biodegradable polymeric NPs

There are many different kinds of polymeric NPs utilized for biomedical application. Among them, Poly (lactic acid) (PLA), poly (glycolic acid) (PGA), and their copolymers, poly (lactide-co-glycolide) (PLGA) are synthetic polymers with good biocompatibility, mechanical properties, as well as controllable biodegradability through natural pathways. Especially, in the case of PLGA, the degradation process can be manipulated by varying the ratio between PLA and PGA, thus the drug release rate can be controlled accordingly [148]. Moreover, based on the preparation method, these NPs can be used as drug delivery vehicles in two ways. One means is by the entrapment of the drug molecule inside polymers, and the other is by adsorption on the surface of polymeric NPs.

Poly (lactide-co-glycolide) (PLGA) NPs

PLGA is one of the best defined biomaterials available for drug delivery with respect to design and performance, which can be dissolved in a wide range of solvents [149]. PLGA NPs offer prolonged drug release (sustained release), and the release kinetics can be controlled by changing the physicochemical properties of the copolymer.

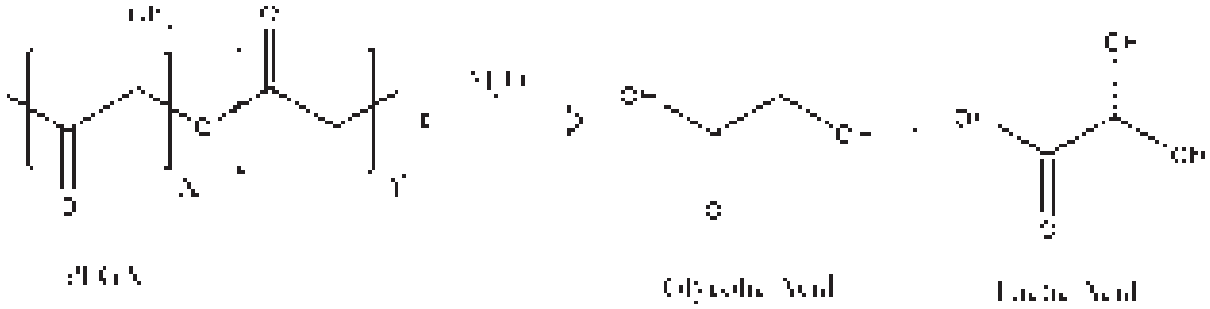

Figure 3 *Hydrolysis of PLGA.*

The degradation of PLGA occurs by the hydrolysis of the ester linkage in the presence of water, The PLGA polymer biodegrades into lactic and glycolic acids which enters the tricarboxylic acid cycle and is eventually eliminated from the body as carbon dioxide and water [149,150]. The degradation behavior of PLGA can be affected by many factors like

hydrophilicty, crystallinity, molecular weight, glass transition temperature, chemical composition and device dimensions (size, shape, surface to volume ratio) [151]. These factors will eventually affect the drug release profile. The ratio of PLA to PGA is one of the most important factors in PLGA degradation [152]. PLA has a methyl side group which makes it more hydrophobic than PGA. Therefore, when the copolymer has a higher ratio of PLA, it absorbs less water and the degradation rate can be slower compared to PLGA with a lower PLA ratio [153].

There are several methods to produce PLGA NPs of which emulsion solvent evaporation is one of the most widely used. In a typical emulsion solvent evaporation method, PLGA is first dissolved in an organic solvent and then mixed with a surfactant containing aqueous solution, An O/W emulsion is obtained through vigorous stirring or sonication. After evaporation of the organic solvent, polymer droplets will finally harden and form NPs. As commonly used drug delivery vehicles, PLGA NPs can encapsulate hydrophilic drugs by applying the W/O/W double emulsion method. Aqueous drug solutions are dispersed in a PLGA organic solution to form a primary W/O emulsion prior to adding surfactant containing aqueous solution. In the case of hydrophobic drugs, the single emulsion method can be applied by dissolving the drug and polymer together in the appropriate organic solvent. Thus, the emulsion solvent evaporation method is applicable for the entrapment of both hydrophilic and hydrophobic drugs inside PLGA NPs [154–156]. There are also many other methods with which to prepare PLGA NPs, such as phase separation [157], salting out [158], spray drying [159,160], and nanoprecipitation [161,162].

4 Surface engineering of NPs

As surface properties play a key role in the cellular uptake process, surface engineering of the NPs is an elementary method to regulate the interaction between NPs and biomolecules (e.g. proteins, lipids, and polysaccharide) and further control their cytotoxicity and biological fate. Regarding the method of surface engineering of NPs, there are two main methods based on the interaction between materials for surface

modification and NPs, i.e. covalent binding, and non-covalent interaction (including electrostatic interaction and supermolecular interaction based self assembly).

Polymer brushes

Polyelectrolyte brushes constitute a new class of materials by themselves. The strong electrostatic interaction involved brings about a number of entirely new properties when compared to monolayers of grafted uncharged macromolecules [163]. In principle, there are two ways of anchoring polymer brushes to a planar surface or a spherical particle: the 'grafting from' and 'grafting to' methods. In the 'grafting to' method, polymer molecules are pre-synthesized and attached to the surface via covalent binding. Typically, these pre-synthesized polymers have reactive functional groups at one end of the polymer chain which is able to form covalent bonds with the reactive groups on the surface. Nevertheless, due to the steric repulsion between the grafted and incoming polymer chains the 'grafting method' usually results in a low grafting density [164].

On the contrary, the 'graft from' method involves *in situ* polymerization of the polymer brush from the previously immobilized substrate with a polymerization initiator. This surface- initiated polymerization is not hindered by the kinetic and thermodynamic barriers among polymer chains, and therefore the 'grafting from' method leads to polymer brushes with high-density and high-molecular weight [163].

Figure 4 *The mechanism of transition metal-catalyzed ATRP. M_t represents a transition metal, R represents the polymer chain, X represents a halogen atom, and Y represents another ligand or the counter ion. Kp is the polymerization rate, k_{act} and k_{dact} are the activation and deactivation constants* [165].

Of all the polymerization techniques that can be applied for the 'grafting from' method, Atom Transfer Radical Polymerization (ATRP) is one of the most effective and versatile techniques, which enables the precise control of the molecular weight, molecular weight distribution and functionality [165]. In ATRP, as shown in ***Figure 4***, the radical forms from the dormant species R-X through a transition metal catalyst. This process is reversible, and is kept in equilibrium between active species and dormant species. With the addition of monomers, the polymer chain grows steadily with a constant rate of propagation. Due to the precise control and mild conditions of ATRP, the 'Grafting from' technique using ATRP is widely applied for the synthesis of polymer bioconjugates [166], surface modification of drug delivery vectors with tunable hydrophilicity [167,168], and the formation of tissue engineering hydrogels [169].

5 Hybrid NPs

Typically, hybrid NPs refer to NPs composed of both inorganic and organic components. They are constituted of either organic molecules, or networks (organic polymers) mixed at the nanoscopic level with inorganic components, which are mainly metal oxides and metal–oxo polymers, and are sometimes phosphates [170], carbonates [171], chalcogenides [172] and allied derivatives [173]. They do not only maintain the beneficial features of both inorganic and organic nanomaterials, but also possess unique advantages. For example, the ability to combine a multitude of organic and inorganic components in a modular fashion allows systematic tuning of the properties of the resultant hybrid nanomaterial [174].

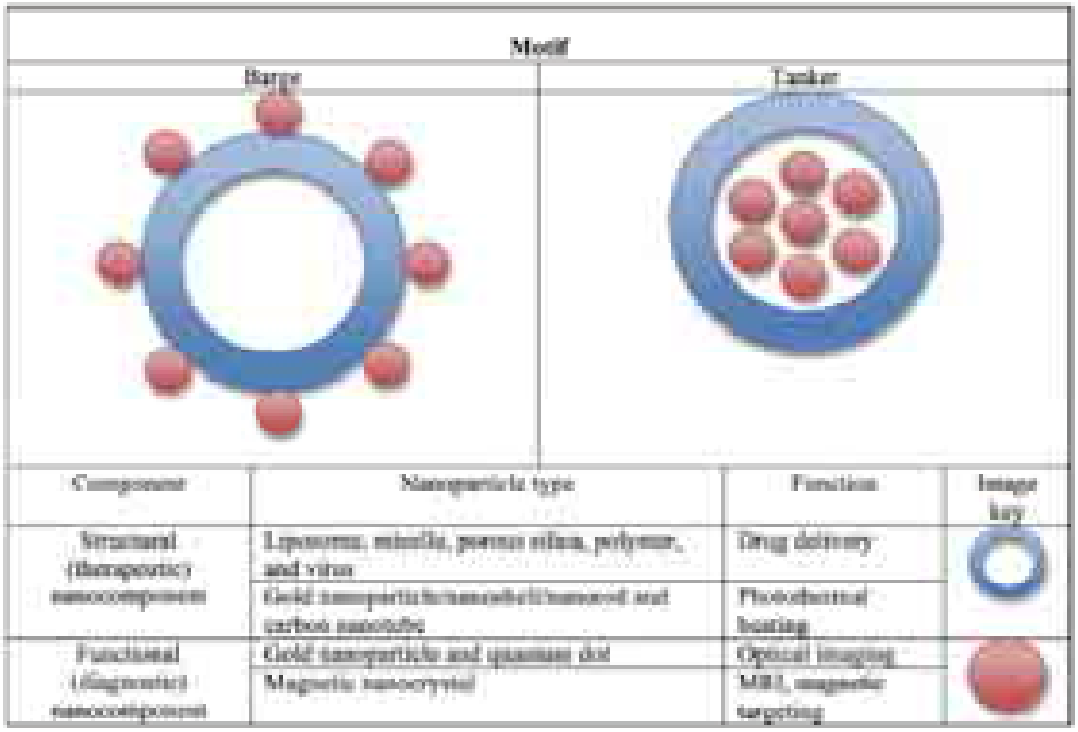

Figure 5 *Two principle design strategies for hybrid NPs containing both therapeutic and diagnostic nanocomponents* [174].

Nanocomposites of polymers and inorganic particles are hybrid NPs widely used for biomedical applications. In order to accomplish the therapeutic and diagnostic functions, they are typically designed to have both structural (therapeutic) and functional (diagnostic) components. The structural components can be organic materials such as liposomes [175], micelles [176], dendrimers [177], biodegradable polymers (e.g. PLGA [178]), or viruses [179]. The functional components can be gold nanostructures (for optical imaging or photothermal therapy), magnetic NPs (for MRI contrast or hyperthermia), or quantum dots (for fluorescence imaging). The functional component can be either incorporated into the inner space of a structural nanocomponent ('tanker') or attached to the surface of the structural nanocomponent ('barge') (***Figure.5***)[180].

Objectives and aims of the thesis

In this dissertation, we intend to gain inside in the interaction of complex nanoparticles (NPs) with cells addressing aspects related NPs' fate such as their degradation, intracellular aggregation and localization, dynamics, and uptake mechanism. These issues are fundamental to understand the impact of NPs on cellular functions, being therefore of importance for the toxicological evaluation of NPs. Moreover, when NPs are intended for a medical applications, the state of aggregation, or degradation, and how these varies with time will clearly impact on its desired medical application: as drug delivery vectors or in contrast imaging.

This thesis will have the following objectives:

- **Understand the impact a thin polymer film coating of NPs on their fate and interaction with cells.** The role of the surface coating of NPs and its charge to control the interaction of NPs with cells will be studied with CeO_2 NPs coated with polyelectrolyte brushes via *in situ* Atomic Transfer Radical Polymerization. The brush provides a high density of charges on the surface of the NP. In addition, brushes provide a means to encapsulate a dye attached to the surface of NPs, which will remain inside the polymer brush and not in the outer surface of the polymer coating. In this way the dye will not alter the surface characteristics of the coating, which will be those of the polymer brush. We aim to show that the polymer brush can have a protective effect on the fluorescent labeling of NPs, provide better colloidal stability aqueous media to CNPs A brush results as well in a thick polymer shell around the NPs that can impact on the interaction of the core NP with cellular molecules. A brush on top of metallic/metal oxide NPs can indeed have an effect on the generation of reactive oxygen species (ROS) as the brush can prevent the contact of biomolecules with the metallic/metal oxide core and limit redox processes. CeO_2 NPs were chosen as core NPs as these NPs

behave as radical scavengers affecting ROS through a redox equilibrium between Ce^{3+} and Ce^{4+} ions in their structure as well as oxygen vacancies.

- **Study the dynamics and aggregation of metallic NPs intracelullarly**. We will study the intracellular dynamics of NPs inside cells by means of Fluorescence Correlation Spectroscopy (FCS). For this work we have chosen glucose derivative conjugated gold NPs (Glc-Au NPs). The glucose derivative coating protects the NPs from non specific interactions with proteins. We will show by means of FCS that NPs have limited aggregation in cell media. Intracellularly we will show that the FCS technique combined with a prebleaching strategy can be used to obtain meaningful data on the state of aggregation and dynamics of NPs inside cells. Through intracellular FCS important information on the state of aggregation, hydrodynamic size and local concentration of the NPs and their intracellular localization will be obtained.

- **Study the intracellular degradation of polymeric NPs**. We will study the intracellular degradation of Poly (lactide-co-glycolide) (PLGA) NPs. NPs degradation is fundamental for the delivery of encapsulated molecules and therefore for the application of these NPs in drug delivery. Despite PLGA degradation has been extensively studied in bulk, very little is known about the degradation of PLGA inside cells since it is not easy to follow changes in the NPs intracellularly. We propose a novel method to trace PLGA NPs degradation based on flow cytometry (FACS). Degradation studies with FACS were conducted first in PBS and compare with Dynamic Light Scattering (DLS), zeta potential and Transmission Electron Microscopy (TEM) data. By using Rhodamine B (RhdB) to fluorescently label PLGA NPs, the changes in the fluorescence intensity of the particles measured by FACS reveal the release of labeled PLGA molecules. The intracellular degradation of PLGA NPs will be followed by the increase in fluorescence intensity of cells with PLGA NPs when labeled polymer is released from the inside of PLGA NPs to the cell interior. This increase is due to the increase in quantum yield of the RhdB in a more polar environment as the cell

interior compared with the apolar core of the PLGA NPs. Additionally, Confocal Raman Microscopy (CRM) will be employed as a label free technique for *in vitro* degradation study of PLGA NPs. CRM can measure the degradation state of NPs at single cell level.

- **Study the interaction of hybrid NPs with cells.** We will show that combining PLGA NPs in the submicron size with quantum dots, SPIONS and gold NPs through surface engineering and encapsulation results into hybrid multifunctional nanomaterials that can be used for cell labeling, sorting and imaging as well as for Magnetic Resonance Imaging. Moreover, the hybrid multimodal NPs can serve in cell sorting using an external magnetic field. Cell uptake and intracellular localization will be studied. The protective effect of the encapsulation of the SPIONS in PLGA diminishing ROS generation will be demonstrated.

This thesis has been divided to six chapters:

- **Chapter 1** provides detailed information on all the materials and methods used in the thesis.

- **Chapter2** is focus on the intracellular behavior of surface engineered cerium oxide NPs (CNPs). CNPs will be coated with either positively or negatively charged polyelectrolyte brushes via in situ Atomic Transfer Radical Polymerization (ATRP). CNPs coated with polymer brushes will be fluorescently labeled with Alexa 488. The fluorescent dye will be attached directly to the surface of the CNPs remaining inside the polymer shell after brush synthesis. Cellular uptake kinetics of CNPs with different polymer coatings will be studied via FACS. Confocal Laser Scanning Microscopy (CLSM), CRM and TEM will be employed for the intracellular location and distribution of CNPs. Cellular uptake mechanism will be investigated by using different uptake pathway inhibitors. Cytotoxicity study will be assessed by MTT assay and CRM. The impact of the polymer brush coating of CNPs on the oxidative stress of cells will

be examined. Cells will be treated with CNPs and exposed to tert-Butyl hydroperoxide (TBHP), a ROS inducer. The intracellular ROS level will be quantified by FACS.

- **Chpater3** focuses on the use of FCS for the study of intracellular dynamics of fluorescently labeled glucose derivative modified gold NPs. The agrregation of Glucose-Au-Hilyte labeled NPs (Glc-Au-Hi NPs) in cell culture medium will be studied by FCS incubated in Dulbecco's Modified Eagle Medium (DMEM) with 10% FBS. A prebleaching strategy will be developed for the study of the intracellular dynamics of single NPs and small aggregates From FCS data the local concentration and information on theintracellular environment of the NPs will be obtained.

- **Chapter4** focuses on the degradation process of PLGA NPs. The degradation of PLGA NPs fabricated upon RhdB labeled polymer will be followed by FACS. The degradation of two types of PLGA NPs with different glycolide concentration (PLGA15 with 15% glycolide and PLGA35 with 35% glycolide) will be studied both in physiological conditions and in cells. In physiological conditions degradation will also be followed by TEM, DLS and zeta potential measurements. The intracellular degradation process of PLGA will be followed by the increase of fluorescence due to the release of RhdB labeled PLGA molecules in the cell from the apolar interior of PLGA, which results in an increase in the quantum yield of RhdB. This will result in an increase of the fluorescence intensity which can be observed by FACS. Additionally, Confocal Raman Microscopy was used to trace degradation intracellularly at single cell level by recording the relative changes of the bands at 1768 cm^{-1} and at 872 cm^{-1}.

- **Chapter5** contains the design and fabrication of hybrid PLGA NPs carrying quantum dots (QDs), superparamagnetic iron oxide NPs (SPIONs) and Au NPs. QDs and SPIONs will be encapsulated inside PLGA NPs by the W/O/W double emulsion method and Au NPs will be assembled on top of the PLGA NPs via

electrostatic interactions. The uptake of the hybrid PLGA NPs by human neutrophils will be studied by FACS and CLSM. In addition, the induction of ROS in neutrophils after incubation with the hybrid PLGA NPs will be assessed. Magnetophoresis experiments will be performed to show that internalized hybrid PLGA NPs can be used for neutrophils sorting. And Magnetic Resonance Imaging (MRI) of the hybrid PLGA NPs will be performed to evaluate the ability of hybrid NPs as MRI contrast agents.

- **Chapter 6** entails the summary of all the result of the thesis. Conclusions and perspectives will be drawn.

Chapter 1

Materials and Methods

1.1 Materials

Cerium Oxide Nanoparticles (CeO_2 NPs) were obtained from Evonik Degussa; Poly (D,L-lactide-co-glycolide) (PLGA) (D, L-lactide 85: glycolide 15, D, L-lactide 65: glycolide 35 and D, L-lactide 50: glycolide 50, Mw=100kDa) were purchased from China Textile Acadeamy; Glc-Au NPs were prepared by the Biofunctional Nanomaterials Laboratory 2 at CIC biomaGUNE, Spain;

3-sulfopropyl methacrylate (SPM), [2-(Methacryloxy) ethyl] trimethylammonium chloride (METAC), (3-Aminopropyl) triethoxysilane (APTS), α-Bromoisobutyric acid, 4-(Dimethylamino) pyridine, 1,3-Dicyclohexylcarbodiimide, 2,2'-Bipyridil Reagent Plus, N, N-dimethylformamide 99.85% (DMF), copper chloride I, polyethylenimine (PEI) 5 nm citrate stabilized Au NPs, bovine serum albumin (BSA), phosphate buffer saline (PBS), PIERCE BCA Protein Assay Kit, Dulbecco's Modified Eagle's Medium (DMEM), fetal bovine serum (FBS) were purchased from Sigma-Aldrich;

Alexa Fluor 488 carboxylic acid succinimidyl ester, Lissamine rhodamine B ethylenediamine, Qdot® 655 ITK™ amino (PEG) quantum dots ,2-Dihexadecanoyl-sn-Glycero-3-Phosphoethanolamine (Oregon Green 488 DHPE), 4',6-Diamidino-2-Phenylindole, Dihydrochloride (DAPI) were purchased from Invitrogen; HiLyte Fluor™ 647 was purchased from AnaSpec; Tetrachloroauric acid was purchased from Strem Chemicals;

Cell lines (HepG2, HEK293, and A549) were purchased from the American Type Culture Collection (ATCC).

All chemicals were used as received.

1.2 Methods

1.2.1. ζ-Potential

When nanoparticles (NPs) are dispersed in an aqueous environment forming a colloidal solution, ions strongly bound to the surface of NPs constitute an inner region called the 'stern layer', and the ions from the solution with opposite charges loosely associated to the surface of the NPs form an outer region called the 'diffuse layer'. These two layers together are termed the 'double layer'. In the diffuse layer, ions close to the stern layer are tightly attached to the surface whereas others are much more mobile. The boundary separating mobile and immobile parts in the diffuse layer is called the 'slipping plane'. In theory, the zeta potential is the electrokinetic potential between the slipping plane and a point in the solution that is far away from the interface. The zeta potential (ζ-Potential) of NPs is highly dependent on the ionic strength of the immediate environment [181].

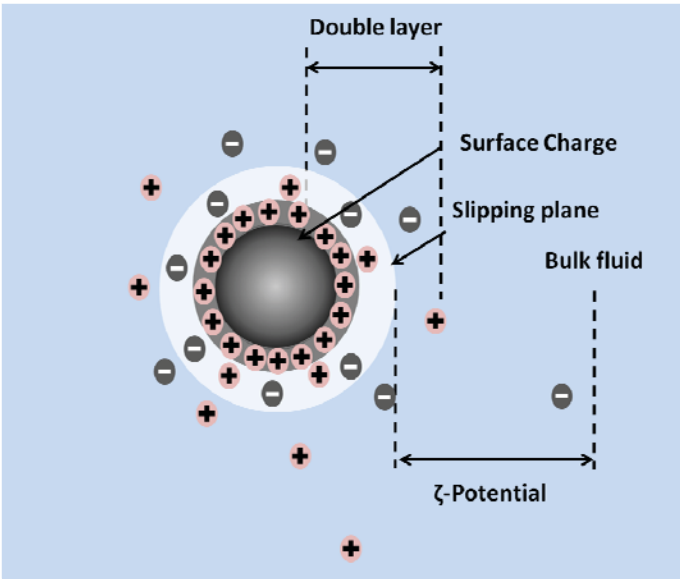

Figure 1.1 *Schematic representation of ζ-Potential of a charged NP in the colloidal solution.*

Electrophoretic Light Scattering (ELS) is the most common method used to measure the ζ-potential of NPs. When an electric field is applied across an electrolyte, suspended NPs with electric surface charge are attracted towards the electrode of opposite charge while

viscous forces acting on the particles tend to oppose this movement. When equilibrium is reached between these two opposing forces, NPs move with constant velocity. This velocity is correlated to the ζ-Potential of the NPs. By applying Henry's equation, we can thus get the value of the ζ-Potential of the NPs. Henry's equation is:

$$U_E = \frac{2\varepsilon z f(Ka)}{3\eta} \quad (Eq.\ 1.1)$$

Where z is the ζ-Potential, U_E is the electrophoretic mobility, ε is the dielectric constant, η is the viscosity, and *f* (Ka) is Henry's function which has a value of 1.5 in aqueous media and moderate electrolyte concentrations and a value of 1.0 in non-aqueous measurements [182].

ζ-potential measurements were used in this work to follow the different surface modifications on CeO_2 NPs and hybrid PLGA NPs. Measurements were performed with a NanoSizer (MALVERN Nano-ZS, U.K.) instrument at 25 °C and with a cell drive voltage of 30 V, using a monomodal analysis model.

1.2.2 Dynamic Light Scattering (DLS)

DLS measures the time-dependent fluctuations in scattering intensity caused by constructive and destructive interference resulting from the relative Brownian movements of the macromolecules and particles within a sample. In a typical DLS experiment, NP suspensions are illuminated with a coherent light source, usually a laser, and the intensity of the scattered light from the scattering object is measured at a given angle as a function of time [183]. The Brownian motion of the dispersed NPs determines the fluctuation of the scattered light intensity. DLS relates this movement to the size of NPs by means of Stokes-Einstein equation. The Stokes-Einstein equation is:

$$D_H = \frac{k_B T}{3\pi\eta D} \quad (Eq.1.2)$$

Where D_H is the hydrodynamic diameter, k is Boltzmann's constant, f is the particle frictional coefficient, η is the solvent viscosity, T is the absolute temperature, and D is the diffusion coefficient. The NPs motion in a fluid with known viscosity at a certain temperature can finally lead to the determination of particle size [184].

The hydrodynamic size of CeO_2 NPs with different surface modifications and PLGA NPs were measured using a NanoSizer (MALVERN Nano-ZS, U.K.) instrument.

1.2.3 Fluorescence spectroscopy

Luminescence is the spontaneous emission of light from excited electronic states of a sample, which has absorbed light or other electromagnetic radiation. And there are two types of luminescence, namely fluorescence and phosphorescence depending on the nature of the excited state. The rapid emission of a photon occurrs during the decay of an excited singlet state (higher energy) to the ground singlet state (lower energy) is called fluorescence [185]. Molecules exhibiting fluorescence are called fluorophores. Fluorescence spectroscopy is a type of electromagnetic spectroscopy in which the fluorescence from fluorophores is recorded following excitation with an appropriate source. The excitation source can be a laser, LED or lamps such as xenon arcs and mercury-vapor lamps [186]. Fluorescence spectroscopy is widely used for analysis of organic compounds in both research and industrial fields.

In this work, fluorescence spectroscopy was used to characterize the modification of NPs with fluorophores using a fluorimeter Fluorolog®-3 HORIBA JOBIN YVON.

1.2.4 UV-Vis Spectroscopy

UV-Vis spectroscopy refers to the absorption or reflectance spectroscopy of a sample in the ultraviolet (200–400 nm) and visible region (400–800 nm). UV-visible spectrophotometers are used to examine electronic transitions associated with absorptions in the UV and visible regions of the electromagnetic spectrum [187]. The energies associated with these regions are capable of promoting outer electrons of a molecule from

one electronic energy level to a higher level. A molecule containing the electrons involved in the electronic transition will result in observed absorptions. The concentration of the absorbing molecule is proportional to the absorbance of a solution. Therefore, UV-Vis spectroscopy is commonly used in chemistry and material field for determine the concentration or thickness of the sample [188].

A Varian Cary 5000 UV-Vis-NIR spectrophotometer (Varian GmbH, Australia Pty Ltd.) was employed to obtain absorption spectra. The light sources of the instrument are a deuterium lamp (185–350 nm) and a halogen lamp (350–3300 nm). The absorption spectra can be collected over a wavelength range of 175 to 3300 nm.

1.2.5 Confocal Laser Scanning Microscopy (CLSM)

Confocal Laser Scanning Microscopy (CLSM) is a widely used microscopy technique, which is used to generate fluorescence images of materials, cells, and tissues at defined planes in the Z-direction, focal plane, with enhanced resolution allowing three dimensional reconstructions.

CLSM has two essential components that are different from the conventional microscopy. One is the point scanning light source, and the other is the pinhole in front of the detector[189]. In CLSM, a laser is used as a point light source that permits focussing only at one point of the specimen. And the laser beam is deflected by two sets of mirrors called the X and Y scanning mirrors to form the scanning light source [190]. A photomultiplier tube (PMT) with a pinhole aperture in front acts as the detector. The pinhole aperture can attenuates out of focus light and only allows light from the focal plane to be collected. The smaller the pinhole, the less out of focus light reaches the PMT detector [191]. When one point of specimen in the focal plane is illuminated by the laser beam, the reflected and emitted fluorescence light is captured by the same objective and passes through the pinhole and collected by PMT. The 2D image is reconstructed from signals of different points within the focal plane via a point by point and line by line raster scanning.

The confocal optical system allows increased lateral resolution and a unique optical sectioning capability Thus, it is possible to get a 3D image of thick specimens with good spatial resolution [191,192]. Depth scans are performed by selecting different focal planes along the Z-axis. A series of 2D images are collected and can be used to reconstruct the 3D structure of the specimen.

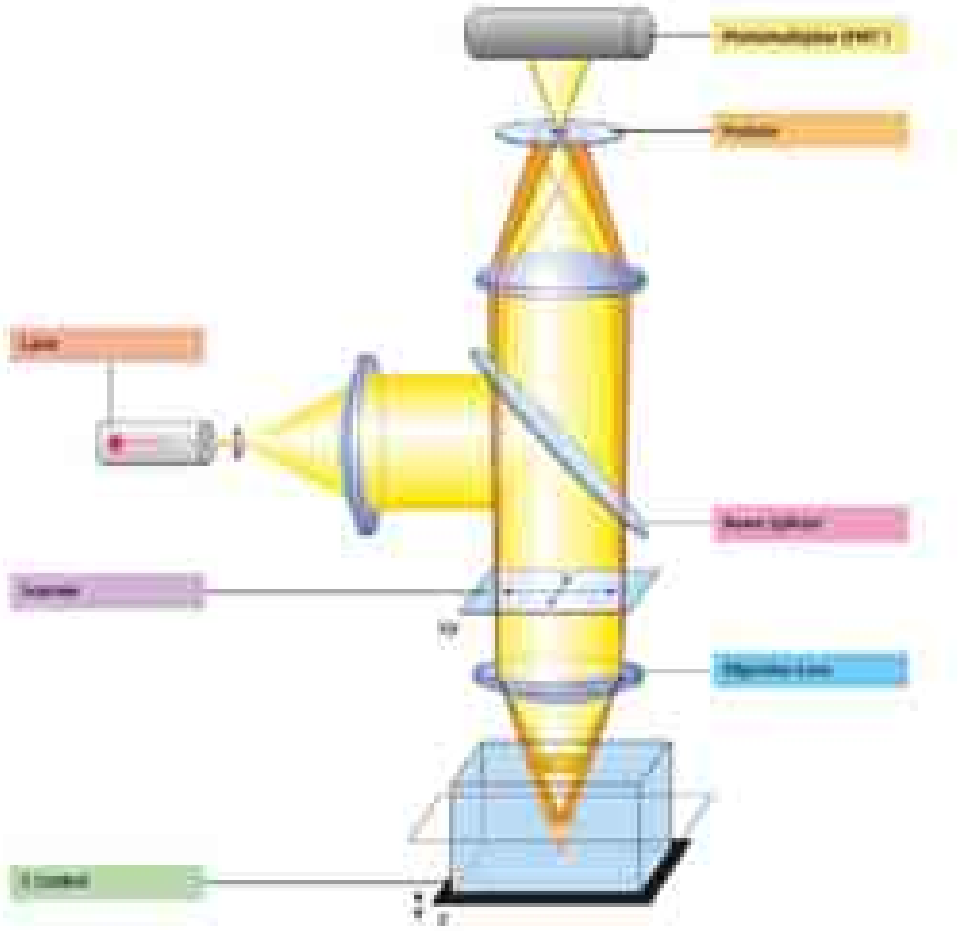

Figure 1.2 *Basic design of a Confocal Laser Scanning Microscopy (image taken from www.zessis.com).*

In this work, confocal images from cells after the uptake of nanomaterials were taken using an LSM 510-META CLSM (Zeiss, Germany) with 63× and 100× oil immersion objectives.

1.2.6 Fluorescence Correlation Spectroscopy (FCS)

FCS was first developed in the 1970's by Elson and Magde [133]. FCS exploits the spontaneous fluctuations of the fluorescence emission of the molecules under investigation. These fluctuations occur at ambient temperatures and are generally represented as unwanted noise in the measured signal. The fluctuations can be quantified in terms of their strength, and also by their residency by temporally autocorrelating the recorded intensity signal. Autocorrelation basically measures the signal against itself and records the self similarity of the time series signal and thus describes the information contained in the signal. In this way it is possible to extract the decay constants of the temporal processes, e.g. diffusion times and reaction relaxation times. If the system is in thermal equilibrium and there are no other external effects on the emitted fluorescence, then, the fluctuations are due to statistical variations in the particle number density in the detection volume, caused by random Brownian motion. A typical FCS setup is illustrated in ***Figure 1.3***.

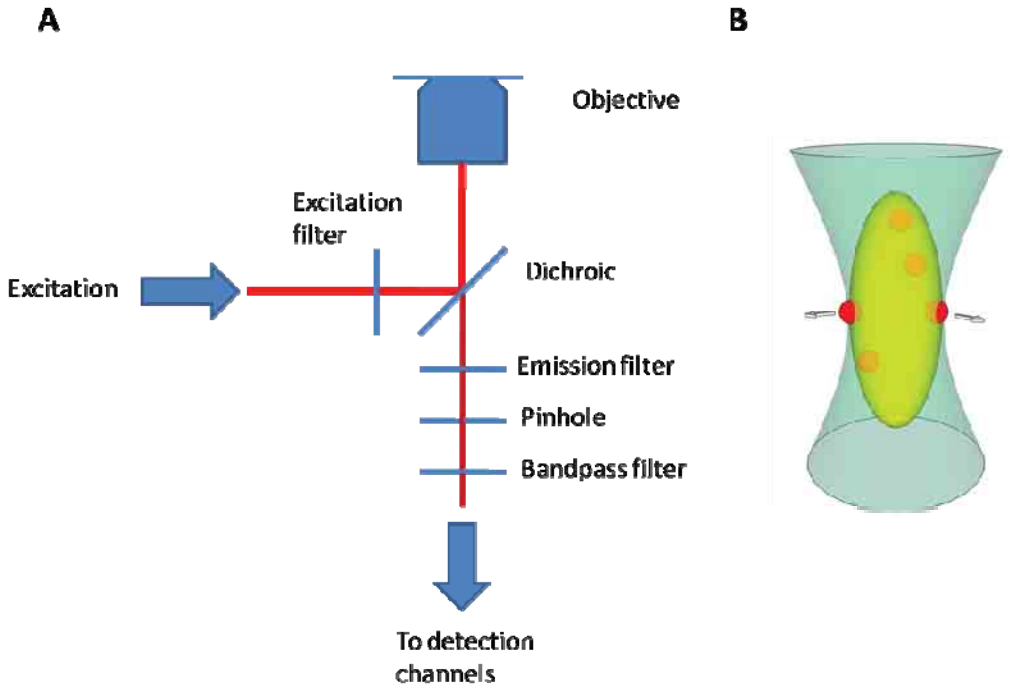

Figure 1.3 *(a) Schematic representation of the FCS measurement system. (b) Molecular mechanism of FCS, diffusion of fluorescent molecules into and out of the confocal detection volume (yellow).*

If we consider a fluorescent intensity signal ($F_i(t)$) for a fluorophore (i) that is illuminated within a detection volume (V). If we now consider time scales during which the excitation and fluorescent emission intensities can be considered constant, temporal changes will only be caused by changes in concentration, giving rise to a fluctuation term ($\delta F_i(t)$), which is defined as:

$$\delta F_i(t) = k_i Q_i \int_V I_{ex}(\underline{r}) CEF_i(\underline{r}) \delta C_i(\underline{r}, t) \cdot dV \quad (Eq.\ 1.3)$$

where $C_i(\underline{r}, t)$ represents the number density of the fluorophore i at time t in the observed volume, $I_{ex,i}$ is a term defining the geometry of the excitation beam, CEF_i represents the collective efficiency function (in confocal optics this is given by the imaging properties of the detection optics i.e. the objective and pinhole) [135]. The CEF is dependent on wavelength and must be indexed in multi-wavelength systems. Similarly, $I_{ex,i}$ is wavelength dependent, therefore excitation lasers must be carefully chosen in order to properly excite the selected fluorophore. Typically, this achieved by using separate laser beams.Q_i and k_i are constants defining the fluorescence quantum yield and the detector efficiency respectively. If we combined the above mention parameters into one single parameter called the 'emission characteristics' denoted by $E_i(\underline{r})$ with amplitudes η_i (with units of photons per molecule) for every fluorophore located at position r in the detection volume then we get the following equation:

$$E_i(\underline{r}) = Q_i k_i \cdot I_{ex,i}(\underline{r}) \cdot CEF_i(\underline{r}) = \eta_i MDE(\underline{r}) \quad (Eq.\ 1.4)$$

where, MDE denotes the molecule detection efficiency in the detection volume with values between 0 and 1 [135]. The spatial distribution of the MDE is approximated as a Gaussian in the axial and lateral directions within the detection volume; thus integration is carried out over the entire space. The normalized auto correlation function of the intensity signal, for a single fluorescent species, i is given by:

$$G_{ii}(\tau) = \langle \delta F_i(t) \delta F_i(t+\tau) \rangle / \langle F_i(t) \rangle^2 \quad (Eq.\ 1.5)$$

Using the above abbreviations we can re-express this as:

$$G_{ii}(\tau) = \frac{\iint E_i(r)E_i(r')\langle \delta C_i(\underline{r},0)\delta C_i(\underline{r'},\tau)\rangle dV dV'}{(\langle C\rangle \int E_i(\underline{r})dV^2)} \quad (Eq.\ 1.6)$$

When we are dealing with a species with a diffusion coefficient,D_i the number density autocorrelation term is described by:

$$\langle \delta C_i(\underline{r},0)\delta C_i(\underline{r'},\tau)\rangle \quad (Eq.\ 1.7)$$

and is given by:

$$\langle \delta C_i(\underline{r},0)\delta C_i(\underline{r'},\tau)\rangle = \langle C_i\rangle(4\pi D\tau)^{-3/2}\exp\left(-(\underline{r}-\underline{r'})^2/4D_i\tau\right) \quad (Eq.\ 1.8)$$

Using the above abbreviations we can now re-express this as:

$$G_{ii}(\tau) = \frac{\iint E_i(r)E_i(r')\langle \delta C_i(\underline{r},0)\delta C_i(\underline{r'},\tau)\rangle dV dV'}{(\langle C\rangle \int E_i(\underline{r})dV^2)} \quad (Eq.\ 1.9)$$

Following on from this we can then formulate an expression for the normalized three dimensional autocorrelation function for a fluorescent species, i, with a Gaussian emission light distribution [135], and lateral and axial radii, r_0 and z_0 respectively, within which the emission intensity drops to $1/e^2$:

$$E_i(\underline{r}) = \eta_i exp(-2(x^2+y^2)/r_0^2)exp(-2z^2/z_0^2) \quad (Eq.\ 1.10)$$

$$G_{ii}(\tau) = V_{eff}^{-1}\langle C_i\rangle^{-1}\left(1+\tau/\tau_{D,i}\right)^{-1}\left(1+r_o^2\tau/z_0^2\tau_{D,i}\right)^{-1/2} \quad (Eq.\ 1.11)$$

where V_{eff} is the effective detection volume and is defined as $V_{eff} = \pi^{3/2}/r_0^2 z_0$. In contrast, the average diffusion time, i.e. the average time it takes for a molecule to diffuse into and out of the detection volume, is given by $\tau_{D,i} = r_0^2/4D_i$. The temporal fluctuation decay function of the diffusing species can be abbreviated to:

$$Diff_i = \left(1 + \tau/\tau_{D,i}\right)^{-1}\left(1 + r_0^2\tau/z_0^2\tau_{D,i}\right)^{-1/2} \quad (Eq.\ 1.12)$$

If there is more than one non-interacting species present in the detected signal, then the autocorrelation represents the summation of all contributions. Under the special circumstances whereby the emission characteristics E_i are equal for the different components; i.e. same fluorescence marker but different molecular weights, the normalised correlation function is then defined as:

$$G_{tot} = \sum_i \langle C_i \rangle Diff_i / V_{eff} (\sum_i \langle C_i \rangle)^2 = N_{tot}^{-1} \sum_i Y_i Diff_i \quad (Eq.\ 1.13)$$

In this case all the components contribute to the time decay signal, weighted by their relative concentration fractions, $Y_i = \langle C_i \rangle / \sum_i \langle C_i \rangle$, while the amplitude G_{tot} for $\tau = 0$ is given by the total number of fluorophores present in the effective volume element, as given by $N_{tot} = V_{eff} \sum_i \langle C_i \rangle$. For a reliable, accurate quantitative evaluation of the fractions from the measured curve, all diffusion times should ideally be known vice versa, i.e. the fractions should ideally also be known. If the fluorophores undergo transitions to the singlet triplet state, which is highly likely, it is necessary for G_{tot} to be multiplied by a triplet correction term to allow for better data fitting. With this, the fitting function is now given by:

$$G_{tot,T} = \left(1 - T + T \cdot e^{-t/\tau_T}\right) \cdot G_{tot} \quad (Eq.\ 1.14)$$

where T denotes the average fraction of the fluorophore that is in the triplet state with relaxation time τ_T.

In this work, all FCS data were recorded on an LSM 510 inverted microscope outfitted with the Confocor 3 FCS module (Carl Zeiss Gmbh.). The microscope objective used was a 40× water immersion objective (NA = 1.2, 0.28 mm working distance). FCS was used in these work to study the dynamics and state of aggregation of gold nanoparticles in cell media and intracellularly.

1.2.7 X-ray photoelectron spectroscopy (XPS)

X-ray photoelectron spectroscopy (XPS) is an analytical technique that uses photoelectrons excited by X-ray radiation (usually Mg Kα or Al Kα) for the characterization of surfaces to a depth of 2–5 nm. From the measured electron energy and energy shifts, elemental identification and chemical bonding information can be obtained respectively. High vacuum or even ultrahigh vacuum (UHV) is required during the analysis, therefore the samples need special handling [193]. XPS has been applied in virtually every area in which the properties of surfaces are important, including studies of catalysis, interfaces, corrosion, adhesion, and superconductors [194].

In this work, for the analysis of CeO_2 NPs, dispersed NPs were put on titania surfaces and dried in vacuum. Then the chemical composition of NPs was measured by XPS in a SPECS SAGE HR 100 system using a non-monochromatic Al Kα X-ray source at 12.5 kV and 300 W.

1.2.8 Electron Microscopy (EM)

There are two major types of electron microscope, one is transmission electron microscopes (TEM) and the other is scanning electron microscopes (SEM).

In a conventional TEM, a thin specimen is 'illuminated' by an electron beam of uniform current density to obtain magnified images. The electrons are emitted by an electron gun, normally equipped with a tungsten filament cathode as the electron source. There are two types of electron sources to produce the electron beam with the necessary properties: the thermionic and field-emission sources. The acceleration voltage of routine instruments is 100–200 kV. Medium-voltage instruments work at 200 to 500 kV to provide better transmission and resolution and in high voltage electron microscopy (HVEM) the acceleration voltage can reach 500 kV to 3 MV [195].

In SEM, the image is obtained through point by point scanning of a focused electron beam across the surface of a solid specimen. The primary electrons penetrate the solid

specimen and are deflected by a number of elastic scattering processes. The energy spectrum of electrons that leave the specimen and are collected by the detector system results in specific information and two different types of contrast. SEM is commonly used for surface morphology studies in material science [196].

For a typical TEM study, a 2.5 µL suspension of NPs was pipette onto a TEM copper grid with carbon film. Samples were left in a vacuum chamber to allow water evaporate completely and then measured with a JEOL JEM-2100F TEM at 200 kV.

For the morphology of hybrid PLGA NPs via SEM, samples were examined with a Zeiss Supra 40 VP SEM at 5 kV with 75000 to 150000× magnification.

1.2.9 Magnetic Resonance Imaging (MRI)

Magnetic Resonance Imaging (MRI) is a non-invasive investigation tool for medical diagnosis of internal tissues and organs of the human body [197]. The MRI mechanism is based on excitation and relaxation of the hydrogen nucleus (proton) which is abundant in the human body as in water molecules. Image intensity of tissues is modulated by the regional abundance (or local density) of water. The initial signal distribution is further altered by a variety of factors that reflect the local physicochemical microenvironment of the water molecules, such as their mobility or the presence of microstructural entities, macromolecules, and membranes [198].

In this work, hybrid PLGA NPs were scanned in MRI with a 7 T MR scanner (Bruker Biospec). T2-weighted spin-echo MRI images were acquired at an echo time of 260 ms.

1.2.10 Flow Cytometry

Flow cytometry is a powerful tool to measure characteristics of cells (or particles) based on their light-scattering and fluorescence properties. It is designed to detect and catalogue cellular/particle elements in a suspension. In order to achieve this, Flow Cytometers employ the use of three major components: the fluidics, optical, and electronic

systems.[199] The fluidics system transports cells/particles in a sample through the cytometer for analysis. In doing this, the fluidics system generates a stream of cells/particles that transit past an examination point one by one in a defined and rapid manner. This is accomplished by generating a pressurized stream of sheath fluid into which the sample suspension is injected. This allows for the focusing of the cells/particles into a uniform, single file stream as they pass through the flow cell, while hydrodynamic focusing maintains the uniformity of the stream. Stream uniformity is vital for ensuring reproducible sample illumination as they intersect the cytometer laser beams.

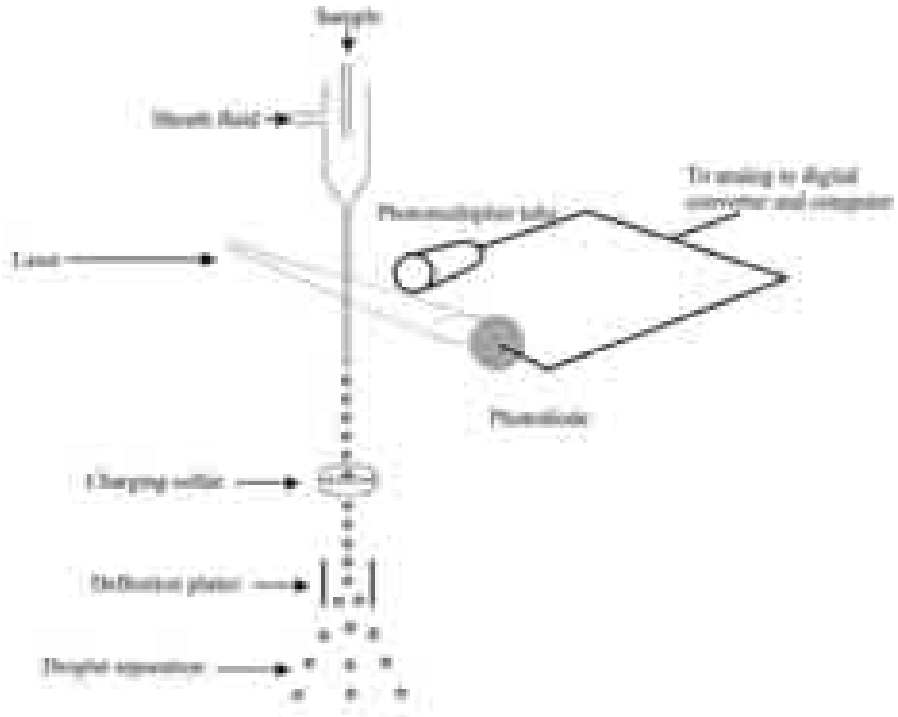

Figure 1.4 *Schematic representation of a flow cytometry* [99].

Cell/particle attributes are assessed by their ability to scatter incident laser light as well as by the emission of fluorescence, if they are fluorescently labeled. Standard Flow Cytometers typically contain two laser lines, offering different excitation wavelengths. As the sample suspension passes through the flow cell, the cells/particles pass the examination point, where they intersect the laser. Each flow cell scatters laser light which

is then collected by a photodiode. Forward scatter is collected in the same direction as the laser light while side scatter and fluorescence are collected at 90° to the laser light. Forward scatter is collected by the forward scatter photodiode. Side scatter and fluorescence are relayed via a series of filters and mirrors to one of several PMTs. Typically flow cytometers have between 5 and 6 PMTs, 1 for side scatter light with the remaining PMTs for fluorescence emission detection. When a photon is incident on one of the PMTs, this generates a voltage which is amplified, converted to a digital signal and sent a PC for storage and analysis.

In this work, a flow cytometer BD FACS (Canto II) was used for the study of the cellular uptake of fluorescent NPs.

1.2.11 Raman Spectroscopy

Raman scattering is an inelastic scattering of photons named after its discoverer C. V. Raman, an Indian physicist. When photons of light pass a sample and interact with the molecules of the sample, different light scattering will happen. Light scattering is a two-photon process, where one photon is absorbed and another photon is emitted simultaneously. Photons are most often emitted with the same frequency as the incident photon (= Rayleigh scattering), but photons can occasionally loose or gain energy due to molecular interactions and therefore result in frequency shift.

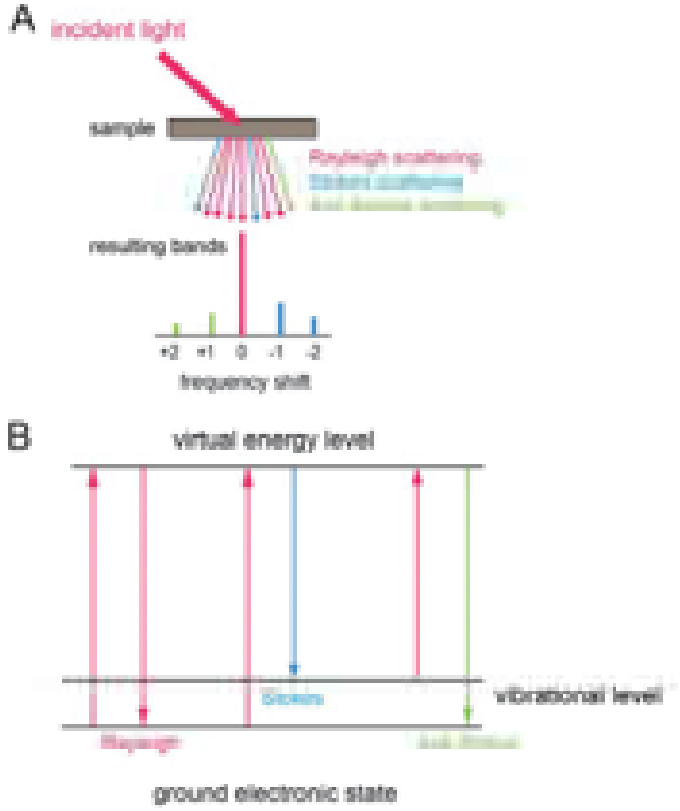

Figure 1.5 *Schematic of Raman spectroscopy* [119]**.**

Raman spectroscopy is based on Raman scattering of photons following their interaction with vibrating molecules of the sample. During this interaction, the photons transfer energy to molecules as vibrational energy (Stokes scattering), Therefore, the energy loss of the scattered photons corresponds to the vibrational energy levels of the molecules. Since the vibrational energy spectrum depends on the chemical composition of the sample (type of atoms, bond strength, bond angles and symmetry etc.), A Raman spectrum represents a chemical fingerprint of the sample. In anti-Stokes scattering, the incident photons receive energy from vibrating molecules, therefore, their frequencies increase. The anti-Stokes spectrum is symmetric to the Stokes spectrum relative to the elastic scattering (Rayleigh scattering) line, although the intensity of the Stokes spectrum is higher because there are more molecules on the lower energy levels than on the higher energy levels (Boltzmann distribution) [120].

Raman spectroscopy is widely used in the biomedical field for different applications such as *in vitro* cell monitoring, *in vivo* diagnostic and investigation of epidemic outbreaks of infections [119].

In this work, Raman spectroscopy analyses were performed with a Renishaw inVia Raman microscope using a 532 nm laser as the excitation source with a grating of 1800 mm^{-1}. The microscope was equipped with interchangeable objective lenses with magnifications of 10×, 50×, and 100×. Most measurements were conducted using the 40× water immersion and 50× objectives. The size of the focal spot was approximately 1 μm. Raman spectra were recorded in the region from 100 to 3200 cm^{-1} with a spectral resolution of around 7 cm^{-1}.

1.2.12 MTT assay

MTT assay is a standard colorimetric assay for in vitro cell proliferation and cytotoxicity study.

It is based on the principle that the compound tetrazolium salt 3-(4, 5-dimethylthiazol-2-yl)-2,5-diphenyltetrazolium bromide (MTT) can penetrate the cell membrane and be reduced to its insoluble formazan intracellularly by NAD(P)H-oxidoreductases and the mitochondrial enzyme succinate dehydrogenase. The number of metabolically active cells is directly proportional to the amount of insoluble formazan. The formazan can be dissolved in an organic solvent and quantified by measuring the absorption at 550 nm [200]. Accordingly the cell viability can be defined as:

$$Viability(\%) = \frac{Absorbance_{sample}}{Absorbance_{control}} \times 100 \quad (Eq.1.15)$$

A TECAN GENios Pro plate reader was used to measure the absorbance for the MTT assay at 550nm.

Chapter 2

Surface modification of CeO_2 NPs and their uptake, intracellular distribution and cytotoxicity

2.1 Motivation and Background

Cerium oxide is one of the most important materials for industrial use and cerium oxide nanoparticles (CNPs) have been widely used for different applications such as in solar cells [201,202], catalysts [203–205], polishing agents [206,207], and fuel additives [208,209]. Yet CNPs have recently drawn increasing interest in the biomedical field. The antioxidant activity of CNPs is one of their most attractive properties for potential biomedical uses. Both bulk cerium oxide material and CNPs possess redox properties because of the coexistence of two oxidation states of cerium (Ce^{3+} and Ce^{4+}) on the surface of the cerium oxide lattice. However, at the nanoscale, cerium oxide can contain intrinsic oxygen defects. These oxygen defects are actually 'hot spots' of catalytic reaction. The concentration of oxygen defects and the concentration of Ce^{3+} ions increased with the reduction in particle size [210,211]. For these reasons, CNPs have improved antioxidant properties with respect to the bulk materials. The antioxidant properties of CNPs are pH-dependent and in slightly acidic conditions CNPs can facilitate the fast oxidation of organic dyes without hydrogen peroxide. This has led to the development of inmunoassys based on of CNPs as a substitute for peroxidase or oxidase which are susceptible to denaturation or decomposition [212,213]. CNPs have also shown different protective effect on cells both *in vitro* and *in vivo,* such as against radiation exposure [214] , against oxidative stress [215,216], and anti-inflammation[217].

Despite the promising and diverse applications of CNPs, the study of the potential impact of engineered CNPs on human health is not fully understood. Several *In vitro* studies indicate that CNPs are toxic to several different cell lines. For example, CNPs were able to reduce the viability and cause the apoptosis and autophagy of human monocytes by mitochondrial damage and over expression of apoptosis inducing factors [218]. CNPs of

different sizes caused certain cytotoxicity when exposed to human lung epithelial cells (BEAS-2B) and led to cell death, Reactive Oxygen Species (ROS) increase, GSH decrease, and the activation of oxidative stress-related genes such as heme oxygenase-1, catalase, glutathione S-transferase, and thioredoxin reductase takes place[219]. When CNPs were exposed to human lung cancer cells, cell viability decreased significantly as a function of NPs dose and exposure time [220]. However, there are also many other studies that show that CNPs are non-toxic and have a protective effects on cell apoptosis. For instance, CNPs were internalized in endosomal compartments in macrophage cell lines (RAW 264.7) and BEAS-2B cells after cell without inflammation or cytotoxicity. Prior incubation with CeO_2 could protect these cells against the cytotoxic effects of exogenous stress stimulus [221]. In another case, CNPs with diameters in the range of 7 to 94 nm were found to be non toxic to the human monocytic cell line (U937) and could scavenge intracellular ROS [222].

Nevertheless, the *in vitro* toxicity of CNPs is somehow conflicting according to the literature. The main impact of CNPs on cell viability and apoptosis depends on the effect on the intracellular oxidation process. When CNPs behave as an antioxidant, they have a pro-survival effect and may protect cells from oxidative stress, whereas when CNPs exhibit pro-oxidant effect behavior, ROS and apoptosis are induced [223]. Cell type, NPs surface characteristics, NPs size and intracellular pH may all play a role that affects the intracellular behavior of CNPs. However, how these factors influence the anti- or pro-oxidant behavior and cellular uptake of CNPs has not yet been determined [224,225].

In this chapter, commercial CNPs were surface modified by coating them with polyelectrolyte brushes via *in situ* Atom Transfer Radical Polymerization (ATRP). ATRP is one of the most effective and versatile techniques to introduce macromolecules onto the surface of inorganic NPs [165]. [226–228]. Densely charged olyelectrolyte brushes can provide better colloidal stability of CNP in aqueous medium, and lead to further modification of the NPs with bio-ligands to provide better biocompatability and facilitate their use in biomedical applications. Though the CeO_2 NPs we used showed a positive ζ-potential, this value was close to 0 which reflects a nearly neutral surface charge. The coating of the NPs with polyelectrolyte brushes brings a higher charge density to the NP

surface, either negative or positive charge. In this way we are able to study the uptake and intracellular localization of the NPs as a function of their surface charge: positive, negative and almost zero. The use of the 'grafted from' polyelectrolyte brushes to modify CeO_2 NPs gives another important advantage over other functionalization strategies for NPs. For uptake studies it is often necessary to attach a dye to the surface of the NPs. The labeling of CeO_2 NPs with fluorescence dyes will affect the surface properties of the NPs. Dyes are often charged but at the same time they usually display conjugated aromatic rings that give them a certain hydrophobic character. By attaching a dye to the surface of the NP, the charge and hydrophobicity of the NP surface may be altered, which in turn will affect the uptake and fate of the NP intracellularly. NP toxicity may also be altered by the presence of the dye as the dye itself may have an inherent toxicity. We will show in this chapter that the brushes can be used to 'encapsulate' dyes at the surface of NPs. Fluorescence dyes will be directly attached to amine terminated silanes. Following brush synthesis, the dyes will be covered by the brushes. In other words, the NPs will be labeled but the label will not be placed on the outer surface of the NPs, thus not affecting surface charge or degree of surface hydrophobicity of the NPs.

In addition the brushes are thin organic layers that can behave as a barrier around the CNPs. This can affect the redox equilibrium between Ce^{3+} and Ce^{4+}, which depends on the electron transfer between the NPs and the cell. The use of brushes as a surface functionalization tool of the NPs allows us to study the effect of the coating in this equilibrium.

2.2 Surface modification of CNPs with Polyelectrolyte brushes

2.2.1 *In situ* polymerization of polymer brushes on the surface of cerium oxide NPs

The surface of cerium oxide NPs was modified via Atomic Transfer Radical Polymerization (ATRP) as shown in ***Figure 2.1***.

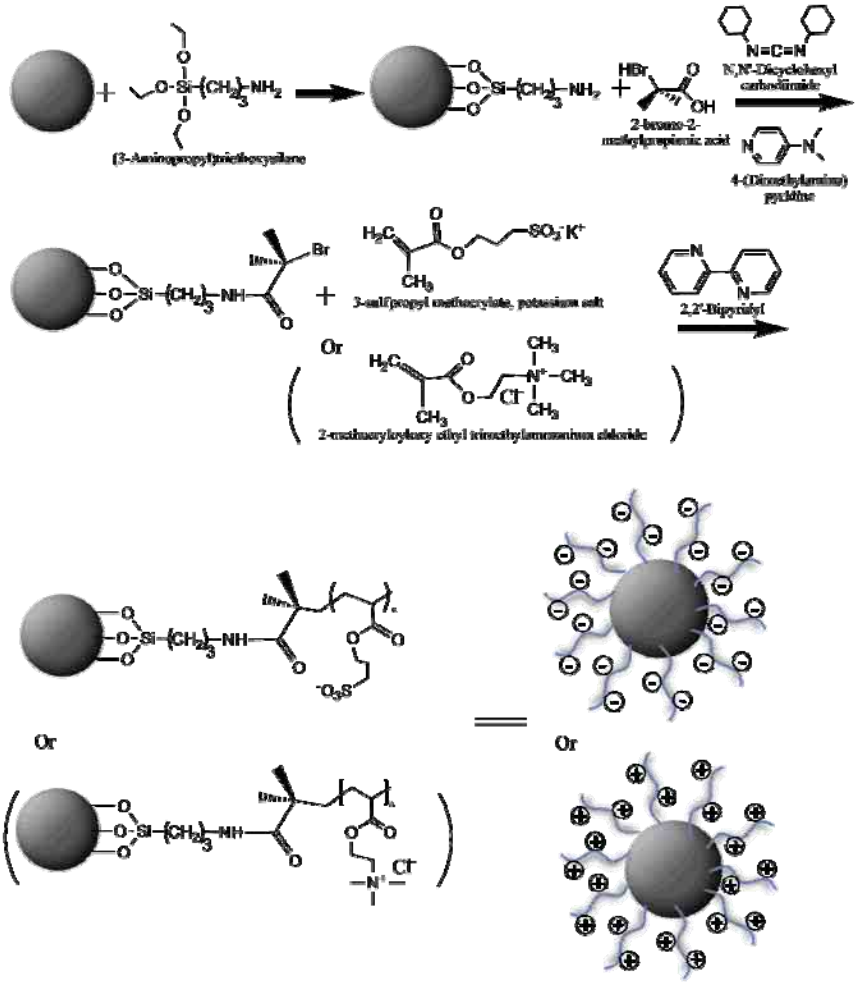

Figure 2.1 *scheme of 'grafting from' polymer brush synthesis at the surface of cerium oxide NPs.*

Polyelectrolyte brushes of poly (3-sulfopropylmatheacrylate) (PSPM) and poly (2-(methacryloyloxy)ethyl-trimethylammonium chloride) PMETAC were synthesized in situ through a 'grafting from' method to the surface of cerium oxide NPs. Firstly, 100mg NPs were well dispersed in DMF and mixed with 20µL (3-aminopropyl) triethoxysilane. This reaction was carried out for 18h in a nitrogen gas environment. NPs were then washed thoroughly by centrifugation to remove chemical residue from the reaction. After attachment of the silane to the surface of cerium oxide NPs, the radical polymerization initiator 2-bromo-2 methylproprionic acid was bounded to the amine group of the silane via a condensation reaction [229]. NPs were re-suspended in CH_2Cl_2 and placed in a

round flask. 2-bromo-2-methylpropionic acid, was added to the suspension along with dimethyl aminopyridine and a $CuCl_2$ (Cu^{2+}), the catalyst. The mixture was cooled down to 0 °C with vigorous stirring. N,N'-Dicyclohexylcarbodiimide , another catalyst,was then added to the flask. The reaction was kept on for another 18h and all under N_2 ambient. After careful washing twice in CH_2Cl_2, twice in acetone and twice in DMF, NPs coated with initiators were dispersed in N,N-dimethylformamide DMF/water (3:2, v/v) solution with monomer, 2,2-bipyridine and CuCl (molar ratio, 10:2:1). The polymerization reaction was carried outfor 5h under N_2 ambient [230].

For the fluorescently labeled NPs, 100 mg silanized NP were firstly mixed with 257 µg Alexa Fluor® 488 (Alexa 488) in DMF and the reaction carried out for 4h. After five washes through centrifugation, polymer brushes were synthesized to the surface of the NPs (as described before).

In order to leave enough amount of amine for attachment of the initiator, a calculation of the amount of amine on the surface of one cerium oxide NPs was performed on the basis of the size of the CNPs and the size of a unit cell of cerium oxide crystal as describe by S. Lee et al. [215] The average size of CNPs is 15 nm (based on the result from over 200 CNPs from TEM images).

The calculation is presented as follows:

Volume of single CNP = $4/3\times3.14\times (15/2\times10^{-9}\ m)^3=1.77\times10^{-24}m^3=1.77\times10^{-18}\ cm^3$ (we consider the shape of a single CNP as a sphere)

.Since there is a layer of atoms in the outer surface of CNPs. Thickness of the layer is assumed to be a half of the lattice constant (The lattice constant of a cerium oxide crystal is 5.39 Å).

Volume of single unit cell (a^3) = $(5.39\times10^{-10}\ m)^3= 1.57\times10^{-28}m^3$ (volume of a cube)

Thickness of outer layer = $1/2\times5.39\times10^{-10}\ m= 2.69\times10^{-10}\ m$

Radius of the inner part =$15/2\times10^{-9}\ m- 2.69\times10^{-10}m=7.23\times10^{-9}\ m$

Volume of the inner part = $4/3\times3.14\times (7.23\times10^{-9}\ m)^3 =1.58\times10^{-24}\ m^3$

Volume of the outer layer = $1.77\times10^{-24}\ m^3-1.58\times10^{-24}\ m^3=1.9\times10^{-25}\ m^3$ (Volume of one CNP subtracts volume of the inner part)

The number of unit cell on the outer layer =$1.9\times10^{-25}/1.57\times10^{-28}$= 1200 (Volume of outer layer / Volume of single unit cell)

Since each unit has 8 oxygen ions,

the number of oxygen ions on the outer layer =8×1200 = 9600

Weight of single CNPs = 1.77×10^{-18} $cm^3\times7.44g/cm^3$ = 1.32×10^{-17} g (The density of CNPs is 7.44g/ cm^3 and the volume of single CNP 1.77×10^{-18} cm^3)

So in 100mg CNPs,

the number of single NPs = 0.1 g /1.32×10^{-17} g = 7.6×10^{15}

And in 100mg CNPs,

the amount of oxygen ion in the outer layer = $9600\times7.6\times10^{15}\times N_A$ (Avogadro constant) = 121μmol

Let us consider the silane covered the surface of all the CNPs completely, then in 100mg CNPs the amount of amines on the surface of CNPs =121 μmol /3=40μmol (one sliane molecule has 1 amine and consumes 3 oxygen ion in the outer layer)

For the fluorescence labeling, the molar ratio between the fluorophore Alexa 488 and the silane is 1 to 100.

This means for 100 mg silanized CNPs,

the needed weight of Alexa 488 = 643.41g/mol×$(40\times10^{-6}/100)$ mol =257μg

By controlling the amount of the fluorophore the initiator of ATRP can be later attached to the surface of CNPs and the labeling has no impact on the ATRP process.

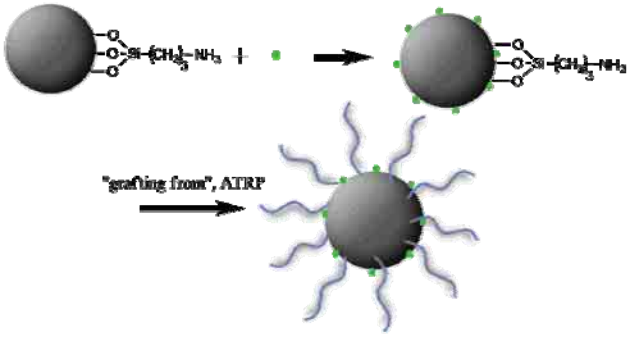

Figure 2.2 *scheme of fluorescence labeling of cerium oxide NPs.*

2.2.2 Characterization of modified CNPs

The surface modification of CNPs with brushes was proved by Transmission Electron Microscopy (TEM) and zeta potential measurements. In ***Figure 2.3***, the polymer coatings can be visualized in the TEM images). CNPs displayed a crystalline structure with single particle size around 15nm. By staining with uranyl acetate, the polymer brush layer around the NPs was revealed as a brighter shell around the NPs, which is absent in the pristine NPs. PSPM brush presented a thickness around 6nm (***Figure 2.3b***) while PMETAC brush presented a thickness around 2nm in dry state (***Figure 2.3c***).

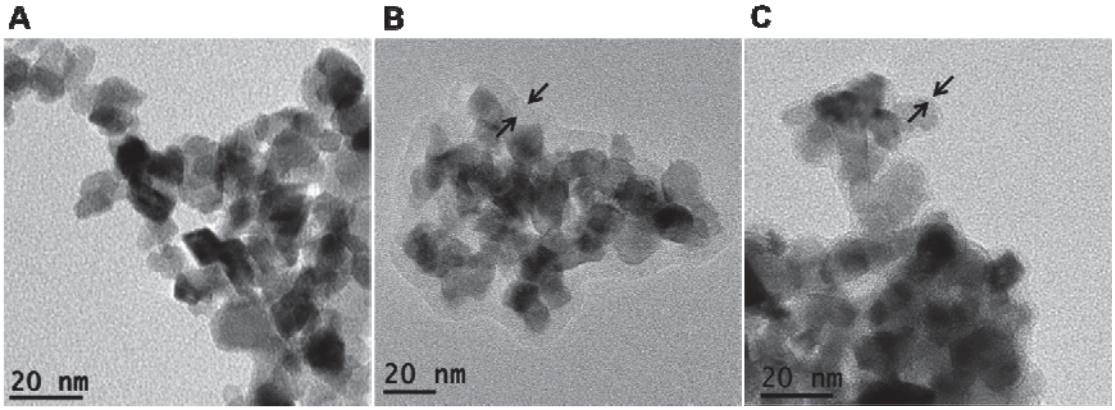

Figure 2.3 *TEM images of cerium oxide NPs with different polymer brush coatings. NPs were all pretreated with uranyl acetate to visualize the polymer coating.*

Table 2.1 *Size and ζ-potential of cerium oxide NPs measured by DLS*

	Size (nm)	Zeta (mV)
CeO_2 NPs	894.2±47.59	8.22±0.35
CeO_2@PSPM NPs	159.3±5.12	-31.9±3.87
CeO_2@PMETAC NPs	247.7±9.01	25.7±0.31

The hydrodynamic size and ζ-potentials of CNPs with different polymer coatings were measured at 25° C and all the CNPs were dispersed in 10 mM NaCl. The results are shown in **Table 2.1**. It can be observed that unmodified CNPs (CeO_2 NPs) show a large hydrodynamic size due to the formation of agglomerates in the aqueous solution due to its low surface charge and limited colloidal stability as previously reported [231], whereas the PSPM coated CNPs (CeO2@PSPM NPs) and PMETAC coated CNPs (CeO_2@PMETAC NPs) presented much smaller hydrodynamic sizes in aqueous solution which indicate the polymer coating effectively reduces agglomeration. CeO_2 NPs show a slightly positive ζ-potential, close to zero, while the CeO2@PSPM NPs show a highly negative potential around -30 mV which can be attributed to the sulfonate groups in PSPM. CeO_2@PMETAC NPs show a high positive charge around +25 mV which is due to the quaternary group in PEMTAC. The polymer brush coating provided a high charge density and the larger charges as revealed by ζ-potential improved the colloidal stability of CNPs in aqueous solution.

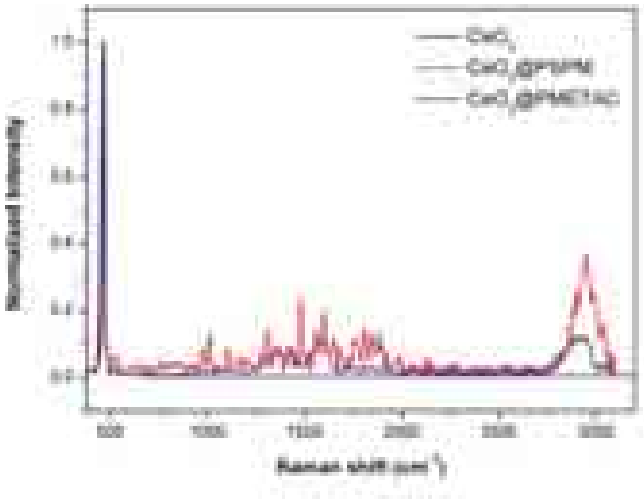

Figure 2.4 *Raman spectra of CNPs with different coatings.*

CNPs were also characterized by Raman spectroscopy. Spectra were taken using a 100× objective with 532 nm excitation and a grating of 1800 mm^{-1}. Raman spectroscopic data of CNPs with different polymer coatings are shown in ***Figure 2.4***. CNP have a distinct peak in Raman spectra at about 465 cm^{-1}. This band is assigned to a symmetric breathing mode of the oxygen atoms around the cerium ions [232]. After polymer coating, this

strong peak is still observed without a significant shift of the spectral position of the band. The broad peak present at 2900 cm^{-1} is assigned to a combination band mainly involving C-H stretching mode of CH_2 from the polymer backbone. And the peaks in the 1200 cm^{-1} to 1600 cm-^{1} region are assigned to the C-H deformation mode [233].

CNPs with different polymer coatings were also characterized by X-ray photoelectron spectroscopy (XPS). All samples were measured at 12.5 kV and 300 W in a SPECS SAGE HR 100 XPS system using a non-monochromatic Al Kα X-ray source at 12.5 kV and 300 W. The pass energy was 30 eV for survey scan and 10 eV for narrow scans. Prior to analysis, spectra were all calibrated to aliphatic carbon at 285 eV.

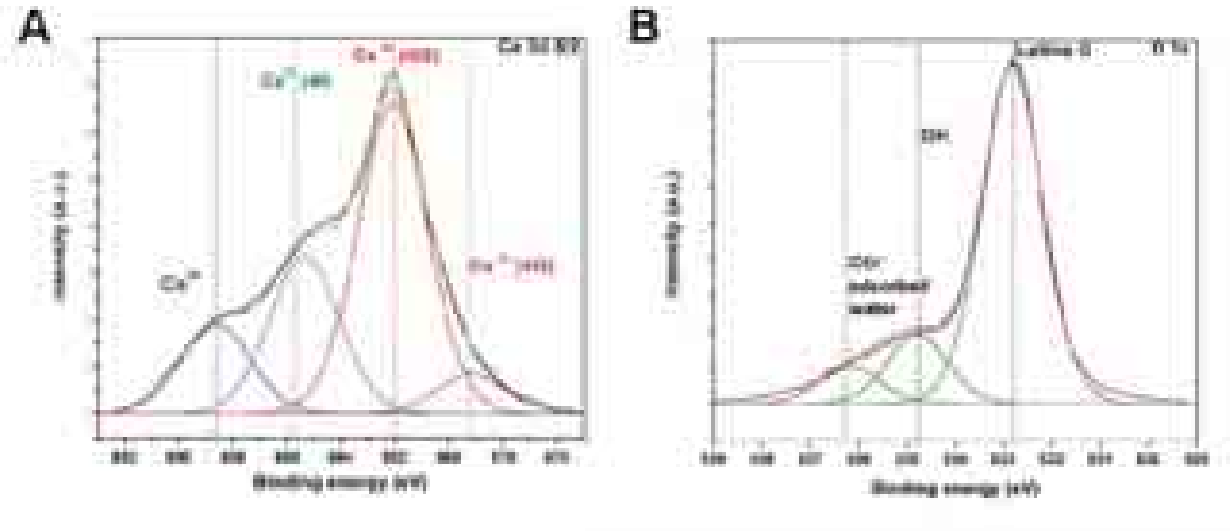

Figure 2.5 *XPS spectra of (A) Ce 3d 5/2; (B) O1s for CeO_2 NPs.*

XPS spectra of Ce 3d 5/2 region, shown in ***Figure 2.5***, represents a coexistence of two oxide states, Ce (III) and Ce (IV), on the surface of the NPs. Unlike most of the rare earths existing in trivalent state, cerium can also occurs in tetravalent state and may shift between these two states in a redox equilibrium. As a result of alterations in the cerium oxidation state, cerium oxide forms oxygen vacancies or defects in the lattice structure by loss of oxygen. The generation of defects in the structure of cerium oxide is a dynamic process and can change spontaneously or in response to physical parameters such as temperature, presence of other ions, and partial pressure of oxygen [211]. This makes cerium oxide an excellent oxygen buffer, which possesses a free radical scavenging

activity by reversibly binding oxygen and shifting between the Ce^{3+} (reduced) and Ce^{4+} (oxidized) forms at the particle surface [15].

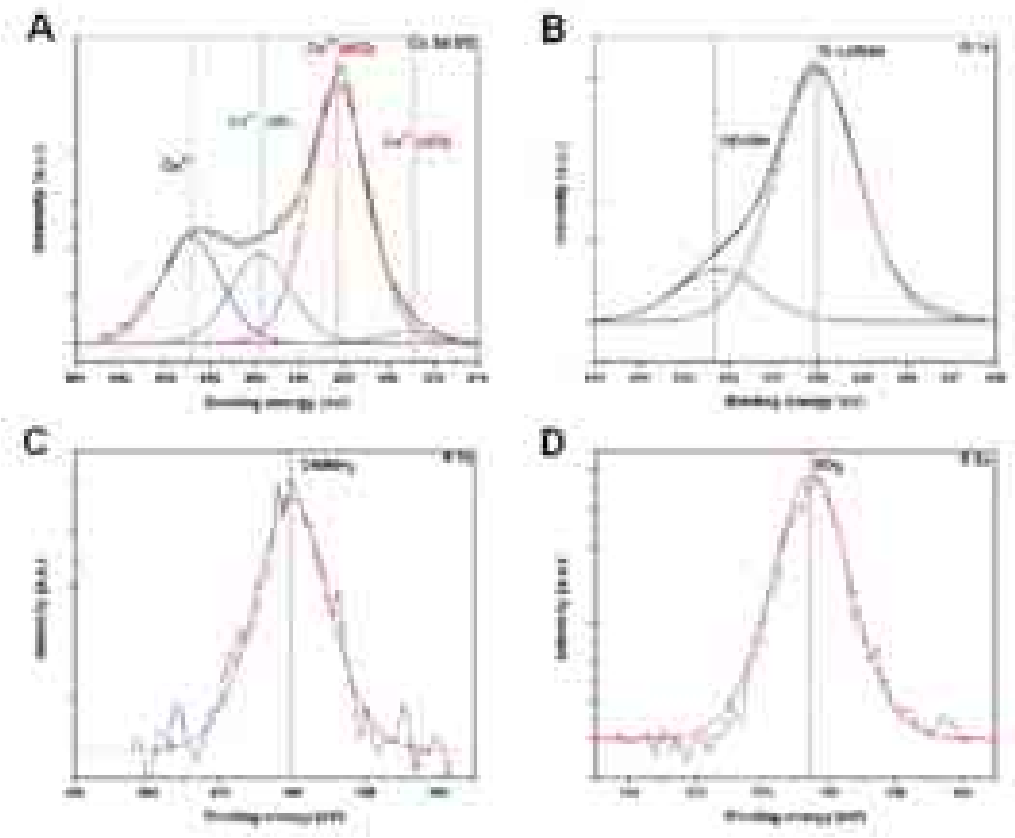

Figure 2.6 *XPS spectra of (A) Ce 3d 5/2;(B)O1s; (C) N 1s; (D)S 2p for CeO_2@PSPM NPs.*

In the spectra of CeO_2@PSPM NPs (***Figure 2.6***), the existence of a sulfonate group in the 2p region of sulfur, at 168.1 eV indicates the existence of PSPM brushes on top of the NPs [235,236].

The NH_2 group at 400.1 eV is observed in the N 1s region, which comes from the silane link the CNPs surface and the polymer brush. In ***Figure 2.7***, the photoelectron peak in the 1s region of nitrogen is resolved in both species; NH_2 at 400 eV and quaternary nitrogen at 402.8 eV respectively [237]. The quaternary ammonium structure arises from the PMETAC polymer and here serves as proof of the existence of the brushes.

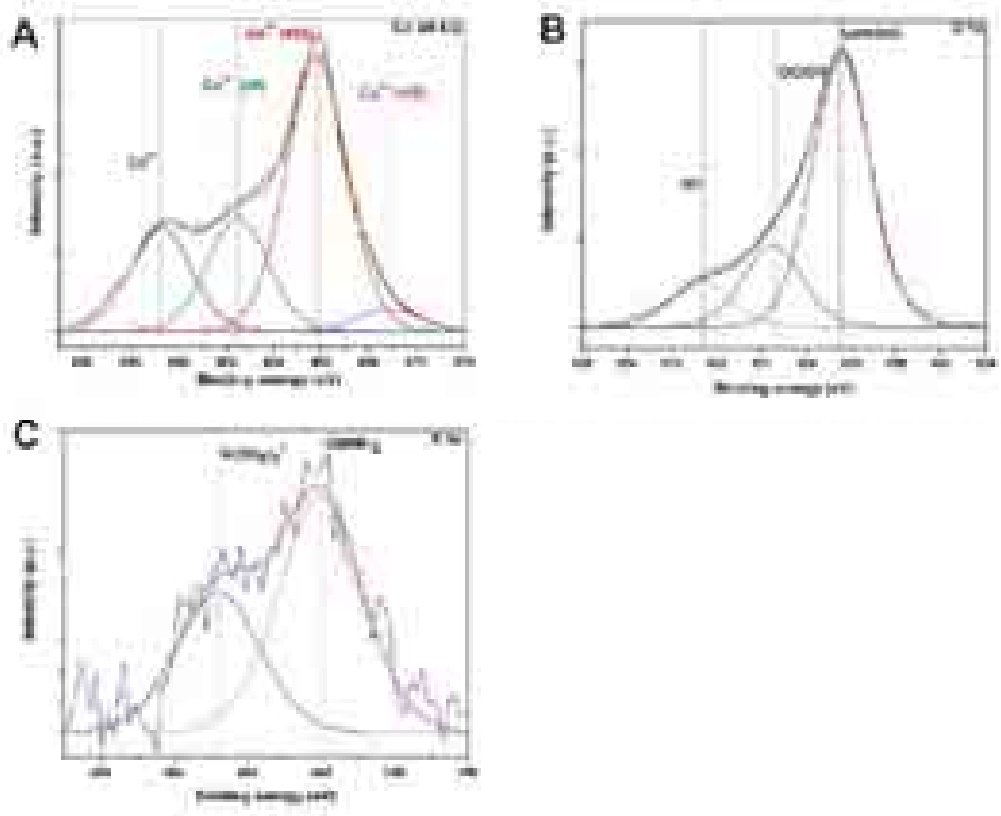

Figure 2.7 *XPS spectra of (A) Ce 3d 5/2;(B)O1s; (C) N 1s; for CeO_2@PMETAC NPs*

Polymer brushes can respond with conformational changes to environmental conditions such as variations of temperature, pH value and ionic strength. The behavior of polymer brush coated CNPs in response to changes of ionic strength of the media was studied by monitoring the change of ζ-potential in NaCl solution with varying salt concentration from 10 to 100 mM.

From the results, it can be seen that CeO_2@PSPM NPs maintain a nearly constant ζ-potential regardless of the change of ionic strength (***Figure 2.8***), while CeO_2 NPs and CeO_2@PMETAC NPs both change ζ-potential by approximately 25 mV from 10 mM NaCl to 100 mM NaCl.

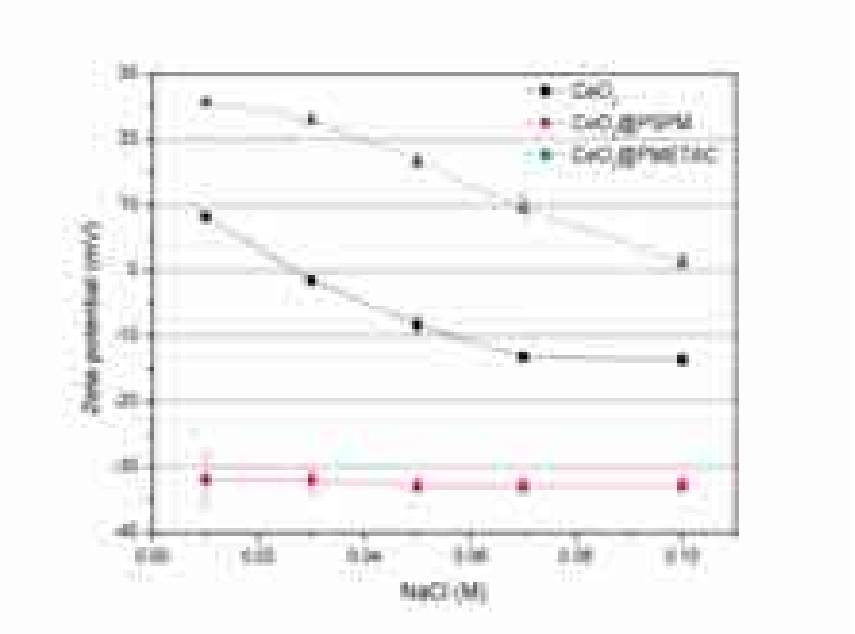

Figure 2.8 *ζ-Potential of CeO_2 NPs (black squares), CeO_2@PSPM NPs (red filled circles) and CeO_2@PMETAC NPs (blue triangles) measured as a function of ionic strength.*

The ζ-Potential change of CeO_2 NPs and CeO_2@PMETAC is similar to what is expected from a solid particle with a constant surface charge in which the higher ionic strength causes the decay of ζ-potential. In the case of CeO_2@PSPM NPs, the almost constant ζ-potential indicated that the NPs surfaces behaved more like soft or 'hairy' surfaces in contrast with the 'hard' surfaces of the non modified NPs. When polyelectrolytes are conjugated to colloidal NPs from one side of the chain, the other end of the chain will be free. Due to this particular arrangement of the polymer chains, polyelectrolyte brushes retain significant conformational freedom, which allows them to regulate their charges by changing conformation in response to variations of the ionic strength [238]. The different behaviors of CeO_2@PSPM NPs and CeO_2@PMETAC NPs are possibly due to the difference in density of the two brushes as observe by TEM. CeO_2@PSPM NPs showed a much thicker layer around the NPs which is approximately 3 times thicker than the layer surrounding the CeO_2@PMETAC NPs.

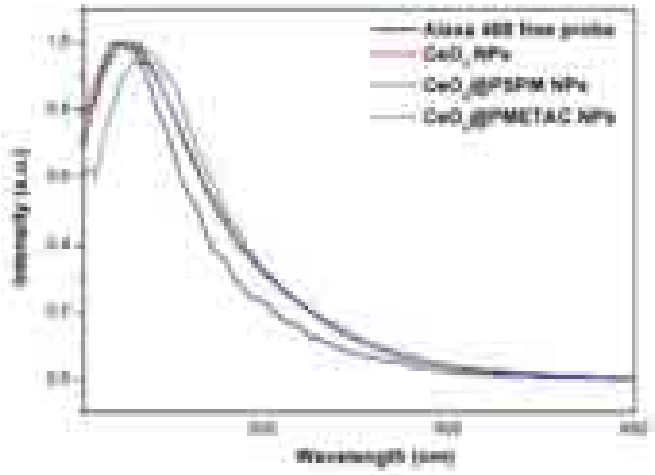

Figure 2.9 *Fluorescence emission spectra of Alexa Fluor™ 488 free probe and of Alexa Fluor™ 488 labeled CNPs in distilled water. 488 nm excitation.*

The emission spectra of the labeled NPs were compared with the emission spectra of free Alexa Fluor™ 488. The peak emission wavelength of CNPs shifted only a few nanometres (***Figure 2.9***), meaning that the attachment of the dye to the NPs did not alter its spectroscopic properties.

2.3 Cellular uptake, intracellular distribution and cytotoxicity of CNPs with different surface modification

2.3.1 Cellular uptake and intracellular distribution study of CNPs

Uptake of Fluorescently labeled CNPs was characterized by flow cytometry, and Confocal Laser Scanning Microscopy (CLSM). As has been previously explained above the labeling of the PSPM and PMETAC coated CNPs is performed by attaching the Alexa 488 to the surface of the NP through silanization prior to the synthesis of the brush. In this way the dye remains encapsulated in the brush and does not affect the surface characteristics of the NPs. To apply CLSM and flow cytometry with the NPs without brushes, we use very low amount of silane (0.2 μL ATPS to 100mg CNPs, 50 times less than those for synthesis of polymer brushes), which will consume proximately 2%

percent of the oxygen on the surface of CNPs based on the oxygen amount on the surface of CNPs as we calculated before. In this way we try to keep the surface as close as possible to the unmodified NP and at the same time be fluorescently labeled The ζ-potential of Alexa-488 labeled CNPs without polymer brush is 3.99±1.31 mV, which is very similar to the value of unmodified CNPs. Alexa 488 labeled CNPs without polymer brush, with PSPM and PMETAC coating will be denoted as CeO_2 NPs, CeO_2@ PSPM NPs and CeO_2@ PMETAC NPs respectively in all the results of CLSM and flow cytometry. The uptake of unlabeled CNPs was studied by Raman spectroscopy, Transmission Electron Microscopy (TEM) and Inductively Coupled Plasma Mass Spectrometry (ICP-MS).

Uptake studies were conducted with HEK 293 cells, a human embryonic kidney cell line. Cells were cultured in DMEM with 10 % FBS and 1000 U penicillin, 10 mg/mL streptomycin at 37° C with 5 % CO_2. 150, 000 cells were seeded into each well of a 24-well plate. Fluorescently labeled CNPs with different coatings were added into the culture medium 24h later and the final concentration was adjusted to 20 μg/mL. After a certain incubation time (from 1h to 48h), cells were washed with PBS to remove excessive CNPs and the cellular uptake of CNPs was studied quantitatively as a function of the incubation time by flow cytometry.

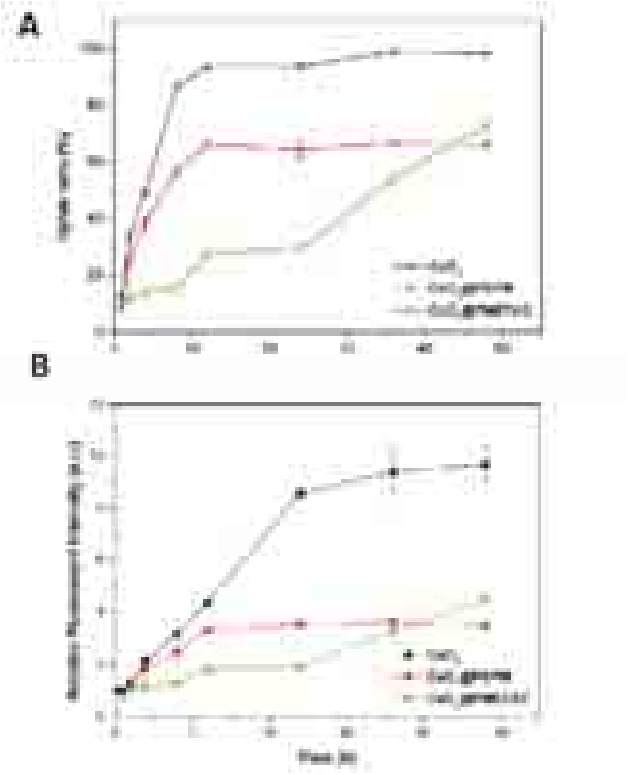

Figure 2.10*(a) Cellular uptake ratio and (b) relative fluorescence intensity of cerium oxide with different coatings as a function of the incubation time (h) with HEK293 cells.*

Flow cytometry data were analyzed using the WinMDI 2.9 software. First, a threshold of fluorescence was generated using untreated HEK293 cells as a control sample. All events corresponding to the control sample were located at intensities below this threshold. Each experiment was set to count 10.000 events per run and each run was recorded using identical parameters. The number of cells carrying fluorescently labeled CNPs is obtained from the area corresponding to the events located at higher intensities than the threshold. The cellular uptake ratio was calculated as the (No. of events over the threshold/total No. of events) × 100%. The fluorescence intensity was set as the maximum of the fluorescence intensity versus cell number distribution. The relative fluorescence intensity is calculated with respect to the fluorescence intensity of three CNPs measured by flow cytometry.

Figure 2.10 clearly reveals that CeO_2 NPs have the fastest uptake. In the first 24 hours, CeO_2@PMETAC NPs show the slowest uptake among all three CNPs, both in uptake ratio and fluorescence intensity. However, after 48 hours CeO_2@PMETAC NPs show a higher value of the number of cells with internalized CNPs and the number of CNPs per cell (fluorescence intensity) than that of CeO_2@PSPM, and still have a tendency to increase unlike the other two CNPs, which have already reached a plateau after 12h. It is understandable that the uptake of CeO_2@PSPM NPs is very slow and the number of CNPs per cell is much lower than that of unmodified CeO_2 NPs since the negative surface charge can hinder the uptake of NPs. But positively charged NPs have been reported to adhere to the negatively charged cell membrane implying improved uptake but this is not observed for the uptake of CeO_2@PMETAC NPs. One possible reason for this could be that although the positive charge helps CeO_2@PMETAC NPs to adhere to the cell surface, the kinetics of uptake are rather slow and a significant uptake can only happen after 24h. And this process is relatively slow with vigorous uptake happening after 24h. And it can be observed that, after 48h, both uptake ratio and the fluorescence intensity of CeO_2@PMETAC NPs is higher than that of CeO_2@PSPM NPs. This indicates that after 48h, the uptake per cell of CeO_2@PMETAC NPs is already higher than that of CeO_2@PSPM NPs.

Cellular uptake and intracellular distribution of CNPs were studied using an LSM 510-META CLSM (Zeiss, Germany). The cell membrane was stained with Cellmask™ deep red. In order to reveal the intracellular localization of CNPs, acidic cell compartments (e.g. endosomes and lysosomes) were stained with LysoTracker® Red.

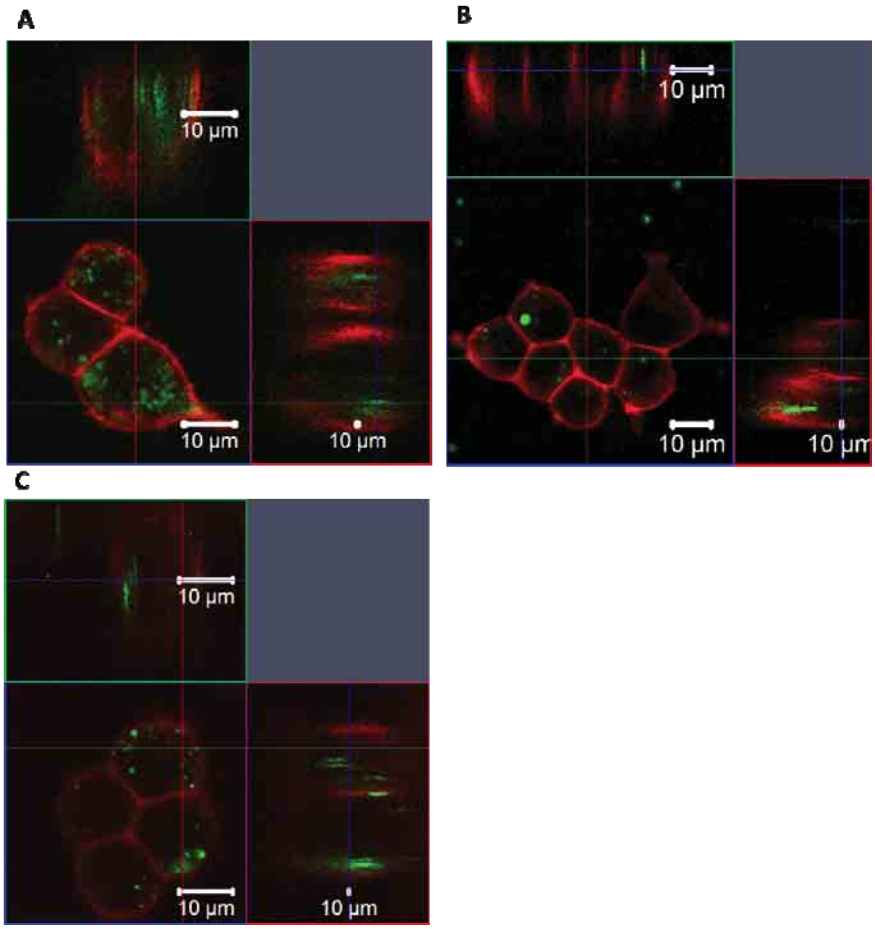

Figure 2.11 *CLSM image of HEK293 cells after incubation with (A) CeO_2 NPs (B) CeO_2@PSPM NPs (C) CeO_2@PMETAC NPs for 24h. Cell membrane was stained by Cellmask™ deep red (red), and CNPs were labeled by Alexa 488 (green)*

CLSM images in XYZ planes revealed that CNPs were internalized by HEK293 after 24h. In ***Figure 2.11***, Alexa® 488 labeled CNPs, showing green fluorescence, are located within the cell membrane labeled in red. The lower left image in ***Figure 2.11 A, B*** and ***C*** corresponds to the middle plane of a cell. The upper image was produced by ZX-stacking and the lower right image corresponds to the ZY stacking. The 3D stacking images proved that after 24h of incubation with HEK293 cells, all three CNPs are completely internalized. In addition, some CeO2@PMETAC NPs could be found adhering to the cell membrane rather than internalized.

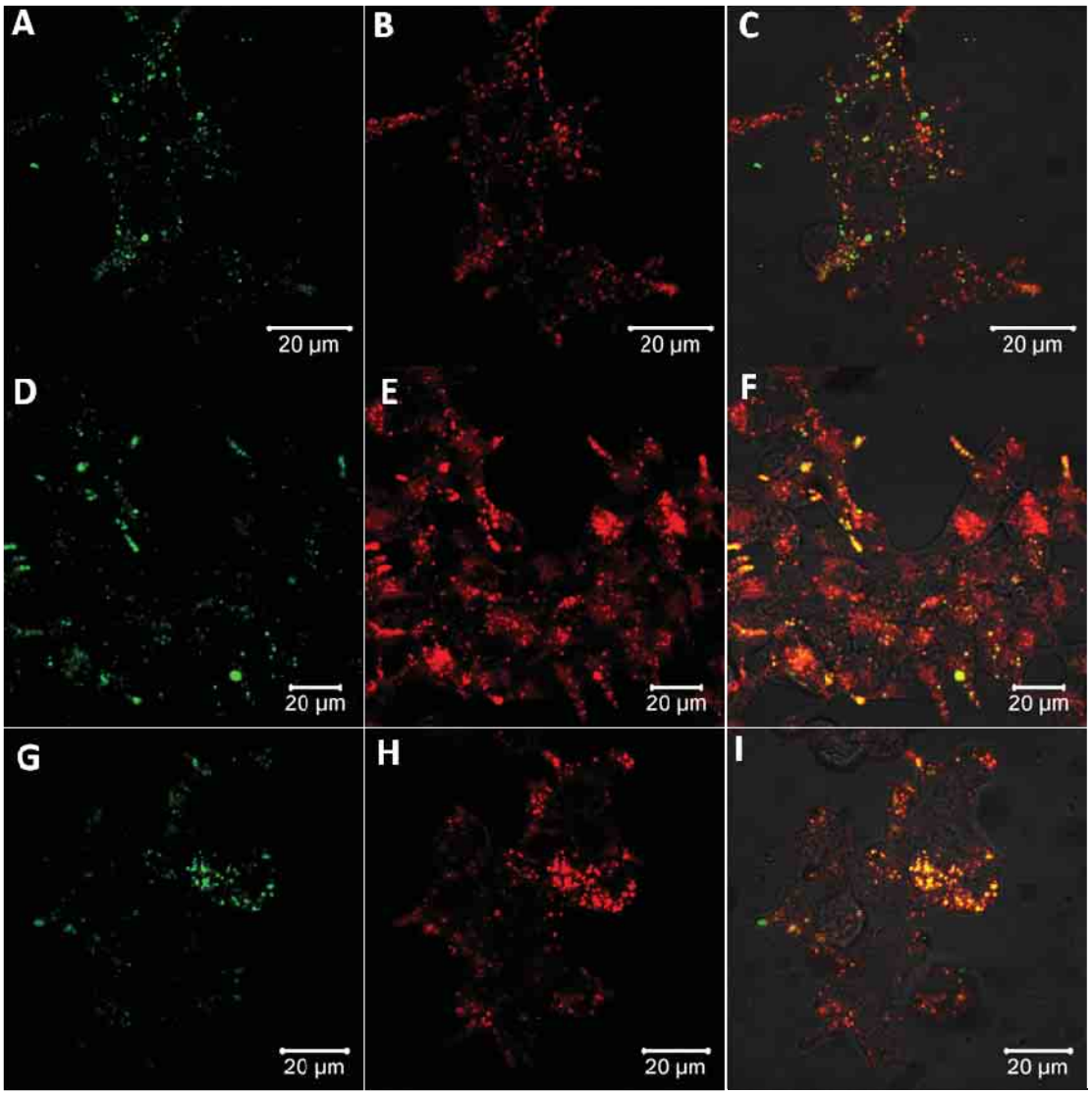

Figure 2.12 *CLSM image of HEk293 cells after incubated with (A) to (C) CeO_2 NPs, (B) to (F) CeO_2@PSPM NPs, (H) to (I) CeO_2@METAC NPs for 24h. Cell acidic compartments were stained with LysoTracker® Red (red) and NPs were labeled with Alexa 488 (green).*

In order to investigate the intracellular distribution of CNPs, acidic cell compartments were visualized by using LysoTracker® Red. Experiments were carried out with HEK 293 cells incubated 24h with fluorescently labeled CNPs. Acidic organelles include endosomes and lysosomes which have a complex maturation process. The formation and maturation of acidic organelles begins with the endocytosis of extracellular material and

continues with the transfer of internalized cargo from early endosomes to late endosomes, and then to the lysosomes. During the maturation process, acidic organelles can fuse and mix their contents which then results in higher amounts of endocytosed material and progressively larger dimensions for the organelles. Another unique characteristic of acidic organelles is that they experience a progressive decrease in pH during the maturation process, leading to much lower pH value inside the mature acidic organelles than that in the cytoplasm of [239]. As shown in ***Figure 2.12***, the potential co-localization between CNPs (green) and lysosomes (red) will yield a yellow/orange overlap in the merged images. Confocal microscopy showed that CNPs with and without polymer brush coatings were normally colocalized with Lysotracker. This indicates that most CNPs were internalized by HEK 293 cells through common endosomal and lysosomal involved endocytosis and located within lysosomes after 24h uptake. However, CeO_2 NPs without brushes show a lower degree of co-localization than CeO_2@PSPM and CeO_2@PMETAC and can also be found in the cytosol. This result can be attributed to the nearly neutral surface charge of CeO_2 NPs without brushes and to the high surface charge of polymer coated CNPs as previously reported [234].

Raman spectroscopy was employed to investigate the uptake of unlabeled CNPs. Cells were seeded onto a CaF_2 crystal substrate with a diameter of 20mm. After 24h, CNPs were added to the cell medium to a final concentration of 20μg/mL and incubated for 24h. Cells were washed with PBS several times, fixed with 3.7 % formaldehyde and characterized by CRM. Measurements were performed with a Renishaw inVia Raman Microscope with 532 nm excitation and a grating of 1800mm^{-1}. Spectra were taken using a 40× water immersion objective. The size of the focal spot was approximately 1 μm. Raman spectra were recorded over the range 800-3200 cm^{-1} with a resolution of approximately 7 cm^{-1}. The system was calibrated to the spectral line of crystalline silicon at 520.7 cm^{-1}.

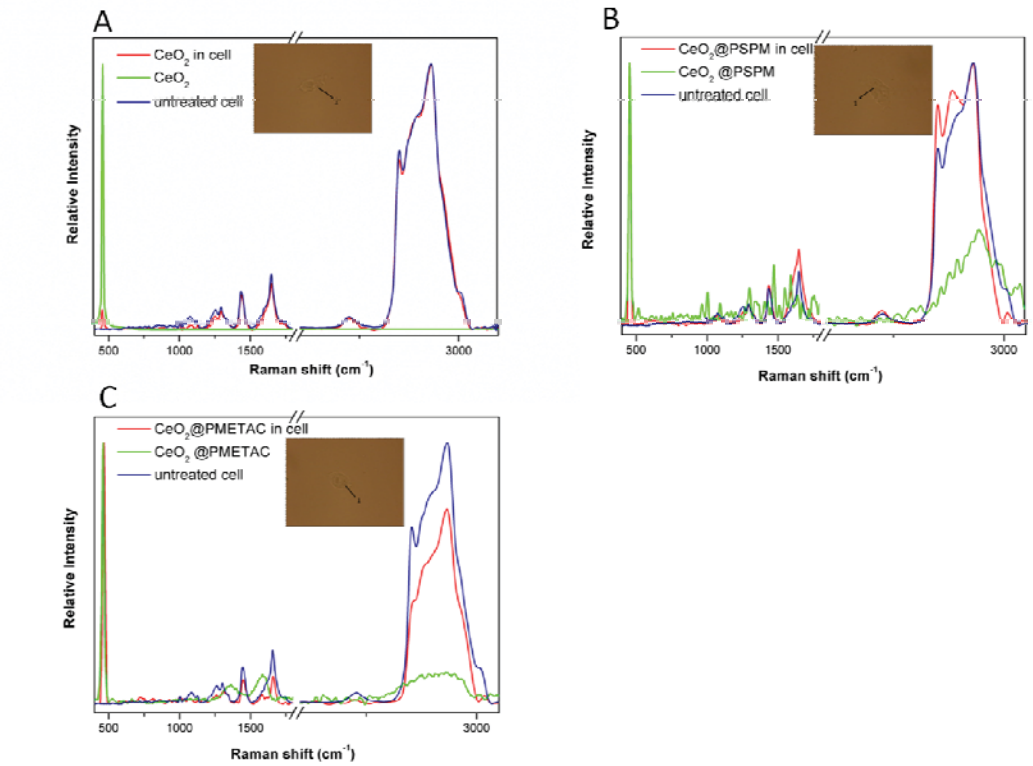

Figure 2.13 *Raman spectra taken in HEK293 Cells after 24h incubation with (A) CeO_2 NPs, (B) CeO_2@PSPM NPs, (C) CeO_2@PMETAC NPs.*

The strong and distinct Raman peak of cerium oxide at about 465 cm^{-1} allows us to distinguish the existence of CNPs in the cells without fluorescence. This is particularly important since it allow us to compare the uptake of the unmodified CeO_2 NPs with the ones coated with polymer brushes. This comparison using fluorescence techniques required the labeling of the CeO_2 NPs without brushes using a procedure that minimizes the changes in the surface characteristics of the NPs but nevertheless the surface of the CeO_2 NPs is to a certain extent modified. As we have shown before, the coating with polymer brushes does not affect the Raman spectra of the NPs, allowing us to have a direct comparison of the impact of the polymer modification of the NPs and change in their uptake in relation to the non modified NPs. The molecules present in the cells: proteins, lipids and nucleic acids have distinctive Raman bands, which are indicative of their molecular characteristics and can also be related to their conformation, in the case of proteins. Since the proportion of lipids, proteins and nucleic acids varies in the different

cell compartments the relative intensive of the different bands can be used to distinguish regions within the cell from the Raman spectra measured intracellularly, without labeling the cell. When nanomaterials, with a measurable Raman spectra, are uptaken by cells the Raman spectra recorded within the cells result in a combination of the Raman bands of the NPs and that of the cellular components. If the bands of the nanomaterials do not overlap with those of the cellular components we will be able to identify the cellular environment of the NPs [240]. ***Figure 2.13*** shows a Raman spectrum from cells after incubation with CNPs, unmodified and with polymer brushes (red line), the Raman spectrum of CNPs (green line) and a Raman spectrum from untreated cells (blue line). The spectra from cells were taken from the central plane of the cell in both cases. For cells exposed to NPs, the peak of cerium oxide at 465 cm^{-1} can be found together with the signal from cell components such as protein and lipids, which can also be visualized in the non exposed cells. When the NPs were modified with polymer brushes, in addition to the band of the CeO_2 NP, additional bands can be observed in the spectra from 1200 cm^{-1} to 1600cm^{-1} and around 2900 cm^{-1}(***Figure 2.4***). Nevertheless, these additional peaks from polymer brushes cannot be clearly distinguished in the cells (***Figure 2.13 B and C***). This is understandable, because the Raman signals from the thin layer of polymer brushes around the surface of CNPs are too weak to been recognized when internalized by cells. Furthermore, the signals from C-H vibration of the polymer backbone at around 2900 cm^{-1} are merged with the signals from the cell.

Cells with internalized NPs were mapped by applying Confocal Raman Microscope (CRM) recording Raman spectra spot by spot. We performed Raman mapping at the middle plane of each individual cell. XY Raman mapping was performed to obtain information about the distribution and intracellular localization of CNPs. Raman spectra were recorded along a square or circle defined to cover the whole cell area. Between two subsequent measurements there was a distance increment of 0.5 μm. The distributions of different components were analyzed focusing on signals of NPs, nucleic acids, proteins and lipids. (***Figure 2.14 to 2.16***).

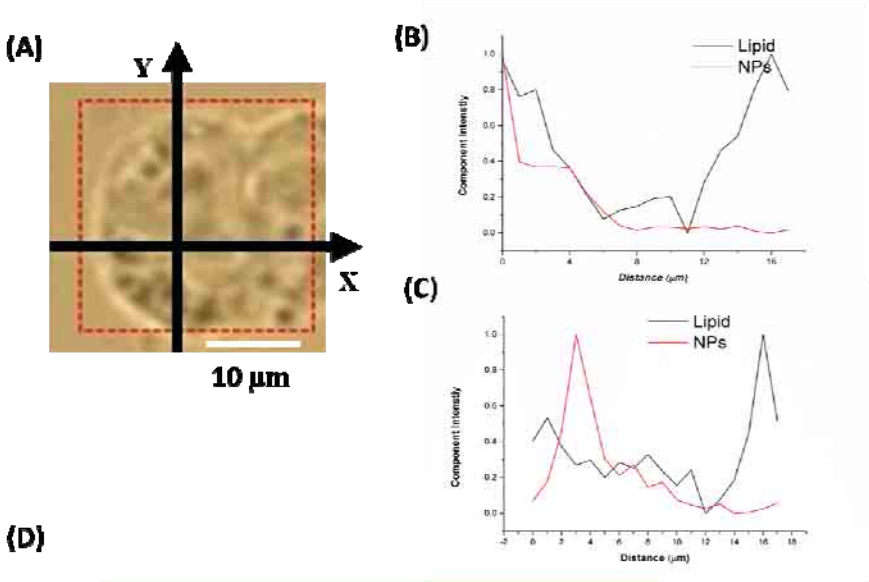

	Correlation coefficient (Pearson)
X axis	0.42
Y axis	0.45

Figure 2.14 *Raman mapping data inside a HEK293 Cell incubated with CeO_2 NPs for 24h. (A) The light microscopy image of scanned cell, the region inside the red square corresponds to the mapping region .(B) Intensity distribution of CeO_2 NPs corresponding to the CeO_2 band (red line) and lipids (black line) inside HEK 293 along the X axis as indicated in (A); (C) Intensity distribution of CeO_2 NP s corresponding to the CeO_2 band (red line) and lipids (black line) inside HEK 293 along the Y axis as indicated in (A); (D) calculated Pearson product-moment correlation coefficient corresponds to the distribution from (B) and (C).*

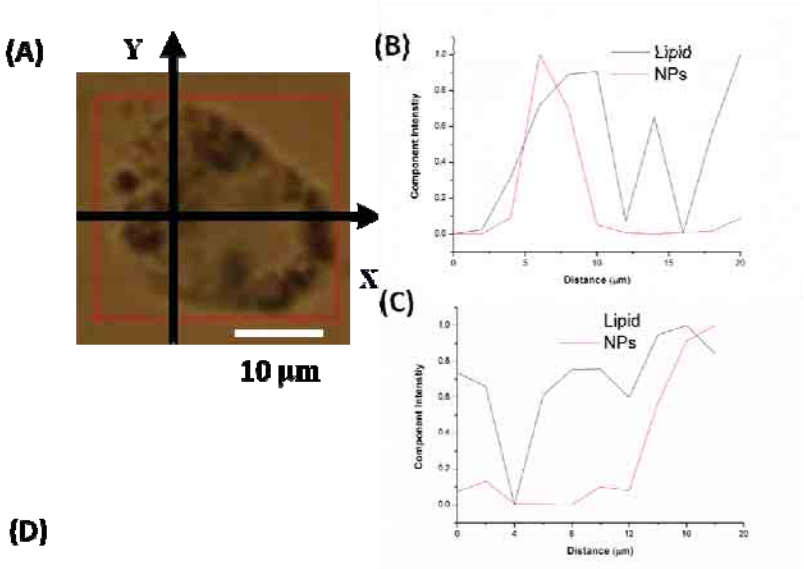

(D)

	Correlation coefficient (Pearson)
X axis	0.79
Y axis	0.60

Figure 2.15 *Raman mapping data inside a HEK293 Cell incubated with CeO_2 @PSPM NPs for 24h. (A) The light microscopy image of scanned cell, the region inside the red square corresponds to the mapping region .(B) Intensity profile of CeO2@PSPM NPs corresponding to the CeO_2 band (red line) and lipids (black line) inside HEK 293 along the X axis as indicated in (A); (C) Intensity profile of CeO2@PSPM NPs corresponding to the CeO_2 band (red line) and lipids (black line) inside HEK 293 along the Y axis as indicated in (A); (D) calculated Pearson product-moment correlation coefficient corresponds to the distribution from (B) and (C).*

The tendency of colacalizaiton of tow components (e.g. NPs and lipid) can be quantified by the Pearson product-moment correlation coefficient $\rho_{X,Y}$. The pearson coefficient is a correlation coefficient used to measure the the linear dependence between two variables X and Y, giving a value between -1 to +1. It is a measure of linear dependence between two variables X,Y. The absolute value 1 indicates a 100% linear dependence between X and Y while 0 shows a total independence [243]. The correlation between distributions of

CNPs and cell lipid rich compartments were calculated as following using Pearson product-moment correlation coefficient:

$$\rho_{X,Y} = \frac{\mathrm{cov}\,(X,Y)}{\sigma x \sigma y} \qquad (Eq\ 2.1)$$

where, $\rho_{X,Y}$ denotes the Pearson product-moment correlation coefficient, cov (X,Y) is the covariance of the two variables, and $\sigma x \sigma y$ is the product of their standard deviations. The two variables in the Raman mapping data along the X and Y axis are the distance component intensity of CNPs and lipids. $\rho_{X,Y}$ can be calculated as a function of spatial shift, Δ. The spatial cross-correlation function can be then defined as $\rho_{X,Y}(\Delta)=\mathrm{cov}(X(r),Y(r\pm\Delta))/(\sigma x \sigma y)$. The maximum value of $\rho_{X,Y}(\Delta)$ can be used as an evaluation of the correlation between CNPs and lipids.

As shown from ***Figure 2.14*** to ***Figure 2.16***, the correlation of Raman signals of CNPs and lipids along the line of X axis and the line of Y axis were calculated for the unmodified and brush coated CNPs. The maximum intensity of CeO_2 NPs and lipid do not coincide along X axis and Y axis meaning a limited colocalization (***Figure 2.14 B*** and **C**). On the contrary, CeO_2@PSPM and CeO_2@PMETAC cells show a higher degree colocalization of both maximum and minimum intensity of NPs and lipids (***Figure 2.15 B*** and ***C, Figure 2.16 B*** and ***C***).

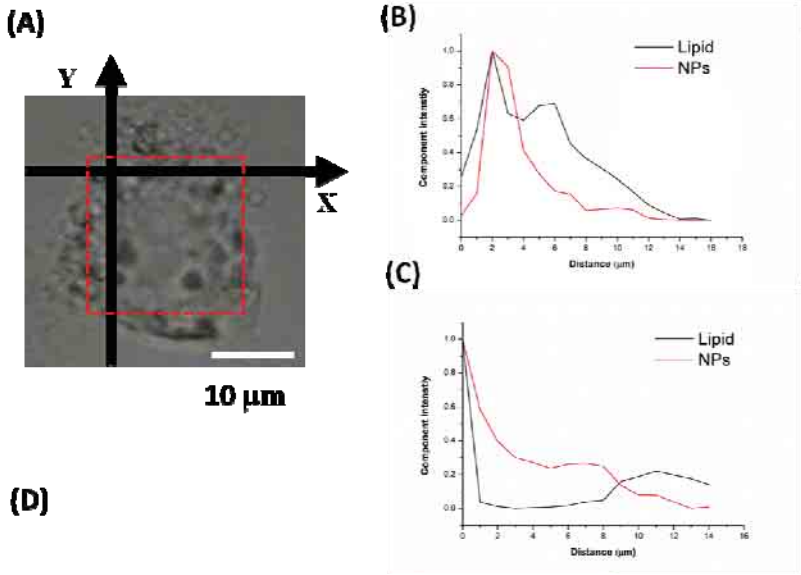

	Correlation coefficient (Pearson)
X axis	0.79
Y axis	0.59

Figure 2.16 *Raman mapping data inside a HEK293 Cell incubated with CeO_2 @PMETAC NPs for 24h. (A) The light microscopy image of scanned cell, the region inside the red square corresponds to the mapping region .(B) Intensity profile for CeO_2 @PMETAC NPs , corresponding to the CeO_2 band(red line) and lipids (black line) inside HEK 293 along the X axis as indicated in (A); (C) Intensity profile for CeO_2 @PMETAC NPs , corresponding to the CeO_2 band (red line) and lipids band (black line) inside HEK 293 along the Y axis as indicated in (A); (D) calculated Pearson product-moment correlation coefficient corresponds to the distribution from (B) and (C).*

This indicate that CeO_2 NPs do not have the tendency to located with the lipid rich region inside cell while the other two modified CNPs showed a preference to colocalize with intracellular lipid rich regions. Moreover, the calculated maximum values of $\rho_{X,Y}(\Delta)$ of CeO_2 are 0.42 and 0.45 along X and Y axis respectively, while that of CeO_2@PSPM NPs are 0.79 and 0.60 along the line of X and Y axes respectively (***Figure 2.15 C***) and that of CeO_2@PMETAC NPs are 0.79 along X axis and 0.59 along the line Y axis (***Figure 2.16 D***). As it is described before, $\rho_{X,Y}(\Delta)$ value closer to 1 means a higher linear dependence

of the two components while closer to 0 means a lower linear dependence. Therefore, it can be conclude that CeO_2 NPs have a lower linear dependence with lipids inside the cell than polymer brush modified CNPs. Intracellular lipid rich regions in the cell can be associated with cell organelles which are enclosed by a lipid bilayer membrane including intracellular endosomal and lysosomal compartments [244]. Since these cell compartments are abundant during cell endocytosis, it is likely that polymer brush modified CNPs had a tendency to localize in endosomes and lysosomes. This is in agreement with observed results from CLSM.

TEM imaging of cells after exposure to CNPs were used to visualize the intracellular location of NPs in addition to CLSM and Raman microscopy. For TEM experiments, a number of 100,000 HEK 293 cells were seeded in a 35 mm diameter perti dish and grown for 24h. Different types of CNPs were then added at concentration of 10 μM/ml. After 1h and 24h co-incubation, cells were washed with PBS and collected by trypsinization. For TEM imaging, cells were further fixed with 3.7% formaldehyde, washed with PBS and stained with 1% of osmium tetroxide. Afterwards, samples were dehydrated in a group of acetone solutions with gradient concentration (from 50 to 100%) and followed by EPO resin embedment. The resin blocks were cut into ultrafine slides of 70 nm by an ultramicrotome. Each slide was placed on a copper grid and contrasted by the Reynolds technique for appropriate visualization.

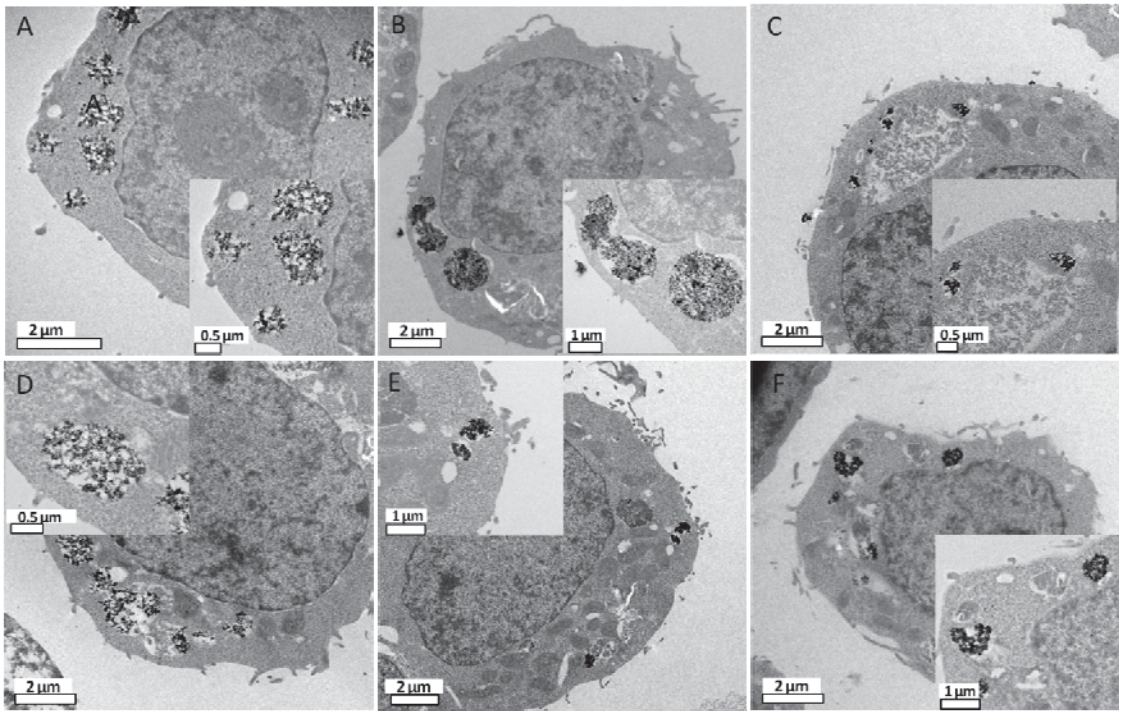

Figure 2.17 *TEM image of HEK293 cells treated with CeO_2 NPs for (A)1h, (D)24h; with CeO_2@PSPM NPs for (B)1h, (E)24h; with CeO_2@PMETAC NPs for (C)1h, (F)24h.The insets are the closer view of the corresponding image.*

In ***Figure 2.17***, CNPs can be recognized by their shape and very high contrast. The image clearly shows that complete cellular internalization of all three types of CNPs occurs after 1h incubation. CNPs inside cells are mostly present in clusters from several hundreds of nanometers to 2 µm. Closer inspection revealed that the majority of NPs were enclosed by intracellular vacuoles. These vacuoles are the lysosomal cell compartments. This indicates that CNPs were internalized typically through endocytosis, which involves the formation of vesicles from the plasma membrane. The TEM results are in good agreement with the CLSM and Raman mapping results that most of internalized CNPs were inside lysosomal compartments. The vacuoles larger than 1 µm (***Figure 2.17 A, B, D***) can be associated with macropinosomes, which are the large, irregular primary endocytic vesicles formed during macropinocytosis[57]. The intracellular fate of macropinosomes varies depending on the cell type but in most cases ends up fusing with lysosomes and shrinking [245]. It is worth noting that, besides the CNPs clusters, there

are also some single CNPs or very small clusters of CNPs present in the cytoplasm which are probably single CNPs that penetrated the cell membrane through passive diffusion.

Cellular uptake was quantitatively studied via ICP-MS. For IPC-MS experiments, HEK 293 cells were exposed to CNPs without fluorescence labeling and collected following the same procedures as for flow cytometry. Collected cells were then dissolved in nitric acid up to a final concentration 0.1 mg/mL. Then, the elemental concentrations of cerium in cells were measured by Perkin Elmer Analyst 800 ICP-MS.

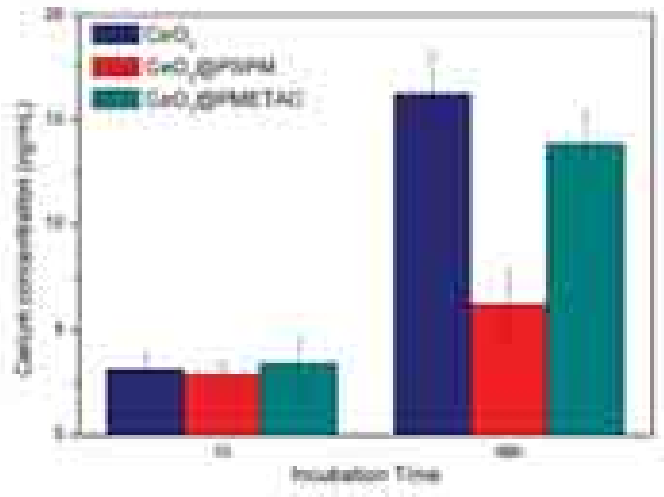

Figure 2.18 *ICP-MS measurement of cellular uptake of CNPs after 1h and 48h.*

ICP-MS results showed a similar result to the flow cytometry data. At the beginning of the incubation time (1h), the three CNPs showed very similar uptake. After 48h, the CeO_2 NPs showed the highest uptake compared to the other two CNPs. Nevertheless, the differences in the amount of NP uptake between CeO2@PSPM and CeO2@PMETAC after 48h are much larger than of the difference between these two types of NPs in fluorescence intensity from flow cytometry (***Figure 2.18*** and ***Figure 2.10B***). One possible reason is that the fluorescence intensity can reveal the quantity of NPs but it is not linearly associated with it.

Extracellular substances can pass through the cell membrane and enter the cell via a process termed 'endocytosis'. In this process, macromolecules and particles are carried into cells in vesicles derived by the invagination and pinching-off of pieces of the plasma membrane. Endocytosis includes several different mechanisms, which can be mainly divided to ‘phagocytosis’ (cell eating) and ‘pinocytosis’ (cell drinking) [53]. Several different cell uptake pathway inhibitors were used in order to determine the uptake mechanism of CNPs. Cells were cultured at low temperature (4 °C) for one hour without any inhibitor to determine if the uptake is energy-dependent [78].

For all the uptake pathway experiments, cells were pretreated with different endocytosis pathway inhibitors (or kept at 4 °C) for 1h and then incubated with Alexa 488 labeled CeO_2 NPs with PSPM and PMETAC without polymer brushes for another 4h and finally thoroughly rinsed with PBS. The average cell fluorescence intensity was measured by FACS. Relative fluorescence intensity was determined by defining the fluorescence intensity of control cells (cells incubated with NPs without inhibitors treatment) as 100.

The amiloride-HCl drug inhibits uptake via macropinocytosis by blocking the Na^+/H^+ exchanger [246,247].Chlorpromazine (CPM) is a clathrin-mediated pathway inhibitor, which inhibits the formation of clathrin-coated pits [90,248]. Genistein is a tyrosine-kinase inhibitor, which causes a local disruption of the actin network at the site of endocytosis and impedes the recruitment of dynamin II, thus, blocking the caveolae-mediated uptake pathway [65,249]. Filipin is a cholesterol binding agent that can inhibit caveolae-mediated uptake by the flattening of caveolae and the disruption of caveolin protein coating [250] [64]. Cytochalacin D is a actin filament depolymerising agent which can block cell uptake via membrane ruffling involving actin filament (macropinocytosis) [251,252];

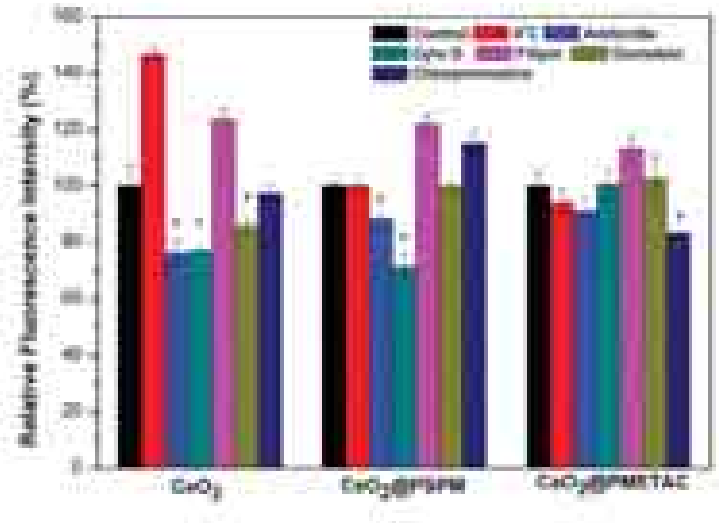

Figure 2.19 *Relative uptake of cerium oxide NPs by HEK 293 cells with pretreatment with endocytosis pathway inhibitors: amiloride (2.5 mM), cytochalasin D (10µg/ml), flilipin (5 µg/ml), genistein (100 µM) or chlorpromazine (10 µg/ml). To determine if NPs were internalized via energy dependent process, cells were first cultured at 4 ^oC. Asterisk indicates the significant inhibition compare to the control ($p<0.05$).*

The uptake of CeO_2 and CeO_2@PSPM by HEK 293 cells was significantly inhibited by amiloride and cytochalacin D, while genistein showed significant inhibition for the uptake of CeO_2 (***Figure 2.19***). So it can be summarized that CeO_2 NPs mainly entered HEK 293 cell via macropinocytosis and caveolae-mediated endocytosis. The uptake of CeO_2@PSPM takes place mainly via macropinocytosis. In the case of CeO_2@PMETAC, only chlorpromazine showed a significant inhibition for uptake, which suggests that the main pathway is clathrin-mediated endocytosis. This result is similar to some previous work, which showed that positively charged NPs favor clathrin-mediated pathways [253]. Interestingly, cells treated at 4° C did not show any significant inhibition at all with the uptake of all three CNPs. This means the CNPs can also be internalized by HEK 293 cell via energy-independent pathways such as passive diffusion.

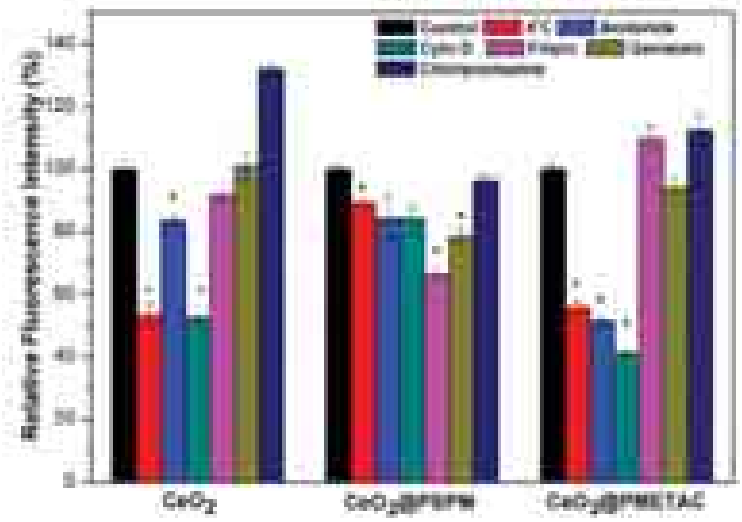

Figure 2.20 *Relative uptake of cerium oxide NPs by A549 cells with pretreatment of endocytosis pathway inhibitors: amiloride (2.5 mM), cytochalasin D (10 µg/ml), flilipin (5 µg/ml), genistein (100 µM) or chlorpromazine (10 µg/ml). To determine if NPs were internalized via energy dependent process, cells were cultured at 4 ^oC. Asterisk indicates the significant inhibition compare to the control ($p<0.05$).*

For A549 cells, the uptake of all three CNPs was inhibited at low temperature (4 °C) which indicated their uptake is energy-dependent (***Figure 2.20***). The uptake of CeO_2 NPs and CeO_2@PMETAC NPs by HEK 293 cells was significantly blocked by amiloride and cytochalacin D, while filipin and genistein showed inhibition for the uptake of CeO_2@PSPM. Therefore, the uptake of CeO_2 and CeO_2@PMETAC by A549 cells takes place mainly via macropinocytosis. The main pathway of CeO_2@PSPM NPs is via caveolae-mediated endocytosis.

From the results of the experiments related to uptake mechanisms, it can be concluded that macropinocytosis is the main cell uptake pathway of CNPs regardless of cell types. Nevertheless, the cell uptake mechanism of CNPs is dependent on the cell type. In the case of the non-malignant cell line (HEK 293), the uptake pathways seem not to be energy dependent as an efficient uptake was observed when energy dependent pathways

were blocked. However, in the case of the malignant cell line (A549) the endocytosis is highly energy dependent. This result is in agreement with recent work, in which K. Saha et al showed that the uptake of gold NPs, of 10 nm hydrodynamic diameter, in both malignant and non-malignant cells showed different mechanisms [90]. Moreover, the surface characteristics of NPs may result in alteration of predominant uptake pathway, which can lead to the change of intracellular distribution and fate of NPs.

2.3.2 Impact of CNPs on cell viability and cell function

The impact of CNPs with different surface coatings on the cell viability and cell function was investigated by the MTT assay and Raman spectroscopy. In addition, the oxidative stress level of cells was measured by quantification of intracellular ROS via flow cytometry.

The cytotoxicity of CNPs was studied by the MTT assay. 5,000 cells were first seeded in one well of a 96-well plate, and after 24h, CNPs were added with different concentrations. After a time interval of 1 day and 4 days, 20 mL of MTT solution (5 mg/mL in PBS) was added to each well and incubated at 37° C for 3h. The absorbance was measured in a plate reader at 550 nm.

Three different cell lines were used for the cytotoxicity studies: human embryonic kidney cell line (HEK 293), human hepatocellular carcinoma cell line (HepG2) and human alveolar adenocarcinoma cell line (A549). As shown in ***Figure 2.21***, cells were exposed to 20 μg/mL CNPs with different coatings and the cell viability was measured after 1 day and 4 days. CeO_2 NPs showed a non to low cytotoxicity to all three cell lines. While CeO_2@PSPM NPs showed the highest cytotoxicity among all three CNPs. Interestingly, the two cancer lines showed fewer changes in cell viability than the non-malignant cell line HEK 293. After 4 days, cells treated with CeO_2 NPs and CeO_2@PMETAC NPs showed a higher viability than after 1 day, which indicates a recovery of cell viability from acute cytotoxicity these two CNPs caused at the first 24h. But cells exposed to CeO_2@PSPM NPs did not show recovery of cell viability after 4 days. This indicates that CeO_2@PSPM NPs may cause long term cytotoxicity effects in different cell lines.

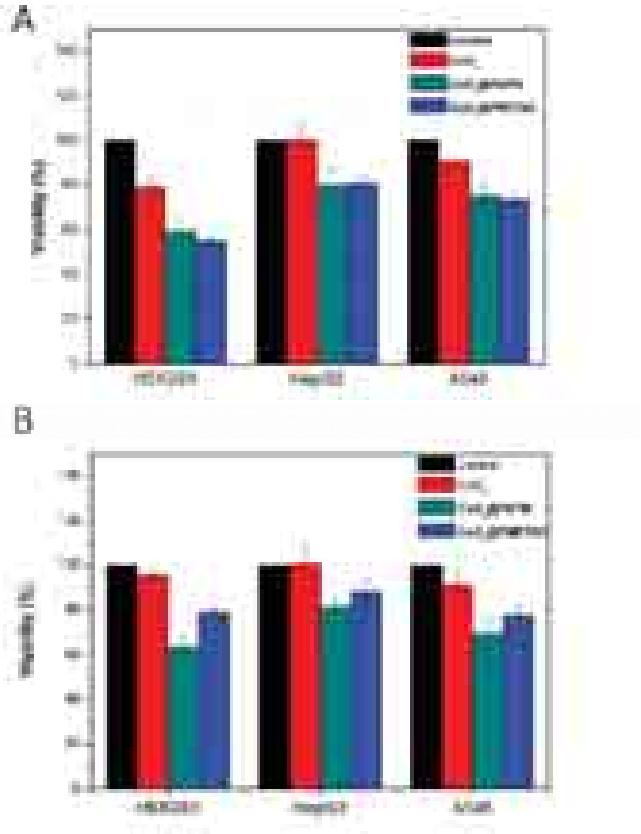

Figure 2.21 *Viability of different cell lines incubated with CNPs (20μg/ml) for (A) 1 day and (B) 4 days.*

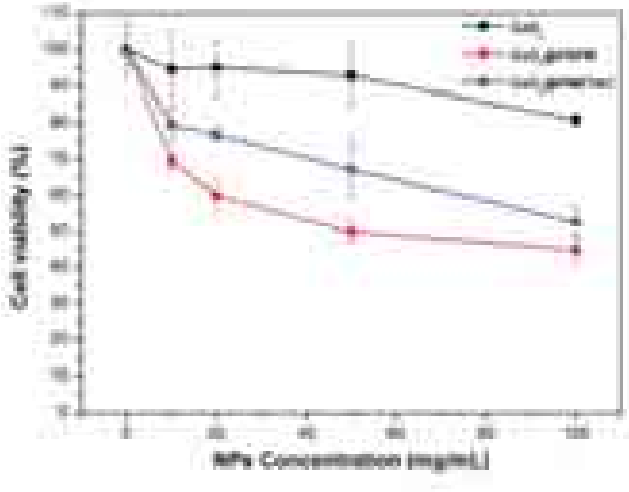

Figure 2.22 *Viability of HEK293 cells exposed to different CNPs with concentration of 20 μg/mL for 96h.*

Changes in cell viability of HEK293 as a function of the concentration of CNPs are shown in ***Figure 2.23***. From the curves one can deduce that CeO_2 NPs induce a low cytotoxicity to HEK293 cells even when the cells are exposed to a very high concentration of CeO_2 NPs (100µg/mL). At this concentration the HEK293 cells only showed a loss of viability of less than 20%. CeO_2@PMETAC NPs induce lower cytotoxicity with lower concentration (less than 20% loss of cell viability), and induce higher cytotoxicity with higher concentration (around 50% loss of cell viability). CeO_2@PSPM NPs has largest impact on cytotoxicity among all three NPs.

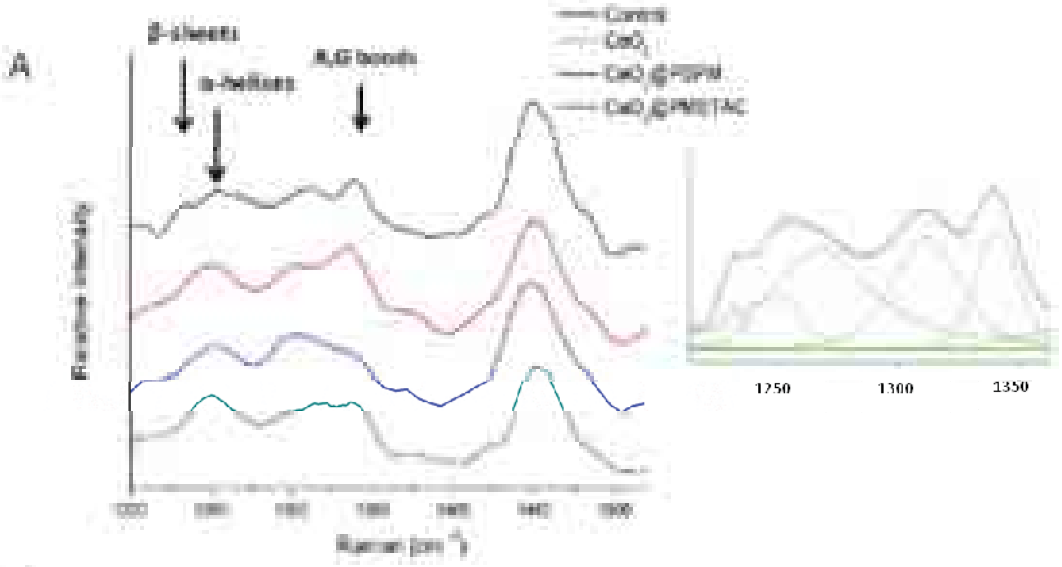

B

	Ratio (1338/amide III)	Relative ratio (1338/amide III) compare to control cells
Control	0.436	100.00
CeO_2	0.458	105.03
CeO_2@PSPM	0.341	78.20
CeO_2@PMETAC	0.224	51.37

Figure 2.23(A) *Raman spectra from the nucleus of HEK293 cells in the region from 1200 to 1500 cm^{-1} exposed to surface modified CNPs compared with the spectrum of untreated cells. The inset shows the peak fitting analysis of Raman spectrum of untreated cells. (B) Table displaying the integral intensity ratios between A,G nucleobases and amide III. The ratio expressed as perceptual in relation with the control cells.*

Raman spectroscopy was used to study the impact of CNPs on nuclear proteins and nucleid acids. The ratio between DNA bands (adenine and guanine, A,G) and the protein bands in the cell nucleus is related to the nucleic acid and protein concentration within the scanning spot and can be used as an evaluation of toxicity. The Raman spectra in the nucleus region after exposing the cells to CNPs were compared with those of the untreated cells. The region of the Raman spectra between 1200 cm^{-1} and 1400 cm^{-1} includes typical vibrational bands related to protein conformation (random coil, β-sheet and α-helix) called Amide band III and to nucleic acids: the adenine and guanine bands. Relative changes in these bands as a result of the exposition of the cells to the CNPs were measured. A deconvolution procedure was used to better analyze the spectra. Through deconvolution and curve fitting, the integral peak ratio between signal related to A,G (1338cm^{-1}) and the signals of protein amid III band (1200-1290 cm^{-1}) were calculated according to the literature [124,254]. Ten Raman spectra from ten different cells were measured to calculate an average ratio.

Figure 2.23, shows the differences in the ratio between DNA and protein bands after treatment with CNPs. Cells treated with unmodified CeO_2 NPs did not show significant differences compared to untreated cells, while cells treated with CeO_2@PEMTAC NPs showed a decrease in the ratio to 78 % and cells treated with CeO_2@PSPM NPs showed a decrease of the ratio to about 50%. The decrease of the DNA/protein ratio in the cell nucleus indicates a decrease in the DNA density within the cell nucleus. This decrease can be associated with DNA damage, such as single strand breaks and loss of DNA diffusing out of the nucleus during apoptosis [255], induced by NPs. The decrease in the ratio may also be due to an over expression of proteins that could be present during apoptosis. Among all three CNPs, CeO_2 NPs do not appear to induce DNA damage, with CeO_2@PSPM NPs inducing the highest degree of DNA damage and may possibly induce cell apoptosis as well.

Cerium oxide NPs are well known for their superoxide scavenging capacity by the reversible binding of oxygen and reversible equilibrium between Ce^{3+} and Ce^{4+}.

Therefore, the oxidative stress level of the cells treated with cerium oxide NPs with different coatings was studied.

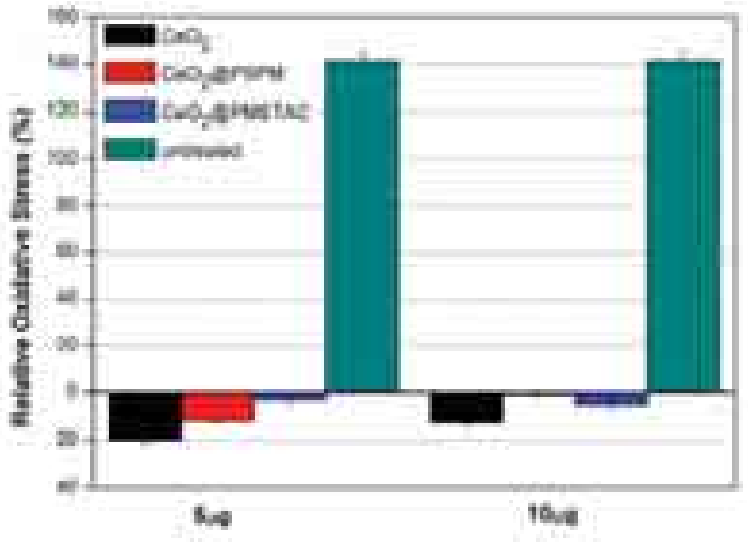

Figure 2.24 *Oxidative stress of HEK293 cell treated with CNPs.*

HEK293 cells were first incubated with Cerium oxide NPs at different concentrations. In order to avoid CNP toxicity, only very low concentrations were used: 5 µg and 10 µg/mL. After 24 hours, cells were washed with PBS 3 times to remove the NPs that were not internalized and incubated with 0.5 mM tert-Butyl hydroperoxide (TBHP), which can induce ROS inside cells for another 2 hours. After washing out the redundant TBHP, all samples were then incubated with 6-carboxy-2', 7'-dichlorodihydrofluorescein diacetate (Carboxy-H2DCFDA) for 30 minutes. Carboxy-H2DCFDA is commonly used as an indicator for ROS in cells. This non fluorescent molecule can be converted to a green-fluorescent form when the acetate groups are removed by intracellular esterases and oxidation occurs within the cell, which is an indication of ROS [256]. The green fluorescence intensity was measured by flow cytometry in the FITC channel. The oxidative stress inside cells was calculated as following:

$$\text{Oxidative Stress}_{\text{relative}}(\%) = \frac{Fluorescence\ (treated) - FLuorescence\ (untreated)}{Fluorescence\ (untreated)} \times 100 \quad (Eq\ 2.2)$$

Here, untreated cells refer to control cells without treatment of TBHP for induction of ROS. The oxidative stress observed in these cells will be taken as a zero value. Oxidative stress after exposing the cells to TBHP with and without NPs will be related to the ROS values displayed by the cells without TBHP. The results showed that cells not exposed to the NPs but exposed to TBHP showed a relatively high level of oxidative stress whereas cells treated with NPs exhibited negative oxidative stress level (***Figure 2.24***). Negatively ROS means, in this case, that the ROS values are lower than those cells not exposed to TBHP. This indicated all the cerium oxide NPs possessed the capacity to scavenge ROS and protect cells from oxidative stress generated by the TBHP . Compared to unmodified CeO_2 NPs, cells treated polymer brush coated NPs exhibited higher oxidative stress level but still much lower than the untreated group. This means the polymer brush on the surface of CNPs hindered the oxygen binding and the redox changes between Ce^{3+} and Ce^{4+} to some extent, but the antioxidant capacity of the NPs is still retained when compared to cells without treatment.

Chapter 3

Quantitative Study of Intracellular Dynamics of Metallic Nanoparticles via Fluorescence Correlation Spectroscopy

---

3.1 Background and Motivation

New developments and advances in nanotechnology give rise to concerns regarding the possible negative impact of nanomaterials on human health and the environment. In parallel there is an increasing interest in the application of nanotechnology in medical fields. Therefore, it is fundamental to have a better understanding of the impact of nanomaterials on human health resulting from deliberate exposure to nanomaterials, such as in nanomedicine, or from accidental exposure due to handling or using devices or products containing nanomaterials. For these reasons, detailed studies are required on the interaction of nanomaterials with biomolecules, cells and organisms. Understanding the fate of nanomaterials at the cellular level is fundamental for the assessment of their toxicity, and impact on cellular functions. Several issues related to the physical state of nanomaterials, including aggregation, the dynamics inside the cell, the interaction with biomolecules in different cellular environments, and the formation of a protein corona are fundamental in understanding the intracellular action of nanomaterials [257–259].

Nanomaterials can be present as single entities or as aggregates, the degree of aggregation can change during their stay in the cell. If the nanomaterial is present as a single structure or as aggregate, this will affect interactions with the different molecules in the cell: proteins, nucleic acids, lipids, etc. It will also affect the localisation of the nanomaterial and intracellular trafficking. Moreover, aggregation will impact on the toxicological action and in the case where the nanomaterial is intended for use in a

medical application, the state of aggregation, and how this varies with time will clearly impact on its desired medical application: drug delivery or contrast imaging. In general, nanomaterials tend to aggregate in cell media or in the presence of proteins. It is well established that proteins attach to nanomaterials forming a sort of 'corona' [260–264]. This is usually observed for metal nanoparticles (NPs), which are the focus of this work. Once in the cell, aggregates can be broken up, or can increase in size as a result of their interaction with the cellular machinery.

There are several techniques that can be applied for the visualization of the different nanomaterials in cells, of which Transmission Electron Microscopy (TEM) is the most effective technique for visualization of metal NPs [265–267]. TEM images, however, clearly show the presence of NP aggregates but single NPs are difficult to visualize since they are not easily discriminated from sub-cellular structures. Also for TEM imaging, cells must be fixed and sectioned which, can affect the actual localization of NPs. Tracking changes in the state of nanomaterial in the cell over time, say by Confocal Laser Scanning Microscopy (CLSM), is not a trivial task. This is often done by attaching a fluorescent dye to the surface of the NP. Due to technical limitations, CLSM is not suitable for determining the size of nanomaterials below certain values. Therefore, it is difficult to use standard optical imaging techniques, to differentiate between single NPs and aggregates, or to follow changes in the aggregation of NPs with time.

FCS is routinely used in measuring dynamic processes in the time range between 1μs and 100ms, and can provide a time resolution below 100ns. This indicates that the limitations in implementing FCS intracellularly will most likely be apparent in slow dynamic processes. When investigating the diffusion of slowly moving molecules or objects such as NPs inside cells, it is crucial to ensure that the acquisition time is sufficiently long so that the process can be captured.

In dealing with a molecule of interest in the intracellular environment it is worth noting that it may be less mobile intracellularly, in comparison to in bulk. Intracellularly, the molecules may represent a heterogeneity of diffusing species with a wide distribution of

diffusion times, e.g. an immobile and mobile fraction [268]. In the case of NPs, the formation of large aggregates is regularly seen inside cells. For FCS measurements these aggregates can be considered as the immobile fraction. The fluorescence of these aggregates will overwhelm that of smaller fractions and essentially render them invisible. Consequently, no fluctuations of the fluorescence signal will be recorded with FCS. In order to overcome this limitation, if the sample is illuminated prior to data acquisition (prebleaching), a potential immobile fraction can be bleached away, leaving the mobile fraction intact. In this way, prebleaching can be used to remove the immobile fraction and facilitate the observation of the mobile fraction [136].

In this Chapter, a prebleaching strategy was used in an intracellular FCS study of internalized fluorescently labeled NPs. We show that it is possible to eliminate the contribution from large aggregates and study the dynamics of the mobile fraction of NPs by means of FCS. Small core-sized gold nanoparticles functionalized with a glucose derivative and fluorescently labeled with HiLyte Fluor™ 647 (Glc-Au-Hi NPs) were chosen for the intracellular FCS study. This type of NPs is well-dispersible and highly stable in water and has been used as multifunctional and multimodal nano-systems to address biological problems [269]. The sugar coating of Glc-Au-Hi NPs minimize non-specific interactions with other biomolecules acting as a short PEG layer in cell-based experiments [259]. Moreover, FCS allows us to obtain of values for the local concentration of NPs and the information of intracellular location of NPs. These results are fundamental for the understanding of the intracellular behavior of NPs probing as well that Glc-Au NPs are present as single entities or small aggregates within the cell.

3.2 Preparation and characterization of glucose-coated nanoparticles labeled with HiLyte Fluor™ 647

Gold nanoparticles coated with $GlcC_5S$ (Glc-Au) were prepared following a reported procedure [270]. In order to obtain luminescent glyco-nanoparticles, HiLyte Fluor™ 647 was chosen as the fluorophore and was suitably functionalized for attachment to Glc-Au NPs. The conjugation of HiLyte Fluor™ 647 is shown as in ***Figure 3.1.***

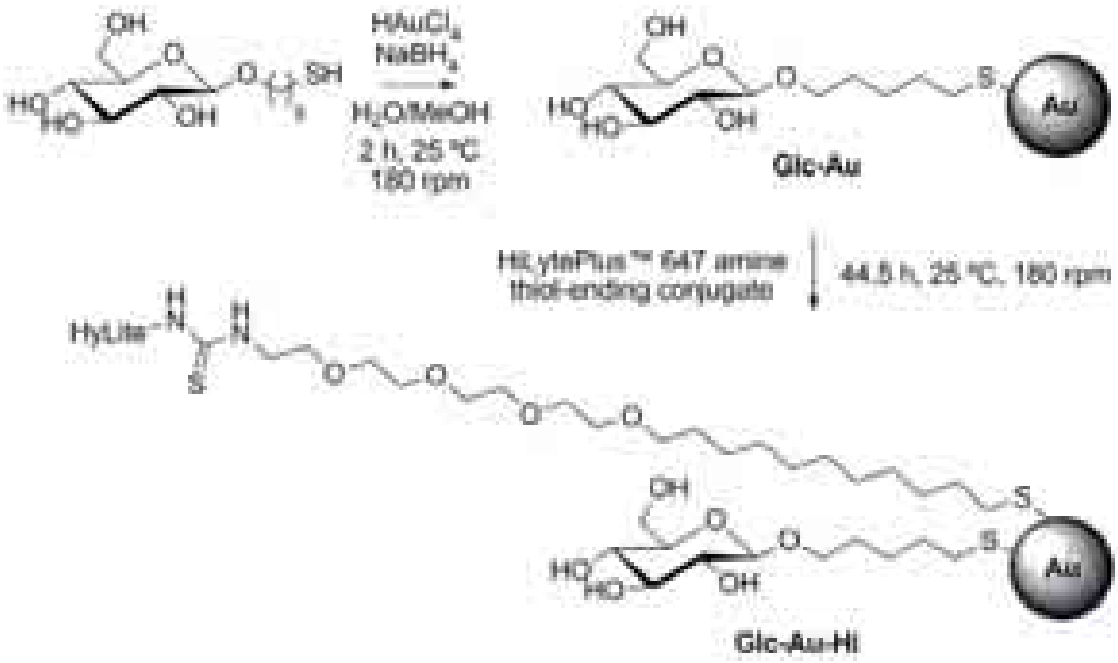

Figure 3.1 *Preparation of fluorescently labeled gold NPs coated with a glucose derivative. Glc-Au-Hi NPs were obtained by incubation of Glc-Au NPs with HiLyte Fluor™ 647 thiol-ending conjugate. The 'thiol by thiol' exchange between incoming HiLyte Fluor™ 647 thiolated conjugate and outgoing $GlcC_5SH$ allowed the incorporation of the fluorescent dye.*

A solution of HiLyte Fluor™ 647 conjugate 1 (1.48 mg) in degassed methanol (500 µL) and water (200 µL) was treated with an excess of sodium methoxide (0.16 mg) in order to achieve deacetylation in Zemplén-like conditions [271]. The resulting HiLyte Fluor™ 647 thiol-ending conjugate was incubated with Glc-Au, prepared as previously reported, in order to obtain luminescent Au NPs by a 'thiol for thiol' ligand place exchange method [270,272]. Briefly, a solution of HiLyte Fluor™ 647 conjugate **2** (0.175 µM) in 105 µL of MeOH/H_2O 5/1 was added with 1 equivalent of tris(2-carboxyethyl)phosphine (TCEP) and stirred for 48 hours. This solution was then added to a dispersion of 0.175 mg of Glc-Au in 250 µL of water and shaken in an IKA® VIBAX VXR basic at 1000 rpm in a dark vial. After 24 hours of incubation, the NPs were diluted to 3 mL with water and centrifugal filtered by using Amicon® Ultra centrifugal filter devices (10,000 MWCO, Millipore) in a Heraeus Megafuge 16R centrifuge (Thermo Scientific) at 18º C and 3000

g up to obtaining a colourless filtrate. The retentate was recovered from the filter unit by diluting with water and loaded into a membrane dialysis (approximate volume 800 μL) by using a 1 mL Spectra/Por Float-A-Lyzer G2 (MWCO 10,000, Spectrum® Labs). The Float-A-Lyzer was floated in the dialysate reservoir recharging with fresh water every 30 min (6 x 25 mL). After dialysis, the sample was freeze-dried to obtain Glc-Au-Hi.

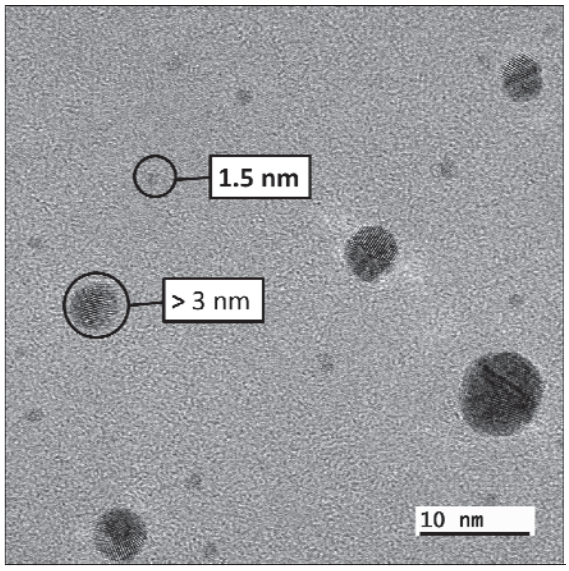

Figure 3.2 *High magnification TEM micrograph (100K) showing the crystalline structure of some Glc-Au-Hi-NPs with a diameter > 3 nm (10 % of the total observed NPs). Smaller nanoparticles (1.5 nm approximately) are visible in the image. These constitute the major fraction (90 %).*

TEM was also used to confirm the size of the NPs and to estimate their level of aggregation in solution. For TEM imaging, 5 μL of the aqueous solution (approximately 0.05 mg mL^{-1} in water) of the gold NPs were placed onto an ultrathin carbon film (< 3 nm thick) supported by a lacey carbon film on a 400 mesh copper grid (Ted Pella). The grid was left to dry in air at room temperature and then set to vacuum. TEM analysis was carried out on a JEOL JEM-2100F operated at 200 kV.

TEM imaging revealed that, in the case of the Glc-Au-Hi NPs, there is a double distribution of particle sizes with average diameters of the NPs estimated as 1.5 nm and > 3 nm respectively (***Figure 3.2***). There is a greater population of Glc-Au-Hi NPs with an

approximate size of 1.5 nm, with NPs bigger than 3 nm being present in much lower numbers (<10 %). The TEM micrographs also revealed that in the case of the Glc-Au-Hi NPs there is little to no aggregation. The particle size distribution of Glc-Au-Hi was evaluated from several TEM micrographs by means of an automatic image analyser. The average diameter and number of gold atoms of the GNPs was assigned according to a previous work [273].

Following the fluorescent labeling of the NPs several characterization experiments were performed to determine whether the labeling of the NPs had affected the emission properties of the fluorescent probe and also to determine the diffusion time of the NPs when in solution.

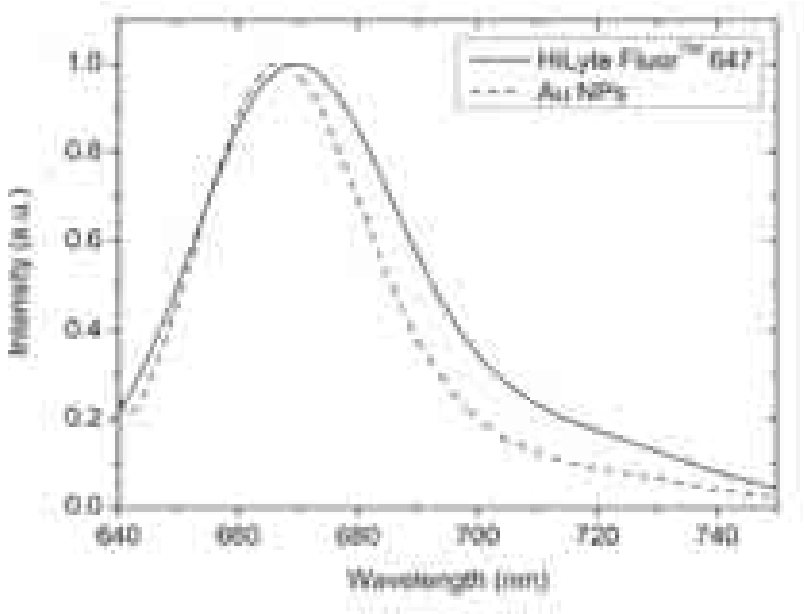

Figure 3.3 *Emission spectra of HiLyte Fluor™ 647 free probe and also of HiLyte Fluor™ 647 labeled Au NPs in distilled water. 633 nm excitation.*

The emission spectrum of HiLyte Fluor™ 647 labeled Au NPs (Fluorlog-3, Horiba Jobin Yvon Ltd.) reveals a peak emission wavelength blue shifted from to 670 nm for free HiLyte Fluor™ 647 in solution, to 665 nm when attached to the Au NPs. The long amphiphilic linker avoids the gold quenching of the fluorophore. However, it should be

noted that there is a spectral shift of the peak emission wavelength and a narrowing of the FWHM following labeling (***Figure 3.3***). For the purposes of these experiments, these slight changes in fluorescence emission of HiLyte Fluor™ 647 do not present any major obstacle in performing FCS measurements.

FCS measurements of HiLyte Fluor™ 647 labeled Au NPs were then carried out. System calibration was performed using HiLyte Fluor™ 647 for the 633 nm excitation wavelength. This probe was selected due to its high photo-stability, quantum yield, and known diffusion coefficients, as shown in **Table 3.1**.

Knowing the diffusion coefficient, while recording the average diffusion time, allows us to estimate the lateral radius and thus the effective detection volume based on the formula:

$$\tau_{D,i} = r_0^2/4D_i \text{ and } V_{eff} = \pi^{3/2}/\omega_0^2 z_0 \qquad (Eq.\ 3.1)$$

Table 3.1 *Fluorescence parameters related to HiLyte Fluor™ 647 used during FCS system optimization.*

Probe	$\lambda_{ex.}$ (nm)	λ_{em} (nm)	ϕ	Diffusion coefficient (m^2s^{-1})*	τ_D (μs)
HiLyte Fluor™ 647	649	670	0.33	$3.88E^{-10}$	61.93

*Determined from the measurement of the diffusion time of pure HiLyte Fluor™ 647 in distilled water using 633 nm excitation

The act of optimizing the FCS system essentially requires optimizing the position of the variable pinhole in front of the relevant APD detector. This is done in a two stage process, a coarse adjustment in both X and Y directions, followed by a fine adjustment in both X and Y directions. Following this two stage process, the signal now incident on the detector is maximized and FCS experiments can now be performed. As a system test, FCS data for HiLyte Fluor™ 647 is collected directly after system optimization. This also gives an indication as to how well optimize the system is. If the FCS data recorded is poor, then the optimization process must be repeated, and tested again.

FCS measurements were first performed using Glc-Au-Hi NPs in distilled water. These measurements revealed the average diffusion time of labeled Glc-Au-Hi NPs to be approximately 113.24 μs. These initial FCS measurements also gave an insight into the level of NP aggregation in solution. In the case of Glc-Au-Hi NPs, as observed from the TEM micrographs, there was little to no aggregation seen, this is also hinted at by the FCS count rate data. From the FCS measurements, using the Stokes Einstein relationship, it was also possible to estimate the hydrodynamic radii of the NPs in distilled water. For the Glc-Au-Hi NPs we calculated an average hydrodynamic radius of approximately 1 nm in solution, a value similar to that estimated via TEM micrographs. This data is in agreement with the literature in which the active ligands fold and collapse making the increase in hydrodynamic radius of the Glc-Au-Hi NPs, with respect to TEM estimates, less than the full length of the ligand [274].

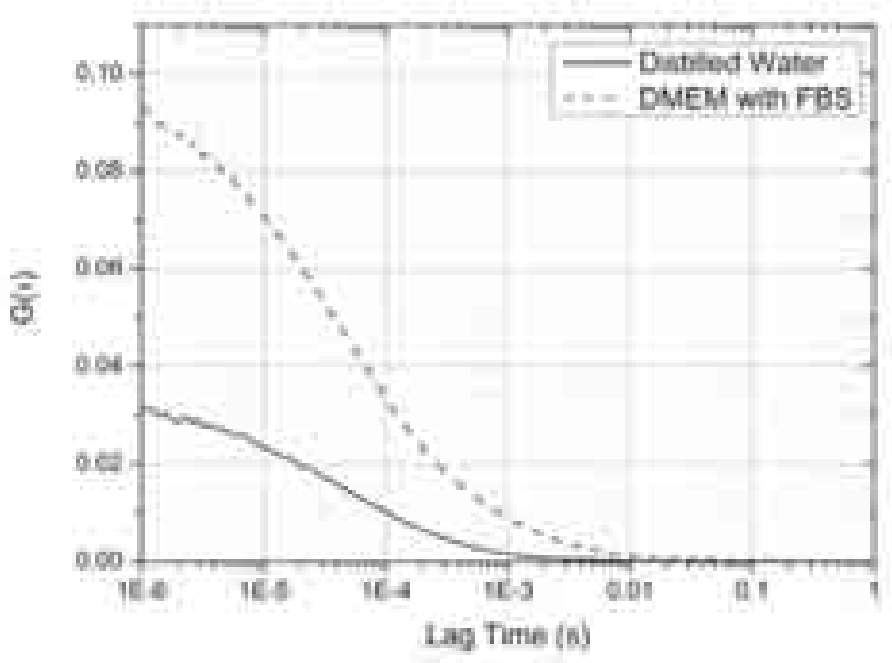

Figure 3.4 *FCS autocorrelation data for Glc-Au-Hi NPs in distilled water and cell culture media.*

The formation of NP aggregates or a protein corona in the intracellular environment is highly likely due to the high concentration of proteins and other biomolecules present. As

such, the dynamic behavior of the Glc-Au-Hi NPs was also investigated in cell culture media to account for the possible formation of NP aggregates or a protein corona around the Glc-Au-Hi NPs before cell uptake. This requires recording the correlation values of samples with identical concentrations in different media.

Here we have used distilled water as a control and cell culture media as a biomolecule rich solution. As the value of the correlation function is related to the concentration, changes in the correlation value would indicate the formation of NP aggregates as opposed to protein corona formation, where one would not expect to see a significant change in correlation value.

Glc-Au-Hi NPs were incubated in DMEM cell culture media at 37° C for a period of 30 minutes at a concentration of 0.05μg/mL. The autocorrelation curves are shown in ***Figure 3.4***, in which it can be clearly observed that there are significant differences in both diffusion time and correlation value for NPs in distilled water and cell culture media. The change in correlation value indicates the possible formation of Glc-Au-Hi NP aggregates in cell culture media however, it does not completely rule out protein corona formation. If protein corona formation was the dominant process then, we would expect to see only a slight increase in the correlation value. The concentration of Glc-Au-Hi NPs, as estimated by FCS, in cell culture media is approximately half that estimated in distilled water (see in **Table 3.2**). The change in concentration from distilled water to cell media can be understood as several large aggregates are formed in culture media. This is hinted at by large peaks in the count rate. For the calculation of the NP concentration we neglected the contribution due to these large aggregates since they entail several fluorescence molecules and therefore the estimated concentration of NPs is lower than in water.

Looking at the hydrodynamic radii of these NP aggregates we can see an approximate twofold increase in radius compared to that measured in distilled water. However, it is unlikely that this increase in radius is solely due to aggregation of Glc-Au-Hi NPs. It is highly likely that there is a fraction of the radius increase that consists of adsorbed

biomolecules contained in the cell culture media. As the intracellular environment is extremely rich in biomolecules we also expect to see the formation of Glc-Au-Hi NPs aggregates intracellularly.

3.3 Intracellular FCS of Glc-Au-Hi NP

In order to study the intracellular dynamics of Glc-Au-Hi NPs, HepG2 (human liver carcinoma cell line) cells were exposed to Glc-Au-Hi NPs and the intracellular behavior was studied via FCS. HePG2 cells were cultured in Dulbecco's Modified Eagle Medium, (DMEM) with 10% Fetal Bovine Serum and 1000 U penicillin, 10 mg/ml streptomycin, at 37 ºC and in 5 % CO_2. 100,000 cells were seeded in a glass-bottom petri dish, and cultured for 24 hours. The Glc-Au-Hi NPs were added into the culture media to a final concentration of 0.05 μg/ml. Following 30 minutes of incubation, the cells were washed 3 times with PBS and were then ready for FCS measurements to be performed. All FCS measurements were performed using live cells.

3.3.1 Prebleach strategy for intracellular FCS

Photobleaching was applied within the detection volume, which is approximately 0.93 fL for the excitation wavelength used (633 nm). The prebleaching volume is identical to the detection volume as it is dependent on the wavelength of excitation. All immobile NPs, present either as large aggregates or single nanoparticles, within the detection volume, at the time of bleaching, will be photobleached. Immobile single nanoparticles or small aggregates should be bleached more rapidly, compared to the larger aggregates, as the amount of dye to be bleached is less than in the larger aggregates.

FCS data are then collected from the mobile fraction, either in the form of single nanoparticles or small aggregates that enter the detection volume after the bleaching phase. It is also possible that a fraction of NPs have not been entirely bleached and retain some fluorescence during the bleaching phase. These NPs may have been diffusing out or in of the edge of the detection volume just prior to the start or end of the bleaching phase,

and as such only experience partial bleaching as they do not remain inside the bleaching volume for a sufficient amount of time.

A similar procedure has been previously applied for tracking protein intracellularly for the detection of mobile proteins in the presence of an immobile fraction of proteins, large aggregates [136,275]. A full mechanistic explanation of how photobleaching in FCS measurements enables the removal of background fluorescence due to an immobile fraction of proteins is given in Schwille et al. in 2002 and Schwille et al. in 2003 [136,275].

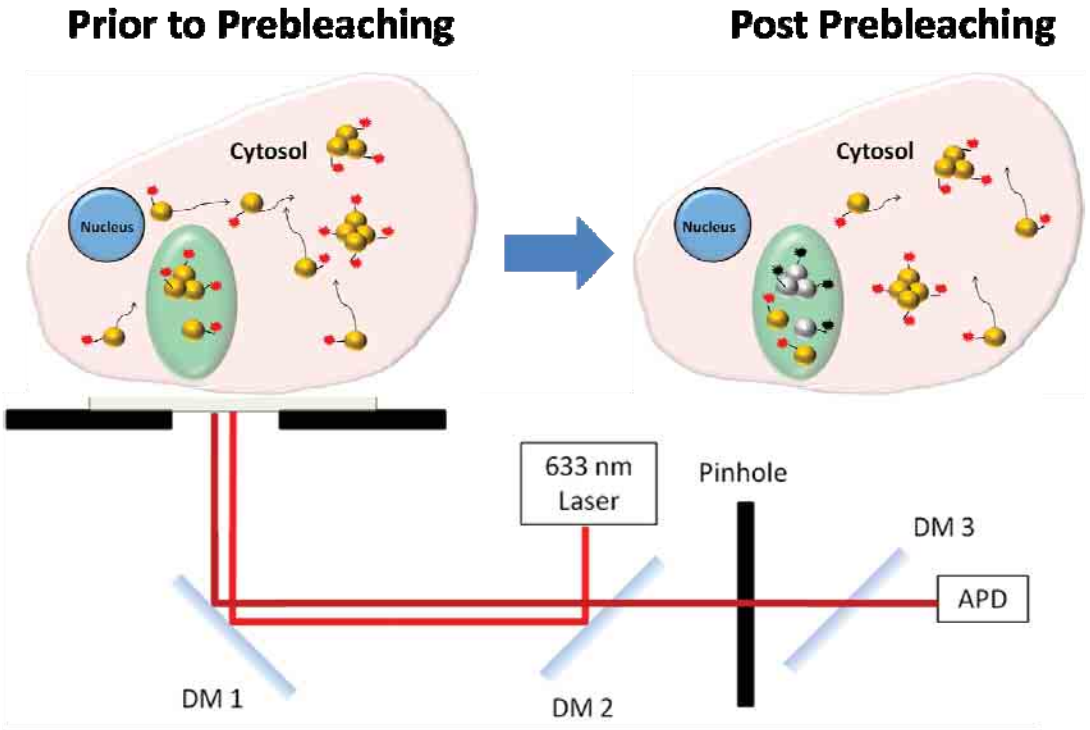

Figure 3.5 *Schematic of intracellular FCS measurements using 633 nm excitation and HiLyte Fluor™ 647 labeled Glc-Au-NPs.*

As mentioned prebleaching was performed using the same laser used during FCS data acquisition and was performed for 20s prior to the collection of intracellular FCS data at each measurement point. Intracellular FCS data was then collected over 100s and fit directly following data collection using the software package, ZEN, provided by Zeiss.

For FCS data fitting, a single component, 3D fitting model was used, with a fixed structural parameter of 5.3 as determined in the system optimization. From data fitting, the average diffusion time is calculated, as is the average concentration and hydrodynamic radii of the NPS. Data sets that showed the presence of aggregates were excluded in all calculations.

Particle size was calculated based upon the Stokes-Einstein, which relates the diffusion coefficient to the hydrodynamic radius of a particle by the expression:

$$r_h = \frac{kT}{6\pi\eta D} \quad (Eq.\ 3.2)$$

Where k is the Boltzmann constant, T is temperature in degrees Kelvin, η is the viscosity, and D is the diffusion coefficient. The diffusion coefficient is calculated by the expression:

$$D = {\omega_0^2}/{4\tau_D} \quad (Eq.\ 3.3)$$

where ω_0 is the lateral radius of the confocal volume and τ_D is the diffusion time.

Assuming that each Glc-Au NP has a single fluorophore attached, we can assume the concentration of the fluorophore is equivalent to that of the NPs. Therefore we can estimate the concentration of the NPs by use of the following formula:

$$C = \frac{N}{N_A V_{FCS}} \quad (Eq.\ 3.4)$$

Where V_{FCS} is the FCS confocal detection volume, N_A is Avogadro's number and N is the average number of particles passing through the confocal detection volume.

3.3.2 Intracellular FCS measurement of Glc-Au-Hi NPs

Several repeating FCS measurements were performed in HepG2 cells that had been incubated with Glc-Au NPs for a period of 30 minutes. Below we can see the CLSM images of the cell samples in which FCS measurements were made, as well as the corresponding FCS autocorrelation curves.

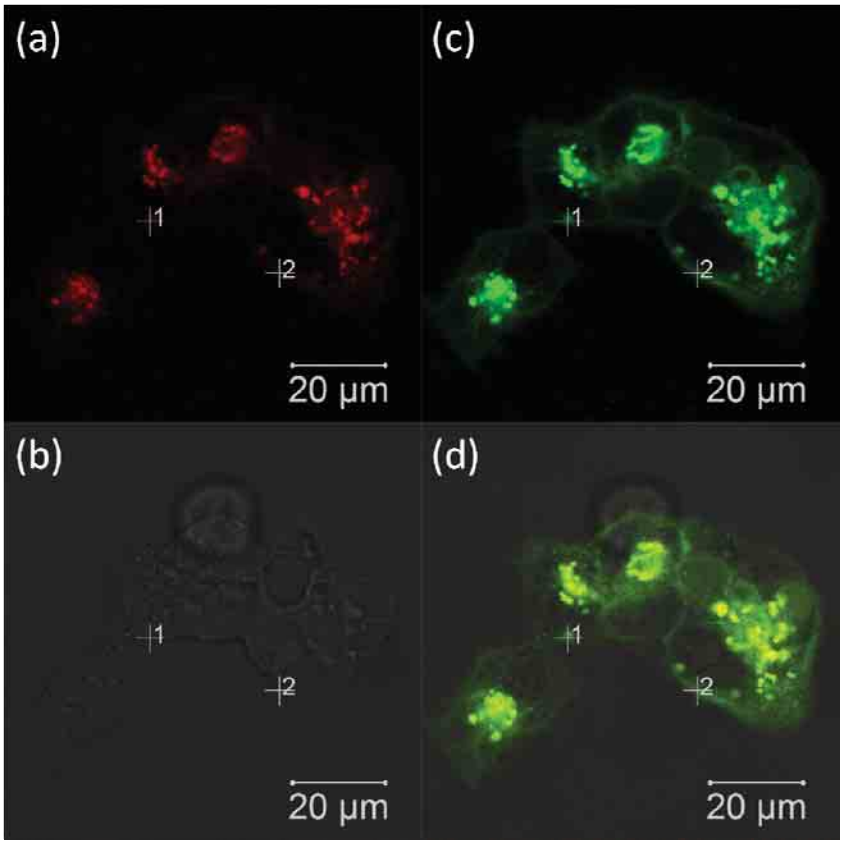

Figure 3.6 *(a) CLSM image of Glc-Au-Hi NPs (shown in red) uptaken by cells. (b) Transmission light image of the cells. (c) HepG2 cells with the membrane stained with Cellmask Orange (shown in green). (d) Images (a, b, and c) combined*

To investigate the intracellular dynamics of the Glc-Au-Hi NPs, HepG2 cells were incubated with Glc-Au-Hi NPs at a concentration of 0.05 µg/mL for a period of 30 minutes at 37° C. Following this incubation period CLSM images were acquired. In ***Figure 3.6***, we see HepG2 cells stained with CellMask™ Orange membrane stain (shown in green) with the Glc-Au-Hi NPs shown in red. The CLSM images allow the locating of

uptaken NPs inside the cell. Points of interest in each CLSM image were then marked and FCS measurements were performed. The selection criterion for points of interest is such that there should not be large amounts of visible aggregates present in the vicinity of the measurement site. Therefore, following the selection of suitable measurement locations, FCS measurements were made.

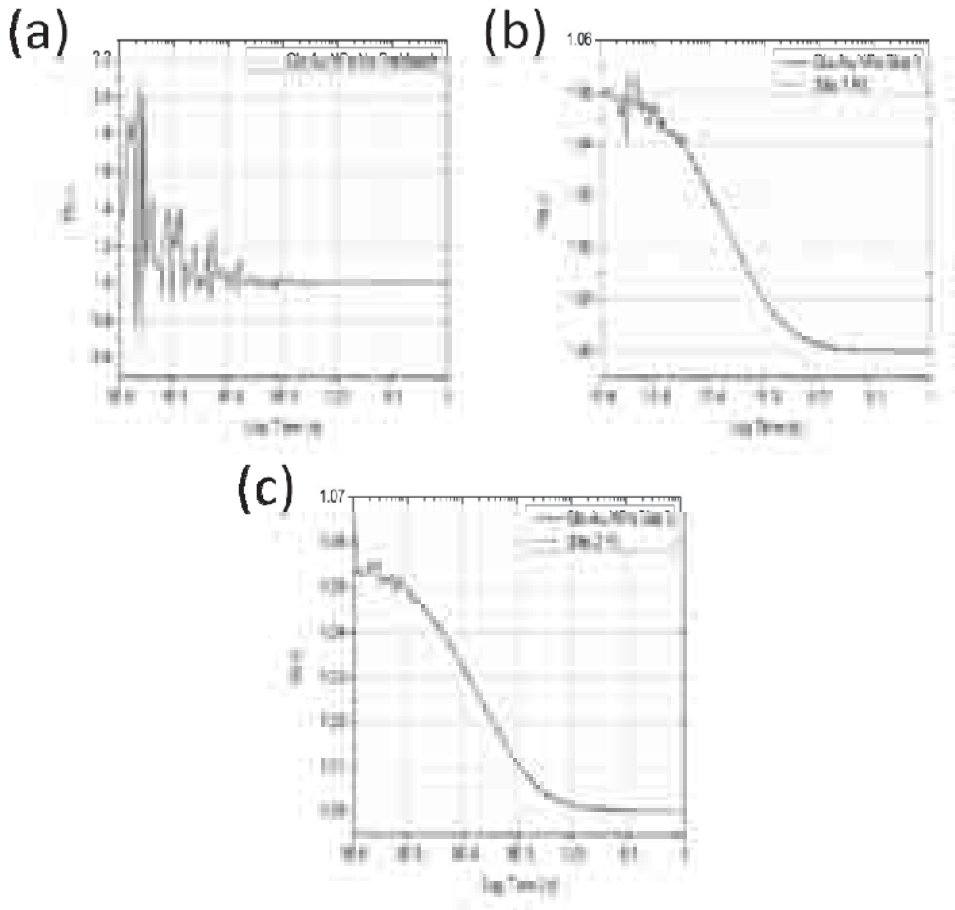

Figure 3.7 *(a) Intracellular FCS data collected prior to the implementation of prebleaching. (b & c) Intracellular FCS data collected after implementing prebleaching. The data shown corresponds to measurement sites 1 and 2 in Figure 3. Where (b) corresponds to site 1 and (c) corresponds to site 2. The diffusion times measured for sites 1 and 2 are 405.1 µs and 390.8 µs respectively.*

FCS data were collected without prebleaching display a lack of coherent correlation data (***Figure 3.7 a***.). As a result we cannot calculate the diffusion time, local concentration,

particle size etc., at the measurement sites. However, contrary to this, while implementing prebleaching, fluorescence fluctuations can be recorded and fitted with a single component autocorrelation function (***Figure 3.7 b & c***) thereby allowing FCS data to be collected. However, it should be noted that not all measurements following prebleaching yield meaningful results. This is maybe due to the immobile fraction not being completely photobleached or the absence of NPs in the selected measurement location.

Table 3.2 *FCS autocorrelation data for Glc-Au-Hi NPs in distilled water and DMEM cell culture media with FBS and for selected intracellular sites.*

Media	$G(\tau)$[1]	τ_D (μs)[2]	Conc (nM)[3]	r_H (nm)[4]	Vol (nm^3)[5]
Distilled water	1.02	113.2	77.4	1.0	4.4
DMEM with 10 % FBS	1.05	243.3	37.0	2.2	44.0
Site 1	1.20	405.1	9.4	3.5	179.6
Site 2	1.20	390.8	9.4	3.7	207.1

[1]correlation value, [2]diffusion time, [3]concentration [4]hydrodynamic radius, [5]volume

As the amplitude of the correlation function is inversely related to the concentration of the HiLyte Fluor™ 647, which are associated to the NPs, we can now use this as a measure of the homogeneity of intracellular concentration of Glc-Au-Hi NPs at the measurement sites. In Figure 4 b & c we can see that the amplitude of the correlation curves for the two chosen sites are almost identical. Assuming that there is only one molecule of HiLyte Fluor™ 647 per Glc-Au-Hi NP and that they are all labeled, we can estimate the concentration of NPs as being equal to the dye concentration which can be calculated from the amplitude of the correlation curves. We see that for the Glc-Au-Hi NPs we calculated relative local concentrations approximately 9.40nM for selected measurements sites (see **Table 3.2**). As the concentration of Glc-Au-Hi NPs used during cell incubation is the same that used for making FCS measurements in distilled water we can easily compare the concentrations. However, as we cannot easily say whether there has been 100 % uptake of Glc-Au-Hi NPs, we cannot easily speculate about whether we

are measuring data related to small NP aggregates or if there is protein corona formation around the NPs.

The diffusion times of Glc-Au-Hi NPs are approximately 400 μs for sites 1 & 2 respectively in ***Figure 3.6***. This information allows to us to estimate the approximate size of the aggregated/protein coated Glc-Au-Hi NPs based on the Stokes Einstein relationship given previously. Following this, several repeat FCS measurements were performed in HepG2 cells incubated with Glc-Au-Hi NPs following the same procedure as described above. The results collected indicate a relatively high degree of reproducibility.

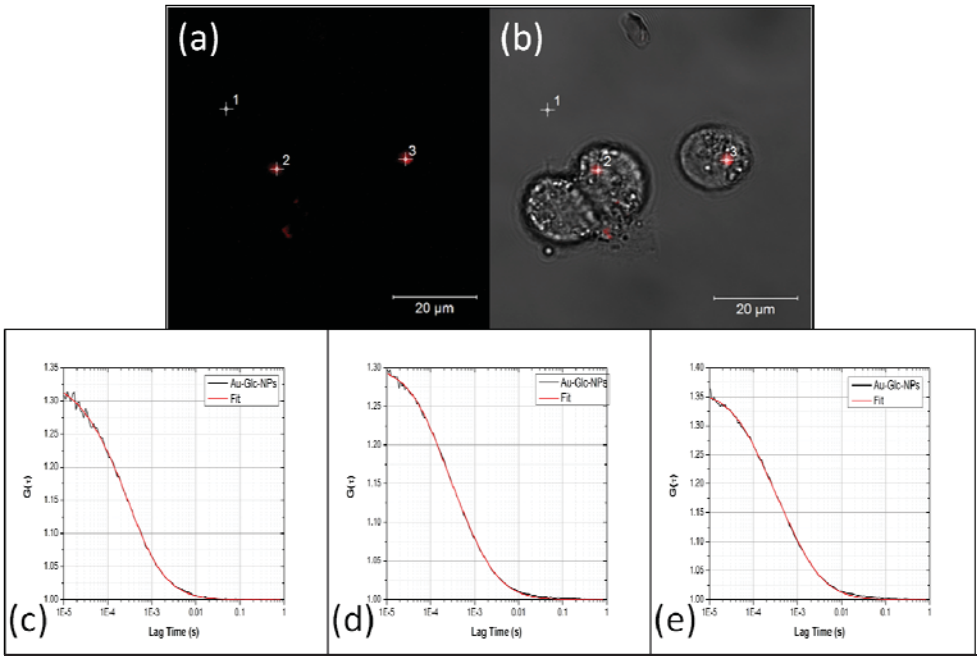

Figure 3.8 *(a) Fluorescence image of Glc-Au NPs. (b) Transmitted light image. (c) Autocorrelation curve for point 1* τ_D *= 305.96 μs (extracellular). (d) Autocorrelation curve for point 2* τ_D *= 567.04 μs. (e) Autocorrelation curve for point 3* τ_D *= 623.11 μs.*

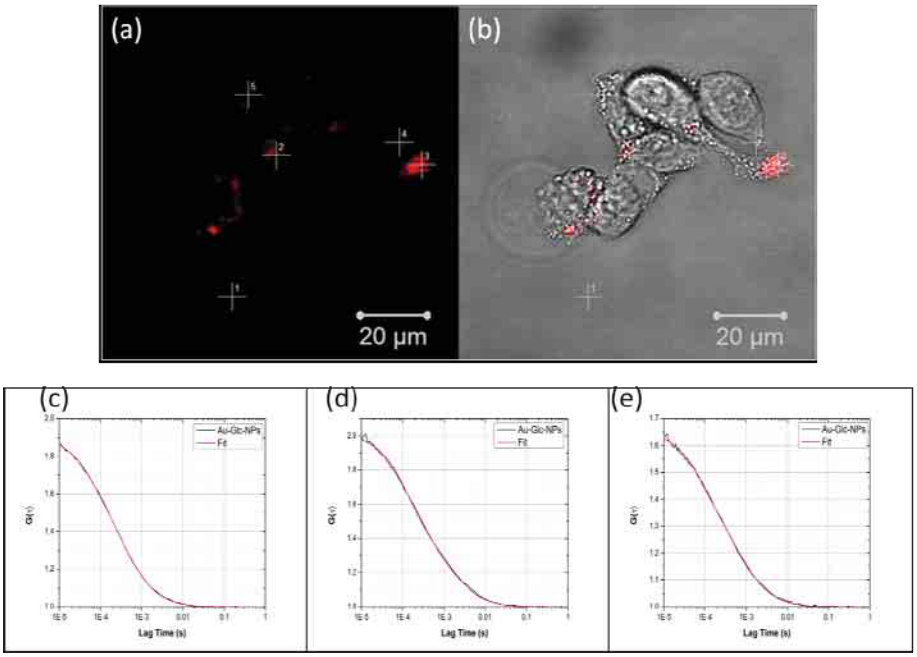

Figure 3.9 *(a) Fluorescence image of Glc-Au NPs. (b) Transmitted light image. (c) Autocorrelation curve for point 1* τ_D *= 310.18 µs (extracellular). (d) Autocorrelation curve for point 3* τ_D *= 966.30 µs. (e) Autocorrelation curve for point 4* τ_D *= 513.40 µs.*

Several repeat FCS measurements were performed in HepG2 cells that had been incubated with Glc-Au NPs for a period of 30 minutes. Below we can see the CLSM images of the cell samples in which FCS measurements were made, as well as the corresponding FCS autocorrelation curves as shown from ***Figure 3.8*** to ***Figure 3.12***.

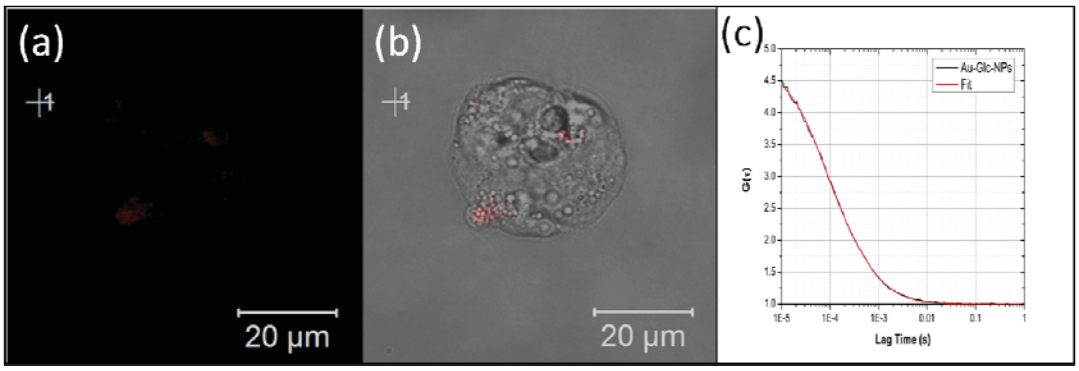

Figure 3.10 *(a) Fluorescence image of Glc-Au NPs. (b) Transmitted light image. (c) Autocorrelation curve for point 1* τ_D *= 211.00 µs (extracellular).*

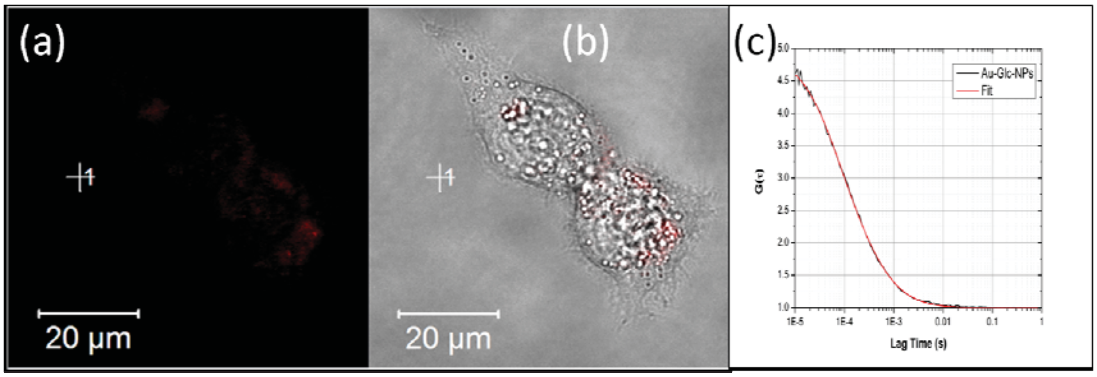

Figure 3.11 *(a) Fluorescence image of Glc-Au NPs. (b) Transmitted light image. (c) Autocorrelation curve for point 1* τ_D *= 164.97 µs (extracellular).*

In the case of all the correlation curves it was possible to fit the data using a single component fitting model. Attempts were made to fit the autocorrelation curves using a two component model however, no improvement in data fitting was observed. Therefore, the single component fitting model was consistently applied. The summary of the intracellular data and extracellular data is presented in **Table 3.3.**

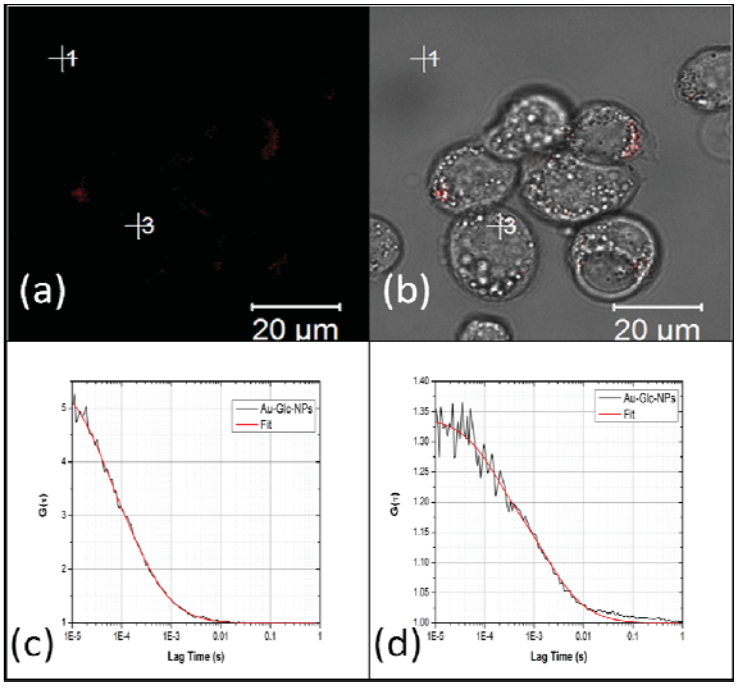

Figure 3.12 *(a) Fluorescence image of Glc-Au NPs. (b) Transmitted light image. (c) Autocorrelation curve for point 1* τ_D *= 159.11 µs (extracellular). (d) Autocorrelation curve for point 3* τ_D *= 263.63 µs.*

Table 3.3 *Extended FCS autocorrelation data for Glc-Au NPs incubated with HepG2 cells.*

Location[1]	G(τ)[2]	CPM (kHz)[3]	N[4]	τ_D (μs)[5]	Conc (nM)[6]	D (x 10^{-10} m^2s^{-1})[7]	r_H (nm)[8]
i	1.2	4.1	4.4	567.0	7.8	0.4	5.1
i	1.3	3.5	3.6	623.1	6.5	0.4	5.6
i	1.1	0.3	15.8	555.1	28.3	0.4	5.0
i	1.1	0.7	6.9	298.1	12.4	0.8	2.7
i	1.5	3.3	2.0	1948.6	3.6	0.1	17.6
i	1.9	16.2	1.1	331.9	2.0	0.7	3.0
i	1.6	9.1	1.7	966.3	3.0	0.2	8.7
i	1.5	5.1	2.1	513.4	3.7	0.5	4.6
i	2.1	2.1	0.9	428.6	1.6	0.6	3.9
i	4.2	5.0	0.3	238.7	0.6	1.0	2.2
i	1.3	0.8	3.0	656.2	5.4	0.4	5.9
i	3.4	3.3	0.4	263.6	0.8	0.9	2.4
i	3.4	6.1	0.4	586.5	0.7	0.4	5.3
i	1.0	3.0	30.0	429.3	53.6	0.6	3.9
i	1.0	3.5	28.6	371.4	51.1	0.6	3.4
i	1.2	0.7	5.3	405.1	9.4	0.6	3.5
i	1.2	0.6	5.3	390.8	9.4	0.6	3.7
Avg. Intracellular	***1.8***	***4.0***	***6.6***	***563.2***	***11.8***	***0.5***	***5.1***
e	1.3	2.0	3.4	306.0	6.1	0.8	2.8
e	1.2	1.2	5.3	322.8	9.5	0.7	2.9
e	1.9	17.3	1.1	308.5	2.0	0.8	2.8
e	1.7	15.9	1.3	310.2	2.4	0.8	2.8
e	3.6	12.6	0.4	211.0	0.7	1.1	1.9
e	4.1	13.8	0.3	165.0	0.6	1.5	1.5
e	3.8	4.5	0.4	225.9	0.6	1.1	2.0
e	3.8	4.1	0.4	255.7	0.6	0.9	2.3
e	4.5	5.2	0.3	159.1	0.5	1.5	1.4
e	7.9	15.0	0.1	177.7	0.3	1.4	1.6
Avg. Extracellular	***3.4***	***9.2***	***1.3***	***244.2***	***2.3***	***1.1***	***2.2***

[1]i indicates intracellular location and e extracellular location, [2]correlation value, this includes an offset value of 1, [3]counts per molecule, [4]number of molecules, [5]diffusion time, [6]concentration, [7]diffusion coefficient, [8]hydrodynamic radius.

It has previously been reported that measurements in cell vesicles demonstrated that the

local microviscosity can be as high as 140 cP, whereas the microviscosity in the aqueous phase of the cellular cytoplasm is 1–2 centipoise, similar to that of pure water [276–279]. Therefore, for all measurements, the viscosity of the media has been taken to be similar to that of pure water; i.e. 1 cP. The reason for this being that in calculating the hydrodynamic radius, viscosity values above 2 cP have no physical sense as the calculated radius is smaller than that measured by both TEM and FCS. This demonstrates that the Glc-Au-Hi NPs are located within cell compartments with similar viscosities to that of pure water. This correlates well with *De La Fuente et al*, who observed that during the first 15 minutes of incubation NPs were seen throughout the cytoplasm.[259] Our results show that FCS can be used to provide an estimation of the localization of the NPs inside cells.

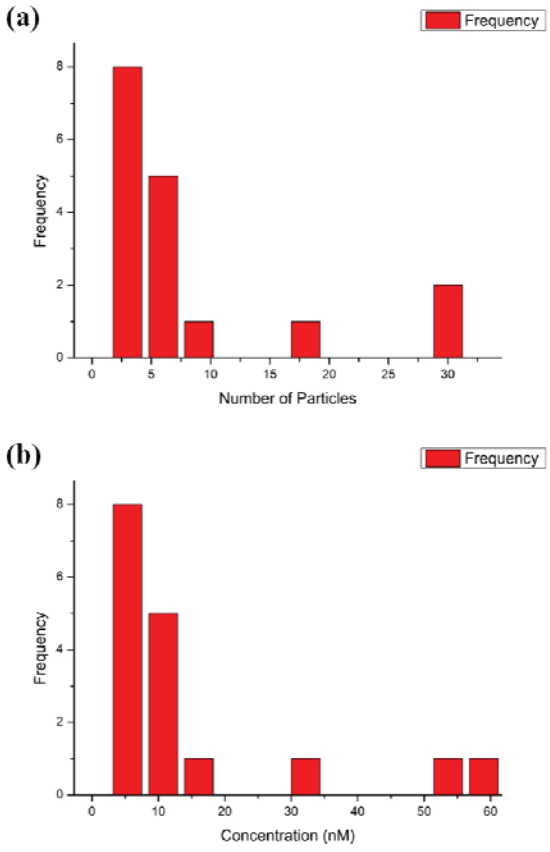

Figure 3.13 *Intracellular distribution histograms for (a) average number of fluorescent particles passing through the detection volume, and (b) local concentration of Glc-Au-Hi NPs measured intracellularly.*

From measuring the diffusion of the Glc-Au-Hi NPs in several individual cells we were then able to build up intracellular distribution histograms for several parameters (see ***Figure 3.13***). As we can see from ***Figure 3.13***, the distribution of the number of fluorescent particles is relatively narrow (approximately 3-6). This indicates a low local concentration as shown in ***Figure 3.13b***, with the local concentration calculated from the number of particles as in equation 3.4 (*Eq. 3.4*). The local concentration cannot be correlated to total NP concentration since the immobile fraction is not taken into account in the calculation. The fact that the measurements were performed in different locations in the cell and that the values for the number of fluorescent particles and concentration are not dispersed reveals a homogeneous distribution of the mobile fraction of NPs in the cell.

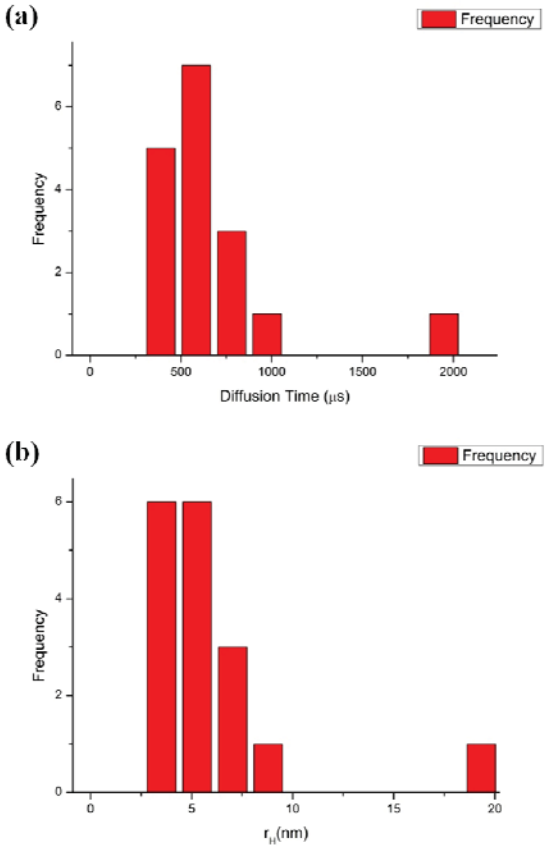

Figure 3.14 *Intracellular distribution histograms for (a) measured diffusion time, and (b) hydrodynamic radius of Glc-Au-Hi NPs measured intracellularly.*

Similarly both the measured diffusion time and hydrodynamic radius (calculated from the diffusion time) distribution histograms are similarly narrow (***Figure 3.14a & b***). Measured diffusion times range from 238 μs to 780 μs. The narrow range of diffusion times allows us to conclude that only single NPs and small aggregates of NPs contribute to the mobile fraction. Approximately 88 % of the aggregates are between 3.5 nm and 7.0 nm. Occasionally aggregates over 780 μs (~12%) can be measured but most of these aggregates can be considered as immobile.

Chapter 4

Monitoring Intracellular Degradation Kinetics of Poly (lactide-*co*-glycolide) Nanoparticles by means of Flow Cytomery

---

4.1 Motivation and background

Polymeric nanoparticles (NPs) in the submicron size are appealing drug delivery vehicles. By the design of size, drug loading amount and surface chemical composition, these NPs are not only able to protect drugs from degradation, increase their therapeutic benefit, but they alsohave ability to target the drugs to the specific organs and deliver drugs of interest beyond the blood-brain barrier for example [280,281]. Poly(lactide-*co*-glycolide) (PLGA) NPs are among the most frequently used polymers as drug delivery carrier because of their properties such as controlled size, quantity of loaded material and release features, excellent biocompatibility and biodegradability [282–295].

One of the critical issues to be studied in the design of polymer carriers for drug delivery is the degradation process of the carrier. The polymer matrix should continuously lose mass to facilitate the slow release of the encapsulated drug. PLGA degradation occurs through autocatalytic hydrolysis of the ester bonds, with a degradation rate that depends on the copolymer composition, i.e.: molecular weight and ratio between the lactide and glycolide blocks, and on the surrounding environment [151,296,297]. PLGA NP hydrolysis has been reported to occur in a heterogeneous way, degrading from the centre with the polymer subsequently diffusing outward [298]. The reason for this has been found to be the autocatalytic action of the carboxylic acid end groups trapped in the interior of the NPs [126]. Degradation of PLGA NPs within live organisms also occurs by enzymatic degradation [299]. When the biodegradable PLGA NPs are in contact with cells, enzymes can interact by catalyzing their hydrolysis degradation process, resulting in a

more rapid rate of degradation. However, due to the complexity of tracking NPs intracellularly, and inside organs, and the limitation of the measurement techniques, very few studies have been carried out concerning the *'in vitro'* or *'in vivo'* degradation of PLGA NPs [300].

Many different techniques have been employed for intracellular degradation studies, such as Raman spectroscopy, Confocal Scanning Laser Microscopy (CLSM) and Flow Cytometry (FACS). With Raman spectroscopy it is possible to obtain detailed information about the chemical composition of PLGA NPs undergoing degradation inside an individual cell [126]. But it is restricted to single cell measurements and it is not trivial to follow changes in intensity with time since NPs can potentially change location within the cell. Studying intracellular degradation using fluorescence techniques such as Confocal Scanning Laser Microscopy (CLSM) or Flow Cytometry (FACS), is also not easy since these techniques measure the fluorescence associated with the cell and it is not possible to distinguish between the fluorescence of non-degraded and degraded PLGA NPs within the cell [240,301]. Nevertheless, the use of high throughput techniques like FACS is desirable for the study of intracellular degradation as a statistical analysis of a large number of cells can be rapidly obtained.

In this chapter, it will be shown that the intracellular degradation of Rhodamine B (RhdB) labeled PLGA NPs can be monitored via FACS, by measuring the increase in fluorescence intensity following the exposure of RhdB labeled PLGA molecules to the intracellular environment during degradation. The possibility of monitoring the degradation, via FACS, relies on the dye attached to the PLGA presenting a different quantum yield when it encounters the cellular environment where changes in the fluorescence intensity within the cell population indicate a change of local environment for the dye, and thus indicates the occurrence of degradation.

Two kinds of PLGA NPs were fabricated with the following compositions: 15 % and 35 % glycolide molar proportion. It will be shown that NPs with 15 % glycolide degrade (PLGA15) progressively in the cell interior, while 35 % glycolide PLGA (PLGA35) NPs remain intact. The results provide a novel method for tracing the intracellular fate of PLGA NPs by recording, via FACS, the liberation of fluorescently labeled polymer from the NPs. This possibility has not been explored to date and

potentially has a high impact on the design of drug delivery carriers with a controlled release mechanism based on PLGA. In addition, confocal Raman microscopy has been used to follow PLGA degradation at cell level.

4.2 PLGA labeling and NPs Preparation

PLGA molecules for FACS study were labeled with lissamine rhodamine B ethylenediamine (RhdB), following the reaction described by Horisawa E. et al [302]. Briefly, PLGA15 or PLGA35 (3 g, 0.052 mmol), and the fluorophore (3.2 mg, 0.0052 mmol of RhdB) were completely dissolved in 30 mL of acetonitrile with 0.04 g of ethylcarbodiimide hydrochloride (EDC), and incubated at room temperature for 40 h while continuously being magnetically stirred. The resulting fluorophore bound DL-lactide/glycolide copolymers (RhdB-PLGA15 or RhdB-PLGA35) were placed in a pleated dialysis tubing (3500 MWCO) against millipure water to purify it. After one week of dialysis the polymer was freeze dried.

Fluorescent PLGA NPs were prepared by means of an O/W emulsion–solvent evaporation method [303]. Firstly, a solution of 20 mg mL^{-1} of fluorescent PLGA in dichloromethane was prepared by using a mixture of 1:1 unlabeled PLGA and RhdB-PLGA. Then, 1 mL of PLGA dichloromethane solution (organic phase) was added to a 4 mL, 2 % BSA solution (water phase) and then emulsified with an ultrasonicator (Sonics VCX 500) for 20 s. This emulsion was then poured into 100 mL of distilled water, and stirred for 3 h with a magnetic stirrer until the organic solvent had totally evaporated. The fluorescent PLGA NPs were collected by centrifugation at 10,000 g for 5 min, and washed with milliQ water five times to remove the free BSA that was initially present in the water phase. Fluorescent NPs were prepared using both labeled PLGA15 and PLGA35.

4.3 PLGA NPs characterization

The size and morphology of fluorescent PLGA NPs stabilised with BSA were characterised by TEM and dynamic light scattering (DLS). The DLS distribution and TEM images for PLGA15 NPs showed diameters of 370 (***Figure 4.1a***) and 220 nm (***Figure 4.1b***), respectively. In the case of PLGA35 NPs the diameter measured by

DLS was of approximately 360 nm (***Figure 4.1c***), while in TEM it is possible to observe NPs with diameters of approximately 315 nm (***Figure 4.1d***). In both scenarios, DLS measurements recorded typically larger diameters for the NPs than those observed in TEM. This can be explained by the hydration of the BSA coating that results in a larger hydrodynamic radius. PLGA35 NPs and PLGA15 NPs are of equivalent size, suggesting that the size of the NPs is independent of the molar composition of the PLGA copolymer. The measured ζ-potential of the fluorescent PLGA15 and PLGA35 NPs were approximately -33 mV and -22 mV respectively.

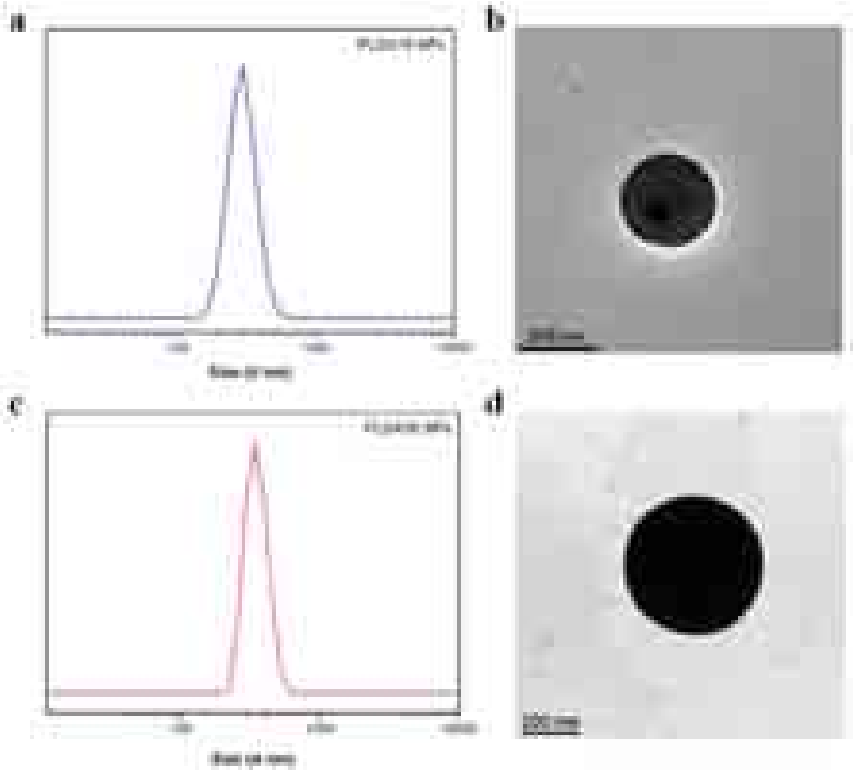

Figure 4.1 *DLS size distribution of (a) PLGA15 NPs and (c) PLGA35 NPs, and TEM micrographs of (b) PLGA15 NPs and (d) PLGA35 NPs. NPs were prepared with fluorescently labeled PLGA copolymers (85:15 and 65:35) and using BSA as stabilizer.*

4.4 Degradation of PLGA NPs under physiological conditions by DLS and TEM

In order to study the degradation of PLGA NPs under physiological conditions, PLGA NPs (PLGA15 or PLGA35 NPs), were dispersed in PBS at a concentration of 1 mg mL^{-1} and incubated at 37 ºC while being agitated. Samples were taken out at

different time intervals and washed with water. The hydrodynamic size of PLGA15 and PLGA35 NPs were measured during degradation by DLS.

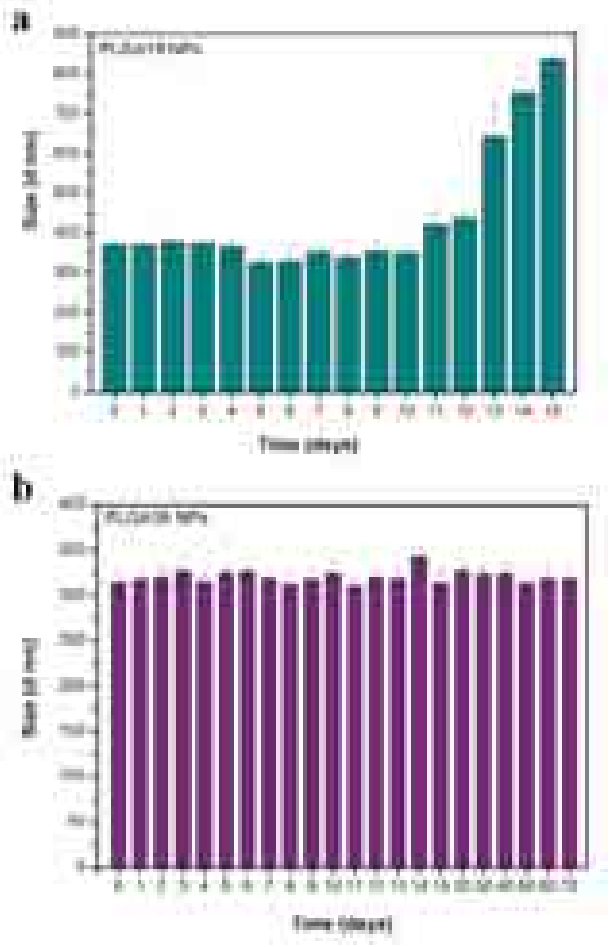

Figure 4.2 *Size variation over time monitored by DLS of (a) PLGA15 NPs and (b) PLGA35 NPs exposed to PBS at 37 ºC.*

Figure 4.2a shows the change in the size of the PLGA15 NPs under physiological conditions with time. It is possible to observe that during the initial stages of exposure to physiological conditions, the size of the NPs remain almost constant at values between 350 and 400 nm in diameter. Only a small decrease, of few nm, in the size of the NPs can be observed between 5 and 8 days of incubation. Nonetheless, after 10 days of incubation in PBS at 37 ºC, the PLGA15 NPs start to gradually increase in size, reaching 836 nm in diameter after 15 days of exposure. The increase in the hydrodynamic size of the PLGA15 NPs during their exposure to physiological conditions can be an indicator of NP degradation. Typically, NPs in contact with PBS start to swell due to the absorption of water and subsequently, PLGA NPs start to

degrade from the centre of the NP via hydrolysis of their ester linkages, as previously mentioned. When PLGA is degrading, the polymer chains begin to break and therefore, the NPs begin to dissolve. Because of their hydrophobicity, the broken polymer chains form large aggregates in solution which showed an increase of hydrodynamic size.

The variation in NP size, with time, of PLGA35 NPs exposed to physiological conditions is shown in ***Figure 4.2b***. The size of PLGA35 NPs do not show significant changes over the 70 days of exposure under physiological conditions, and the diameter of the NPs remains almost constant, at values in the range 330 nm to 360 nm in diameter. The size preservation of PLGA35 NPs during this time suggests that PLGA35 NPs do not degrade even after 70 days of incubation.

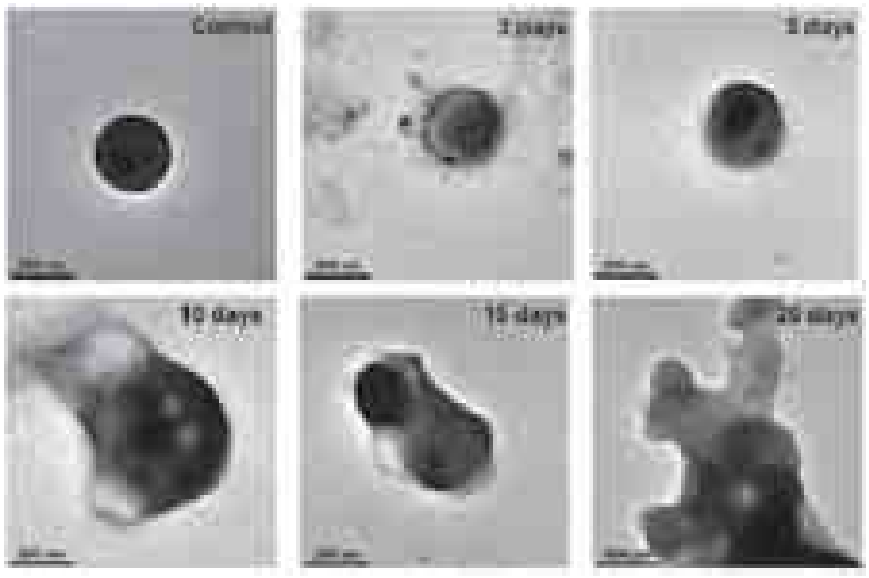

Figure 4.3 *Morphology and size change of PLGA15 NPs in PBS at 37 ºC monitored over time by TEM. Scale bar indicates a scale of 200 nm*

In ***Figure 4.3*** we can observe the TEM images of PLGA15 NPs after different incubation time intervals in PBS at 37 ºC. During the first five days of exposure to physiological conditions, The size of the NPs remain constant; nonetheless, the morphology of the NPs was affected, as is clearly shown in the images corresponding to days 3 and 5. Initially, the NPs are spherical with a clearly defined shape prior to exposure to PBS. After the first 5 days of exposure, the uniform round shape typical of PLGA15 NPs is no longer observable, and the polymer NP wall appears to be

damaged. After 10 and 15 days of exposure, NP swelling and aggregation can be observed in addition to the non uniform round shape and the damage to the NP wall. Moreover, after 20 days under degradation in physiological conditions, it is no longer possible to observe individual PLGA15 NPs by TEM, while large aggregates of polymer, resulting from degradation of PLGA15 NPs, can be clearly distinguished. TEM images confirm the changes in size of the PLGA15 NPs observed by DLS.

Figure 4.4 *Morphology and size change of PLGA35 NPs in PBS at 37 ºC monitored over time by TEM. Scale bar indicates a scale of 200 nm.*

In ***Figure 4.4*** we can also observe the TEM images of PLGA35 NPs taken at different days during exposure to PBS at 37 ºC. In contrast to PLGA15 NPs, PLGA35 NPs do not show any change in size or morphology after 20 days. Both size and morphology remain almost unaltered after 70 days of exposure to physiological conditions. As with PLGA15 NPs; TEM images confirm the results obtained by DLS, proving that PLGA35 NP degradation does not take place.

The ζ-potential change of the PLGA NPs was also monitored during incubation with PBS. ***Figure 4.5a*** shows that the ζ-potential of PLGA15 NPs decreased over the first 11 days of physiological conditions exposure. Prior to incubation in PBS at 37 ºC, PLGA15 NPs showed a negative ζ-potential value of -33 mV, after day 5 the ζ-potential had decreased to -60 mV and on day 11 the NPs reached the lowest ζ-potential value of approximately -68 mV. However, on day 13 of incubation, the NP ζ-potential value increased dramatically to -10 mV and remained almost constant in the succeeding days. The decrease in ζ-potential at the beginning of the degradation process could be due to acid groups of the broken polymer chains that may arrange on the surface of the PLGA15 NPs. The dramatic increase of the surface charge of the NPs after day 13 could be a result of the complete degradation of the PLGA15 NPs

that cause large aggregates as observed by TEM and DLS. These large aggregates must have rests of hydrophobic PLGA with a diluted surface charge emanating from the oxidised products of the PLGA or the remains of BSA still presented on the surface of the NPs.

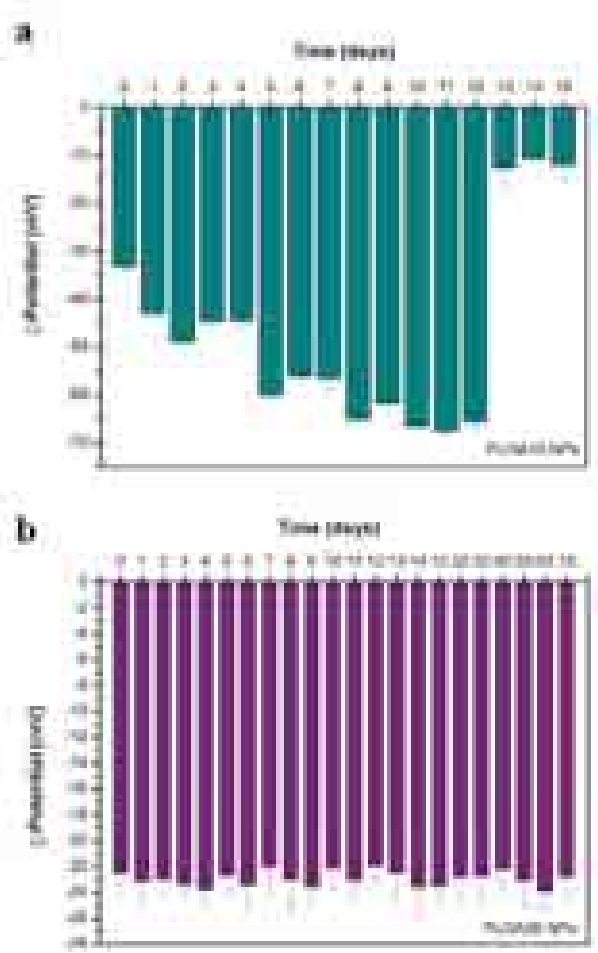

Figure 4.5 *Monitoring of the ζ-Potential over time of (a) PLGA15 NPs and PLGA35 (b) NPs under degradation in PBS at 37 ºC.*

Figure 4.5b shows the ζ-potential of PLGA35 NPs at different incubation time intervals in PBS at 37 ºC. In contrast to the changes in ζ-potential observed for PLGA15 NPs, the ζ-potential of PLGA35 NPs remained almost constant over the same time period, ranging between -22 mV and -25 mV. After 70 days of exposure to physiological conditions, the ζ-potential of the PLGA35 NPs did not experience any significant change, indicating that there was little to no change in the surface characteristics of the NPs during exposure.

4.5 Study of degradation of PLGA NPs under physiological conditions via FACS

RhdB labeled PLGA NPs were exposed to the same physiological conditions as described above. And the fluorescence intensity changes of RhdB labeled PLGA NPs were measured by FACS to assess the capability of the technique to follow changes in the fluorescent intensity due to the release of labeled PLGA out of the NPs.

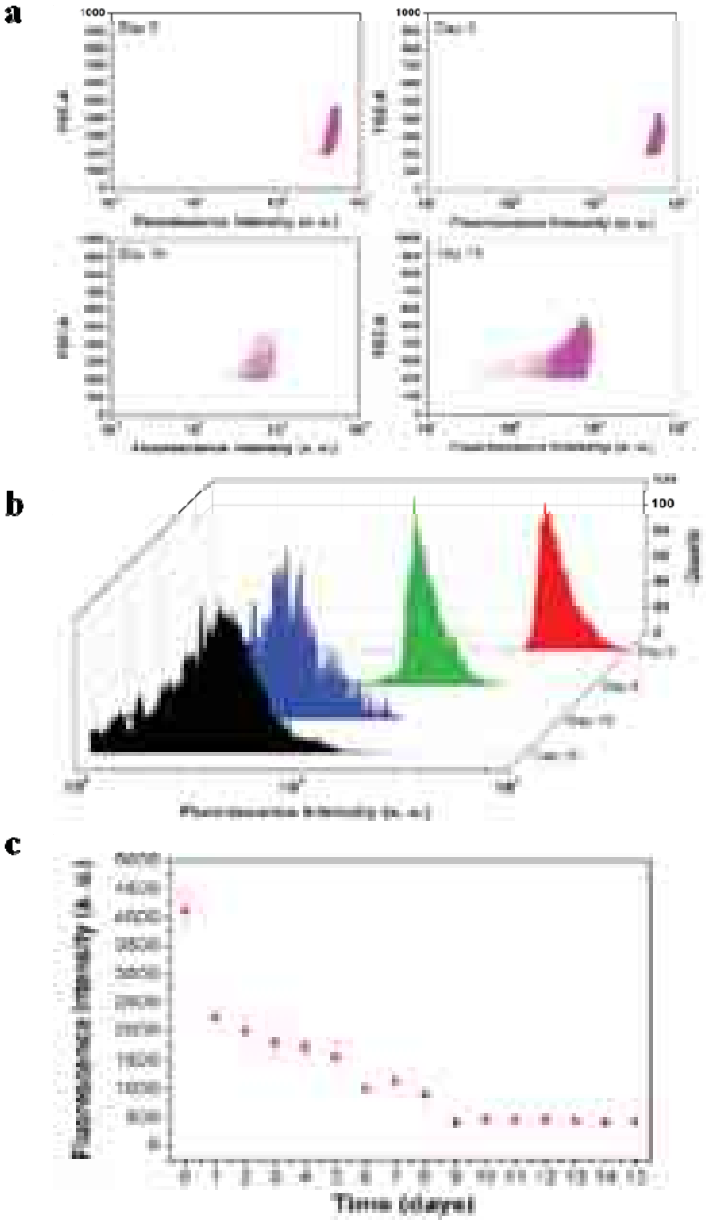

Figure 4.6 *(a) Forward Scatter (FSC) vs. Fluorescence Intensity dot plot, (b) Fluorescence Intensity histogram as a function of time and (c) Plot of the Fluorescence Intensity Maxima over time for PLGA15 NPs undergoing exposure to physiological conditions.*

In ***Figure 4.6a***, the Forward Scattering (FSC) against Fluorescence Intensity is presented as a dot plot at different time points for PLGA15 NPs undergoing degradation in physiological conditions. The dot plot clearly shows a single population of events with a gradual decrease, up to 10-fold, in the fluorescence intensity over time. The changes in fluorescence intensity are more evident in the fluorescence intensity histograms shown in ***Figure 4.6b*** for initial conditions, and 5, 10 and 15 days after exposure to physiological conditions. Finally, in ***Figure 4.6c***, the fluorescence intensity maximum has been plotted as a function of time after 15 days under physiological conditions.

From the plot it can be clearly seen that after 10 days the intensity remained constant, most likely indicating that the release of labeled PLGA has ceased or progressed more slowly thereafter. After day 10 the intensity curve became broader but the position of the intensity maxima remained unchanged. As the PLGA NPs degrade, due to the release of degradation product, one would expect a decrease in fluorescence intensity since FACS measures fluorescence emanating from the particlesFluorescent molecules released into the sheath fluid will not be included as their FSC intensity will be very small which is below the threshold. The distributions in ***Figure 4.6b*** clearly show broadening over time. From a narrow distribution with intensity values between 30^3 and 80^3 a. u. on day 1, the distribution broadens to values between 10^2 and 20^3 a.u. after 15 days. The broadening of the fluorescence distribution becomes significant than after 10 days.

Prior to day 10 there is only a shift towards lower intensities compared to the maximum but the distribution remained narrow. This indicates that the NPs are degrading from the beginning but it is only after day 10 that there is a significant change in the structure that accounts for the broadening of the distribution. Interestingly, by day 10, in addition to the dropping of mean fluorescence intensity to ~400 a.u., the whole fluorescence intensity distribution curve shifted to the lower region that significantly below the minimum intensity shown by the NPs at the initial time (***Figure 4.6a a and b***). This means that all the NPs had degraded to a certain extent by day 10. Moreover, the broadening of fluorescence intensity after 15 days indicates the degradation went on after 10 days though there was no significant change of the mean fluorescence intensity. Some NPs underwent more degradation

than the others since the degradation is a heterogeneous progress, thus exhibited lower fluorescence intensity as shown in ***Figure 4.6a***.

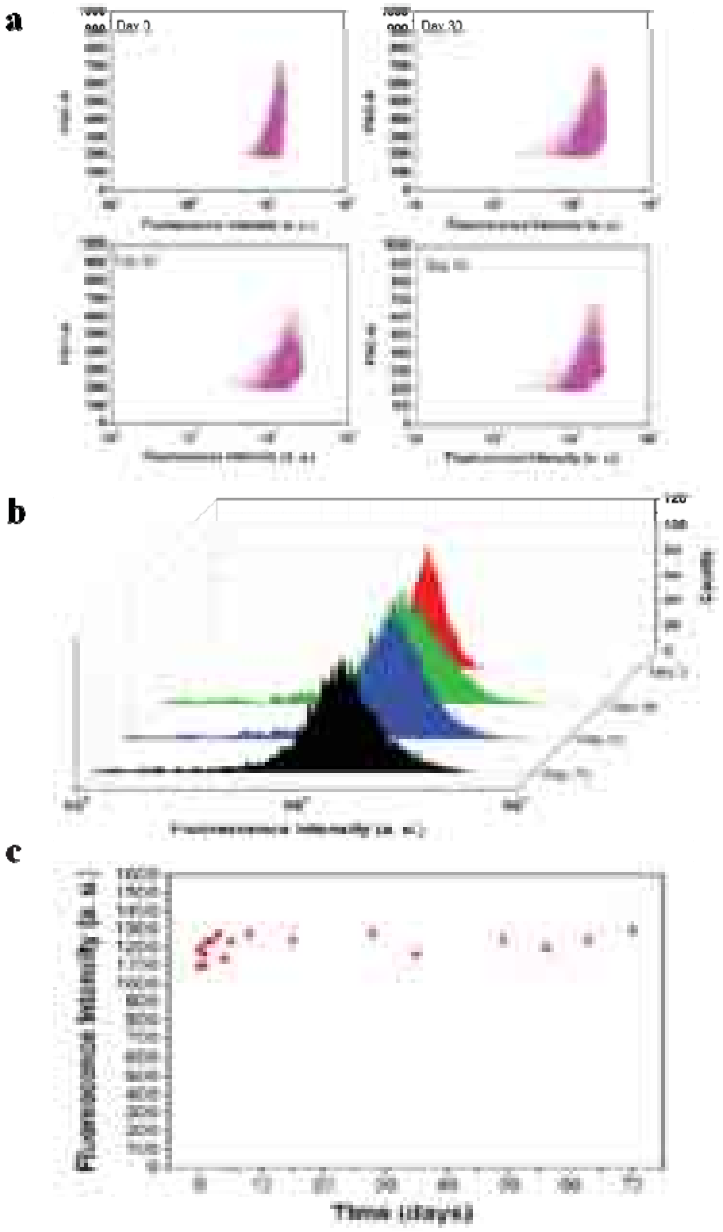

Figure 4.7 *(a) Forward Scatter (FSC) vs. Fluorescence Intensity dot plot, (b) Fluorescence Intensity histogram and (c) Fluorescence Intensity changes over time for PLGA35 NPs undergoing exposure to physiological conditions.*

The degradation of the RhdB labeled PLGA35 NPs in physiological conditions was also monitored by FACS. No significant changes in the intensity distribution over 70 days were observed. The maximum of the intensity distribution remains constant over 70 days as can be seen in ***Figure 4.7c***. The dot plot (***Figure 4.7a***) and the histogram (***Figure 4.7b***) corresponding to the initial time point, the final time point and two

intermediate time points of the experiment clearly showed that not only the maximum of the intensity remained constant but also the width of the distribution remained almost unaltered hinting that no labeled polymer has been released.

4.6 *'In vitro'* degradation of PLGA NPs

4.6.1 Study of '*in vitro*' degradation of PLGA NPs via FACS

Since that PLGA NPs are commonly used drug delivery vehicles, the study of their '*in vitro*' degradation profiles has great importance as it is directly associated with the intracellular drug release. In the experiments with PLGA particles under physiological conditions, if labeled PLGA molecules are released, the total amount of fluorescence per particle measured is also reduced. This could be easily traced by FACS. Nevertheless, in the cell population, this is not the case. If the NPs have been internalized by the cells, their products of degradation will not necessarily be released from the cell. If the NPs degrade and both the remains of the NPs and their products are retained in the cell, the total fluorescence should not vary. In this case, flow cytometry should not show any change in the fluorescence intensity distribution.

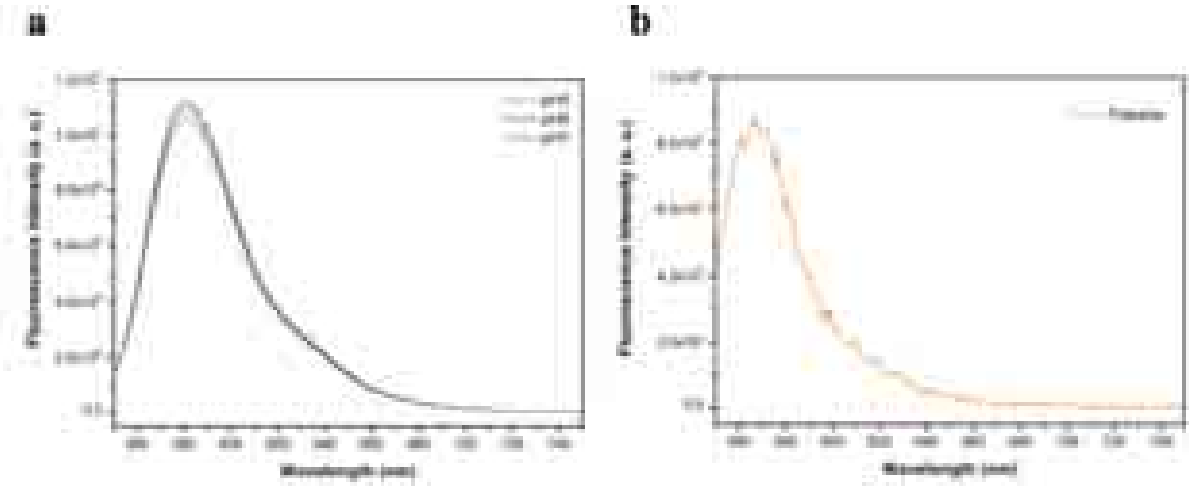

Figure.4.8 *Emission spectra of RhdB solutions at 4×10^{-6} M in: (a) aqueous media at different pH and (b) in toluene.*

Rhodamine B (RhdB) was chosen as a label to account for this problem. RhdB is known to increase fluorescence upon changing from non polar organic solvents to aqueous solution [304,305]. The quantum yield of RhdB varies significantly from a non polar environment, such as the interior of the PLGA NPs, to an aqueous

environment, especially at low pH as in the acid environment found in lysosomes or the cytoplasm. Emission spectra of RhdB in different environments are provided in ***Figure 4.8***. We can observe that in a non polar solvent like toluene the fluorescence intensity was around $9x10^3$ a.u.(***Figure 4.8a***), but when the dye was dissolved in water the intensity increases to $1.1x10^7$ a.u.(***Figure 4.8b***).

The PLGA NP degradation inside HepG2 cells was investigated by FACS. Degradation of NPs was studied via changes in fluorescence intensity of RhdB labeled PLGA present in PLGA15 or PLGA35 NPs upon uptake by the cell. NPs were exposed to the cells as following: HepG2 cell line was cultured in DMEM with 10 % FBS and 1000 U penicillin, 10 mg mL^{-1} streptomycin at 37 ºC and in 5 % CO_2. When the cell confluence was around 70 %, all the cells were trypsinized. 100 000 cells were seeded into each well of a 24-well plate. 24 h later, fluorescent PLGA NPs (PLGA15 or PLGA35 NPs) were added into the culture media at a final concentration of 100 μg mL^{-1}. After 24 h of incubation, the NPs were removed and replaced with fresh culture media. Finally, at different time intervals, the cells were washed with PBS twice, trypsinized and studied via Flow Cytometry (BD FACS Canto II). The fluorescence intensity measured per cell corresponds to the amount of fluorescent NPs associated with the cell.

In ***Figure 4.9a*** we see the mean fluorescence intensity dot plot of HepG2 cells exposed to PLGA15 NPs measured after 12, 24 and 72 h after removing the NPs. From the dot plot it is possible to distinguish that the cell population became not only more confined but also has higher fluorescence intensity over time. The increase in fluorescence intensity can be observed more readily in the histogram of ***Figure 4.9b***. First, a sample of HepG2 cells which were not exposed to PLGA15 NPs, with a mean fluorescence intensity value of 43 a.u., was used as a control. Then, the fluorescence intensity after incubation and removal of the PLGA15 NPs increases to 85 a.u. at 12 h, 155 a.u. at 24 h and 175 a.u. at 72 h. The stepwise increment in fluorescence intensity of PLGA15 NPs inside HepG2 cells is represented in ***Figure 4.9c***.

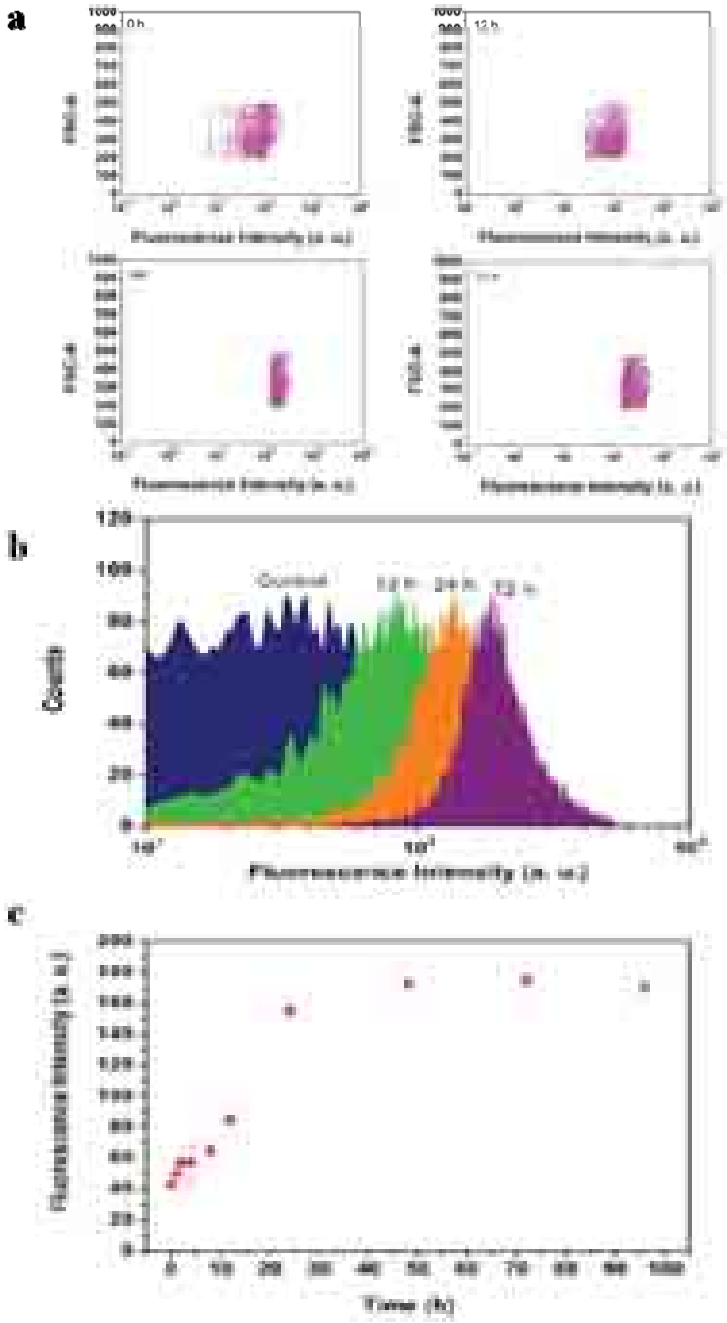

Figure 4.9 *(a) Forward Scatter (FSC) vs. Fluorescence intensity dot plot, (b) Fluorescence intensity histogram and (c) Fluorescence intensity changes over time for PLGA15 NPs undergoing degradation inside HepG2 cells.*

The observed increase in RhdB fluorescence intensity with time, which reflects that the amount of fluorescence associated within the cell is higher at longer time intervals, can be explained by a NPs degradation process. PLGA NP uptake occurs relatively quickly with 90 % uptake after 24 h of incubation, mainly via endocytosis pathways,

in which PLGA NPs preferably colocalize within the endosomes and lysosomes of the cell [293,306–310].

The different compartments of the cell exhibit different pH values. Endosomes and lysosomes are acidic organelles, in which endosome has a pH value around 6 [310] and lysosomal pH value varies between 4.3 and 4.5 [311]. The increment of RhdB fluorescence intensity suggests either, unfolding of the PLGA15 NPs or the breaking of the copolymer chains, resulting in RhdB molecules being directly exposed to the acidic pH of the endosomes and lysosomes of the HepG2 cell, resulting in a protonation of the RhdB molecules and therefore an increase in their fluorescence intensity. After 24h of incubation, the RhdB fluorescence remained almost constant. The broad fluorescence distribution at the beginning can be attributed to the fact that there were both RhdB molecules inside the PLGA NPs and on the surface of NPs which exposed to the cell interior initially.

In this scenario, it is possible to find RhdB molecules with fluorescence with two quantum yields, that accounts for NPs with low intensity (not fully degraded) and NPs with higher intensity (more degraded). At later times, most of the RhdB will be in the degraded state and the fluorescence should be coming from molecules with the similar quantum yields. Since the maxima of the intensity reached a constant value after 24 h, it can be interpreted that the degradation rate of PLGA NPs reached a limit after 24h compared to the initial rapid degrading within 24h, and the degradation process became extremely slow afterwards. The intracellular degradation process seems to be much faster than in the physiological buffer. This is to be expected because enzymes in the cell can contribute to the degradation of PLGA. The time scale for experiments involving cells and also differs greatly. Experiments over 4 days with a cell population are not feasible while in physiological condition we have extended up to 70 days.

PLGA35 NPs coincubated within HepG2 cells were also followed by monitoring the RhdB fluorescence intensity changes via flow cytometry. ***Figure 4.10a*** displays the fluorescence intensity distribution dot plot after 24 h, 72 h and 120 h after NP incubation. ***Figure 4.10b*** shows the fluorescence intensity histograms for the same time intervals, and ***Figure 4.10c*** shows the changes of the mean fluorescence intensity

during different time intervals. Changes in the fluorescence intensity of RhdB were not observed in the 120 hours after PLGA35 NPs incubation with the cells.

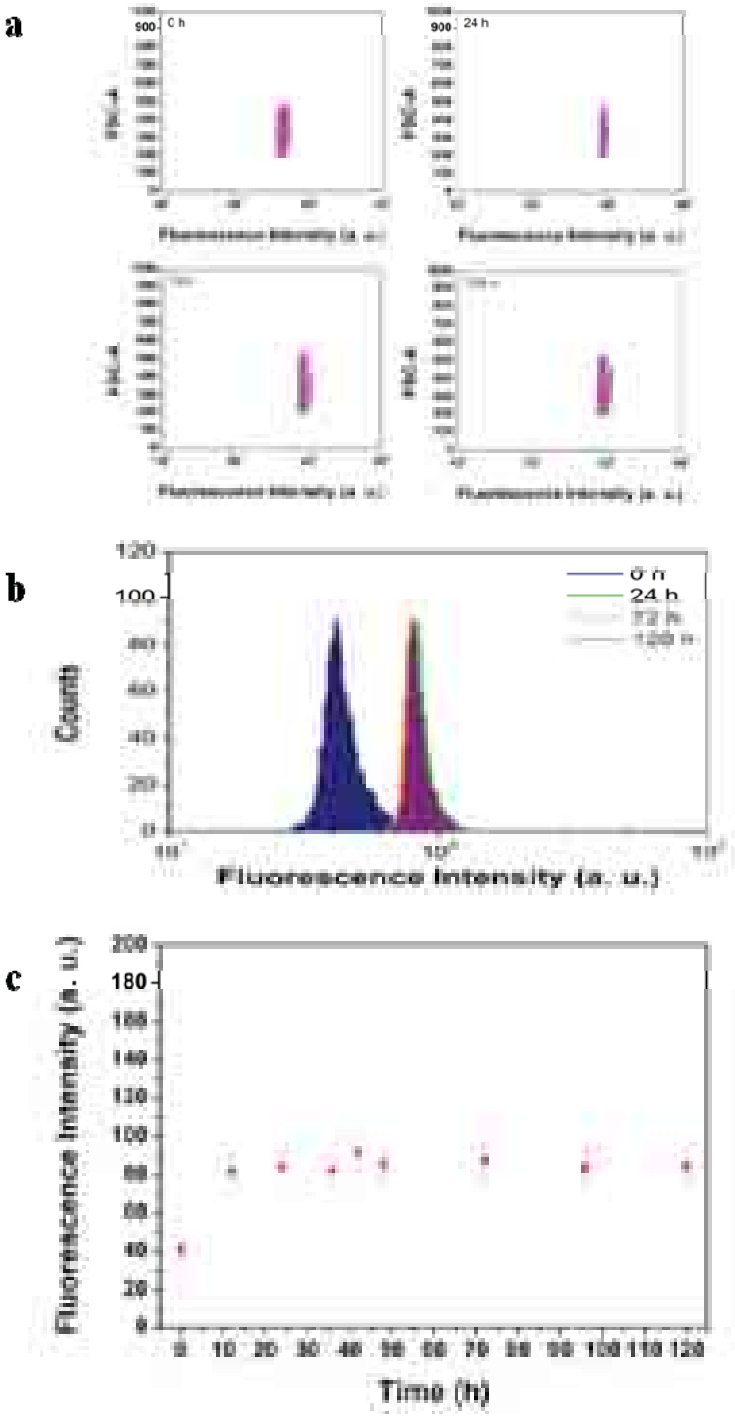

Figure 4.10 *(a) Forward Scatter (FSC) vs. Fluorescence intensity dot plot, (b) Fluorescence intensity histogram and (c) Fluorescence intensity changes over time for PLGA35 NPs undergoing degradation inside HepG2 cells.*

4.6.2 Study of '*in vitro*' degradation of PLGA NPs via Raman Confocal Microscopy (CRM)

In addition to the FACS study with labeled PLGA NPs, the intracellular degradation of unlabeled PLGA NPs was also following with CRM as in the work of Van Apeldoorn et al [126].

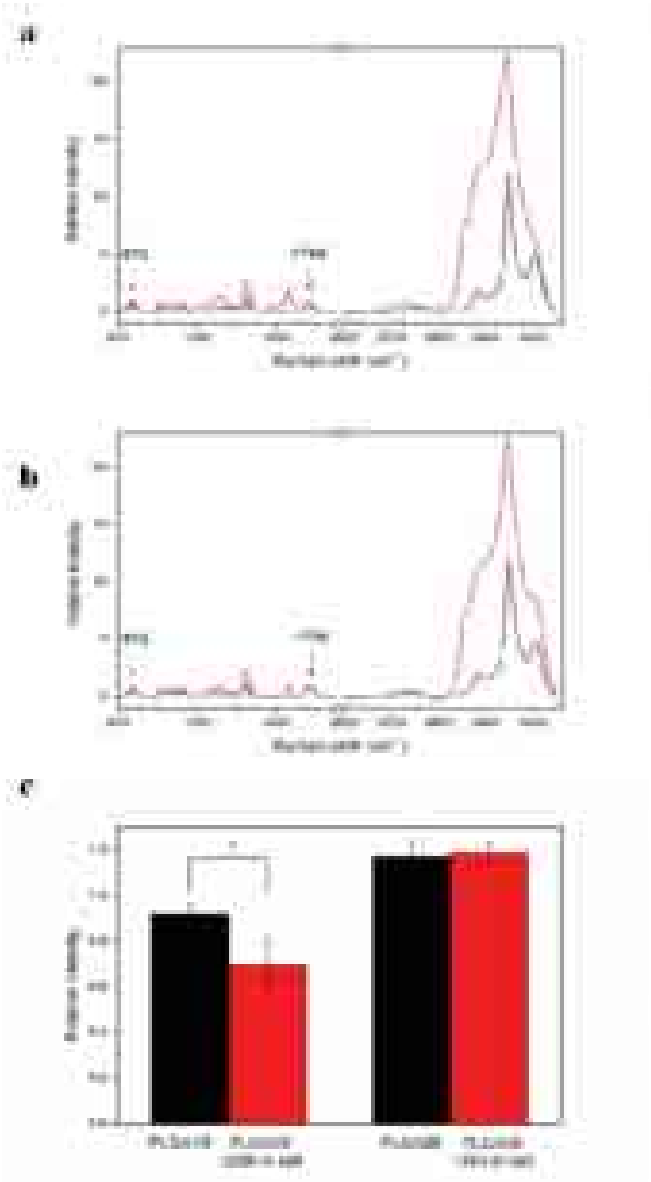

Figure 4.11 *Raman spectra of (A) PLGA15 pure NPs (black), incubated with HepG2 for 120h (red) (scaled to 872 cm^{-1} band), (B) PLGA35 pure NPs (black), incubated with HepG2 for 120h (red) (scaled to 875 cm^{-1} band), (C) the relative intensity at 1768cm^{-1} (scaled to 872 cm^{-1}) between pure PLGA NPs and PLGA NPs in cells after 120h incubation (the average value is from 6 spectra collected from 6 different cells), * indicated a significant difference ($p<0.05$).*

In the CRM experiments, 100,000 HepG2 cells were firstly seeded in a 35 mm glass bottom petri dish. 24 h later, PLGA NPs (PLGA15 or PLGA35 NPs) were added into the culture media at a final concentration of 100 μg mL-^{1}. After 24 h of incubation, the NPs were removed and replaced with fresh culture media. After 120 h of incubation, the petri dish was rinsed with PBS several times and the cells were fixed with 3.7% formaldehyde in PBS at 4 °C for 30 minutes, and then rinsed again to remove excess formaldehyde.

The CRM study was performed by a Renishaw inVia Raman Microscope with a 532 nm laser as excitation source and a grating of 1800 mm^{-1}. Spectra were taken using a 40× water immersion objective. The size of the focal spot was approximately 1 μm. Raman spectra were recorded over the range 800-3200 cm^{-1} with a resolution of approximately 7 cm^{-1}. The system was calibrated to the spectral line of crystalline silicon at 520.7 cm^{-1}. All spectra were corrected taking into account the PBS solution and glass coverslip baseline.

In ***Figure 4.11*** the Raman spectra of PLGA15 NPs (***Figure 4.11a***) and PLGA 35 (***Figure 4.11b***) in PBS and inside HepG2 cells after 5 days of incubation are shown. In the spectra, two bands were highlighted: the bands at 1768 cm^{-1} and at 872cm^{-1}.The band present at 1768 cm^{-1} is assigned to C=O vibration of the ester group of PLGA. As degradation takes place, the hydrolysis of the ester should decrease the intensity of the band at 1768 cm^{-1}. The 872 cm^{-1} band is assigned to the C-COO vibration of lactic acid. This band will not be affected by the hydrolysis process during the degradation [312]. The average relative intensities at 1768 cm^{-1} of PLGA NPs before and after incubation with cells were compared as seen in ***Figure 4.11c***. After 5 days of incubation with HepG2 cells, the PLGA15 NPs showed a decrease in intensity for the ester group as demonstrated by the relative decrease of the 1768 cm^{-1} band. On the contrary, the PLGA35 NPs do not show a significant change change in the relative intensity of this band. The results from Confocal Raman Microscopy confirm the FACS data.

Chapter 5

Design of Hybrid Multimodal PLGA Polymeric Nanoparticles for Neutrophil Labeling, Imaging and Tracking

---

5.1 Motivation and background

Neutrophils are the most abundant leukocytes in human body and as an integral part of the innate immune system, they play a key role in the elimination of bacterial pathogens [313]. They are the first responders to tissue damage and migrate immediately to the inflamed tissues [313,314]. Neutrophils also take part in immune system cross-talk by interacting with monocytes, dendritic cells, natural killer cells and macrophages. Moreover, the importance of neutrophils in cancer, and in autoimmune diseases now begins to emerge [315]. Due to the diversity of roles the neutrophils play in the human body, it is of great interest to understand the spatio-temporal aspects related to neutrophil recruitment to the site of infection and inflammation. This will potentially be beneficial for disease diagnosis and monitoring of the effect of drugs and therapeutic agents.

In this direction, approaches focused on magnetic resonance imaging (MRI), photoacoustic imaging, X-ray computed tomography and optical imaging techniques are currently being developed [316–318]. These techniques often rely on formulations based on nanoparticles (NPs) such as iron oxide, colloidal gold (Au) and quantum dots (QDs) among others [318–321]. There is a growing interest in the development of novel multimodal NPs for *in vivo* applications. However, due to limitations related to toxicity, non-specific targeting and undefined interactions at bio-interfaces of metallic NPs and semiconductor QDs, new engineering strategies are currently being implemented by creating hybrids using biocompatible materials.

As one of the most widely used polymers in drug delivery field, PLGA has good

biocompatibility and biodegradability which has been approved by the US Food and Drug Administration [322] . Therefore, it is reasonable to use PLGA as a polymeric base to create a hybrid NPs which entrapped QDs and superparamagnetic iron oxide nanoparticles (SPIONs) that can meet different needs.

The use of a polymer matrix, i.e. PLGA particles, as carrier for the SPIONs could have several advantages including the possibility to control or at least significantly reduce SPION aggregation in biological fluids, a common phenomenon resulting from the interaction of NPs with proteins and other biomolecules [323,324]. Aggregation of SPIONs before reaching the target cells/tissues or upon their intracellular delivery influences their magnetic properties and consequently their applicability in MRI [323]. By encapsulating the SPIONs in an organic matrix and carefully controlling the encapsulation conditions, the state of aggregation of the SPIONs can be controlled. Moreover, a localized concentration of SPIONs can be achieved by encapsulating them into PLGA NPs, a critical parameter for creating enhanced contrast in MRI applications. Using PLGA NPs for QDs encapsulation would provide a way to reach a sufficient circulation time avoiding release of toxic agents *in vivo* while keeping the optical properties of the QDs [325]. The assembly of the Au NPs on the surface of the PLGA NPs can generate a high concentration of Au NPs that can be used for the production of localized heat in photothermal therapies applied in cancer treatment.

A hybrid PLGA NPs carrying and Au NPs would combine the properties of all these nanomaterials in one composite multimodal nanoparticle. Therefore, they could be applied for imaging, tracking and manipulating transplanted neutrophils *in vivo*. Besides the potential *in vivo* tracking of neutrophils, the hybrid multimodal NPs can serve in cell sorting using an external magnetic field. Moreover, it is known that neutrophils are recruited by certain tumors [326]. Hybrid multimodal PLGA NPs loaded into neutrophils can be used to promote particle accumulation in the tumor, facilitating diagnosis by MRI or fluorescence imaging and monitoring anti-tumor therapies. Furthermore, the Au NPs in the hybrid NPs could then be used for localized photothermal treatment, for enhancement of drug release and to direct the hybrid NPs intracellularly through their modificatication with thiols.

In this chapter, a hybrid PLGA NPs incorporating QDs, superparamagnetic iron oxide nanoparticles (SPIONs) and Au NPs for neutrophil labeling were fabricated via the w/o/w double emulsion method. QDs and SPIONs were entrapped in the PLGA core during emulsification while Au NPs were assembled on top of the PLGA NPs *via* electrostatic interactions. Transmission Electron Microscopy (TEM), Scanning Electron Microscopy (SEM) and Confocal Scanning Laser Microscopy (CSLM) were applied to characterize the hybrid PLGA NPs. Magnetic Resonance Imaging (MRI) of the hybrid PLGA NPs resulted in images with a contrast enhancement linearly dependent on the concentration of the hybrid PLGA NPs. The uptake of the hybrid PLGA NPs by human neutrophils was studied by flow cytometry (FACS) and CSLM. In addition, the induction of reactive oxygen species (ROS) in neutrophils after incubation with the hybrid PLGA NPs was assessed. Magnetophoresis experiments showed that neutrophils with internalized hybrid PLGA NPs can be effectively laterally displaced towards magnetic field.

5.2 Synthesis of core-shell silica coated superparamagnetic iron oxide nanoparticles (SPIONs)

1.5 g of Iron (III) chloride hexahydrate and 3.5 g of sodium oleate were dissolved in a solvent mixture containing 14mL hexane, 8 mL ethanol and 6 mL deionized water. The solution was heated up to 75 °C in an oil bath for three hours under continuous stirring. The resulting iron-oleate complex was obtained by washing the organic phase with deionized water. To prepare SPIONs, 3.5 g iron oleate complex and 0.5 of oleic acid were dissolved in 20 g 1-Octadecene and the mixture was heated up to 300 °C for 60 min. The resulting brownish suspension of oleic acid coating iron oxide NPs were collected by centrifugation at 10,000 g for 30 min and was suspended in chloroform. Next, the oleic acid capped iron oxide NPs suspension in chloroform was mixed with an aqueous solution of cetyltrimethyl ammonium bromide and the mixture was heated up to 65 °C with vigorous stirring for 2 hours in order to evaporate the chloroform. Upon cooling, the pH of the NP suspension was raised to 12.0 by adding sodium hydroxide. Next, a mixture of tetraethyl orthosilicate:ethyl acetate (1:4) was added to the suspension and kept under continuous stirring at 75 °C for 6 hours. Silica coated

iron oxide NPs were collected by centrifugation and washed three times in ethanol ammonium nitrate to remove residual cetyltrimethyl ammonium bromide. The resulting SPIONs were about 25 nm in size (*see in* ***Figure 5.2D***).

5.3 Preparation of hybrid multimodal PLGA NPs and self-assembly of Au NPs on the surface of PLGA NPs

Hybtid PLGA NPs were prepared by w/o/w double emulsion solvent evaporation method [327]. 20mg·mL^{-1} PLGA was dissolved in dichloromethane. 2 μL QDs (8μM) and 5 μL SPIONs (10mg/mL) were dispersed in water and sonicated for 5 min in a bath sonicator to obtain a homogeneous dispersion. The dispersion was added to 500 μL PLGA solution (organic phase) and emulsified by an ultrasonicator for 1 min. The emulsion was then mixed with 8mL, 5% polyethylenimine (PEI) and emulsified by ultrasonication for 1 min to form the second emulsion. The second emulsion was added dropwise into 100 mL deionized water for 3 hours to allow the organic solvent to evaporate completely. PLGA NPs were collected by centrifugation at 10,000 g for 5 min and washed four times with deionized water.

The w/o/w double emulsion solvent evaporation method [327] provides a facile route to encapsulate water soluble drugs inside polymer as well as small hydrophilic NPs. As shown in ***Figure 5.1***, QDs and SPIONs were first homogenously dispersed in deionized water and then added into the PLGA hexane solution (organic phase).

QDs and SPIONs were entrapped in small water drops suspended in the organic phase via sonication to obtain the primary w/o emulsion. The secondary w/o/w emulsion was formed by adding the primary emulsion into a continuous aqueous phase of PEI. The PEI molecules behave as emulsifying agent stabilizing the organic droplets. After solvent evaporation, PEI molecules remain forming a stable thin layer on the surface of the PLGA particle [328,329].

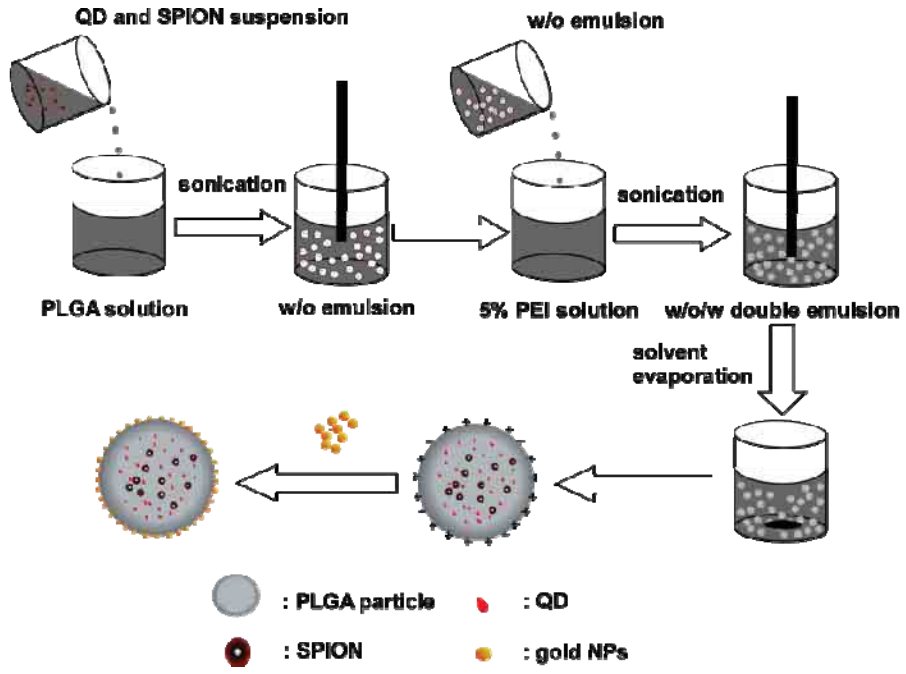

Figure 5.1 *Schematic of the preparation of hybrid multimodal PLGA NPs.*

For further Au NPs self-assembly on the surface of hybrid PLGA NPs, 5 mg PLGA NPs containing QDs and SPIONs were mixed with 1 mL citrate-stabilized Au NPs ($5.5x10^{13}$ particle/mL). The negatively charged Au NPs were assembled on the positively charged PLGA NPs via electrostatic interactions. The mixture was then incubated for 2 hours at room temperature. PLGA NPs were then collected by centrifugation at 10,000g for 5 min and washed five times with deionized water.

5.4 Characterization of Hybrid PLGA NPs

Transmission Electron Microscopy (TEM) and Scanning Electron Microscopy (SEM) were used to observe the morphology of hybrid NPs. For TEM measurement, 2.5 µL suspension of hybrid PLGA NPs were dropped to a TEM copper grid with carbon film. Samples were left in a vacuum chamber to let the water evaporate completely and then measured with a JEOL JEM-2100F TEM at 200 kV. For SEM experiment, 1 µL suspension of hybrid PLGA NPs were dropped to a silicon chip (Plano GmbH, Wetzlar, Germany), stained with 2% OsO4 in PBS buffer for 12 hours to make PLGA conductive, washed with water, dried and finally examined with a Zeiss Supra 40 VP SEM at 75000-150000 X magnification (5 kV).

Dynamic Light Scattering (DLS) and ζ-potential measurements were performed to characterize the hydrodynamic sizes and surface charge properties of hybrid NPs. For DLS measurements, 10 μg hybrid PLGA NPs were well suspended in 1mL deionized water and the hydrodynamic size were measured with a NanoSizer (MALVERN Nano-ZS). The ζ-potential of hybrid PLGA NPs was measured on the samples characterized by DLSusing a cell drive voltage of 30V. All measurements were performed in 10 mM NaCl at 25 °C.

Sample	Average size (nm)	ζ-potential (mV)
PLGA_QD_SPION NPs	677.5±132.5	49.8±1.0
PLGA_QD_SPION_Au NPs	891.7±25.6	-14.5±1.19

Table 5.1 *Hydrodynamic size and ζ-potential of hybrid NPs.*

Figure 5.2A shows a representative TEM image of PLGA NPs with encapsulated SPIONs and QDs (PLGA_QD_SPION NPs). The PLGA NP in the image has a size of 250-300 nm. DLS experiments showed an average hydro dynamic size of 677.5±132.5 nm for the PLGA_QD_SPION NPs (**Table 5.1**). In ***Figure 5.2A*** we can also appreciate a smooth polymer shell on the surface of the PLGA NPs coming from PEI. The positive zeta potential: + 49.8 ± 1.0 mV (**Table 5.1**) is consistent with the charge of the PEI. The SPIONs and rod-like QDs inside the PLGA NPs in ***Figure 5.2A*** can be recognized by their sizes, 25 and 15 nm, respectively. TEM images of both SPIONs and QDs are also shown in ***Figure 5.2C*** and ***D***. The inset in ***Figure 5.2A*** shows a magnified region of the PLGA NPs. The white and yellow arrows in the magnified figure indicate the SPIONs and QDs, respectively.

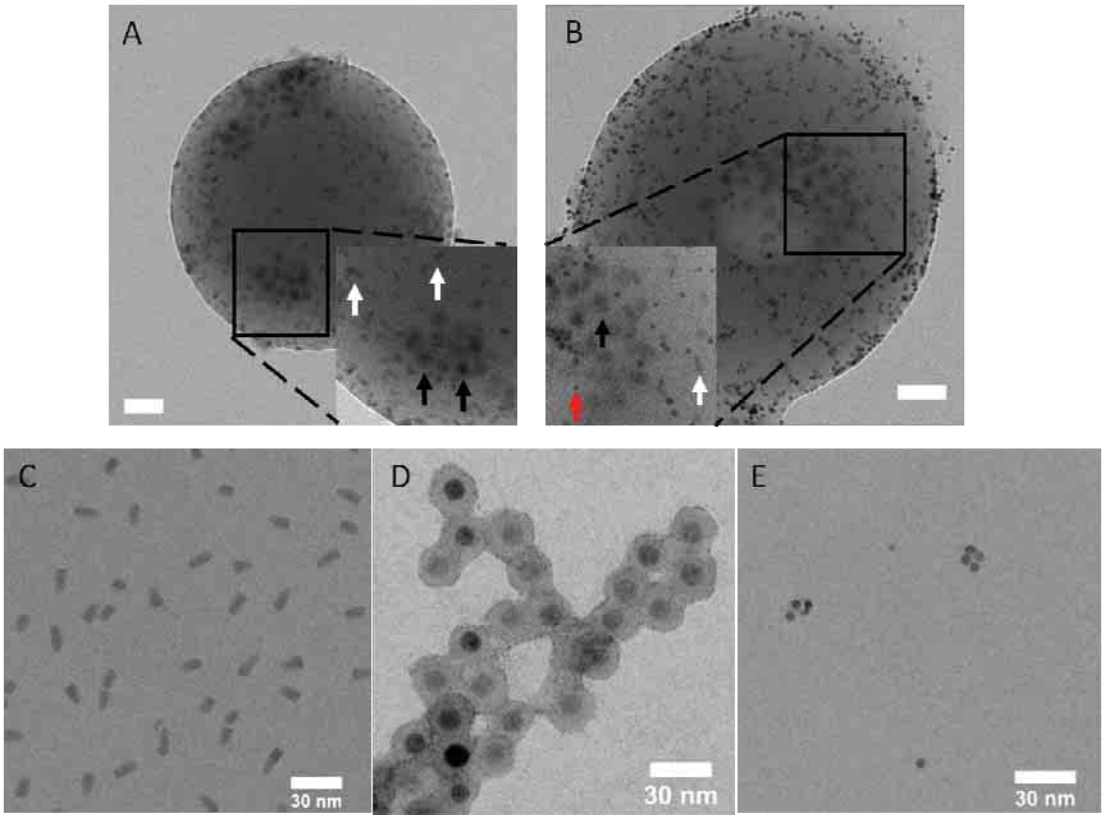

Figure 5.2 *(A) TEM image of PLGA NPs incorporating QDs and SPIONs (PLGA_QD_SPION NPs), scale bar 50 nm. White arrows indicate QDs, yellow arrows indicate SPIONs. The inset is the magnification of the corresponding marked area (B) TEM image of PLGA NPs incorporating QDs and SPIONs and functionalized with Au NPs on their surface (PLGA_QD_SPION_Au NPs), scale bar 50 nm. The inset is the magnification of the corresponding marked area in the main image. White arrows indicate QDs, yellow arrows indicate SPIONs, and red arrows indicate Au NPs, (C)QDs ,scale bar 30nm; (D)SPIONs, bar 30nm ;(E)Au NPs, bar 30nm.*

Some clustering of the NPs inside PLGA could be observed, mostly restricted to the SPIONs. In any case, the clusters do not include more than 10 SPIONs together. The size of the clusters of SPIONs is significantly smaller than that of the SPION aggregates in cell media.

The TEM image (***Figure 5.2B***) corresponds to the hybrid PLGA NPs after the assembly of the Au NPs. Gold NPs were assembled on the surface and not inside the PLGA particles because gold can act as a quencher for the quantum dots diminishing

their fluorescence emission as shown by Pons T. et al.[330], and Zhang J. et al[331]. Having both the QDs and AuNPs confined inside the PLGA NPs could significantly reduce particle fluorescence. To avoid this, the AuNPs were assembled on top of the PLGA NPs.

The Au NPs were recognized by their size (5 nm) and round shape (***Figure 5.2E***), and are indicated in the magnified image with red arrows (***Figure 5.2B***). The assembly of the Au NPs changed the zeta potential of the PLGA NPs from a positive value to a negative value of -14.5±1.19 mV, as shown in ***Table 5.1***, which is consistent with the charge of the Au NPs.

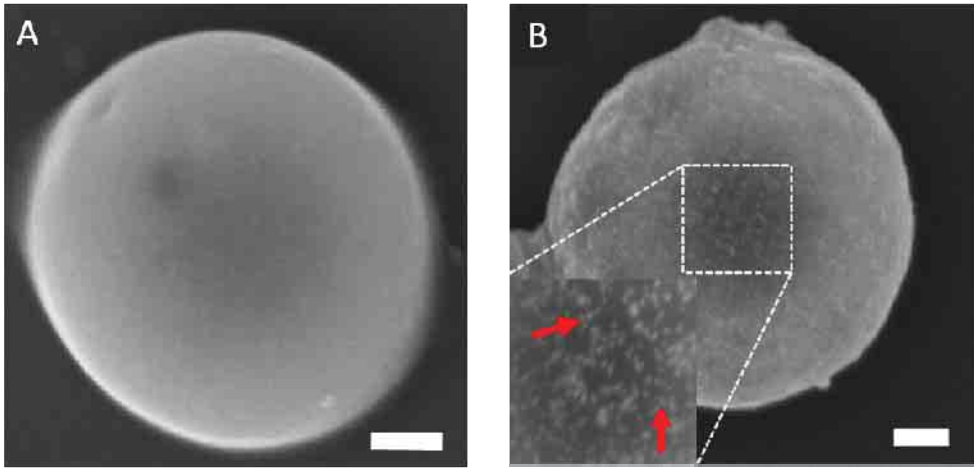

Figure 5.3 *SEM image of (A) PLGA_QD_SPION NPs, (B) PLGA_QD_SPIO_Au NPs scale bar corresponds to 100nm.*

SEM was applied to prove the localization of the Au NPs on the surface of PLGA_QD_SPION_NPs as it can be seen in ***Figure 5.3***. The Au NPs could be recognized as well by their size. PLGA NPs without Au NPs shows a smooth surface (***Figure 5.3A***). While after assembly of Au NPs, the hybrid NPs exhibit a rougher surface with the coating of small NPs on the top with the sizes of around 5nm which can be recognized as Au NPs. The Au NPs form a dense coating on the PLGA as can be seen in the magnified section of image in ***Figure 5.3B*** and small clusters of a few Au NPs can be seen as well. Additionally, some SPION NPs can be observed in the surface of the PLGA_QD_SPION_with Au NPs (PLGA_QD_SPION_Au NPs). These seem to have remained at the o/w interface during NP preparation.

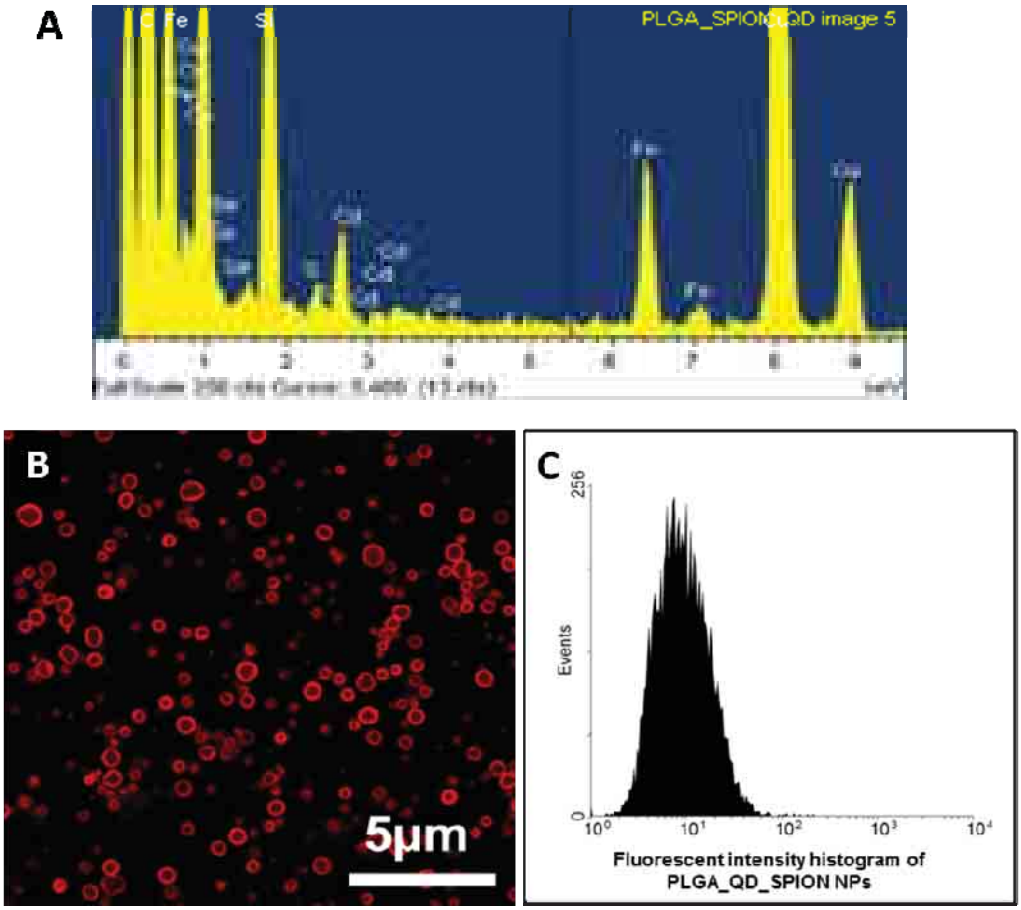

Figure 5.4 *(A) EDX spectrum of PLGA_QD_SPION NPs SPIONs; (B) CLSM image of PLGA_QD_SPION NPs; (C) Fluorescence intensity histogram of PLGA_QD_SPION NPs measured with flow cytometry.*

To further confirm the incorporation of QDs and SPIONs with PLGA NPs, EDX characterization was performed along with TEM. The signals from elemental cadmium and iron confirmed the nature of the encapsulated nanomaterials (***Figure 5.4***A). The hybrid PLGA NPs are fluorescent as result of the encapsulation of QDs, as it can be seen in the CLSM image (***Figure 5.4B***). The encapsulation of QDs in PLGA NPs was studied by flow cytometry. The histogram of fluorescence intensity versus number of PLGA NPs in ***Figure 5.4C*** shows a homogenous distribution with a narrow peak. The distribution curve is almost symmetrical, meaning that all PLGA NPs have QDs encapsulated and the distribution of loaded QDs is narrow

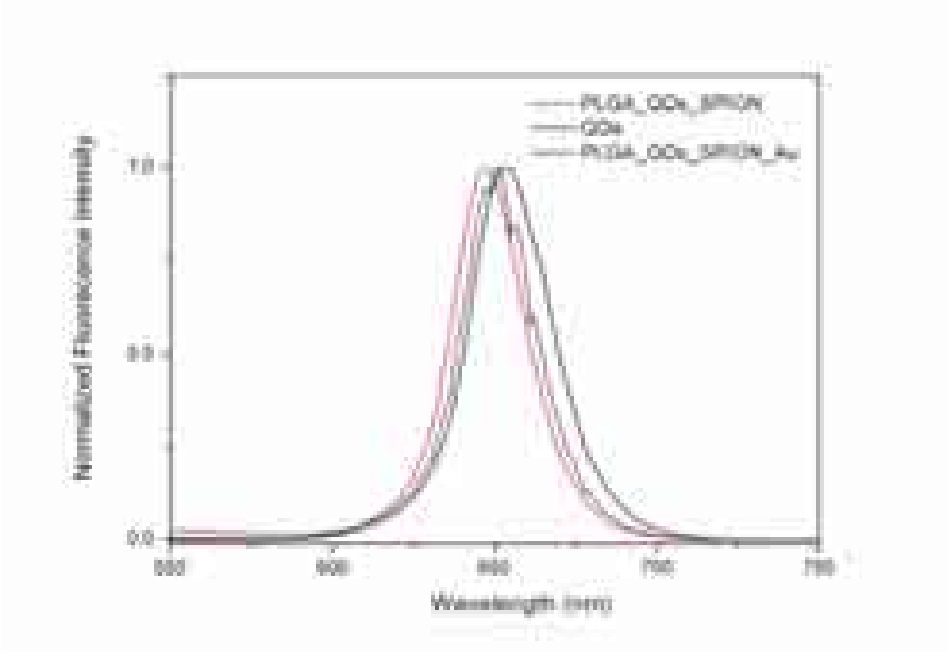

Figure 5.5 *Fluorescence emission spectra of hybrid Nps and QDs.*

The emission spectra of hybrid PLGA NPs were measured in nanopure water with excitation wavelength at 530 nm. The emission spectra of the hybrid PLGA NPs is similar to the spectrum of QDs with an intensity maximum at 650 nm slightly shifted from the spectra of the QDs (***Figure 5.5***). This indicates that the hybrid NPs retain the fluorescence property of QDs.

The final concentration of Au, Fe and Cd in the hybrid PLGA NPs has been estimated by Inductively Coupled plasma Atomic Emission Spectroscopy (ICP-AES).

Data shows concentration of 7.8×10^{-3} (Au), 1.6×10^{-3} (Fe) and 1×10^{-3} (Cd) mg/mg hybrid PLGA NPs. These values indicate that the concentrations/ratios of the AuNPs, SPIONs and QDs are of the same order of magnitude.

5.5 PLGA_QD_SPION NPs as T2 contrast agents in Magnetic Resonance Imaging (MRI)

The MRI mechanisms are based on excitation and relaxation of hydrogen nuclei that are abundant in water and lipids of tissue. Intrinsic longitudinal (T1) and transverse (T2) relaxation times of different parts of the tissues bring about changes of MR signal intensity and give imaging contrast. The relaxation times can be manipulated

using T1 and T2 contrast agents, which give brighter (T1-weighted) and darker (T2-weighted) images when they are accumulated. Gadolinium or manganese chelates are commonly used T1 contrast agents and iron oxide NPs are common T2 contrast agents [332].

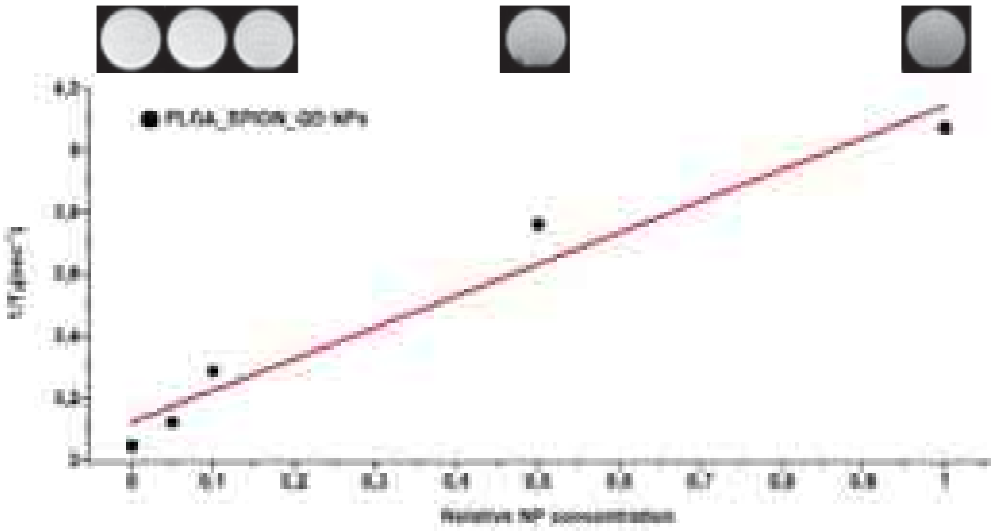

Figure 5.6 *Spin-spin relaxation time (T2)-weighted spin-echo versus relative PLGA_QD_SPION NPs concentration.*

To evaluate the possible application of the hybrid PLGA NPs in MRI imaging, especially as T2 contrast agents, T_2-weighted spin-echo time versus PLGA_QD_SPION NPs concentration were measured by MRI. In MRI measurements, all samples were placed inside a 50 mL centrifuge tube. 30 mL of 2% agarose water solution (60 °C) were poured into the tube taking care of avoiding bubbles. The tube was then cooled down. Samples were scanned in MRI with a 7T MR scanner (Bruker Biospec). T2-weighted spin-echo MRI images were acquired at echo time of 260 ms.

The MRI images at the top of ***Figure 5.6*** correspond to the different concentration of PLGA employed. Images are presented following their sequential increase in concentration. The red line is the linear fit of the data points. The relative concentration 1 corresponds to 10 mg/mL PLGA_QD_SPION NPs in water, the 0 value corresponds to deionized water. From the $1/T_2$ versus NPs concentration function, we can see that $1/T_2$ increased with the concentration of PLGA NPs. The

corresponding images have an enhanced MRI contrast with increased PLGA NP concentration. The enhanced MRI contrast shown by the PLGA NPs is a requisite in their application for *in vivo* imaging.

5.6 Cellular uptake of the PLGA particles by neutrophils

To study the imaging and tracking of neutrophils, cell uptake experiments were performed by exposed hybrid PLGA NPs to neutrophils in a certain time interval.

Neutrophil used in the experiments are isolated from heparinized blood collected from healthy human donors. After dextran sedimentation, neutrophils were isolated from the supernatant leukocyte-rich plasma by Ficoll-Hypaque gradient centrifugation. Red blood cells were lysed with ammonium chloride solution. 100 μL RPMI 1640 medium with 200,000 neutrophils and 100 μL of the solution of hybrid PLGA NPs (with and without Au NPs, 2mg/mL) were mixed well in a 0.5 mL Eppendorf tube and further co-incubated at 37 °C at 500 rpm shaking speed on a horizontal shaker.

The cell uptake was studied using a BD LSRII flow cytometer. The fluorescence from the neutrophils after NP uptake was detected through Qdot 655 channel (Longpass:630nm, Bandpass:655±5 nm) using the 405 nm laser for excitation. All events corresponding to the control sample were located at intensities below this threshold. Each experiment was set to count 10,000 events per run and each run was recorded using identical measurement parameters. The number of cells carrying fluorescently labeled NPs is obtained from the area corresponding to the events located at higher intensities than the threshold. The cellular uptake ratio was calculated as the (No. of events over the threshold/total No. of events) × 100%. The fluorescence intensity was set as the mean fluorescence intensity vs cell number distribution. The uptake of NPs by neutrophils was also studied using an Olympus FLUOVIEW FV1000 CLSM. The membranes of neutrophils were stained with Oregon green 488 DHPE.

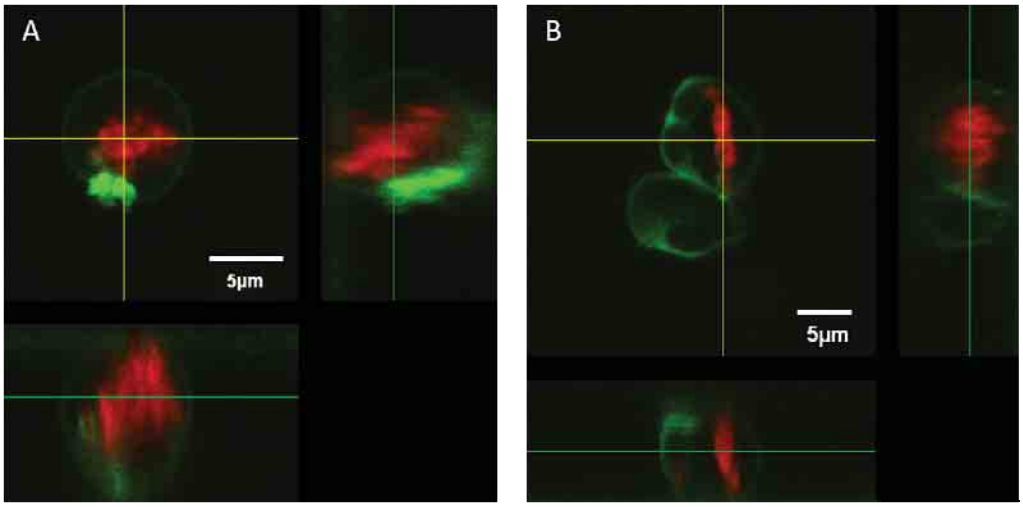

Figure 5.7 *The CLSM image of neutrophils after coincubation with PLGA particles. neutrophils incubated with (A) PLGA_QD_SPION NPs for 30min, (B) PLGA_QD_SPION NPs for 2h.*

CLSM images in XYZ planes revealed that hybrid PLGA NPs are internalized by neutrophils. In ***Figure 5.7*****A** and **B** the hybrid PLGA NPs, showing red fluorescence, are located within the cell membrane labeled in green. The top right image in ***Figure 5.7*****A** corresponds to the middle plane of a neutrophil. The left image has been produced by ZX-stacking and the bottom right image corresponds to the ZY stacking. The 3D stacking images prove after a certain incubation time (30min and 2h), the location of the PLGA NPs can be found completely internalized by neutrophils.

The uptake of PLGA NPs by neutrophils was quantified by flow cytometry (***Figure 5.8***. The cell uptake ratio indicates the percentage of cells that have internalized the PLGA NPs as compared to the whole population of neutrophils used during co-incubation experiments. PLGA_QD_SPION NPs showed 80% uptake ratio at 15 min which decreased with longer incubation time to 65% after 120 min (***Figure 5.8D***). PLGA_QD_SPION_Au NPs showed an initial uptake ratio of 20% which increased to 30% at 120 min (***Figure 5.8D***). The fluorescence intensity of the neutrophils with internalized NPs revealed the same tendency as the uptake ratio for both NPs (***Figure 5.8E***). The fluorescence intensity of neutrophils exposed to PLGA_QD_SPION NPs decreases from 14 a.u. at 15 min to 7 a.u. at 20 min remaining afterwards almost constant. For neutrophils exposed to PLGA_QD_SPION Au NPs the intensity increased from approximately 2 a.u. at 15 min to 4 a.u. at 120 min. Since the

fluorescence intensity is proportional to the number of internalized NPs, we can assume that the total amount of internalized PLGA_QD_SPION NPs is much higher compared to PLGA_QD_SPION_Au NPs. The faster and higher uptake of PLGA_QD_SPION NPs may be associated with the positive surface charge. Positively charged synthetic and natural polymers have been widely reported to be used to promote cell binding as a result of electrostatic interactions [333], thus enhancing their rapid cellular uptake. In view of the fact that flow cytometry cannot really distinguish between NPs that bind tightly with the cell membrane and NPs that are internalized within the cells, the initial high uptake ratio can be explained as rapid binding of PLGA_QD_SPION NPs with cationic PEI surface to the cell membrane. More surprising is the fact that both uptake and intensity decrease with incubation time. This may be related to a loss of the phagocytosis capability of the neutrophils with time. After initial internalization, the PLGA NPs must be expelled from the neutrophils in larger amounts than those PLGA NPs which were internalized later. Despite the significant decrease in number of internalized NPs per neutrophil, as evident from the change in fluorescence intensity, the percentage of cells with internalized NPs diminishes significantly only in a 10% at latest time of measurement. The PLGA_QD_SPION_Au NPs show an increase in internalization and intensity with time but it is moderated and their internalization and intensity values can be considered constant in the time frame of the incubation.

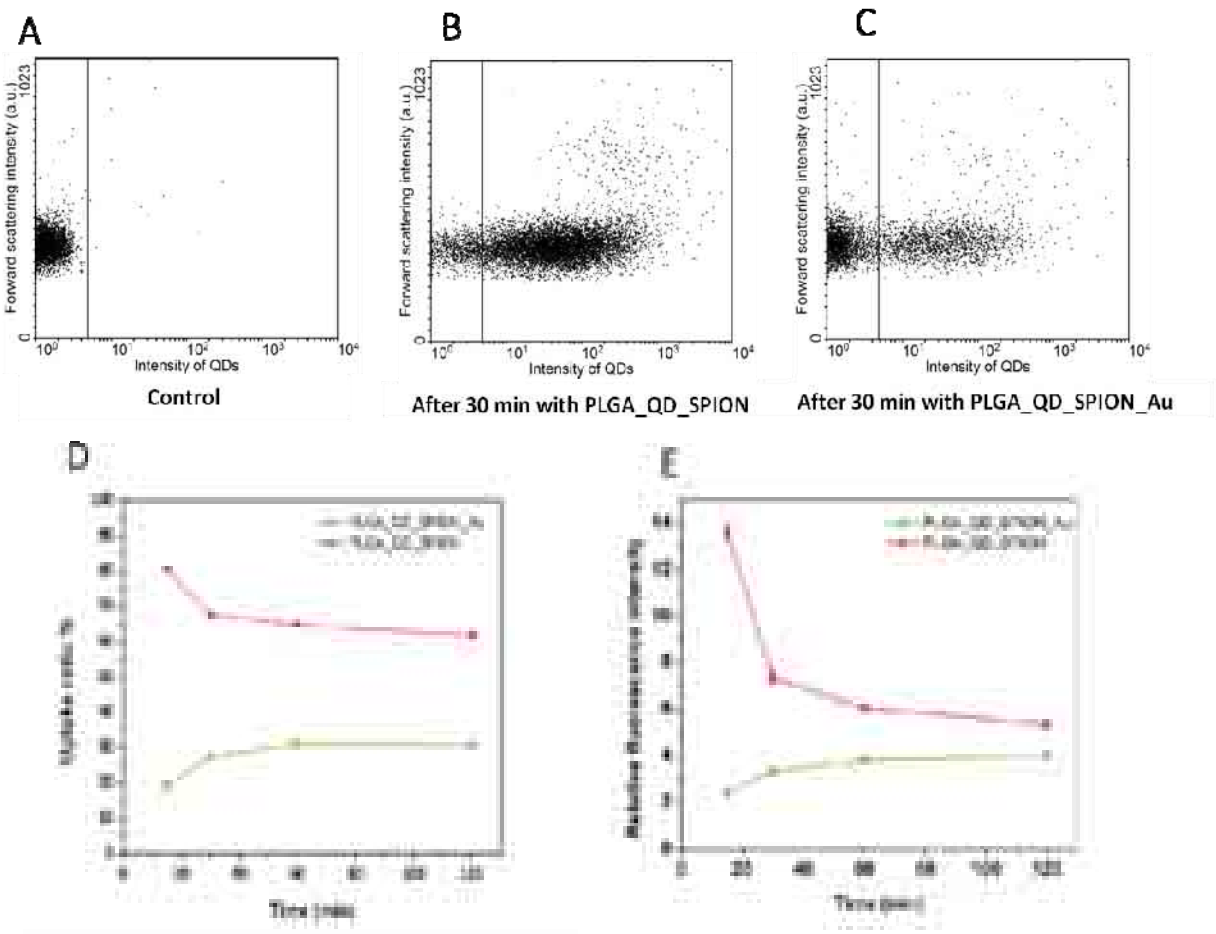

Figure 5.8 *Dot plots of the number distribution of neutrophils versus fluorescence intensity (A) Control cells without NPs; (B) after 30 min exposure to PLGA_QD_SPION Au NPs. (C) Dot plots of the number distribution of neutrophils versus fluorescence intensity after 30 min exposure to PLGA_QD_SPION NPs. (D) Uptake ratio in percentage for neutrophils exposed to PLGA_QD_SPION_Au NPs (green curve) and PLGA_QD_SPION NPs (red curve) after different incubation times. (E) Mean relative fluorescence intensity distribution for neutrophils exposed to PLGA_QD_SPION Au NP (green curve) and PLGA_QD_SPION NPs (red curve) after different incubation times.*

5.7 Effect of hybrid PLGA NPs on reactive oxygen species (ROS) production

When neutrophils are activated by inflammatory stimuli, the fast generation of ROS mediated by the NADPH oxidase or so-called oxidative burst (or respiratory burst) occurs [334][335]. Superoxide anion (O_2^-) is the principal product of this oxidase system[334]. DHE is a dye frequently used to measure the oxidative burst of

neutrophils by its rapid oxidation in the presence of O_2^-.[336] The product of the intracellular oxidization of DHE is the fluorescent oxyethidium, which can be measured by flow cytometry or fluorescence microscope [337].

To measure ROS production, neutrophils were first co-incubated with hybrid PLGA NPs (with and without Au NPs, 2mg/mL) and then stained for 10 min at 37 °C with 100 nM dihydroethidium (DHE). Superoxide anions (O_2^-) production was detected by flow cytometry measuring fluorescent DHE. Oxidized DHE were excited by 488 nm laser and emission was detected using Longpass: 570 nm, Bandpass: 585 ± 42 nm. Neutrophils treated with 100 nM H_2O_2 were used as positive control.

The DHE positive population was determined as the population over the gate made according to the histogram of untreated cells. Only the events have intensity above the gate value were count as DHE positive. The gate is established as the highest fluorescence intensity shown by the untreated neutrophils.

In ***Figure 5.9***, it shows the dot plots of forward scattering vs fluorescence intensity for the neutrophils exposed to PLGA_QD_SPION NPs, PLGA_QD_SPION_Au NPs and H_2O_2 at three times of incubation: 15 min, 60 min, 120 min. The percentage of neutrophiles displaying ROS is shown in Fig. 4E. The percentage of neutrophils displaying ROS when co-incubated 15 min with the hybrid PLGA NPs is less than 10% of the total neutrophils population. For the same time, H_2O_2 induced an increase in DHE fluorescence over the gate for 35% of the neutrophils population. After 60 min co-incubation of neutrophils with the hybrid PLGA NPs, the number of neutrophils increased in 15% while for the neutrophils exposed H_2O_2, the number of cells displaying ROS reaches 50% (***Figure 5.9J***). After 120 min, the number of cells with ROS increased to approximately 35% for PLGA_QD_SPION NPs and to 25% for PLGA_QD_SPION_AU NPs. After 120 min incubation, the number of neutrophils displaying ROS in the presence of H_2O_2 increased to 70%. We observed that the number of neutrophils showing oxidative burst increases with prolonged incubation time.

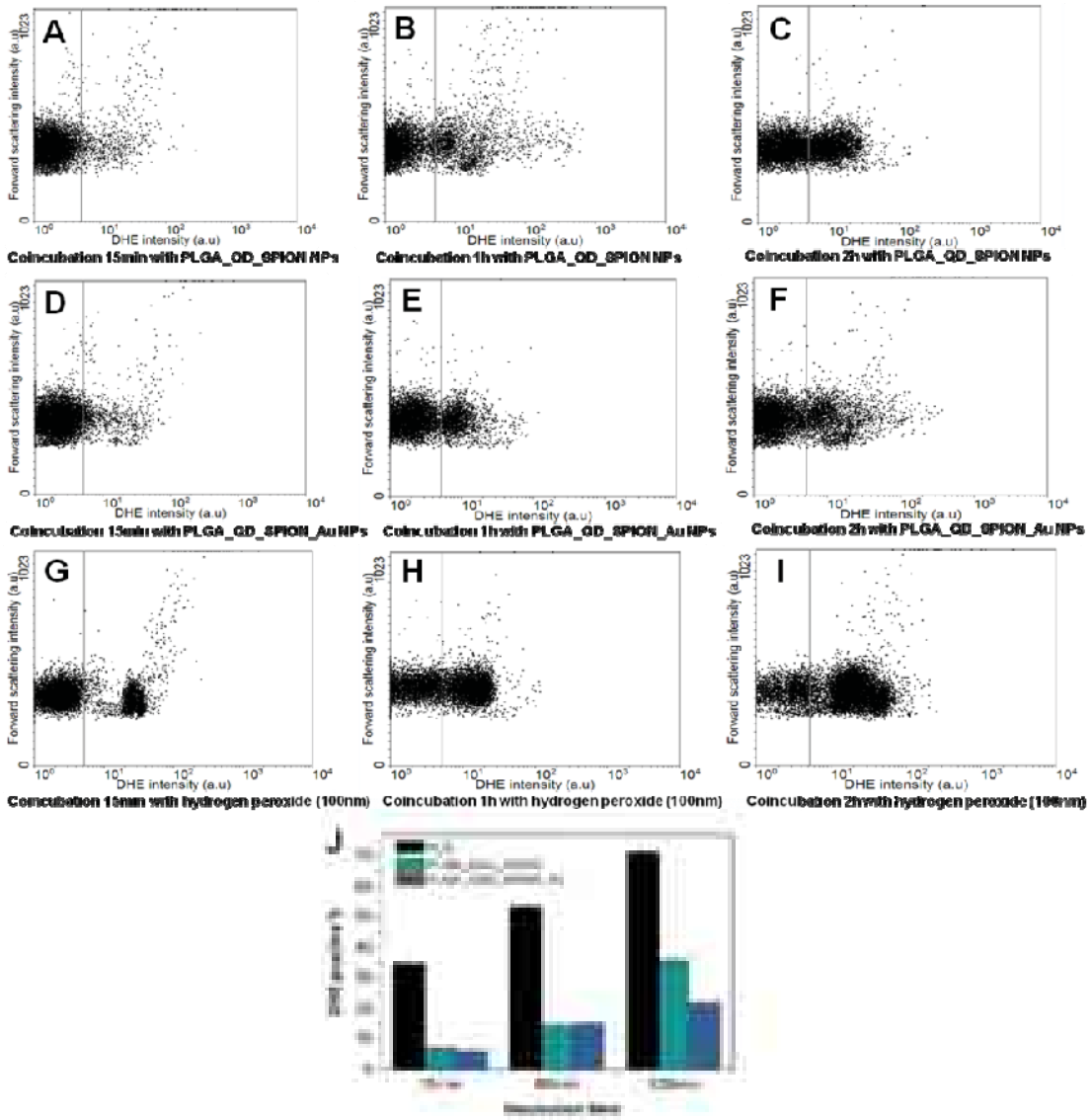

Figure 5.9 *Dot plots of the intracellular fluorescence intensity of oxidized DHE in the presence of hybrid PLGA particles. Neutrophils co-incubated with PLGA_QD_SPION NPs for 15min (A), 60 min (B) and 120 min (C). Neutrophils co-incubated with PLGA_QD_SPION_Au NPs for 15 min (D), 60 min (E) and 120 min (F). Neutrophils co-incubated with 100 nM H_2O_2 for 15 min (G), 60 min (H) and 120 min (I). (J) The percentage of DHE-positive population for neutrophils co-incubated with H_2O_2, PLGA_QD_SPION NPs and PLGA_QD_SPION_Au NPs.*

Nevertheless, at the longest considered incubation time, the number of neutrophils showing ROS is less of the hybrid PLGA NPs can be attributed to the fact the SPIONs are encapsulated in the polymer matrix and there are limited possibilities for electron exchange between the SPIONs and QDs on one side and the cells on the other side. No significant differences in ROS production could be observed for the two types of

PLGA NPs at shorter times (***Figure 5.9J***). The PLGA_QDs_SPION NPs caused ROS in a larger proportion of neutrophils than PLGA_QDs_SPION_Au NPs when the incubation time was 120 min.. This difference in ROS generation between the two PLGA NPs can be attributed to the antioxidant effect of Au NPs that reduce the production of ROS [338].

5.8 Magnetophoresis of neutrophils incorporating PLGA_QD_SPION NPs

Magnetophoresis experiments were further carried out to determine whether neutrophils that have phagocyted the PLGA_SPION_QD NPs can be separated from those that have not internalized the hybrid NPs. Magnetophoresis experiments were performed in a μ-Slide (VI 0.4, Ibidi, Munich, Germany), with microchannels in the presence of a magnetic gradient created by a neodynium magnet (NdFeB, magnetization N42, Cat. No. W-05-N, Supermagnete, Gottmadingen, Germany). The magnethophoresis was followed with an Olympus FLUOVIEW FV1000 CLSM in a life cell mode.

After 15 min incubation, neutrophils were transferred into microchannel chambers and a magnetic gradient was applied to laterally displace and selectively separate only neutrophils containing PLGA_QD_SPION NPs. The displacement of neutrophils was followed by CLSM placing the microfluidic chamber in the microscope. Images were taken from an arbitrary position to an end of the chamber, where the magnet was placed. All cells have their cell membrane green labeled. Neutrophils that have uptaken the PLGA NPs display additionally red fluorescence from the PLGA_ QD_SPION NPs. Once applied the magnetic field, the trajectory of the cell was followed during 750 s. The snapshots of the live cell imaging during magnetophoresis of the neutrophils are shown in ***Figure 5.10*** Images were taken every 150 s. Free PLGA NPs in solution can be observed in the first image. The NPs move faster than neutrophils to the end position in the channel when the magnet is applied and accumulate there. The number of neutrophils at the end position increases with time. Only those neutrophils containing the hybrid PLGA NPs were attracted twoards the magnet and lined along the wall of the microchamber. These results demonstrate that PLGA_ QD_SPION NPs can be efficiently used to separate the neutrophils that have internalized them from those free of NPs.

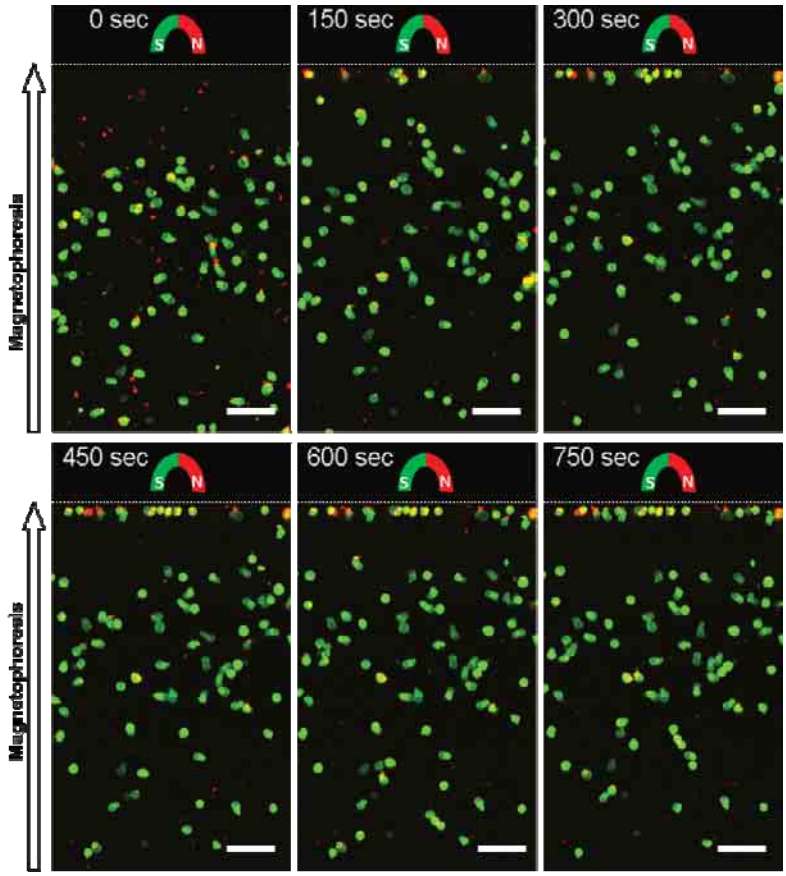

Figure 5.10 *Live cell CLSM images of magnetophoresis of neutrophils incorporating PLGA_QD_SPION NPs under the influence of magnetic gradient. Scale bar corresponds to 50µm.*

The magnethoporesis experiments prove that the magnetic labeling of the PLGA NPs and neutrophils has been successful and that can be applied for their manipulation and tracking. The experiments also prove the usefulness of the multifunctionality of the hybrid PLGA NPs. In parallel to the magnetic labeling with SPIONs used for dragging the cells, the QD labeling allows to identify which neutrophils were uptaken the PLGA NPs. While one of the labelings allows controlling the displacement of the neutrophils, the other allows for their visualization. This concept could be as well applied *in vivo* to direct injected neutrophils to specific organs and to visualize their location. Then, the labeled neutrophils could be used for contrast imaging in MRI and with the Au NPs for hyperthermia after assembly of Au NPs on the top. In addition, the heat generated by irradiating AuNPs assembled on top of the hybrid PLGA NPs can be as well applied to increase the delivery of molecules encapsulated in the PLGA particles. Heating the PLGA over its glass transition (i.e. 40-60 °C) should facilitate

the release of encapsulated drugs.

Chapter 6
Conclusions

The main goal of this thesis is to study the cellular uptake, fate and *in vitro* toxicity of engineered metallic, metal oxide, polymeric and hybrid nanoparticles (NPs). The influence of the surface charge, chemical composition, and aggregation states on the uptake mechanism, intracellular dynamics, intracellular distribution, biological fate, cytotoxicity, and degradation of the different NPs were systematically investigated. For this scope, NPs were synthesized or modified with polymers and other functional molecules. The choice of NPs of different nature: metallic/metal oxide and polymers with different size ranges and properties allowed us addressing different issues related to the intracellular fate of the NPs. Using PLGA NPs we were able of following the degradation of the polymers NPs inside cells. Gold NPs engineered with glycol conjugated are highly dispersible in cell media and facilitated the use of Fluorescence Correlation Spectroscopy to study intracellular dynamics. The use of polyelectrolyte brushes to modify CeO_2 NPs allows us to develop a strategy for fluorescently labeling the NPs without altering the surface properties of the coating by the dye which is encapsulated inside the brush. By choosing CeO_2, whose ions display a redox equilibrium between Ce^{3+} and Ce^{4+} that can be altered by metabolic, we have been as well able of studying how the polymer coating impact on the redox equilibrium between the cells and the NPs. Moreover, a hybrid NPs combining both metallic and polymeric NPs were designed and fabricated. Quantum dots and SPIONs were encapsulated in PLGA nanoparticles. The protective action of a polymer matrix like PLGA on the quantum dots and SPIOS could be studied. *In vitro* experiments showed that these hybrid NPs are suitable for multimodal imaging, cell tracking and sorting, and has potential applications for bio-application.

The main results and conclusions of the thesis are summarized as below:

In Chapter 2,

- *In situ* Atom Transfer Radical Polymerization (ATRP) was successfully performed on the surface of cerium oxide NPs (CNPs). Negatively charged poly (3-sulfopropylmatheacrylate) (PSPM) and positively charged poly [2-(methacryloyloxy) ethyl] trimethylammonium chloride (PMETAC were introduced to the surface of CNPs via ATRP. PSPM (CeO_2@PSPM) and PMETAC (CeO_2@PMETAC) modified CNPs presented negative and positive zeta potential respectively, while the zeta potential of pristine cerium oxide NPs was around zero. Polymer brushes brought higher surface charge density and better colloidal stability aqueous media to CNPs.

- Polyelectrolyte brush coated CNPs were fluorescently labeled without that the fluorescent label affects the surface properties of the NPs. The fluorescent dye was not linked to the outer surface of the polymer brush but directly to the surface of the CNPs remaining inside the polymer shell after brush synthesis. In this way the dye is not exposed to the outer surface of the NP.

- Cellular uptake, intracellular distribution and cyotoxicity of surface modified CNPs have been studied as a function of the charge of the surface coating. Regarding uptake kinetics, unmodified CNPs showed faster uptake than surface modified CNPs. But CeO_2@PMETAC NPs showed a slow but continuously increasing uptake even after 48h incubation, while the uptake of other two CNPs reached the plateau after 24h incubation. Polymer brush coated CNPs showed high colocalization with acidic cell compartments after 24h incubation with HEK 293 cells. This suggests these NPs were mostly internalized through endocytosis involving endosomal and lysosomal cell compartment. Unmodified CeO_2 NPs were typically internalized via macropinocytosis by both HEK 293 and A 549 cell lines. While CeO2@PSPM NPs were mostly internalized by A549 cells via caveolae-mediated endocytosis. And CeO2@PMETAC NPs were mostly internalized by HEK 293 cells via clathrin-mediated endocytosis.

- The nature of the polymer coating impacts on the cytotoxicity action of cerium oxide NPs, varying as well with the nature of the cell line. Nevertheless, CeO_2@PSPM NPs were the most cytotoxic having a higher impact on the cell viability, proliferation and DNA damage than the other NPs. This can be attributed to their high surface charge and the presence of sulfonate groups on the NPs surface.

- The effect of the surface modification of CNPs on the intracellualr reactive oxygen species (ROS) was as well examined. CNPs usually exhibit antioxidant properties. After polymer coating the CNPs retained these properties. Cells with internalized CNPs showed a lower ROS level after exposed to tert-Butyl hydroperoxide (TBHP), a ROS inducer, than untreated cells. This means that brush coated CNPs can be used as antioxidant agent protect cells from ROS generation. The polymer brush coating maintained the antioxidant properties of the Cerium Oxide.

In Chapter 3,

- Fluorescence correlation spectroscopy (FCS) was applied to study the dynamics of gold nanoparticles functionalized with glucose derivates (Glc-Au NPs) in distilled water and cell culture medium. The formation of NP aggregates was demonstrated by FCS for Glc-Au-Hi NPs incubated in Dulbecco's Modified Eagle Medium (DMEM) with 10% FBS,. Aggregate formation was demonstrated via the increase in diffusion time of the NPs. NP in water display a size of around 2 nm while in media this size increased to 4.4 nm Additionally a decrease in the concentration from 77.4 nM to 37.0 nM of mobile species was measured as consequence of the aggregation of single NPs.

- FCS was also applied to study the intracellular dynamics of the Glc-Au NPs. FCS data could not be collected directly because the internalized NPs for large aggregates which behave as an inmobile fraction. Because of this no fluctuations

in the fluorescence of this aggregates could be observed and FCS could not be applied. However, the fluorescence of large aggregates could be removed applying a bleaching for 1 second at the point the FCS data will be recorded. After this prebleaching fluorescence from smaller aggregates and single NPs could be measured in the confocal volume. These NPs were probably located outside the confocal volume at the time of the bleaching.

- For the mobile fraction intracellular distribution histograms showed narrow distributions of all parameters measured/calculated indicating a generally monodisperse population of concentration and hydrodynamic radius at the measurement sites. It can be concluded that only single NPs and small aggregates of NPs contribute to the mobile fraction, and approximately 88 % of the aggregates display sizes between 3.5 nm and 7.0 nm and concentrations were around 11.8 nM.

- The overall result of this work broadens the field of FCS applied in studying the intracellular dynamics of NPs by facilitating the reproducible and reliable collection of FCS data via the presented strategy. In this way, FCS can be applied to increase the knowledge of the state of NPs within the cell and how this can be changed through proper surface functionalization of the NPs or the presence of specific biomolecules and changes in cell function and physiology. This strategy can be extended to other fluorescent NPs.

In Chapter 4,

- Biodegradable poly (lactide-co-glycolide) (PLGA) NPs were fabricated through O/W emulsion method with two different ratios of the D,L-lactide and glycolide blocks.

- The degradation of RhdB labeled PLGA NPs with 15 % and 35 % glycolide was studied under physiological and intracellular conditions by means of FACS. In a physiological solution, it was shown that FACS can trace the variations in the

fluorescence of the PLGA15 NPs due to the release of labeled polymer as degradation proceeds over 20 days while no change in fluorescence is observed for the PLGA35 NPs after 70 days. TEM and DLS of the PLGA NPs were measured in parallel during the time the NPs were exposed to physiological media corroborating the times for the degradation process of the PLGA15 NPs and that PLGA35 NPs remain stable.

- Intracellular degradation of the RhdB labeled PLGA NPs was followed by FACS measuring the changes in fluorescence intensity per cell over time. For the PLGA35 NPs, no change in the fluorescence intensity distribution of cells with PLGA35 NPs could be observed after 5 days. For the PLGA15 NPs the fluorescence intensity increases steadily during the first 24 h to reach a plateau that remains constant for the next 72 h. The increase in fluorescence is due to the change in the environment of RhdB from the apolar NP interior to the more polar environment of the cell, which results in higher fluorescence emission intensity. The degradation of the NPs intracellularly is faster than in physiological media. This is to be expected since in the cell interior and enzymes may be acting in the degradation.

- Confocal raman microscopy (CRM) was used to follow NP degradation intracellularly looking at the relative changes of the bands at 1768 cm^{-1} and at 872 cm^{-1}. The band at 1768 cm^{-1} corresponds to C=O vibration of the ester group of PLGA. As degradation takes place, the hydrolysis of the ester should decrease the intensity of the band at 1768 cm^{-1}. The band at 872 cm^{-1} is assigned to the C-COO vibration of lactic acid, which will not be affected by the hydrolysis process during the degradation. Therefore, the change of ratio between the band at 1768cm^{-1} and that of 872 cm^{-1} reveals the change of the amount of ester group during the degradation. For intracellular PLGA15 NPs, the relative signal of these bandsdecrease progressively over 48 h, hinting degradation as in FACS. And for intracellular PLGA35, no changes in the relative intensities of these two bands could be recorded, which corroborating again the results from FACS. The data of

CRM confirmed the degradation of the PLGA15 and the stability of the PLGA35 NPs intracellularly.

- The use of FACS and RhdB labeled PLGA to trace NP degradation has the advantage over other methodologies that it allows for a large statistical analysis of both NPs and cells. Combining FACS with other techniques such as, Confocal Raman Microscopy, as we have shown, provides an insight into the behavior of PLGA NPs in cells as a function of their chemical composition.

In Chapter 5,

- Poly(lactic-co-glycolic acid) (PLGA) NPs incorporating quantum dots (QDs), superparamagnetic iron oxide nanoparticles (SPIONs) and gold (Au) NPs in their formulation for the labeling, multimodal imaging, tracking and sorting of human neutrophils were fabricated via the w/o/w double emulsion method. QDs and SPIONs were entrapped in the PLGA core during emulsification while Au NPs were assembled on top of the PLGA NPs via electrostatic interactions. QDs and SPIONs were encapsulated in PLGA NPs as agents for fluorescence and magnetic resonance imaging, respectively, while Au NPs can be used for potential applications suhc as photothermal therapy, drug delivery and diagnostic biomedical sensing.

- QDs encapsulation makes the hybrid PLGA NPs highly fluorescent. Using this fluorescence, NP uptake by neutrophils has been monitored. Uptake of PLGA_QD_SPION NPs by neutrophils was proven to be much higher than the uptake of PLGA_QD_SPION_Au NPs.

- Neutrophils incubated with hybrid PLGA NPs showed low oxidative burst irrespectively of the incubation time. This result hints the protective effect of the encapsulation within PLGA. The possible application of the hybrid PLGA NPs in MRI imaging has been evaluated by measuring the spin-spin relaxation time. And

using a magnetic gradient, it has been shown that neutrophils with internalized hybrid PLGA NPs can be specifically sorted and manipulated.

- A way to fabricate hybrid PLGA NPs on the basis of encapsulation and self-assembly has been presented. Their functionalities: magnetic response and fluorescent labeling have been proved. It shows some of the advantages of incorporating the small inorganic NPs in a larger polymer nanomaterial and their specific potential as labels for neutrophils. The hybrid NPs has potential for *in vivo* applications, e.g., tumor visualization and localized photothermal treatment. And the applicability of these hybrid PLGA NPs could be extended to other cells and the PLGA NPs could also entail other combination of NPs. Further work can be continued focusing on the use of the labeled neutrophils in MRI *in vivo*.

References

[1] Zhao F, Zhao YYYY, Liu Y, Chang X, Chen C. Cellular uptake, intracellular trafficking, and cytotoxicity of nanomaterials. Small 2011;7:1322–37.

[2] Roduner E. Size matters: why nanomaterials are different. Chem Soc Rev 2006;35:583–92.

[3] Lee H, Yu MK, Park S, Moon S, Min JJ, Jeong YY, et al. Thermally cross-linked superparamagnetic iron oxide nanoparticles: synthesis and application as a dual imaging probe for cancer in vivo. J Am Chem Soc 2007;129:12739–45.

[4] Zhou Z, Wang L, Chi X, Bao J, Yang L, Zhao W, et al. Engineered iron-oxide-based nanoparticles as enhanced t1 contrast agents for efficient tumor imaging. ACS Nano 2013;7:3287–96.

[5] Gupta AK, Gupta M. Synthesis and surface engineering of iron oxide nanoparticles for biomedical applications. Biomaterials 2005;26:3995–4021.

[6] Chen K-J, Wolahan SM, Wang H, Hsu C-H, Chang H-W, Durazo A, et al. A small MRI contrast agent library of gadolinium(III)-encapsulated supramolecular nanoparticles for improved relaxivity and sensitivity. Biomaterials 2011;32:2160–5.

[7] Park JY, Baek MJ, Choi ES, Woo S, Kim JH, Kim TJ, et al. Paramagnetic ultrasmall gadolinium oxide nanoparticles as advanced T1 MRI contrast agent: account for large longitudinal relaxivity, optimal particle diameter, and in vivo T1 MR images. ACS Nano 2009;3:3663–9.

[8] Chan K, Wong W. Small molecular gadolinium (III) complexes as MRI contrast agents for diagnostic imaging. Coord Chem Rev 2007;251:2428–51.

[9] Portney NG, Ozkan M. Nano-oncology: drug delivery, imaging, and sensing. Anal Bioanal Chem 2006;384:620–30.

[10] Chen J, Saeki F, Wiley BJ, Cang H, Cobb MJ, Li Z-Y, et al. Gold nanocages: bioconjugation and their potential use as optical imaging contrast agents. Nano Lett 2005;5:473–7.

[11] Mallidi S, Larson T, Tam J, Joshi PP, Karpiouk A, Sokolov K, et al. Multiwavelength photoacoustic imaging and plasmon resonance coupling of gold nanoparticles for selective detection of cancer. Nano Lett 2009;9:2825–31.

[12] Lu W, Huang Q, Ku G, Wen X, Zhou M, Guzatov D, et al. Photoacoustic imaging of living mouse brain vasculature using hollow gold nanospheres. Biomaterials 2010;31:2617–26.

[13] Hainfeld JF, Slatkin DN, Focella TM, Smilowitz HM. Gold nanoparticles: a new X-ray contrast agent. Br J Radiol 2006;79:248–53.

[14] Kim D, Park S, Lee JH, Jeong YY, Jon S. Antibiofouling polymer-coated gold nanoparticles as a contrast agent for in vivo X-ray computed tomography imaging. J Am Chem Soc 2007;129:7661–5.

[15] So H-M, Won K, Kim YH, Kim B-K, Ryu BH, Na PS, et al. Single-walled carbon nanotube biosensors using aptamers as molecular recognition elements. J Am Chem Soc 2005;127:11906–7.

[16] Zhang W-D, Chen J, Jiang L-C, Yu Y-X, Zhang J-Q. A highly sensitive nonenzymatic glucose sensor based on NiO-modified multi-walled carbon nanotubes. Microchim Acta 2010;168:259–65.

[17] Liu Y, Yu D, Zeng C, Miao Z, Dai L. Biocompatible graphene oxide-based glucose biosensors. Langmuir 2010;26:6158–60.

[18] Wu L, Chu H, Koh W, Li E. Highly sensitive graphene biosensors based on surface plasmon resonance. Opt Express 2010;18:14395–400.

[19] Liu S, Dai Z, Chen H, Ju H. Immobilization of hemoglobin on zirconium dioxide nanoparticles for preparation of a novel hydrogen peroxide biosensor. Biosens Bioelectron 2004;19:963–9.

[20] Liu G, Lin Y. Electrochemical sensor for organophosphate pesticides and nerve agents using zirconia nanoparticles as selective sorbents. Anal Chem 2005;77:5894–901.

[21] Mu Y, Jia D, He Y, Miao Y, Wu H-L. Nano nickel oxide modified non-enzymatic glucose sensors with enhanced sensitivity through an electrochemical process strategy at high potential. Biosens Bioelectron 2011;26:2948–52.

[22] Casero E, Alonso C, Petit-Domínguez MD, Vázquez L, Parra-Alfambra AM, Merino P, et al. Lactate biosensor based on a bionanocomposite composed of titanium oxide nanoparticles, photocatalytically reduced graphene, and lactate oxidase. Microchim Acta 2013;181:79–87.

[23] Khan R, Kaushik A, Solanki PR, Ansari A a, Pandey MK, Malhotra BD. Zinc oxide nanoparticles-chitosan composite film for cholesterol biosensor. Anal Chim Acta 2008;616:207–13.

[24] Cantale V, Simeone FC, Gambari R, Rampi M a. Gold nano-islands on FTO as plasmonic nanostructures for biosensors. Sensors Actuators B Chem 2011;152:206–13.

[25] Pingarrón JM, Yáñez-Sedeño P, González-Cortés A. Gold nanoparticle-based electrochemical biosensors. Electrochim Acta 2008;53:5848–66.

[26] Sun H, Choy TS, Zhu DR, Yam WC, Fung YS. Nano-silver-modified PQC/DNA biosensor for detecting E. coli in environmental water. Biosens Bioelectron 2009;24:1405–10.

[27] Wu H, Wang J, Kang X, Wang C, Wang D, Liu J, et al. Glucose biosensor based on immobilization of glucose oxidase in platinum nanoparticles/graphene/chitosan nanocomposite film. Talanta 2009;80:403–6.

[28] Jie G, Liu B, Pan H, Zhu J-J, Chen H-Y. CdS nanocrystal-based electrochemiluminescence biosensor for the detection of low-density lipoprotein by increasing sensitivity with gold nanoparticle amplification. Anal Chem 2007;79:5574–81.

[29] Ibsen S, Benchimol M, Simberg D, Schutt C, Steiner J, Esener S. A novel nested liposome drug delivery vehicle capable of ultrasound triggered release of its payload. J Control Release 2011;155:358–66.

[30] Dhar S, Gu FX. Targeted delivery of cisplatin to prostate cancer cells by aptamer functionalized Pt (IV) prodrug-PLGA–PEG nanoparticles. Proc Natl Acad Sci 2008;105:17356.

[31] Gaucher G, Satturwar P, Jones M-C, Furtos A, Leroux J-C. Polymeric micelles for oral drug delivery. Eur J Pharm Biopharm 2010;76:147–58.

[32] Brown SD, Nativo P, Smith J-A, Stirling D, Edwards PR, Venugopal B, et al. Gold nanoparticles for the improved anticancer drug delivery of the active component of oxaliplatin. J Am Chem Soc 2010;132:4678–84.

[33] Svenson S. Dendrimers as versatile platform in drug delivery applications. Eur J Pharm Biopharm 2009;71:445–62.

[34] Garrigues NW, Little D, Sanchez-Adams J, Ruch DS, Guilak F. Electrospun cartilage-derived matrix scaffolds for cartilage tissue engineering. J Biomed Mater Res A 2013;59784:28–30.

[35] Chen J-P, Su C-H. Surface modification of electrospun PLLA nanofibers by plasma treatment and cationized gelatin immobilization for cartilage tissue engineering. Acta Biomater 2011;7:234–43.

[36] Chang C, Peng N, He M, Teramoto Y, Nishio Y, Zhang L. Fabrication and properties of chitin/hydroxyapatite hybrid hydrogels as scaffold nano-materials. Carbohydr Polym 2013;91:7–13.

[37] Zhou H, Lee J. Nanoscale hydroxyapatite particles for bone tissue engineering. Acta Biomater 2011;7:2769–81.

[38] Gupta A, Main BJ, Taylor BL, Gupta M, Whitworth C a, Cady C, et al. In vitro evaluation of three-dimensional single-walled carbon nanotube composites for bone tissue engineering. J Biomed Mater Res A 2014:1–9.

[39] Hirata E, Uo M, Takita H, Akasaka T, Watari F, Yokoyama A. Multiwalled carbon nanotube-coating of 3D collagen scaffolds for bone tissue engineering. Carbon N Y 2011;49:3284–91.

[40] Goenka S, Sant V, Sant S. Graphene-based nanomaterials for drug delivery and tissue engineering. J Control Release 2014;173:75–88.

[41] Gloria A, Russo T, Amora UD, Zeppetelli S, Alessandro TD, Sandri M, et al. Magnetic poly(ε-caprolactone)/iron-doped hydroxyapatite nanocomposite substrates for advanced bone tissue engineering. J R Soc Interface 2013;10 .

[42] Shi J, Votruba AR, Farokhzad OC, Langer R. Nanotechnology in drug delivery and tissue engineering: from discovery to applications. Nano Lett 2010;10:3223–30.

[43] Yilgor P, Tuzlakoglu K, Reis RL, Hasirci N, Hasirci V. Incorporation of a sequential BMP-2/BMP-7 delivery system into chitosan-based scaffolds for bone tissue engineering. Biomaterials 2009;30:3551–9.

[44] Park K, Kim H, Moon S, Na K. Bone morphogenic protein-2 (BMP-2) loaded nanoparticles mixed with human mesenchymal stem cell in fibrin hydrogel for bone tissue engineering. J Biosci Bioeng 2009;108:530–7.

[45] Peng L, Cheng X, Zhuo R, Lan J, Wang Y, Shi B, et al. Novel gene-activated matrix with embedded chitosan/plasmid DNA nanoparticles encoding PDGF for periodontal tissue engineering. J Biomed Mater Res A 2009;90:564–76.

[46] Hosseinkhani H, Hosseinkhani M, Gabrielson NP, Pack DW, Khademhosseini A, Kobayashi H. DNA nanoparticles encapsulated in 3D tissue-engineered scaffolds enhance osteogenic differentiation of mesenchymal stem cells. J Biomed Mater Res A 2008;85:47–60.

[47] Nelson CE, Gupta MK, Adolph EJ, Shannon JM, Guelcher S a, Duvall CL. Sustained local delivery of siRNA from an injectable scaffold. Biomaterials 2012;33:1154–61.

[48] Nelson CE, Kim AJ, Adolph EJ, Gupta MK, Yu F, Hocking KM, et al. Tunable delivery of siRNA from a biodegradable scaffold to promote angiogenesis in vivo. Adv Mater 2014;26:607–14, 506.

[49] Lewinski N, Colvin V, Drezek R. Cytotoxicity of nanoparticles. Small 2008;4:26–49.

[50] Yildirimer L, Thanh NTK, Loizidou M, Seifalian AM. Toxicology and clinical potential of nanoparticles. Nano Today 2011;6:585–607.

[51] Kim ST, Saha K, Kim C, Rotello VM. The role of surface functionality in determining nanoparticle cytotoxicity. Acc Chem Res 2013;46:681–91.

[52] Soenen SJ, Rivera-Gil P, Montenegro J-M, Parak WJ, De Smedt SC, Braeckmans K. Cellular toxicity of inorganic nanoparticles: Common aspects and guidelines for improved nanotoxicity evaluation. Nano Today 2011;6:446–65.

[53] Conner SD, Schmid SL. Regulated portals of entry into the cell. Nature 2003;422:37–44.

[54] Li F, Zhu A, Song X, Ji L, Wang J. The internalization of fluorescence-labeled PLA nanoparticles by macrophages. Int J Pharm 2013;453:506–13.

[55] Essa S, Rabanel JM, Hildgen P. Characterization of rhodamine loaded PEG-g-PLA nanoparticles (NPs): effect of poly(ethylene glycol) grafting density. Int J Pharm 2011;411:178–87.

[56] Busch W, Bastian S, Trahorsch U, Iwe M, Kühnel D, Meißner T, et al. Internalisation of engineered nanoparticles into mammalian cells in vitro: influence of cell type and particle properties. J Nanoparticle Res 2010;13:293–310.

[57] Nichols BJ, Lippincott-Schwartz J. Endocytosis without clathrin coats. Trends Cell Biol 2001;11:406–12.

[58] Sokolova V, Kozlova D, Knuschke T, Buer J, Westendorf AM, Epple M. Mechanism of the uptake of cationic and anionic calcium phosphate nanoparticles by cells. Acta Biomater 2013;9:7527–35.

[59] Sharma R, Ghasparian A, Robinson J a, McCullough KC. Synthetic virus-like particles target dendritic cell lipid rafts for rapid endocytosis primarily but not exclusively by macropinocytosis. PLoS One 2012;7:e43248.

[60] Kerr MC, Teasdale RD. Defining macropinocytosis. Traffic 2009;10:364–71.

[61] Von Kleist L, Stahlschmidt W, Bulut H, Gromova K, Puchkov D, Robertson MJ, et al. Role of the clathrin terminal domain in regulating coated pit dynamics revealed by small molecule inhibition. Cell 2011;146:471–84.

[62] Hu Z, Pan Y, Wang J, Chen J, Li J, Ren L. Meso-tetra (carboxyphenyl) porphyrin (TCPP) nanoparticles were internalized by SW480 cells by a clathrin-mediated endocytosis pathway to induce high photocytotoxicity. Biomed Pharmacother 2009;63:155–64.

[63] Harush-Frenkel O, Debotton N, Benita S, Altschuler Y. Targeting of nanoparticles to the clathrin-mediated endocytic pathway. Biochem Biophys Res Commun 2007;353:26–32.

[64] Cohen AW, Hnasko R, Schubert W, Lisanti MP. Role of caveolae and caveolins in health and disease. Physiol Rev 2004;84:1341–79.

[65] Rejman J, Bragonzi A, Conese M. Role of clathrin- and caveolae-mediated endocytosis in gene transfer mediated by lipo- and polyplexes. Mol Ther 2005;12:468–74.

[66] Bareford LM, Swaan PW. Endocytic mechanisms for targeted drug delivery. Adv Drug Deliv Rev 2007;59:748–58.

[67] Wang Z, Tiruppathi C, Cho J, Minshall RD, Malik AB. Delivery of nanoparticle: complexed drugs across the vascular endothelial barrier via caveolae. IUBMB Life 2011;63:659–67.

[68] Mayor S, Pagano RE. Pathways of clathrin-independent endocytosis. Nat Rev Mol Cell Biol 2007;8:603–12.

[69] Cartiera MS, Johnson KM, Rajendran V, Caplan MJ, Saltzman WM. The uptake and intracellular fate of PLGA nanoparticles in epithelial cells. Biomaterials 2009;30:2790–8.

[70] Taylor U, Klein S, Petersen S, Kues W, Barcikowski S, Rath D. Nonendosomal cellular uptake of ligand-free, positively charged gold nanoparticles. Cytometry A 2010;77:439–46.

[71] Sharifi S, Behzadi S, Laurent S, Forrest ML, Stroeve P, Mahmoudi M. Toxicity of nanomaterials. Chem Soc Rev 2012;41:2323–43.

[72] Yen H-J, Hsu S-H, Tsai C-L. Cytotoxicity and immunological response of gold and silver nanoparticles of different sizes. Small 2009;5:1553–61.

[73] Jiang W, Kim BYS, Rutka JT, Chan WCW. Nanoparticle-mediated cellular response is size-dependent. Nat Nanotechnol 2008;3:145–50.

[74] Win KY, Feng S-S. Effects of particle size and surface coating on cellular uptake of polymeric nanoparticles for oral delivery of anticancer drugs. Biomaterials 2005;26:2713–22.

[75] Andersson PO, Lejon C, Ekstrand-Hammarström B, Akfur C, Ahlinder L, Bucht A, et al. Polymorph- and size-dependent uptake and toxicity of TiO_2 nanoparticles in living lung epithelial cells. Small 2011;7:514–23.

[76] Pan Y, Neuss S, Leifert A, Fischler M, Wen F, Simon U, et al. Size-dependent cytotoxicity of gold nanoparticles. Small 2007;3:1941–9.

[77] Carlson C, Hussain SM, Schrand AM, Braydich-Stolle LK, Hess KL, Jones RL, et al. Unique cellular interaction of silver nanoparticles: size-dependent generation of reactive oxygen species. J Phys Chem B 2008;112:13608–19.

[78] Rejman J, Oberle V, Zuhorn IS, Hoekstra D. Size-dependent internalization of particles via the pathways of clathrin- and caveolae-mediated endocytosis. Biochem J 2004;377:159–69.

[79] Fröhlich E. The role of surface charge in cellular uptake and cytotoxicity of medical nanoparticles. Int J Nanomedicine 2012;7:5577–91.

[80] Rana S, Bajaj A, Mout R, Rotello VM. Monolayer coated gold nanoparticles for delivery applications. Adv Drug Deliv Rev 2012;64:200–16.

[81] Doorley GW, Payne CK. Cellular binding of nanoparticles in the presence of serum proteins. Chem Commun 2011;47:466–8.

[82] Chung T-H, Wu S-H, Yao M, Lu C-W, Lin Y-S, Hung Y, et al. The effect of surface charge on the uptake and biological function of mesoporous silica nanoparticles in 3T3-L1 cells and human mesenchymal stem cells. Biomaterials 2007;28:2959–66.

[83] Krasnici S, Werner A, Eichhorn ME, Schmitt-Sody M, Pahernik S a, Sauer B, et al. Effect of the surface charge of liposomes on their uptake by angiogenic tumor vessels. Int J Cancer 2003;105:561–7.

[84] Wender P a, Mitchell DJ, Pattabiraman K, Pelkey ET, Steinman L, Rothbard JB. The design, synthesis, and evaluation of molecules that enable or enhance cellular uptake: peptoid molecular transporters. Proc Natl Acad Sci U S A 2000;97:13003–8.

[85] Lai W-F, Lin MC-M. Nucleic acid delivery with chitosan and its derivatives. J Control Release 2009;134:158–68.

[86] Vinogradov S V, Bronich TK, Kabanov A V. Nanosized cationic hydrogels for drug delivery: preparation, properties and interactions with cells. Adv Drug Deliv Rev 2002;54:135–47.

[87] Lee K, Lee H, Lee KW, Park TG. Optical imaging of intracellular reactive oxygen species for the assessment of the cytotoxicity of nanoparticles. Biomaterials 2011;32:2556–65.

[88] Bhattacharjee S, de Haan LHJ, Evers NM, Jiang X, Marcelis ATM, Zuilhof H, et al. Role of surface charge and oxidative stress in cytotoxicity of organic monolayer-coated silicon nanoparticles towards macrophage NR8383 cells. Part Fibre Toxicol 2010;7:25.

[89] Dombu CY, Kroubi M, Zibouche R, Matran R, Betbeder D. Characterization of endocytosis and exocytosis of cationic nanoparticles in airway epithelium cells. Nanotechnology 2010;21:355102.

[90] Saha K, Kim ST, Yan B, Miranda OR, Alfonso FS, Shlosman D, et al. Surface functionality of nanoparticles determines cellular uptake mechanisms in mammalian cells. Small 2013;9:300–5.

[91] Balogh L, Nigavekar SS, Nair BM, Lesniak W, Zhang C, Sung LY, et al. Significant effect of size on the in vivo biodistribution of gold composite nanodevices in mouse tumor models. Nanomedicine 2007;3:281–96.

[92] Xiao K, Li Y, Luo J, Lee JS, Xiao W, Gonik AM, et al. The effect of surface charge on in vivo biodistribution of PEG-oligocholic acid based micellar nanoparticles. Biomaterials 2011;32:3435–46.

[93] Lockman PR, Koziara JM, Mumper RJ, Allen DD. Nanoparticle surface charges alter blood-brain barrier integrity and permeability. J Drug Target 2004;12:635–41.

[94] Malugin A, Ghandehari H. Cellular uptake and toxicity of gold nanoparticles in prostate cancer cells: a comparative study of rods and spheres. J Appl Toxicol 2009:n/a–n/a.

[95] Huang X, Li L, Liu T, Hao N, Liu H, Chen D, et al. The shape effect of mesoporous silica nanoparticles on biodistribution, clearance, and biocompatibility in vivo. ACS Nano 2011;5:5390–9.

[96] Arnida, Janát-Amsbury MM, Ray a, Peterson CM, Ghandehari H. Geometry and surface characteristics of gold nanoparticles influence their biodistribution and uptake by macrophages. Eur J Pharm Biopharm 2011;77:417–23.

[97] Huang X, Teng X, Chen D, Tang F, He J. The effect of the shape of mesoporous silica nanoparticles on cellular uptake and cell function. Biomaterials 2010;31:438–48.

[98] Wang S, Lu W, Tovmachenko O, Rai US, Yu H, Ray PC. Challenge in Understanding Size and Shape Dependent Toxicity of Gold Nanomaterials in Human Skin Keratinocytes. Chem Phys Lett 2008;463:145–9.

[99] Macey M. Principles of Flow Cytometry. In: Macey M, editor. Flow Cytom., Humana Press; 2007, p. 1–15.

[100] Neumeyer A, Bukowski M, Veith M, Lehr C-M, Daum N. Propidium iodide labeling of nanoparticles as a novel tool for the quantification of cellular binding and uptake. Nanomedicine 2011;7:410–9.

[101] Salvati A, Aberg C, dos Santos T, Varela J, Pinto P, Lynch I, et al. Experimental and theoretical comparison of intracellular import of polymeric nanoparticles and small molecules: toward models of uptake kinetics. Nanomedicine 2011;7:818–26.

[102] Höcherl A, Landfester K, Mailänder V. Absolute quantitation of sub-micrometer particles in cells by flow cytometry. Macromol Biosci 2013;13:1568–75.

[103] Suzuki H, Toyooka T, Ibuki Y. Simple and Easy Method to Evaluate Uptake Potential of Nanoparticles in Mammalian Cells Using a Flow Cytometric Light Scatter Analysis. Environ Sci Technol 2007;41:3018–24.

[104] Ibuki Y, Toyooka T. Nanoparticle Uptake Measured by Flow Cytometry. In: Reineke J, editor. Nanotoxicity SE - 11, vol. 926, Humana Press; 2012, p. 157–66.

[105] Greulich C, Diendorf J, Simon T, Eggeler G. Uptake and intracellular distribution of silver nanoparticles in human mesenchymal stem cells. Acta Biomater 2011;7:347–54.

[106] Serda R, Gu J, Bhavane R, Liu X. The association of silicon microparticles with endothelial cells in drug delivery to the vasculature. Biomaterials 2009;30:2440–8.

[107] Foldbjerg R, Olesen P, Hougaard M, Dang DA, Hoffmann HJ, Autrup H. PVP-coated silver nanoparticles and silver ions induce reactive oxygen species, apoptosis and necrosis in THP-1 monocytes. Toxicol Lett 2009;190:156–62.

[108] De Berardis B, Civitelli G, Condello M, Lista P, Pozzi R, Arancia G, et al. Exposure to ZnO nanoparticles induces oxidative stress and cytotoxicity in human colon carcinoma cells. Toxicol Appl Pharmacol 2010;246:116–27.

[109] Khan MI, Mohammad A, Patil G, Naqvi S a H, Chauhan LKS, Ahmad I. Induction of ROS, mitochondrial damage and autophagy in lung epithelial cancer cells by iron oxide nanoparticles. Biomaterials 2012;33:1477–88.

[110] Lee Y-H, Cheng F-Y, Chiu H-W, Tsai J-C, Fang C-Y, Chen C-W, et al. Cytotoxicity, oxidative stress, apoptosis and the autophagic effects of silver nanoparticles in mouse embryonic fibroblasts. Biomaterials 2014;35:4706–15.

[111] Liu X, Sun J. Endothelial cells dysfunction induced by silica nanoparticles through oxidative stress via JNK/P53 and NF-kappaB pathways. Biomaterials 2010;31:8198–209.

[112] Acharya S, Dilnawaz F, Sahoo SK. Targeted epidermal growth factor receptor nanoparticle bioconjugates for breast cancer therapy. Biomaterials 2009;30:5737–50.

[113] Liu Y, Li W, Lao F, Liu Y, Wang L, Bai R, et al. Intracellular dynamics of cationic and anionic polystyrene nanoparticles without direct interaction with mitotic spindle and chromosomes. Biomaterials 2011;32:8291–303.

[114] Wu Y-N, Chen D-H, Shi X-Y, Lian C-C, Wang T-Y, Yeh C-S, et al. Cancer-cell-specific cytotoxicity of non-oxidized iron elements in iron core-gold shell NPs. Nanomedicine 2011;7:420–7.

[115] Panyam J, Sahoo SK, Prabha S, Bargar T, Labhasetwar V. Fluorescence and electron microscopy probes for cellular and tissue uptake of poly(d,l-lactide-co-glycolide) nanoparticles. Int J Pharm 2003;262:1–11.

[116] Angermüller S, Fahimi HD. Imidazole-buffered osmium tetroxide: an excellent stain for visualization of lipids in transmission electron microscopy. Histochem J 1982;14:823–35.

[117] Gratton SE a, Ropp P a, Pohlhaus PD, Luft JC, Madden VJ, Napier ME, et al. The effect of particle design on cellular internalization pathways. Proc Natl Acad Sci U S A 2008;105:11613–8.

[118] Jamuna K V. Immuno-histochemistry–application in ovarian function. Funct Genomic Approaches Enhancing Fertil Livest n.d.:17.

[119] Brauchle E, Schenke-Layland K. Raman spectroscopy in biomedicine - non-invasive in vitro analysis of cells and extracellular matrix components in tissues. Biotechnol J 2013;8:288–97.

[120] Notingher I, Hench LL. Raman microspectroscopy: a noninvasive tool for studies of individual living cells in vitro. Expert Rev Med Devices 2006;3:215–34.

[121] Cao YC, Jin R, Mirkin C a. Nanoparticles with Raman spectroscopic fingerprints for DNA and RNA detection. Science 2002;297:1536–40.

[122] Chernenko T, Matthäus C, Milane L, Quintero L, Amiji M, Diem M. Label-free Raman spectral imaging of intracellular delivery and degradation of polymeric nanoparticle systems. ACS Nano 2009;3:3552–9.

[123] Romero G, Estrela-Lopis I, Zhou J, Rojas E, Franco A, Espinel CS, et al. Surface Engineered Poly(lactide-co-glycolide) Nanoparticles for Intracellular Delivery: Uptake and Cytotoxicity-A Confocal Raman Microscopic Study. Biomacromolecules 2010;11:2993–9.

[124] Romero G, Estrela-Lopis I, Castro-Hartmann P, Rojas E, Llarena I, Sanz D, et al. Stepwise surface tailoring of carbon nanotubes with polyelectrolyte brushes and lipid layers to control their intracellular distribution and 'in vitro' toxicity. Soft Matter 2011;7:6883.

[125] Pyrgiotakis G, Bhowmick TK, Finton K, Suresh a K, Kane SG, Bellare JR, et al. Cell (A549)-particle (Jasada Bhasma) interactions using Raman spectroscopy. Biopolymers 2008;89:555–64.

[126] Van Apeldoorn A a, van Manen H-JJ, Bezemer JM, de Bruijn JD, van Blitterswijk CA, Otto C. Raman imaging of PLGA microsphere degradation inside macrophages. J Am Chem Soc 2004;126:13226–7.

[127] Sathuluri RR, Yoshikawa H, Shimizu E, Saito M, Tamiya E. Gold nanoparticle-based surface-enhanced Raman scattering for noninvasive molecular probing of embryonic stem cell differentiation. PLoS One 2011;6:e22802.

[128] Samanta A, Maiti KK, Soh K-S, Liao X, Vendrell M, Dinish US, et al. Ultrasensitive near-infrared Raman reporters for SERS-based in vivo cancer detection. Angew Chem Int Ed Engl 2011;50:6089–92.

[129] Baniukevic J, Hakki Boyaci I, Goktug Bozkurt A, Tamer U, Ramanavicius A, Ramanaviciene A. Magnetic gold nanoparticles in SERS-based sandwich immunoassay for antigen detection by well oriented antibodies. Biosens Bioelectron 2013;43:281–8.

[130] Radziuk D V, Mohwald H. Highly Effective Silver Nanoparticles for SERS Molecular Prints of Live Fibroblasts. Nanoscale 2014.

[131] Mütze J, Ohrt T, Schwille P. Fluorescence correlation spectroscopy in vivo. Laser Photon Rev 2011;5:52–67.

[132] Valeur B. Advanced Techniques in Fluorescence Spectroscopy. Mol. Fluoresc. Princ. Appl., vol. 8, 2001, p. 351–80.

[133] Elson EL. Fluorescence Correlation Spectroscopy. I. Conceptual Basis and Theory. Biopolymers 1974;13:1–27.

[134] Elson EL, Webb WW. Fluorescecne Correlation Spectroscopy. II. An Experimental Realization. Biopolymers 1974;13:29–61.

[135] Rigler R, Mets Ü, Widengren J, Kask P. Fluorescence correlation spectroscopy with high count rate and low background: analysis of translational diffusion. Eur Biophys J 1993;22:169–75.

[136] Bacia K, Schwille P. A dynamic view of cellular processes by in vivo fluorescence auto-and cross-correlation spectroscopy. Methods 2003;29:74–85.

[137] Leng X, Starchev K, Buffle J. Studied by Fluorescence Correlation Spectroscopy. Adsorpt J Int Adsorpt Soc 2002:7602–8.

[138] Waizenegger T, Fischer R, Brock R. Quantification of Cellular Uptake of Small Molecules. Microsc from Carl Zeiss n.d.

[139] Chen H, Farkas ER, Webb WW. Chapter 1: In vivo applications of fluorescence correlation spectroscopy. vol. 89. Elsevier Inc.; 2008.

[140] Gartner M, Mütze J, Ohrt T, Schwille P. Fluorescence lifetime correlation spectroscopy for precise concentration detection in vivo by background subtraction. Proc SPIE 2009;7368:73681V–73681V–7.

[141] Montenegro M, Amin F, Soenen SJ, Manshian B, Thiron T, Cornelissen M, et al. Cytotoxic Effects of Gold Nanoparticles: A Multiparametric Study. ACS Nano 2012;6:5767–83.

[142] Han JJ, Kiss C, Bradbury ARM, Werner JH. Time-Resolved, Confocal Single-Molecule Tracking of Individual Organic Dyes and Fluorescent Proteins in Three Dimensions. ACS Nano 2012;6:8922–32.

[143] Neugart F, Zappe A, Jelezko F, Tietz C, Boudou JP, Krueger A, et al. Dynamics of diamond nanoparticles in solution and cells. Nano Lett 2007;7:3588–91.

[144] Chen J, Nag S, Vidi P-A, Irudayaraj J. Single molecule in vivo analysis of toll-like receptor 9 and CpG DNA interaction. PLoS One 2011;6:e17991.

[145] Wang Y, Chen J, Irudayaraj J. Nuclear targeting dynamics of gold nanoclusters for enhanced therapy of HER2+ breast cancer. ACS Nano 2011;5:9718–25.

[146] Dong C, Irudayaraj J. Hydrodynamic size-dependent cellular uptake of aqueous QDs probed by fluorescence correlation spectroscopy. J Phys Chem B 2012;116:12125–32.

[147] Chen J, Irudayaraj J. Quantitative investigation of compartmentalized dynamics of ErbB2 targeting gold nanorods in live cells by single molecule spectroscopy. ACS Nano 2009;3:4071–9.

[148] Hans ML, Lowman AM. Biodegradable nanoparticles for drug delivery and targeting. Curr Opin Solid State Mater 2002;6:319–27.

[149] Makadia HK, Siegel SJ. Poly Lactic-co-Glycolic Acid (PLGA) as Biodegradable Controlled Drug Delivery Carrier. Polymers (Basel) 2011;3:1377–97.

[150] Lu L, Garcia CA, Mikos AG. In vitro degradation of thin poly(DL-lactic-co-glycolic acid) films. J Biomed Mater Res 1999;46:236–44.

[151] Anderson JJM, Shive MSM. Biodegradation and biocompatibility of PLA and PLGA microspheres. Adv Drug Deliv Rev 2012;28:5–24.

[152] Kumari A, Yadav SK, Yadav SC. Biodegradable polymeric nanoparticles based drug delivery systems. Colloids Surf B Biointerfaces 2010;75:1–18.

[153] Park TG. Degradation of poly (lactic-co-glycolic acid) microspheres: effect of copolymer composition. Biomaterials 1995;16:1123–30.

[154] Van De Ven H, Vermeersch M, Matheeussen A, Vandervoort J, Weyenberg W, Apers S, et al. PLGA nanoparticles loaded with the antileishmanial saponin β-aescin: Factor influence study and in vitro efficacy evaluation. Int J Pharm 2011;420:122–32.

[155] Reix N, Parat A, Seyfritz E, Van Der Werf R, Epure V, Ebel N, et al. In vitro uptake evaluation in Caco-2 cells and in vivo results in diabetic rats of insulin-loaded PLGA nanoparticles. Int J Pharm 2012;437:213–20.

[156] Chu C-H, Wang Y-C, Huang H-Y, Wu L-C, Yang C-S. Ultrafine PEG-coated poly(lactic-co-glycolic acid) nanoparticles formulated by hydrophobic surfactant-assisted one-pot synthesis for biomedical applications. Nanotechnology 2011;22:185601.

[157] Husmann M, Schenderlein S, Lück M, Lindner H, Kleinebudde P. Polymer erosion in PLGA microparticles produced by phase separation method. Int J Pharm 2002;242:277–80.

[158] Şengel-Türk CT, Hasçiçek C, Dogan AL, Esendagli G, Guc D, Gönül N. Preparation and in vitro evaluation of meloxicam-loaded PLGA nanoparticles on HT-29 human colon adenocarcinoma cells. Drug Dev Ind Pharm 2012;38:1107–16.

[159] Jensen DMK, Cun D, Maltesen MJ, Frokjaer S, Nielsen HM, Foged C. Spray drying of siRNA-containing PLGA nanoparticles intended for inhalation. J Control Release 2010;142:138–45.

[160] Nie H, Lee LY, Tong H, Wang CH. PLGA/chitosan composites from a combination of spray drying and supercritical fluid foaming techniques: New carriers for DNA delivery. J Control Release 2008;129:207–14.

[161] Xie H, Smith JW. Fabrication of PLGA nanoparticles with a fluidic nanoprecipitation system. J Nanobiotechnology 2010;8:18.

[162] Yadav KS, Sawant KK. Modified nanoprecipitation method for preparation of cytarabine-loaded PLGA nanoparticles. AAPS PharmSciTech 2010;11:1456–65.

[163] Ballauff M, Borisov O. Polyelectrolyte brushes. Curr Opin Colloid Interface Sci 2006;11:316–23.

[164] Azzaroni O. Polymer brushes here, there, and everywhere: Recent advances in their practical applications and emerging opportunities in multiple research fields. J Polym Sci Part A Polym Chem 2012;50:3225–58.

[165] Siegwart DJ, Oh JK, Matyjaszewski K. ATRP in the design of functional materials for biomedical applications. Prog Polym Sci 2012;37:18–37.

[166] Claxton N, Fellers T, Davidson M. Laser scanning confocal microscopy. Olympus Available Online … 2006.

[167] Wei Q, Ji J, Shen J. Synthesis of Near-Infrared Responsive Gold Nanorod/PNIPAAm Core/Shell Nanohybrids via Surface Initiated ATRP for Smart Drug Delivery. Macromol Rapid Commun 2008;29:645–50.

[168] Yuan L, Tang Q, Yang D, Zhang JZ, Zhang F, Hu J. Preparation of pH-Responsive Mesoporous Silica Nanoparticles and Their Application in Controlled Drug Delivery. J Phys Chem C 2011;115:9926–32.

[169] Yoon JA, Gayathri C, Gil RR, Kowalewski T, Matyjaszewski K. Comparison of the Thermoresponsive Deswelling Kinetics of Poly(2-(2-methoxyethoxy)ethyl methacrylate) Hydrogels Prepared by ATRP and FRP. Macromolecules 2010;43:4791–7.

[170] Sugawara A, Yamane S, Akiyoshi K. Nanogel-Templated Mineralization: Polymer-Calcium Phosphate Hybrid Nanomaterials. Macromol Rapid Commun 2006;27:441–6.

[171] Wang J, Chen J-S, Zong J-Y, Zhao D, Li F, Zhuo R-X, et al. Calcium Carbonate/Carboxymethyl Chitosan Hybrid Microspheres and Nanospheres for Drug Delivery. J Phys Chem C 2010;114:18940–5.

[172] Fischer V, Bannwarth MB, Jakob G, Landfester K, Munoz-Espi R. Luminescent and Magnetoresponsive Multifunctional Chalcogenide/Polymer Hybrid Nanoparticles. J Phys Chem C 2013;117:5999–6005.

[173] Sanchez C, Belleville P, Popall M, Nicole L. Applications of advanced hybrid organic-inorganic nanomaterials: from laboratory to market. Chem Soc Rev 2011;40:696–753.

[174] Taylor-Pashow KML, Della Rocca J, Huxford RC, Lin W. Hybrid nanomaterials for biomedical applications. Chem Commun (Camb) 2010;46:5832–49.

[175] Aili D, Mager M, Roche D, Stevens MM. Hybrid nanoparticle-liposome detection of phospholipase activity. Nano Lett 2011;11:1401–5.

[176] Park J-H, von Maltzahn G, Ruoslahti E, Bhatia SN, Sailor MJ. Micellar Hybrid Nanoparticles for Simultaneous Magnetofluorescent Imaging and Drug Delivery. Angew Chemie 2008;120:7394–8.

[177] Shi X, Wang S, Sun H, Baker JR. Improved biocompatibility of surface functionalized dendrimer-entrapped gold nanoparticles. Soft Matter 2007;3:71.

[178] Quesada M, Muniesa C, Botella P. Hybrid PLGA-Organosilica Nanoparticles with Redox-Sensitive Molecular Gates. Chem Mater 2013;25:2597–602.

[179] Huh Y-M, Lee E-S, Lee J-H, Jun Y -w., Kim P-H, Yun C-O, et al. Hybrid Nanoparticles for Magnetic Resonance Imaging of Target-Specific Viral Gene Delivery. Adv Mater 2007;19:3109–12.

[180] Sailor MJ, Park J-H. Hybrid nanoparticles for detection and treatment of cancer. Adv Mater 2012;24:3779–802.

[181] Doane TL, Chuang C-H, Hill RJ, Burda C. Nanoparticle ζ -potentials. Acc Chem Res 2012;45:317–26.

[182] Malvern Instruments Ltd. Zetasizer Nano User Manual. Malvern Instruments Ltd.; 2007.

[183] Merkus H. Particle size measurements, 2008.

[184] Brar SK, Verma M. Measurement of nanoparticles by light-scattering techniques. TrAC Trends Anal Chem 2011;30:4–17.

[185] Bartolo B. Fluorescence Spectroscopy and Energy Transfer Processes in Biological Systems. In: Bartolo B Di, Collins J, editors. Biophotonics Spectrosc. Imaging, Sensing, Manip. SE - 6, Springer Netherlands; 2011, p. 107–71.

[186] García-González D, Baeten V, Pierna JF, Tena N. Infrared, Raman, and Fluorescence Spectroscopies: Methodologies and Applications. In: Aparicio R, Harwood J, editors. Handb. Olive Oil SE - 10, Springer US; 2013, p. 335–93.

[187] Neto LM, Milori DMBP, Silva WTL Da, Sim ML. Biophysico-Chemical Processes Involving Natural Nonliving Organic Matter in Environmental Systems, John Wiley & Sons, Inc.; 2009.

[188] Stuart B. Analytical techniques in materials conservation, John Wiley & Sons, Inc.; 2007.

[189] Wilson T. Confocal Microscopy. Microscopy 2005:69–77.

[190] Lavrentovich O. Confocal Fluorescence Microscopy. Charact Mater 2012.

[191] Földes-Papp Z, Demel U, Tilz GP. Laser scanning confocal fluorescence microscopy: an overview. Int Immunopharmacol 2003;3:1715–29.

[192] Caruso JL, Levenson RM, Howell DN. 4 - Diagnostic applications of confocal microscopy. In: Ingram P, Shelburne JD, Roggli VL, LeFurgey ABT-BA of MA, editors., San Diego: Academic Press; 1999, p. 123–48.

[193] Oswald S. X-Ray Photoelectron Spectroscopy in Analysis of Surfaces. Encycl. Anal. Chem., John Wiley & Sons, Ltd; 2006.

[194] Rivière JC. Surface Analysis. Handb. Anal. Tech., Wiley-VCH Verlag GmbH; 2001, p. 851–949.

[195] Introduction. Transm. Electron Microsc. SE - 1, vol. 36, Springer New York; 2008, p. 1–15.

[196] Klang V, Valenta C, Matsko NB. Electron microscopy of pharmaceutical systems. Micron 2013;44:45–74.

[197] Lascialfari A, Corti M. Basic concepts of Magnetic Resonance Imaging. NMR-MRI, μSR Mössbauer Spectrosc. Mol. Magnets SE - 4, Springer Milan; 2007, p. 89–110.

[198] Roberts TPL, van Bruggen N. Principles of MRI contrast. Biomed Imaging Exp Neurosci 2003:1–20.

[199] Henel G, Schmitz J. Basic Theory and Clinical Applications of Flow Cytometry. Lab Med 2007;38:428–36.

[200] Belyanskaya L, Manser P, Spohn P, Bruinink A, Wick P. The reliability and limits of the MTT reduction assay for carbon nanotubes–cell interaction. Carbon N Y 2007;45:2643–8.

[201] Yang S, Gao L. Controlled synthesis and self-assembly of CeO2 nanocubes. J Am Chem Soc 2006;128:9330–1.

[202] Srinivas A, Rao PJ, Selvam G, Murthy PB, Reddy PN. Acute inhalation toxicity of cerium oxide nanoparticles in rats. Toxicol Lett 2011;205:105–15.

[203] Wang C, Lin S. Preparing an active cerium oxide catalyst for the catalytic incineration of aromatic hydrocarbons. Appl Catal A Gen 2004;268:227–33.

[204] Zhuang Q, Qin* Y, Chang L. Promoting effect of cerium oxide in supported nickel catalyst for hydrocarbon steam-reforming. Appl Catal 1991;70:1–8.

[205] Silva AM., Marques RR., Quinta-Ferreira RM. Catalysts based in cerium oxide for wet oxidation of acrylic acid in the prevention of environmental risks. Appl Catal B Environ 2004;47:269–79.

[206] Kosynkin VD, Arzgatkina A a. The study of process production of polishing powder based on cerium dioxide. J Alloy … 2000;303-304:421–5.

[207] Janoš P, Petrák M. Preparation of ceria-based polishing powders from carbonates. J Mater Sci 1991;26:4062–6.

[208] Cassee FR, van Balen EC, Singh C, Green D, Muijser H, Weinstein J, et al. Exposure, health and ecological effects review of engineered nanoscale cerium and cerium oxide associated with its use as a fuel additive. Crit Rev Toxicol 2011;41:213–29.

[209] Park B, Donaldson K, Duffin R, Tran L, Kelly F, Mudway I, et al. Hazard and risk assessment of a nanoparticulate cerium oxide-based diesel fuel additive - a case study. Inhal Toxicol 2008;20:547–66.

[210] Deshpande S, Patil S, Kuchibhatla SVNT, Seal S. Size dependency variation in lattice parameter and valency states in nanocrystalline cerium oxide. Appl Phys Lett 2005;87.

[211] Korsvik C, Patil S, Seal S, Self WT. Superoxide dismutase mimetic properties exhibited by vacancy engineered ceria nanoparticles. Chem Commun (Camb) 2007:1056–8.

[212] Asati A, Santra S, Kaittanis C, Nath S, Perez JM. Oxidase-like activity of polymer-coated cerium oxide nanoparticles. Angew Chem Int Ed Engl 2009;48:2308–12.

[213] Perez JM, Asati A, Nath S, Kaittanis C. Synthesis of biocompatible dextran-coated nanoceria with pH-dependent antioxidant properties. Small 2008;4:552–6.

[214] Tarnuzzer RW, Colon J, Patil S, Seal S. Vacancy engineered ceria nanostructures for protection from radiation-induced cellular damage. Nano Lett 2005;5:2573–7.

[215] Lee SS, Song W, Cho M, Puppala HL, Nguyen P, Zhu H, et al. Antioxidant properties of cerium oxide nanocrystals as a function of nanocrystal diameter and surface coating. ACS Nano 2013;7:9693–703.

[216] Karakoti A, Singh S, Dowding JM, Seal S, Self WT. Redox-active radical scavenging nanomaterials. Chem Soc Rev 2010;39:4422–32.

[217] Hirst SM, Karakoti AS, Tyler RD, Sriranganathan N, Seal S, Reilly CM. Anti-inflammatory properties of cerium oxide nanoparticles. Small 2009;5:2848–56.

[218] Hussain S, Al-Nsour F, Rice AB, Marshburn J, Yingling B, Ji Z, et al. Cerium dioxide nanoparticles induce apoptosis and autophagy in human peripheral blood monocytes. ACS Nano 2012;6:5820–9.

[219] Park E-J, Choi J, Park Y-K, Park K. Oxidative stress induced by cerium oxide nanoparticles in cultured BEAS-2B cells. Toxicology 2008;245:90–100.

[220] Lin W, Huang Y, Zhou X-D, Ma Y. Toxicity of Cerium Oxide Nanoparticles in Human Lung Cancer Cells. Int J Toxicol 2006;25:451–7.

[221] Xia T, Kovochich M, Liong M, Ma L, Gilbert B, Shi ŕH, et al. Comparison of the mechanism of toxicity of zinc oxide and cerium oxide nanoparticles based on dissolution and oxidative stress properties. ACS Nano 2008;2:2121–34.

[222] Lord MS, Jung M, Teoh WY, Gunawan C, Vassie JA, Amal R, et al. Cellular uptake and reactive oxygen species modulation of cerium oxide nanoparticles in human monocyte cell line U937. Biomaterials 2012;33:7915–24.

[223] Celardo I, Pedersen JZ, Traversa E, Ghibelli L. Pharmacological potential of cerium oxide nanoparticles. Nanoscale 2011;3:1411–20.

[224] Singh S, Kumar A, Karakoti A, Seal S, Self WT. Unveiling the mechanism of uptake and sub-cellular distribution of cerium oxide nanoparticles. Mol Biosyst 2010;6:1813–20.

[225] Wason M, Zhao J. Cerium oxide nanoparticles: potential applications for cancer and other diseases. Am J Transl Res 2013;5:126–31.

[226] Limbach LK, Li Y, Grass RN, Brunner TJ, Hintermann M a, Muller M, et al. Oxide nanoparticle uptake in human lung fibroblasts: effects of particle size, agglomeration, and diffusion at low concentrations. Environ Sci Technol 2005;39:9370–6.

[227] Kim CK, Kim T, Choi I-Y, Soh M, Kim D, Kim Y-J, et al. Ceria nanoparticles that can protect against ischemic stroke. Angew Chemie 2012;51:11039–43.

[228] Das S, Dowding JM, Klump KE, McGinnis JF, Self W, Seal S. Cerium oxide nanoparticles: applications and prospects in nanomedicine. Nanomedicine 2013;8:1483–508.

[229] Romero G, Estrela-Lopis I, Castro-Hartmann P. Stepwise surface tailoring of carbon nanotubes with polyelectrolyte brushes and lipid layers to control their intracellular distribution and 'in vitro' toxicity. Soft Matter 2011:6883–90.

[230] Llarena I, Ramos JJI, Donath E, Moya SE. Holes and ledges created by multilayer assembly on polyelectrolyte brushes: a novel route for the three-dimensional nanoscale design of surfaces. Macromol Rapid Commun 2010;31:526–31.

[231] Jiang J, Oberdörster G, Biswas P. Characterization of size, surface charge, and agglomeration state of nanoparticle dispersions for toxicological studies. J Nanoparticle Res 2008;11:77–89.

[232] Goharshadi EK, Samiee S, Nancarrow P. Fabrication of cerium oxide nanoparticles: characterization and optical properties. J Colloid Interface Sci 2011;356:473–80.

[233] Willis H., Zichy VJ., Hendra P. The laser-Raman and infra-red spectra of poly(methyl methacrylate). Polymer (Guildf) 1969;10:737–46.

[234] Asati A, Santra S, Kaittanis C, Perez JM, Florida O. Surface-charge-dependent cell localization and cytotoxicity of cerium oxide nanoparticles. ACS Nano 2010;4:5321–31.

[235] Wagner CD, Naumkin AV, Kraut-Vass A, Allison JW, Powell CJ, Rumble JRJ. NIST Standard Reference Database 20 version 3.4. 2004.

[236] Pireaux JJ. High resolution XPS of organic polymers: the scienta ESCA300 database. J Electron Spectros Relat Phenomena 1993;62:371–2.

[237] Pireaux JJ. High resolution XPS of organic polymers: the scienta ESCA300 database. J Electron Spectros Relat Phenomena 1993;62:371–2.

[238] Irigoyen J, Arekalyan VB, Navoyan Z, Iturri J, Moya SE, Donath E. Spherical polyelectrolyte brushes' constant zeta potential with varying ionic strength: an electrophoretic study using a hairy layer approach. Soft Matter 2013;9:11609.

[239] Chen Y, Xiong G, Arriaga E a. CE analysis of the acidic organelles of a single cell. Electrophoresis 2007;28:2406–15.

[240] Romero G. Zhou J., Rojas E., Franco A., Sanchez Espinal C., González Fernández A., Gao C., Donath E. and Moya S. E-LII, Romero G, Estrela-Lopis I, Zhou J, Rojas E, Franco A, et al. Surface Engineered Poly(lactide-co-glycolide) Nanoparticles for Intracellular Delivery: Uptake and Cytotoxicity- A Confocal Raman Microscopic Study. Biomacromolecules 2010;11:2993–9.

[241] Krafft C. Mapping of single cells by near infrared Raman microspectroscopy. Vib Spectrosc 2003;32:75–83.

[242] Movasaghi Z, Rehman S, Rehman IU. Raman Spectroscopy of Biological Tissues. Appl Spectrosc Rev 2007;42:493–541.

[243] Estrela-Lopis I, Romero G, Rojas E, Moya SE, Donath E, Romero G. Estrela-Lopis I., Donath E. and Moya S. RE. Nanoparticle uptake and their co-localization with cell compartments – a confocal Raman microscopy study at single cell level. J Phys Conf Ser 2011;6:012017.

[244] Behnia R, Munro S. Organelle identity and the signposts for membrane traffic. Nature 2005;438:597–604.

[245] Meng H, Yang S, Li Z, Xia T, Chen J, Ji Z, et al. Aspect ratio determines the quantity of mesoporous silica nanoparticle uptake by a small GTPase-dependent macropinocytosis mechanism. ACS Nano 2011;5:4434–47.

[246] Dangoria NS, Breau WC, Anderson HA, Cishek DM, Norkin LC. Extracellular simian virus 40 induces an ERK/MAP kinase-independent signalling pathway that activates primary response genes and promotes virus entry. J Gen Virol 1996;77 (Pt 9):2173–82.

[247] Werling D, Hope J. Involvement of caveolae in the uptake of respiratory syncytial virus antigen by dendritic cells. J Leukoc Biol 1999;66:50–8.

[248] Wang LH, Rothberg KG, Anderson RG. Mis-assembly of clathrin lattices on endosomes reveals a regulatory switch for coated pit formation. J Cell Biol 1993;123:1107–17.

[249] Vercauteren D, Vandenbroucke RE, Jones AT, Rejman J, Demeester J, De Smedt SC, et al. The use of inhibitors to study endocytic pathways of gene carriers: optimization and pitfalls. Mol Ther 2010;18:561–9.

[250] Tahara K, Sakai T, Yamamoto H, Takeuchi H, Hirashima N, Kawashima Y. Improved cellular uptake of chitosan-modified PLGA nanospheres by A549 cells. Int J Pharm 2009;382:198–204.

[251] Jackman MR, Shurety W, Ellis J a, Luzio JP. Inhibition of apical but not basolateral endocytosis of ricin and folate in Caco-2 cells by cytochalasin D. J Cell Sci 1994;107 (Pt 9:2547–56.

[252] Chiu Y-L, Ho Y-C, Chen Y-M, Peng S-F, Ke C-J, Chen K-J, et al. The characteristics, cellular uptake and intracellular trafficking of nanoparticles made of hydrophobically-modified chitosan. J Control Release 2010;146:152–9.

[253] Dausend J, Musyanovych A, Dass M, Walther P, Schrezenmeier H, Landfester K, et al. Uptake mechanism of oppositely charged fluorescent nanoparticles in HeLa cells. Macromol Biosci 2008;8:1135–43.

[254] Perna G, Lastella M, Lasalvia M, Mezzenga E, Capozzi V. Raman spectroscopy and atomic force microscopy study of cellular damage in human keratinocytes treated with HgCl2. J Mol Struct 2007;834-836:182–7.

[255] Lee J, Mahendra S, Alvarez PJJ. Nanomaterials in the Construction Industry: A Review of Their Applications 2010;4.

[256] Description of Carboxy-H2DCFDA 2014:http://www.lifetechnologies.com/order/catalog/prod.

[257] Moros M, Pelaz B, López-Larrubia P, García-Martin ML, Grazú V, de la Fuente JM. Engineering biofunctional magnetic nanoparticles for biotechnological applications. Nanoscale 2010;2:1746–55.

[258] El-Boubbou K, Huang X. Glyco-nanomaterials: translating insights from the 'sugar-code' to biomedical applications. Curr Med Chem 2011;18:2060–78.

[259] Moros, María; Hernáez, Bruno; Garet, Elina; Dias, Jorge T.; Sáez, Berta; Grazú, Valeria; González-Fernández, África; Alonso, Covadonga; De la Fuente J. Monosaccharides versus PEG- Functionalized NPs: Influence in the Cellular Uptake. ACS Nano 2012;6:1565–77.

[260] Lynch I, Salvati A, Dawson K a. Protein-nanoparticle interactions: What does the cell see? Nat Nanotechnol 2009;4:546–7.

[261] Milani S, Bombelli FB, Pitek AS, Dawson K a, Rädler J. Reversible versus irreversible binding of transferrin to polystyrene nanoparticles: soft and hard corona. ACS Nano 2012;6:2532–41.

[262] Dominguez-Medina S, McDonough S, Swanglap P, Landes CF, Link S. In situ measurement of bovine serum albumin interaction with gold nanospheres. Langmuir ACS J Surfaces Colloids 2012;28:9131–9.

[263] Maffre P, Nienhaus K, Amin F, Parak WJ, Nienhaus GU. Characterization of protein adsorption onto FePt nanoparticles using dual-focus fluorescence correlation spectroscopy. Beilstein J Nanotechnol 2011;2:374–83.

[264] Jiang X, Weise S, Hafner M, Röcker C, Zhang F, Parak WJ, et al. Quantitative analysis of the protein corona on FePt nanoparticles formed by transferrin binding. J R Soc Interface 2010;7 Suppl 1:S5–S13.

[265] Westcott SL, Oldenburg SJ, Lee TR, Halas NJ. Formation and Adsorption of Clusters of Gold Nanoparticles onto Functionalized Silica Nanoparticle Surfaces 1998;7463:5396–401.

[266] Nam J, Won N, Jin H, Chung H, Kim S. pH-Induced aggregation of gold nanoparticles for photothermal cancer therapy. J Am Chem Soc 2009;131:13639–45.

[267] Bao F, Yao J-L, Gu R-A. Synthesis of magnetic Fe2O3/Au core/shell nanoparticles for bioseparation and immunoassay based on surface-enhanced Raman spectroscopy. Langmuir ACS J Surfaces Colloids 2009;25:10782–7.

[268] Sengupta P, Garai K, Balaji J, Periasamy N, Maiti S. Measuring size distribution in highly heterogeneous systems with fluorescence correlation spectroscopy. Biophys J 2003;84:1977–84.

[269] Marradi M, Chiodo F, García I, Penadés S. Glyconanoparticles as multifunctional and multimodal carbohydrate systems. Chem Soc Rev 2013;42:4728–45.

[270] Martínez-Avila O, Hijazi K, Marradi M, Clavel C, Campion C, Kelly C, et al. Gold manno-glyconanoparticles: multivalent systems to block HIV-1 gp120 binding to the lectin DC-SIGN. Chemistry 2009;15:9874–88.

[271] Zemplén G. Abbau der reduzierenden Biosen, VII.: Konstitutions-Ermittlung der Maltose. Berichte Der Dtsch Chem Gesellschaft (A B Ser 1927;60:1555–64.

[272] Hostetler MJ, Templeton AC, Murray RW, Hill C, Carolina N. Dynamics of Place-Exchange Reactions on Monolayer-Protected Gold Cluster Molecules. Langmuir 1999;15:3782–9.

[273] Hostetler MJ, Wingate JE, Zhong C, Harris JE, Vachet RW, Clark MR, et al. Alkanethiolate Gold Cluster Molecules with Core Diameters from 1.5 to 5.2 nm: Core and Monolayer Properties as a Function of Core Size. Langmuir 1998;14:17–30.

[274] Reynolds M, Marradi M, Imberty A, Penadés S, Pérez S. Multivalent gold glycoclusters: high affinity molecular recognition by bacterial lectin PA-IL. Chemistry 2012;18:4264–73.

[275] Bacia K, Majoul I V, Schwille P. Probing the endocytic pathway in live cells using dual-color fluorescence cross-correlation analysis. Biophys J 2002;83:1184–93.

[276] Luby-Phelps K, Mujumdar S, Mujumdar R. A novel fluorescence ratiometric method confirms the low solvent viscosity of the cytoplasm. Biophys J 1993;65:236–42.

[277] Suhling K, Siegel J, Lanigan PMP, Leveque-Fort S, Webb SED, Phillips D, et al. Time-resolved fluorescence anisotropy imaging applied to live cells. Opt Lett 2004;29:584.

[278] Kuimova MK, Yahioglu G, Levitt J a, Suhling K. Molecular rotor measures viscosity of live cells via fluorescence lifetime imaging. J Am Chem Soc 2008;130:6672–3.

[279] Dix JA, Verkman AS. Mapping of fluorescence anisotropy in living cells by ratio imaging Application to cytoplasmic viscosity Polarizer alignment. Biophys J 1990;57:231–40.

[280] Soppimath KS, Aminabhavi TM, Kulkarni a R, Rudzinski WE. Biodegradable polymeric nanoparticles as drug delivery devices. J Control Release 2001;70:1–20.

[281] Roney C, Kulkarni P, Arora V, Antich P, Bonte F, Wu A, et al. Targeted nanoparticles for drug delivery through the blood-brain barrier for Alzheimer's disease. J Control Release 2005;108:193–214.

[282] Langer R. New methods of drug delivery. Science (80-) 1990;249:1527–33.

[283] Ishihara T, Mizushima T, Ishihara T. T and M. Techniques for efficient entrapment of pharmaceuticals in biodegradable solid micro/nanoparticles. Expert Opin Drug Deliv 2010;7:565–75.

[284] Patil YB, Swaminathan SK, Sadhukha T, Ma L, Panyam J. The use of nanoparticle-mediated targeted gene silencing and drug delivery to overcome tumor drug resistance. Biomaterials 2010;31:358–65.

[285] Cohen H, Levy RJ, Gao J, Fishbein I, Kousaev V, Sosnowski S, et al. Sustained delivery and expression of DNA encapsulated in polymeric nanoparticles. Gene Ther 2000;7:1896–905.

[286] Allémann E, Leroux JC, Gurny R, Doelker E. In vitro extended-release properties of drug-loaded poly(DL-lactic acid) nanoparticles produced by a salting-out procedure. Pharm Res 1993;10:1732–7.

[287] Panyam J, Labhasetwar V. Biodegradable nanoparticles for drug and gene delivery to cells and tissue. Adv Drug Deliv Rev 2003;55:329–47.

[288] Scholes PD, Coombes AGA, Illum L, Davis SS, Vert M, Davies MC. The preparation of sub-200 nm poly(lactide-co-glycolide) microspheres for site-specific drug delivery. J Control Release 1993;25:145–53.

[289] Weiss B, Schneider M, Muys L, Taetz S, Neumann D, Schaefer UF, et al. Coupling of biotin-(poly(ethylene glycol))amine to poly(D,L-lactide-co- glycolide) nanoparticles for versatile surface modification. Bioconjug Chem 2007;18:1087–94.

[290] Mundargi RC, Babu VR, Rangaswamy V, Patel P, Aminabhavi TM. Nano/micro technologies for delivering macromolecular therapeutics using poly(d,l-lactide-co-glycolide) and its derivatives. J Control Release 2008;125:193–209.

[291] Yang Y, Chia H, Chung T. Effect of preparation temperature on the characteristics and release profiles of PLGA microspheres containing protein fabricated by double-emulsion solvent extraction/evaporation method. J Control Release 2000;69:81–96.

[292] Hornig S, Heinze T, Becer CR, Schubert US. Synthetic polymeric nanoparticles by nanoprecipitation. J Mater Chem 2009;19:3838–40.

[293] Bilati U, Allémann E, Doelker E. Development of a nanoprecipitation method intended for the entrapment of hydrophilic drugs into nanoparticles. Eur J Pharm Sci 2005;24:67–75.

[294] Zambaux MF, Bonneaux F, Gref R, Dellacherie E, Vigneron C. Preparation and characterization of protein C-loaded PLA nanoparticles. J Control Release 1999;60:179–88.

[295] Doiron AL, Homan KA, Emelianov S, Brannon-Peppas L. Poly(lactic-co-glycolic) acid as a carrier for imaging contrast agents. Pharm Res 2009;26:674–82.

[296] Panyam J, Dali MM, Sahoo SK, Ma W, Chakravarthi SS, Amidon GL, et al. Polymer degradation and in vitro release of a model protein from poly(D,L-lactide-co-glycolide) nano- and microparticles. J Control Release Off J Control Release Soc 2003;92:173–87.

[297] Fortunati E, Latterini L, Rinaldi S, Kenny JM, Armentano I. PLGA/Ag nanocomposites: in vitro degradation study and silver ion release. J Mater Sci Mater Med 2011;22:2735–44.

[298] Park TG. Degradation of poly(lactic-co-glycolic acid) microspheres: effect of copolymer composition. Biomaterials 1995;16:1123–30.

[299] Shalaby SW. Biomedical Polymers: Designed-To-Degrade Systems. Hanser Publishers; 1994.

[300] Mittal G, Sahana DK, Bhardwaj V, Ravi Kumar MN V. Estradiol loaded PLGA nanoparticles for oral administration: effect of polymer molecular weight and copolymer composition on release behavior in vitro and in vivo. J Control Release Off J Control Release Soc 2007;119:77–85.

[301] Zhou J, Romero G, Rojas E, Ma L, Moya S, Gao C. Layer by Layer chitosan/alginate coatings on poly(lactide-co-glycolide) nanoparticles for antifouling protection and Folic acid binding to achieve selective cell targeting. J Colloid Interface Sci 2010;345:241–7.

[302] Horisawa E, Kubota K, Tuboi I, Sato K, Yamamoto H, Takeuchi H, et al. Size-dependency of DL-lactide/glycolide copolymer particulates for intra-articular delivery system on phagocytosis in rat synovium. Pharm Res 2002;19:132–9.

[303] Jeffery H, Davis S, O'hagan D. The preparation and characterisation of poly (lactide-co-glycolide) microparticles. I: Oil-in-water emulsion solvent evaporation. Int J Pharm 1991;77:169–75.

[304] Lopez Arbeloa F, Lopez Arbeloa T, Tapia Estevez MJ, Lopez Arbeloa I. Photophysics of rhodamines: molecular structure and solvent effects. J Phys Chem 1991;95:2203–8.

[305] Upez F. Molecular structure effects on the lasing properties of rhodamines. J Photochem Photobiol A Chem 1990;55:97–103.

[306] Fessi H, Piusieux F, Devissaguet JP, Ammoury N, Benita S. Nanocapsule formation by interfacial polymer deposition following solvent displacement. Int J Pharm 1989;55:R1–R4.

[307] Romero G. Zhou J., Rojas E., Franco A., Sanchez Espinal C., González Fernández A., Gao C., Donath E. and Moya S. E-LI. Surface Engineered Poly(lactide-co-glycolide) Nanoparticles for Intracellular Delivery: Uptake and Cytotoxicity- A Confocal Raman Microscopic Study. Biomacromolecules 2010;11:2993–9.

[308] Zhou J. Rojas E., Ma L., Moya S. and Gao C. RG. Layer by Layer chitosan/alginate coatings on poly(lactide-co-glycolide) nanoparticles for

antifouling protection and Folic acid binding to achieve selective cell targeting. J Colloid Interface Sci 2010;345:241–7.

[309] Qaddoumi MG, Gukasyan HJ, Davda J, Labhasetwar V, Kim K-J, Lee VHL. Clathrin and caveolin-1 expression in primary pigmented rabbit conjunctival epithelial cells: role in PLGA nanoparticle endocytosis. Mol Vis 2003;9:559–68.

[310] Best QA, Xu R, McCarroll ME, Wang L, Dyer DJ. Design and Investigation of a Series of Rhodamine-Based Fluorescent Probes for Optical Measurements of pH. Org Lett 2010;12:3219–21.

[311] Bach G, Chen CS, Pagano RE. Elevated lysosomal pH in mucolipidosis type IV cells. Clin. Chim. Acta, vol. 280, 1999, p. 173–9.

[312] Astete CEC, Sabliov CCM. Synthesis and characterization of PLGA nanoparticles. J Biomater Sci Polym Ed 2006;17:247–89.

[313] Nathan C. Neutrophils and immunity: challenges and opportunities. Nat Rev Immunol 2006;6:173–82.

[314] Tseng JC, Kung AL. In vivo imaging of inflammatory phagocytes. Chem Biol 2012;19:1199–209.

[315] Amulic B, Cazalet C, Hayes GL, Metzler KD, Zychlinsky A. Neutrophil Function: From Mechanisms to Disease. Annu Rev Immunol 2012;30:459–89.

[316] Dorward DA, Lucas CD, Rossi AG, Haslett C, Dhaliwal K. Imaging inflammation: Molecular strategies to visualize key components of the inflammatory cascade, from initiation to resolution. Pharmacol Ther 2012;135:182–99.

[317] Srinivas M, Aarntzen EHJG, Bulte JWM, Oyen WJ, Heerschap A, de Vries IJM, et al. Imaging of cellular therapies. Adv Drug Deliv Rev 2010;62:1080–93.

[318] Bao G, Mitragotri S, Tong S. Multifunctional nanoparticles for drug delivery and molecular imaging. Annu Rev Biomed Eng 2013;15:253–82.

[319] Gil PR, Parak WJ. Composite nanoparticles take aim at cancer. ACS Nano 2008;2:2200–5.

[320] Ntziachristos V, Ripoll J, Wang L V, Weissleder R. Looking and listening to light: the evolution of whole-body photonic imaging. Nat Biotechnol 2005;23:313–20.

[321] Baraki H, Zinne N, Wedekind D, Meier M, Bleich A, Glage S, et al. Magnetic Resonance Imaging of Soft Tissue Infection with Iron Oxide Labeled Granulocytes in a Rat Model. PLoS One 2012;7.

[322] Sah H, Thoma L a, Desu HR, Sah E, Wood GC. Concepts and practices used to develop functional PLGA-based nanoparticulate systems. Int J Nanomedicine 2013;8:747–65.

[323] Jokerst J V, Khademi C, Gambhir SS. Intracellular aggregation of multimodal silica nanoparticles for ultrasound-guided stem cell implantation. Sci Transl Med 2013;5:177ra35.

[324] Moros M, Hernáez B, Garet E, Dias JT, Sáez B, Grazú V, et al. Monosaccharides versus PEG-functionalized NPs: influence in the cellular uptake. ACS Nano 2012;6:1565–77.

[325] Kim JS, Cho KJ, Tran TH, Nurunnabi M, Moon TH, Hong SM, et al. In vivo NIR imaging with CdTe/CdSe quantum dots entrapped in PLGA nanospheres. J Colloid Interface Sci 2011;353:363–71.

[326] Ji H, Houghton AM, Mariani TJ, Perera S, Kim CB, Padera R, et al. K-ras activation generates an inflammatory response in lung tumors. Oncogene 2006;25:2105–12.

[327] Scholes P, Coombes A, Illum L. The preparation of sub-200 nm poly (lactide-co-glycolide) microspheres for site-specific drug delivery. J Control … 1993;25:145–53.

[328] Zhou J, Romero G, Rojas E, Moya S, Ma L, Gao C, et al. Folic Acid Modified Poly(lactide-co-glycolide) Nanoparticles, Layer-by-Layer Surface Engineered for Targeted Delivery. Macromol Chem Phys 2010;211:404–11.

[329] Zhou J, Moya S, Ma L, Gao C, Shen J, Zhou J. Ma L., Gao C. and Shen J. MS. Polyelectrolyte coated PLGA nanoparticles: templation and release behavior. Macromol Biosci 2009;9:326–35.

[330] Pons T, Medintz IL, Sapsford KE, Higashiya S, Grimes AF, English DS, et al. On the quenching of semiconductor quantum dot photoluminescence by proximal gold nanoparticles. Nano Lett 2007;7:3157–64.

[331] Zhang J, Badugu R, Lakowicz JR. Fluorescence Quenching of CdTe Nanocrystals by Bound Gold Nanoparticles in Aqueous Solution. Plasmonics 2008;3:3–11.

[332] Qin J, Laurent S, Jo YS, Roch a., Mikhaylova M, Bhujwalla ZM, et al. A High-Performance Magnetic Resonance ImagingT2 Contrast Agent. Adv Mater 2007;19:1874–8.

[333] Mant A, Tourniaire G, Diaz-Mochon JJ, Elliott TJ, Williams AP, Bradley M. Polymer microarrays: Identification of substrates for phagocytosis assays. Biomaterials 2006;27:5299–306.

[334] Elbim C, Lizard G. Flow cytometric investigation of neutrophil oxidative burst and apoptosis in physiological and pathological situations. Cytometry A 2009;75:475–81.

[335] Dahlgren C, Karlsson A. Respiratory burst in human neutrophils. J Immunol Methods 1999;232:3–14.

[336] Rothe G, Valet G. Flow cytometric analysis of respiratory burst activity in phagocytes with hydroethidine and 2',7'-dichlorofluorescin. J Leukoc Biol 1990;47:440–8.

[337] Zhao H, Joseph J, Fales HM, Sokoloski EA, Levine RL, Vasquez-Vivar J, et al. Detection and characterization of the product of hydroethidine and intracellular superoxide by HPLC and limitations of fluorescence. Proc Natl Acad Sci U S A 2005;102:5727–32.

[338] Shukla R, Bansal V, Chaudhary M, Basu A, Bhonde RR, Sastry M. Biocompatibility of gold nanoparticles and their endocytotic fate inside the cellular compartment: a microscopic overview. Langmuir 2005;21:10644–54.

List of Publications

Surface modification of cerium oxide NPs with oppositely charged polyelectrolyte brushes and their effect on cell uptake
Yuan Qiu, Elena Rojas, Danjiena, Danijela Gregurec, Pablo Castro Hartmann and Sergio Moya (Manuscript in preparation)

Design of hybrid multimodal poly(lactic-*co*-glycolic acid) polymer nanoparticles for neutrophil labeling, imaging and tracking
Yuan Qiu, Raghavendra Palankar, María Echeverría, Nikolay Medvedev, Sergio E. Moya and Mihaela Delcea;
Nanoscale; 2013, 5, 12624-12632; DOI: 10.1039/C3NR04013E

A Quantitative Study of the Intracellular Dynamics of Fluorescently Labelled Glyco-Gold Nanoparticles via Fluorescence Correlation Spectroscopy
Richard A. Murray, **Yuan Qiu**, Fabrizio Chiodo , Marco Marradi, Soledad Penadés and Sergio E. Moya
Small ; Article first published online: 17 MAR 2014**;** DOI: 10.1002/smll.201303604

A novel approach to monitor intracellular degradation kinetics of poly (lactide-*co*-glycolide) nanoparticles by means of flow cytometry
Gabriela Romero, María Echeverría, **Yuan Qiu**, Richard A. Murray and Sergio E. Moya
Journal of Materials Chemistry B; 2014, 2, 826-833 DOI: 10.1039/C3TB21330G

Study of Intracellular Delivery of Doxorubicin from Poly (lactide-*co*-glycolide) Nanoparticles by Means of Fluorescence Lifetime Imaging and Confocal Raman Microscopy;
Gabriela Romero, **Yuan Qiu**, Richard A. Murray and Sergio E. Moya
Macromolecular Bioscience; 2013, 13(2), 234-41. DOI: 10.1002/mabi.201200235

Lipid layer engineering of poly(lactide-*co*-glycolide) nanoparticles to control their uptake and intracellular co-localisation;
Gabriela Romero, David J. Sanz, **Yuan Qiu**, Dahai Yu, Zhengwei Mao, Changyou Gao and Sergio E. Moya
Journal of Materials Chemistry B; 2013, 1, 2252-2259; DOI: 10.1039/C3TB00284E

Layer by layer surface engineering of poly (lactide-co-glycolide) nanoparticles: A versatile tool for nanoparticle engineering for targeted drug delivery
Gabriela Romero, Richard A. Murray, **Yuan Qiu**, David Sanz, Sergio E. Moya
Science China Chemistry; 2013, 56(8), 1029-1039; DOI: 10.1007/s11426-013-4891-z